

**Computational studies of transition metal-catalyzed olefin functionalization and cross-coupling reactions**

by

**Ilia Kevlishvili**

Bachelor of Arts, Franklin & Marshall College, 2016

Submitted to the Graduate Faculty of the  
Dietrich School of Arts and Sciences in partial fulfillment  
of the requirements for the degree of  
Doctor of Philosophy

University of Pittsburgh

2021

UNIVERSITY OF PITTSBURGH

DIETRICH SCHOOL OF ARTS AND SCIENCES

This dissertation was presented

by

**Ilia Kevlishvili**

It was defended on

June 1, 2021

and approved by

Dennis Curran, Professor, University of Pittsburgh

Yiming Wang, Assistant Professor, University of Pittsburgh

John Keith, Associate Professor, University of Pittsburgh

Dissertation Advisor: Peng Liu, Associate Professor, University of Pittsburgh

Copyright © by Ilia Kevlishvili

2021

# **Computational studies of transition metal-catalyzed olefin functionalization and cross-coupling reactions**

Ilia Kevlishvili, PhD

University of Pittsburgh, 2021

Transition metal-catalyzed reactions have become one of the most critical tools for organic chemists. In particular, olefin functionalization and cross-coupling reactions provide access to a wide array of interesting compounds. Understanding reaction mechanisms play a crucial role in discovering new reactions and increasing the selectivity and scope of existing reactions. However, experimental methods are often insufficient to understand key mechanistic insights, and new reaction discovery often relies on trial-and-error. To address these challenges, I present a series of density functional theory (DFT) calculations to study the reaction mechanisms of various transition metal-catalyzed olefin functionalization and cross-coupling reactions. I applied a wide variety of computational methods, including energy decomposition analysis (EDA), distortion-interaction analysis, ligand steric contour plots, and conformational sampling, to understand complex factors that could promote reactivity or selectivity, such as ligand and substrate effects, conformational flexibility of ligands and substrates, and solvent and additive effects. Insights into the factors that promote reactivity are then used for a mechanistically guided catalyst design for improving reactivity.

Specifically, these computational approaches were applied to study copper-catalyzed hydroamination of olefins, copper-catalyzed allylation of indazoles, palladium-catalyzed regio-

divergent cross-coupling of 3,5-dibromo-pyrone, a series of cross-coupling reactions of carbohydrates, and tandem nickel/zinc-catalyzed boron insertion into alkyl ether bonds.

## Table of contents

Preface.....	xx
1.0 Introduction.....	1
2.0 Computational study of ligand effects to guide the experimental design of ligands with improved efficiency in CuH-catalyzed hydroamination reactions.....	7
2.1 Introduction .....	7
2.2 Computational details .....	13
2.3 Results and discussions .....	15
2.3.1 Origin of the reactivity trends with 2-L3 and 2-L4.....	15
2.3.2 Proposal of a more reactive CuH-catalyst supported by ligand 2-L5 .....	21
2.3.3 Computational studies of hybrid SEGPHOS ligands .....	22
2.3.4 Validation of computationally predicted reactivity trends .....	29
2.3.5 Comparison of the 1 <sup>st</sup> and 2 <sup>nd</sup> generation ALMO-EDA methods.....	30
2.3.6 The effect of quasiharmonic approximation .....	31
2.3.7 Catalyst reactivity with other substrates .....	33
2.4 Conclusions .....	34
3.0 Reactivity of amine electrophiles in CuH-catalyzed hydroamination of olefins .....	36
3.1 Introduction .....	36
3.2 Computational details .....	39
3.3 Results and discussions .....	41
3.3.1 Hemilabile nature of SEGPHOS ligands in the oxidative addition of hydroxylamine electrophiles .....	41

3.3.2 Oxidative addition to copper hydride is more sensitive to electrophile electronic effects than oxidative addition to alkyl complexes. ....	48
3.3.3 Tertiary alkyl copper complexes hinder oxidative addition due to unfavorable steric effects.....	53
3.3.4 Through space ligand electrophile dispersion interactions promote oxidative addition transition states .....	55
3.4 Conclusion .....	61
4.0 Cu-H catalyzed allylation of indazoles to form a C3-quaternary chiral center .....	64
4.1 Introduction .....	64
4.2 Computational details .....	67
4.3 Results and discussions .....	68
4.3.1 Hydrocupration of allenes .....	68
4.3.2 Reactivity differences between indole and indazole.....	69
4.3.3 Origin of enantioselectivity.....	73
4.4 Conclusion .....	79
5.0 Regio-controlled cross-coupling of 3,5-dibromo-2-pyrones.....	81
5.1 Introduction .....	81
5.2 Computational details .....	85
5.3 Results and discussions .....	86
5.3.1 Oxidative addition in the absence of CuI.....	86
5.3.2 Oxidative addition in the presence of CuI .....	89
5.3.3 C5 selectivity in Stille coupling .....	97
5.4 Conclusion .....	100

<b>6.0 Cross-coupling of carbohydrates for the synthesis of C-aryl glycosides .....</b>	<b>102</b>
<b>6.1 Introduction .....</b>	<b>102</b>
<b>6.2 Computational study on the stereospecific cross-coupling reactions of anomeric stannanes for the synthesis of C-aryl glycosides .....</b>	<b>106</b>
<b>6.2.1 Mechanistic background .....</b>	<b>106</b>
<b>6.2.2 Computational details .....</b>	<b>109</b>
<b>6.2.3 Results and discussions .....</b>	<b>110</b>
<b>6.2.3.1 Reaction mechanisms .....</b>	<b>110</b>
<b>6.2.3.2 <math>\beta</math>-Methoxy elimination suppressed by the JackiePhos ligand .....</b>	<b>113</b>
<b>6.2.3.3 Reactivities of <math>\alpha</math> and <math>\beta</math> anomers .....</b>	<b>114</b>
<b>6.2.3.4 Summary .....</b>	<b>116</b>
<b>6.3 Nickel-catalyzed C-2 arylation of carbohydrates via radical migratory coupling .....</b>	<b>117</b>
<b>6.3.1 Mechanistic background .....</b>	<b>117</b>
<b>6.3.2 Computational details .....</b>	<b>119</b>
<b>6.3.3 Results and discussions .....</b>	<b>120</b>
<b>6.3.3.1 C-Br activation mechanism .....</b>	<b>120</b>
<b>6.3.3.2 Carbon-carbon coupling pathways and regioselectivity .....</b>	<b>122</b>
<b>6.3.3.3 Origin of stereoselectivity .....</b>	<b>126</b>
<b>6.3.3.4 Summary .....</b>	<b>128</b>
<b>6.4 Conclusion .....</b>	<b>129</b>
<b>7.0 Boron insertion into alkyl ether bonds via reductive zinc and nickel catalysis .....</b>	<b>131</b>
<b>7.1 Introduction .....</b>	<b>131</b>
<b>7.2 Computational details .....</b>	<b>134</b>



<b>7.3 Results and discussions .....</b>	<b>135</b>
<b>7.3.1 Most favorable pathway .....</b>	<b>135</b>
<b>7.3.2 Mechanisms of the C–O cleavage (ring-opening) cycle .....</b>	<b>138</b>
<b>7.3.3 C-Br cleavage and C–B bond formation mechanisms .....</b>	<b>142</b>
<b>7.3.4 C–Br cleavage mechanism in the reaction with secondary alkyl ether .....</b>	<b>144</b>
<b>7.3.5 Radical chain mechanism .....</b>	<b>146</b>
<b>7.3.6 Born-Oppenheimer molecular dynamics (BOMD) trajectory simulations .....</b>	<b>149</b>
<b>7.3.7 Calculations of the C–Br and B–Br cleavage of 7-4 with different nickel species .....</b>	<b>151</b>
<b>7.3.8 Calculations of the reduction of Ni species by Zn .....</b>	<b>153</b>
<b>7.3.9 Reaction energy of transmetalation between an organozinc and a nickel(I) bromide .....</b>	<b>155</b>
<b>7.4 Conclusion .....</b>	<b>156</b>
<b>Appendix A List of publications .....</b>	<b>158</b>
<b>Bibliography .....</b>	<b>160</b>

## List of tables

Table 2-1 Activation free energies of the hydrocupration transition states and energy components derived from the ligand-substrate interaction model for initially screened ligands. <sup>a</sup> .....	17
Table 2-2 Gibbs free energies of the $\pi$ -complexes and hydrocupration transition states with the DTBM-SEGPHOS (2-L2) and CF3-SEGPHOS (2-L4) ligands. <sup>a</sup> .....	19
Table 2-3 Activation free energies of the hydrocupration transition states and energy components derived from the ligand-substrate interaction model for newly designed ligands. ....	24
Table 2-4 Comparison of 1 <sup>st</sup> and 2 <sup>nd</sup> generation ALMO-EDA methodologies. <sup>a,b</sup> .....	31
Table 2-5 Computed hydrocupration barriers with SEGFAST and DTBM-SEGPHOS-supported CuH catalysts and different substrates. All energies are in kcal/mol relative to a free olefin and LCuH.....	34
Table 3-1 Distortion interaction analysis of the three competing oxidative addition transition states <sup>a</sup> .....	46
Table 3-2 Activation energies for the oxidative addition of hydroxylamine 3-E1 to various different alkyl copper complexes. All energies are relative to the alkyl copper complex and electrophile 3-E1. ....	54
Table 5-1 Suzuki couplings with 3,5-dibromo-2-pyrone .....	83

## List of figures

<b>Figure 2-1 Selected examples of copper-catalyzed hydroamination .....</b>	<b>8</b>
<b>Figure 2-2 a) LCuH-catalyzed anti-Markovnikov hydroamination reaction. b) Proposed catalytic cycle for LCuH-catalyzed anti-Markovnikov hydroamination reaction. c) SEGPHOS 2-L1 and DTBM-SEGPHOS 2-L2 ligands.....</b>	<b>9</b>
<b>Figure 2-3 a) Ligand-substrate interaction model to study the origin of reactivity in hydrocupration. b) London dispersion interactions lowering the hydrocupration barrier for L<sub>2</sub>CuH. ....</b>	<b>11</b>
<b>Figure 2-4 Iterative ligand design approach .....</b>	<b>13</b>
<b>Figure 2-5 Hydrocupration with CuH catalysts supported by different SEGPHOS-derived ligands .....</b>	<b>16</b>
<b>Figure 2-6 Contributions of different types of catalyst-substrate interactions to the reactivity. The <math>\Delta\Delta E</math> values are calculated from the energy difference between 2-TS3 (L=TMS-SEGPHOS)/ 2-TS4 ( L=CF<sub>3</sub>-SEGPHOS) and 2-TS2 (L=DTBM-SEGPHOS). Positive <math>\Delta\Delta E</math> values indicate effects that promote reactions catalyzed by the DTBM-SEGPHOS supported catalyst; negative <math>\Delta\Delta E</math> values indicate effects that promote reactions catalyzed by the other ligand supported catalyst. The energies are in kcal/mol.....</b>	<b>19</b>
<b>Figure 2-7 Optimized geometries of hydrocupration transition states with the DTBM-SEGPHOS (2-TS-2) and CF<sub>3</sub>-SEGPHOS ligands (2-TS-4). Distances are in Ångström [Å]. ....</b>	<b>20</b>

Figure 2-8 Contributions of different types of catalyst-substrate interactions to the regioselectivity. The $\Delta\Delta E$ values are calculated from the energy difference between 2-TS5 (L= <i>i</i> -C <sub>3</sub> F <sub>7</sub> -SEGPLHOS) and 2-TS2 (L=DTBM-SEGPLHOS). Positive $\Delta\Delta E$ values indicate effects that promote reactions catalyzed by the DTBM-SEGPLHOS catalyst; negative $\Delta\Delta E$ values indicate effects that promote reactions catalyzed by the <i>i</i> -C <sub>3</sub> F <sub>7</sub> -SEGPLHOS-supported catalyst. The energies are in kcal/mol.....	21
Figure 2-9 Experimental kinetic studies of hydroamination of 4-phenyl-1-butene. Experiments conducted by the Buchwald group .....	23
Figure 2-10 Optimized geometries of hydrocupration transition states with the <i>i</i> -C <sub>3</sub> F <sub>7</sub> -SEGPLHOS (2-TS-5) and the hybrid DTBM- <i>i</i> -C <sub>3</sub> F <sub>7</sub> -SEGPLHOS ligand (2-TS-6 and 2-TS-6a). Distances are reported in angström [Å]. .....	26
Figure 2-11 Electrostatic and dispersion interactions between heptafluoro isopropyl groups and propene. Energies are reported in kcal/mol.....	27
Figure 2-12 Scope of hydroamination of terminal olefins with SEGPLAST 2-L6 ligand. Experiments were conducted by the Buchwald group. <sup>a</sup> Reaction conducted with DTBM-SEGPLHOS. ....	29
Figure 2-13 Linear correlation between the computed relative rates ( $\ln(k/k_0)$ ) <sub>theory</sub> ) and experimental relative initial rates ( $\ln(k/k_0)$ ) <sub>experiment</sub> ). ....	30
Figure 2-14 Linear correlation between the computed relative rates ( $\ln(k/k_0)$ ) <sub>theory</sub> ) without quasi-harmonic correction and experimental relative initial rates ( $\ln(k/k_0)$ ) <sub>experiment</sub> ). ....	32
Figure 2-15 Linear correlation between the computed relative solvated activation energies ( $-\Delta\Delta H^\ddagger_{\text{solv}}$ ) and experimental relative initial rates ( $\ln(k/k_0)$ ) <sub>experiment</sub> ). ....	33

<b>Figure 2-16 Summary of the computationally guided ligand design for CuH-catalyzed olefin hydroamination. ....</b>	<b>35</b>
<b>Figure 3-1 (a) Reactivity of trans-4-octene in CuH-catalyzed hydroamination with different hydroxylamine electrophile reagents. (b) Possible reactions of copper hydride with different reaction components. (c) Challenges associated with the hydroamination of olefins. ....</b>	<b>36</b>
<b>Figure 3-2 Catalytic cycles for the hydroamination and amine reduction in CuH catalyzed olefin hydroamination .....</b>	<b>38</b>
<b>Figure 3-3 Reaction mechanism for the hydroamination of trans-2-butene. All energies are relative to 3-1, 3-S1, and 3-E1.....</b>	<b>43</b>
<b>Figure 3-4 A. 3D structures of bidentate alkyl copper complex 3-2 and the monodentate ligated complex 3-3. B. potential energy surface for the rotation of CCPCu dihedral. All energies are relative to complex 3-2.....</b>	<b>44</b>
<b>Figure 3-5 3D structures for different ligand conformations during electrophile oxidative addition. All energies are relative to the intermediate 3-2 and 3-E1.....</b>	<b>45</b>
<b>Figure 3-6 Competing conformations for the oxidative addition transition states to the copper hydride, leading to the amine reduction. All energies are relative to 3-1 and 3-E1.....</b>	<b>48</b>
<b>Figure 3-7 A. 3D structures of two oxidative addition transition states. The activation free energies for 3-TS3 and 3-TS2 are in kcal/mol with respect to 3-2 and 3-1, respectively B. Ligand substrate-interaction analysis of two oxidative addition transition states. Color code: Brown – catalyst distortion, light brown – electrophile distortion, light green – through space interaction, dark green – bonding interaction, black –</b>	

activation energy. C. NPA charge analysis of 3-E1 and oxidative transition states 3-TS3 and 3-TS2.....	50
<b>Figure 3-8 A. Activation energies for the oxidative addition to copper hydride (3-TS2) and alkyl copper complex (3-TS3) with different hydroxylamines. B. Correlation between the activation energies for the oxidative addition transition states with LCuH and with LCuR where R = 2-butyl and NPA charge on the nitrogen atom of the hydroxylamine.....</b>	<b>52</b>
<b>Figure 3-9 A. 3D structures of oxidative addition transition states with primary alkyl copper complex 3-TS3-S2 and tertiary alkyl copper complex 3-TS3-S6.....</b>	<b>55</b>
<b>Figure 3-10 Competing conformations for the oxidative addition transition states to the SEGPHOS-ligated copper 2-butyl complex. All energies are relative to 3-2-L2 and 3-E1.....</b>	<b>56</b>
<b>Figure 3-11 Ligand effects on the CuH catalyzed hydroamination of olefins. Computed activation free energies (<math>\Delta G^\ddagger</math>) of the hydrocupration and oxidative addition to copper hydride steps with respect to the separated LCuH, olefin 3-S1, and hydroxylamine 3-E1. Oxidative addition to copper alkyl groups is calculated with respect to the LCuR complex and hydroxylamine 3-E1.....</b>	<b>58</b>
<b>Figure 3-12 3D structures of oxidative addition transition states with SEGPHOS ligated copper 3-TS3-L2 and 3-TS2-L2. B. Ligand substrate-interaction analysis of three oxidative addition transition states. Color code: Brown – catalyst distortion, yellow – electrophile distortion, blue – through space interaction, green – through bond interaction, black – activation energy. C. Energy decomposition analysis of through space ligand-electrophile interaction.....</b>	<b>60</b>

<b>Figure 3-13 Key dispersion interactions between the electrophile and tert-butyl groups.</b>	
Numbers in purple represent the favorable dispersion interactions between an electrophile and corresponding tert-butyl group in kcal/mol.....	61
<b>Figure 3-14 Reactivity of different olefin reagents .....</b>	<b>62</b>
<b>Figure 4-1 (a) CuH-catalyzed asymmetric alkylation of indole electrophiles. (b) Proposed     CuH-catalyzed asymmetric C3-allylation of indazole electrophiles.....</b>	<b>65</b>
<b>Figure 4-2 Comparison of indazole and indole electrophiles with styrene and allene     pronucleophiles. B. Goals of computational investigation. ....</b>	<b>66</b>
<b>Figure 4-3 Enantioselectivity of allenes with different substitution patterns in the indazole     allylation reaction.....</b>	<b>67</b>
<b>Figure 4-4 Calculated energies and 3D structures of competing hydrocupration transition     states. All energies are relative to the separated LCuH catalyst 4-13 and allene 4-9.     All energies are in kcal/mol.....</b>	<b>69</b>
<b>Figure 4-5 Energy profiles of the allylation of indazole (4-2) and indole (4-3) electrophiles.     .....</b>	<b>71</b>
<b>Figure 4-6 (A) Optimized structures of the C3-oxidative addition transition states with     indazole (4-TS3) and indole (4-TS6) substrates. (B) Calculated N–O bond dissociation     enthalpies (BDEs) of 4-2 and 4-3. ....</b>	<b>72</b>
<b>Figure 4-7 Calculations of competing six-member reaction pathways .....</b>	<b>74</b>
<b>Figure 4-8 (A) Newman projections along the forming C-C bond. (B) Origin of     enantioselectivity .....</b>	<b>76</b>
<b>Figure 4-9 Calculated ligand distortion energies (<math>\Delta E_{\text{dist-Ph-PBE}}</math>) and steric contour plots of     the Ph-BPE ligand in 4-13, 4-TS2a, and 4-TS2b. All energies are in kcal/mol. ....</b>	<b>78</b>

Figure 4-10 Computed enantioselectivities with different allene substrates. ....	79
Figure 5-1 A. Regiodivergent coupling of 3,5-dibromo-2-pyrone (5-1) controlled by the solvent and additives. B. Goals of computational investigation .....	82
Figure 5-2 Influence of temperature on ratios of C3- to C5-Pd complexes. ....	85
Figure 5-3 Oxidative addition in the absence of copper iodide .....	87
Figure 5-4 The distortion energies of the PdL <sub>2</sub> catalyst ( $\Delta E_{\text{dist-cat}}$ ) and the pyrone substrate ( $\Delta E_{\text{dist-sub}}$ ), and the interaction energies between these two fragments in the oxidative addition transition states ( $\Delta E_{\text{int}}$ ) in the absence of CuI .....	88
Figure 5-5 Alternative oxidative addition mechanisms in the presence of CuI .....	90
Figure 5-6 Computed ligand exchange energies from the bis-phosphine ligated Pd complex 5-7 to form the mono-phosphine ligated complexes 5-15 and 5-16 .....	92
Figure 5-7 Oxidative addition in the presence of CuI .....	93
Figure 5-8 The distortion energies of the PdL <sub>1</sub> catalyst ( $\Delta E_{\text{dist-cat}}$ ) and the pyrone substrate ( $\Delta E_{\text{dist-sub}}$ ) and the interaction energies between these two fragments in the oxidative addition transition states ( $\Delta E_{\text{int}}$ ) in the presence of CuI.....	94
Figure 5-9 A) Decomposition of substrate distortion energy. B) BDEs of C–Br bonds of 3,5- dibromo-pyrone 5-1. ....	95
Figure 5-10 Oxidative addition with mono-phosphine ligated palladium bound to DMF...	96
Figure 5-11 Binding of CuI to all bis-phosphine ligated palladium (II) oxidative addition products. ....	96
Figure 5-12 A. Stille cross-coupling reaction of 3,5-dibromo-pyrone. The experiment was conducted by the Sarpong group. B. Transmetallation and reductive elimination steps in the Pd-catalyzed Stille cross-coupling reaction of 3,5-dibromo-2-pyrone.....	98



Figure 5-13 Relative activation energies of transmetallation in an implicit solvent ( $\Delta\Delta G^\ddagger_{\text{DMF}}$ ) and in the gas phase ( $\Delta\Delta G^\ddagger_{\text{gas}}$ ). .....	100
Figure 6-1 A. Stereoretentive Stille coupling of anomeric stannanes. The use of JackiePhos suppresses the production of undesirable glycal 6-3. B. Goals of computational investigation.....	104
Figure 6-2 Competition of the $\alpha$ and $\beta$ anomeric stannanes. ....	105
Figure 6-3 A. Ni-catalyzed migratory cross-coupling reaction for the catalytic synthesis of challenging 2-aryl-2-deoxy sugars B. Goals of computational investigation.....	106
Figure 6-4 Proposed catalytic cycle for the Stille coupling reaction. ....	108
Figure 6-5 Reaction energy profile of the Pd-catalyzed Stille coupling of bromobenzene and tetrahydropyranyl stannane 3-12 using JackiePhos ligand. ....	111
Figure 6-6 Different possible transmetallation mechanisms.....	112
Figure 6-7 Reaction energy profile of the $\beta$ -methoxy elimination pathway. All energies are with respect to complex 3-16.....	114
Figure 6-8 Transition states of transmetallation of $\alpha$ and $\beta$ anomers (6-19 and 6-10). .....	116
Figure 6-9 Possible Ni(I) catalyzed migratory cross-coupling mechanisms .....	118
Figure 6-10 Determination of the most favorable reaction pathway .....	121
Figure 6-11 Ligand substrate interaction analysis of two bromine atom abstraction transition states .....	122
Figure 6-12 Mechanism for bond formation at the C1 position .....	123
Figure 6-13 Mechanism for coupling at the C2 position .....	124
Figure 6-14 NPA charge analysis of Ni(III) intermediates, 6-26 and 6-30, and corresponding reductive elimination transition state structures. ....	126

Figure 6-15 Relative energies of radical rebound transition states using real substrate and their distortion interaction analysis. ....	128
Figure 6-16 Proposed catalytic cycle .....	129
Figure 7-1 Nickel/Zinc tandem catalyzed C–O bond borylation reaction.....	132
Figure 7-2 a. Identification of reaction intermediate. b. Radical-clock experiment. c. Control experiments with a 98% ee substrate. d. Goals of computational investigations. ..	133
Figure 7-3 Computed energy profile of the catalytic borylation of ether 1a. ....	137
Figure 7-4 A. Gibbs free energies of monomeric zinc complexes. All energies are in kcal/mol relative to 7-20. B. Gibbs free energies of dimeric zinc complexes. All energies are in kcal/mol relative to 7-10. ....	139
Figure 7-5 Reaction Gibbs free energies of dimerization of 7-20 and 7-10 to form Zn(II) dimer and tetramers (7-10 and 7-28, respectively). ....	139
Figure 7-6 Different mechanisms explored for the ring-opening of the ether.....	141
Figure 7-7 Possible mechanisms for the C–Br cleavage and C–B bond formation from the nickel(I) boryl intermediate. All energies are relative to complex 7-15.....	143
Figure 7-8 C–Br cleavage mechanisms and radical rebound in the reaction with the secondary alkyl ether. All energies are in kcal/mol relative to 7-29.....	145
Figure 7-9 Modified nickel-catalyzed radical chain mechanism with intermediate 7-4. ...	146
Figure 7-10 Potential energy profile of the radical chain mechanism. All energies are Gibbs free energies in kcal/mol relative to 7-4 and NiL <sub>2</sub> Br.....	148
Figure 7-11 Snapshots from a representative trajectory of the BOMD simulation from 7-TS4.....	150

<b>Figure 7-12 Activation Gibbs free energies of the B–Br and C–Br cleavage pathways to initiate the C–B rebound cycle.....</b>	<b>152</b>
<b>Figure 7-13 Gibbs free energies of half-reactions used to calculate the reaction energies of the Zn-mediated reduction of Ni(II) species. ....</b>	<b>154</b>
<b>Figure 7-14 Calculated Gibbs free energy of the transmetalation reaction between the organozinc and nickel bromide.....</b>	<b>156</b>
<b>Figure 7-15 Proposed reaction mechanism based on the DFT calculations and mechanistic experiments.....</b>	<b>157</b>

## **Preface**

I would like to express my sincerest gratitude towards my advisor, Prof. Peng Liu, for his guidance and support during my studies at Pitt. I have benefitted greatly from his guidance and learned how to approach new and interesting subject matter and gain a deep understanding of challenging topics.

I would like to show my appreciation to all my collaborators for many meaningful discussions.

I would like to thank all of my group members for their support. I would also like to express my great appreciation for Prof. Xiaotian Qi from our group for many meaningful discussions throughout his time in the group.

I would like to thank the School of Arts and Sciences Fellowship, Goldblatt Fellowship, and PQI Fellowship for their financial support.

I would like to thank my parents and the rest of my family for their continuous support throughout my academic career. Finally, I would like to thank and dedicate this thesis to my wife, Natia Karchava, and my children Leah and George for their love and support.

## 1.0 Introduction

Transition metal-catalyzed reactions are among the most important reactions to achieve novel reactivity and selectivity for synthetic organic applications. Some of the most important applications in transition metal-catalyzed reactions include cross-coupling reactions, which have found wide applications in organic synthesis since the early 1970s<sup>1</sup> and have become one of the most common classes of transformations used in the pharmaceutical industry.<sup>2</sup> Another important application of the transition metal-catalyzed reactions includes the functionalization of olefins,<sup>3</sup> which is an atom economical approach for installing novel functional groups onto naturally abundant building blocks. In particular, hydroamination of olefins provides an efficient route for the enantioselective C–N bond formations.<sup>4</sup> With more than 80 percent of FDA approved small molecule drugs containing a carbon-nitrogen bond,<sup>5</sup> efficient methods for forming new C–N bonds are of utmost importance. Often, achieving high reactivity and selectivity in transition metal-catalyzed reactions relies on the proper understanding of the reaction mechanism and rate- and enantioselectivity-determining steps. The design of transition metal-catalyzed reactions is heavily dependent on the proper choice of ancillary ligands, such as phosphines<sup>6</sup> and N-heterocyclic carbenes.<sup>7</sup> A properly chosen ligand can promote the reactivity, regio-, diastereo-, and enantioselectivity, as well as suppress undesired reactions. These outcomes can be fine-tuned by carefully optimizing ligand-substrate interactions in the rate- and selectivity-determining transition states. However, studying reaction mechanisms and ligand effects using experimental approaches are often complicated by challenges associated with trapping reaction intermediates and lack of experimental procedures to observe short-lived transition states. Instead, experimental groups

often rely on screening large libraries of available ligands during the reaction development,<sup>8</sup> which can be associated with high costs and time consumption.

Recently, computational approaches, in particular density functional theory (DFT) calculations, have been used to address some of the challenges associated with experimental mechanistic studies.<sup>9</sup> Through DFT calculations, reaction intermediates and transition states are calculated. The reaction potential energy profile is constructed, where rate- and selectivity determining steps (RDS and SDS) can be identified using transition state theory. Their structures can be used to understand factors promoting reactivity and selectivity.

Therefore, DFT calculations can be successfully applied to study the reaction mechanisms and understand factors that promote reactivity that would be difficult to understand through conventional experimental mechanistic studies. While there have been several methods developed to study the ligand effects, they primarily focus on the through-bond metal-substrate interactions dependent on the ligand's electronic parameters and the through-space repulsion between the ligand and the substrate described by ligand steric parameters.<sup>10</sup> However, attractive through-space interactions between the ligand and the substrate are often employed as a design principle in catalyst development and ligand screening. Several examples have been demonstrated where these attractive through-space interactions, such as electrostatic<sup>11</sup> and dispersion<sup>12</sup> interactions between the ligand and the substrate, play an important role in promoting transition metal-catalyzed reactions. In this thesis, I performed calculations to study the mechanisms, reactivity, and selectivity of various transition metal-catalyzed systems, to understand the effects of ancillary ligands, solvents, and additives in these reactions. Then, I used these understandings to make predictions for the design of improved ancillary ligands, which can guide the experimental development of new catalytic systems with improved reactivity, regio-, and stereoselectivity.

The study of ligand effects can consist of two primary aspects. First, a detailed understanding of the mechanism is essential to understand the role of the ligand. Deciphering the mechanism can help identify the elementary steps in the mechanism that controls the rate, regio-, and stereoselectivity of the reaction, as well as pathways leading to undesirable byproducts. With the proper understanding of important transition states, the effects of the ligand can be dissected further to gain valuable insight into the ability of a certain ligand to promote the reactivity and selectivity of a reaction.

The computational studies of the mechanisms were performed using density functional theory (DFT) in Gaussian 09<sup>13</sup> and Gaussian 16.<sup>14</sup> DFT strikes a good balance in studying these systems, between the accuracy and cost, compared to wave function theory (WFT) methods. The most common density functional employed in transition metal-catalyzed reactions for geometry optimization is B3LYP,<sup>15</sup> which is employed in my studies and usually provides satisfactory geometries for transition states and intermediates. More recently, dispersion-corrected functionals have been used more often to improve calculated geometries. Dispersion correction usually relies on Grimme's DFT-D3 correction<sup>16</sup> and has been employed in my more recent studies. Depending on the system, M06<sup>17</sup> and  $\omega$ -B97X-D<sup>18</sup> functionals with a larger basis set are employed for the single point energy calculations. Implicit solvation models such as the SMD<sup>19</sup> and CPCM<sup>20</sup> have been used in my calculations to account for solvent effects.

To further dissect important interactions in the key transition states, one of the important methods used in my studies includes the 2<sup>nd</sup> generation of absolutely localized molecular orbital energy decomposition analysis (ALMO-EDA)<sup>21</sup> in Q-Chem 5.0.<sup>22</sup> The 1<sup>st</sup> generation of ALMO-EDA<sup>23</sup> decomposes interaction energy between interacting species into various chemically meaningful terms, namely, the "frozen density" component ( $\Delta E_{\text{froz}}$ ), calculated from the energy

arising from bringing two infinitely separated fragments together without any relaxation of molecular orbitals (MOs), polarization energy ( $\Delta E_{\text{pol}}$ ), calculated by allowing intrafragment MO relaxation, corresponding to temporary electrostatic interactions, and charge transfer ( $\Delta E_{\text{ct}}$ ), calculated by allowing interfragment MO relaxation, and corresponding to secondary donor-acceptor-type orbital interactions. The 2<sup>nd</sup> generation of ALMO-EDA further decomposes the  $\Delta E_{\text{frz}}$  term to the combination of permanent electrostatic ( $\Delta E_{\text{elec}}$ ), London dispersion ( $\Delta E_{\text{disp}}$ ), and Pauli repulsion ( $\Delta E_{\text{pauli}}$ ) interactions. Permanent electrostatic interactions ( $\Delta E_{\text{elec}}$ ) can be calculated by looking at the Coulomb interactions between isolated fragment charge distributions. London dispersion ( $\Delta E_{\text{disp}}$ ) interactions can be calculated by taking the difference between the primary functional and a dispersion free functional (for example, the Hartree-Fock “functional”). Then, Pauli repulsion ( $\Delta E_{\text{pauli}}$ ) can be calculated by subtracting  $\Delta E_{\text{elec}}$  and  $\Delta E_{\text{disp}}$  from the “frozen density” component ( $\Delta E_{\text{frz}}$ ). Although there have been some examples in the application of EDA to study transition metal-catalyzed reactions,<sup>24</sup> they primarily focus on bond forming interactions, while through-space interactions between the ligand and the substrate are often overlooked. While the magnitude of ligand-substrate interactions is often much smaller than the magnitude of bonding interactions, they often play a key role in controlling reactivity and selectivity, and EDA of through-space interaction provides a simple interpretation of its nature. I calculated through-space interaction by constructing a theoretical ligand-substrate complex, by removing the metal center, and retaining the transition state geometry of the ligand and the substrate. Through-space interaction analysis is a powerful tool because by understanding the nature of the interaction between the ligand and the substrate, the ligand can be rationally fine-tuned to either further promote existing favorable interactions or promote other factors that are not relevant to the existing ligand.



Another important aspect in studying reaction mechanisms involves careful consideration of conformational space for flexible ligands and substrates. To address this challenge during my studies, I have used the Conformer–Rotamer Ensemble Sampling Tool (CREST).<sup>25</sup> CREST is a conformer sampling program that relies on generating conformer-rotamer ensembles using extensive metadynamic sampling based on the semiempirical tight-binding GFNn-XTB method.<sup>26</sup> Iterative approach coupled together with farther MD sampling of the low energy conformers ensures good coverage of conformational space. I applied the conformer sampling approach to study conformationally flexible systems, such as cross coupling of carbohydrates, where the substrate is conformationally flexible, or to consider ligand conformations of SEGPPOS-derived ligands, where the catalyst is conformationally flexible. To study the ligand effects of conformationally flexible systems, I have used approaches such as distortion-interaction analysis<sup>27</sup> for quantitative understanding of ligand distortions and ligand steric contour plots<sup>28</sup> that can describe the steric environment around the metal center for qualitative analysis of ligand effects.

While most of my work relies heavily on the transition state theory, sometimes, transition states fail to describe reactivities and selectivities, possibly due to nonstatistical dynamic effects. To address this challenge, I have used quasiclassical trajectory simulations using Born-Oppenheimer molecular dynamics (BOMD)<sup>29</sup> calculations as implemented in Gaussian 16.<sup>14</sup> This approach relies on using quasi-classical molecular dynamics simulation calculating optimized geometries, energies, and forces on the potential energy surface using quantum mechanical methods such as DFT. Therefore, BOMD simulations can be used to generate an accurate time-resolved mechanism of a chemical transformation starting from a transition state. This approach has often been used to understand bifurcating mechanisms<sup>30</sup> and dynamically concerted/stepwise mechanisms.<sup>31</sup> In my work, I used BOMD calculation to study whether a cross-coupling reaction

involved a dynamically stepwise or concerted mechanism for oxidative addition/reductive elimination because the oxidative addition product ground state intermediate could not be located due to a low-lying transition state.

In this thesis, I present my computational investigations for the transition metal-catalyzed olefin functionalization and cross-coupling reactions. The primary goal of these investigations includes understanding the reaction mechanisms and ligand, substrate, additive, and solvent effects on reactivity and selectivity, with further aspirations to use these insights for the design of more reactive and selective reactions:

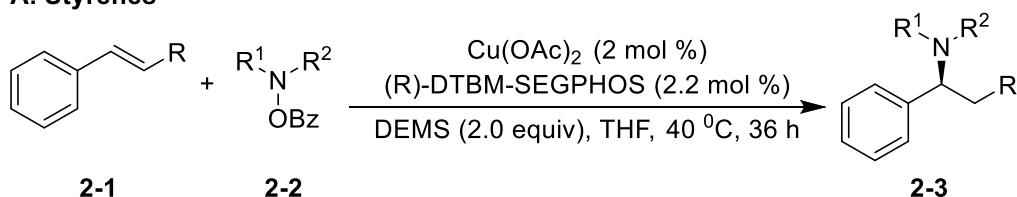
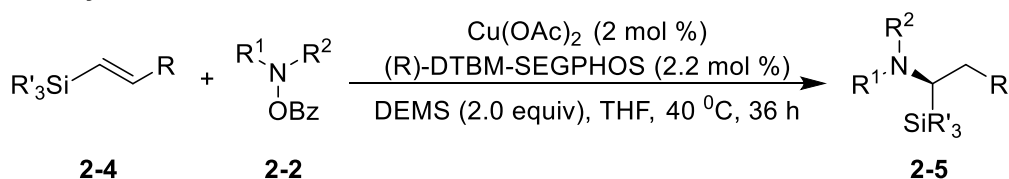
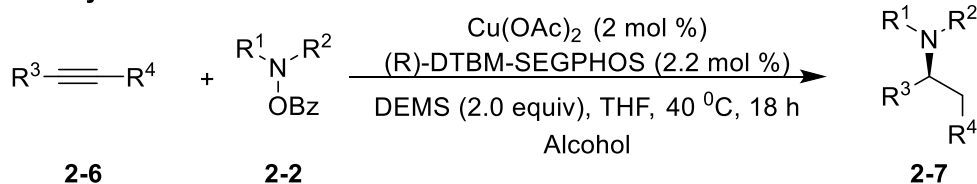
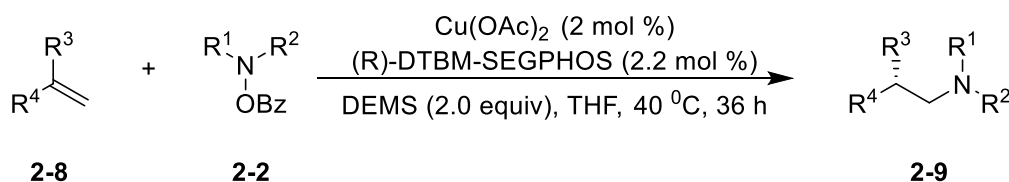
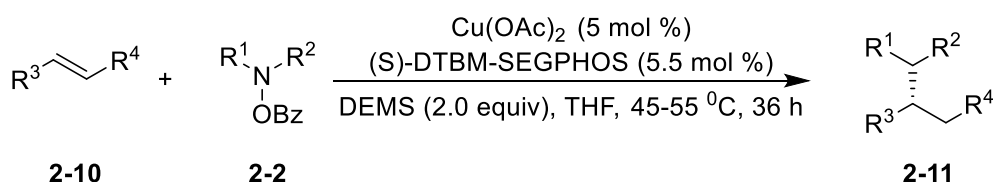
- Chapter 2 demonstrates using calculations to understand ligand effects in CuH-catalyzed hydroamination of olefins and to use these insights for the design of more reactive catalytic systems.
- Chapter 3 involves the study of the reactivity of hydroxylamine electrophiles in CuH-catalyzed hydroamination and studying the effects of different ligands, substrates, and electrophiles in these reactions.
- Chapter 4 presents a mechanistic study on CuH-catalyzed enantioselective allylation of indazoles and indoles and ligand and substrate effects on enantioselectivity.
- Chapter 5 demonstrates the application of DFT calculations to understand the solvent and additive effects on the regioselectivity of cross-coupling of 3,5-dibromopyrone.
- Chapter 6 presents a set of DFT calculations on the mechanisms of cross-coupling reactions of carbohydrates.
- Chapter 7 highlights a computational investigation of the mechanism of Ni/Zn-tandem catalyzed boron insertion into the alkyl ether bonds.

## 2.0 Computational study of ligand effects to guide the experimental design of ligands with improved efficiency in CuH-catalyzed hydroamination reactions

A significant part of this chapter was published as Thomas, A. A.; Speck, K.; Kevlishvili, I.; Lu, Z.; Liu, P.; Buchwald, S. L. *J. Am. Chem. Soc.* **2018**, *140*, 13976–13984.

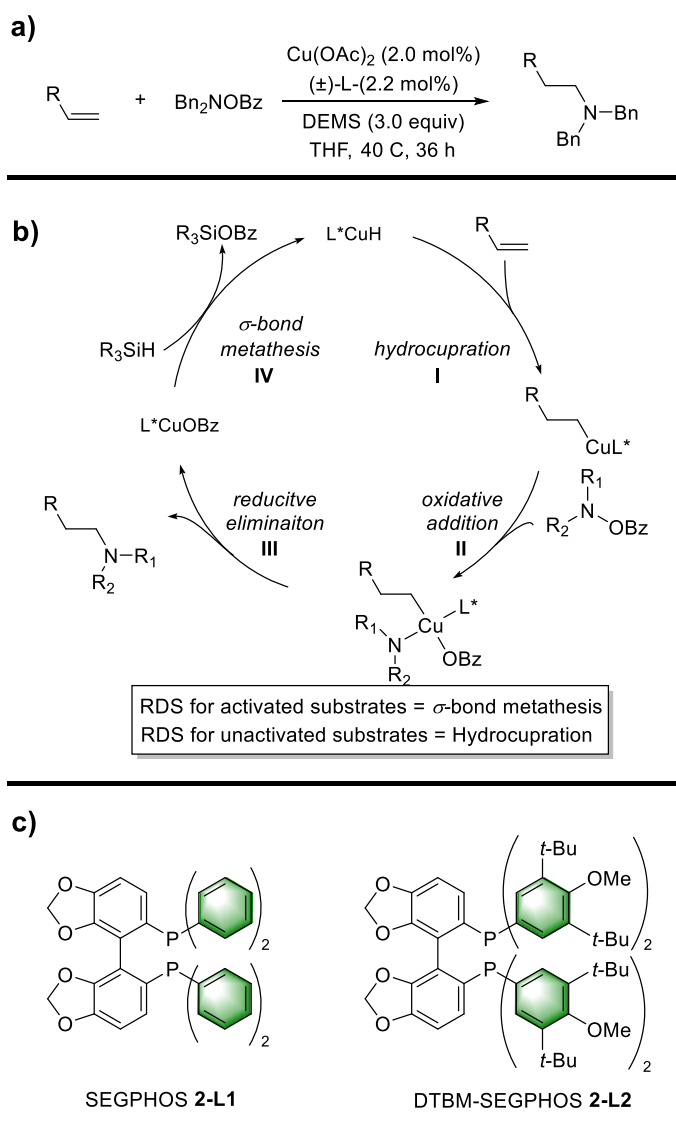
### 2.1 Introduction

Hydroamination reactions of olefins have become a powerful approach in chemical synthesis due to direct access to amines, which are common structural motifs in pharmaceutically active compounds.<sup>32</sup> Hydroamination of olefins provides a direct C–N bond formation from an easily accessible starting material. The reaction utilizing copper hydride catalyst, discovered in 2013,<sup>33</sup> has since expanded the scope to include a variety of substrates, such as styrenes,<sup>34</sup> vinylsilanes,<sup>35</sup> alkynes,<sup>36</sup> and to an extent, unactivated olefins (Figure 2-1).<sup>37</sup> Despite these tremendous strides in extending the scope, reactions with some unactivated olefins, such as cyclic and internal acyclic olefins, as well as less reactive terminal olefins, remain challenging. They are often unproductive or require elevated temperatures and long reaction times. The hydroamination of terminal alkenes is also interesting because these reactions favor *anti*-Markovnikov products, *i.e.*, primary amines, which often possess biological activity.

**A. Styrenes****B. Vinylsilanes****C. Alkynes****C. Unactivated Terminal Olefins****D. Unactivated Internal Olefins****Figure 2-1 Selected examples of copper-catalyzed hydroamination**

In recent years, several groups undertook the task of studying the mechanisms of the CuH-catalyzed hydroamination<sup>38</sup> as well as the mechanisms of CuH-catalyzed hydroborylation,<sup>39</sup> both experimentally and computationally.<sup>40</sup> The commonly accepted hydroamination mechanism consists of hydrocupration (I), oxidative addition (II), reductive elimination (III), and  $\sigma$ -bond metathesis (IV) (Figure 2-2b). These studies show that the rate determining step (RDS) can

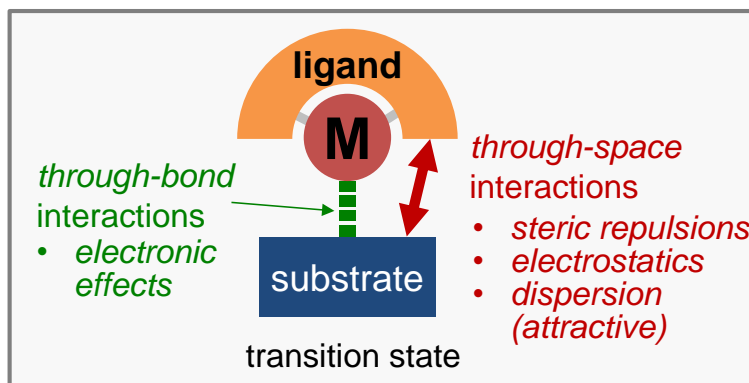
alternate between the  $\sigma$ -bond metathesis for activated olefins<sup>38</sup> and hydrocupration for unactivated olefins.<sup>40</sup> Thus, to further promote the reactivity for hydroamination of unactivated olefins, it is necessary to decrease the barrier towards hydrocupration.



**Figure 2-2 a) LCuH-catalyzed anti-Markovnikov hydroamination reaction. b) Proposed catalytic cycle for LCuH-catalyzed anti-Markovnikov hydroamination reaction. c) SEGPHOS 2-L1 and DTBM-SEGPHOS 2-L2 ligands**

Our group's previous collaboration with Buchwald's group was centered on understanding the fundamental driving force that leads to the favorable hydrocupration between LCuH (L=**2-L1**, and **2-L2**) and unactivated olefins. This was achieved by performing the ligand-substrate interaction model analysis (Figure 2-3a),<sup>40</sup> where the overall activation energy ( $\Delta E^\ddagger$ ) was separated into three components (1) the distortion energy required for the LCuH and the substrate to reach their transition state geometries ( $\Delta E_{\text{dist}}$ );<sup>27</sup> (2) the through-space interactions between the ligand and the substrate ( $\Delta E_{\text{int-space}}$ ); and (3) the through-bond interactions between the CuH moiety and the substrate ( $\Delta E_{\text{int-bond}}$ ) (Figure 2-3a). From this analysis, it was found that changes in distortion energy ( $\Delta\Delta E_{\text{dist}}$ ) and through-bond interaction energy ( $\Delta\Delta E_{\text{int-bond}}$ ) did not correlate well with the activation energy differences between two ligands ( $\Delta\Delta E^\ddagger = -4.6$ ). However, through space interaction energy ( $\Delta\Delta E_{\text{int-space}} = -5.7$ ) provided an excellent correlation with the activation energy ( $\Delta E^\ddagger$ ). In fact, energy decomposition analysis (EDA) revealed that the primary factor driving the reactivity could be attributed to the stabilization via London dispersion forces ( $\Delta\Delta E_{\text{int-space}} = -6.4$ , Figure 2-3b). While the individual contribution from each pairwise interaction was not large (0.5~1.5 kcal/mol for interactions with each *t*-Bu substituent),<sup>40,41</sup> collectively they significantly reduced the barrier.<sup>42,43</sup>

a) Ligand substrate interaction model to dissect activation energies



$$\Delta E^\ddagger = \Delta E_{\text{dist}} + \Delta E_{\text{int-space}} + \Delta E_{\text{int-bond}}$$

$$\Delta E_{\text{int-space}} = \Delta E_{\text{rep}} + \Delta E_{\text{elec}} + \Delta E_{\text{pol}} + \Delta E_{\text{ct}} + \Delta E_{\text{disp}}$$

b) Reactivity differences in SEGPHOS (2-L1) and DTBM-SEGPHOS (2-L2) ligated CuH catalysts

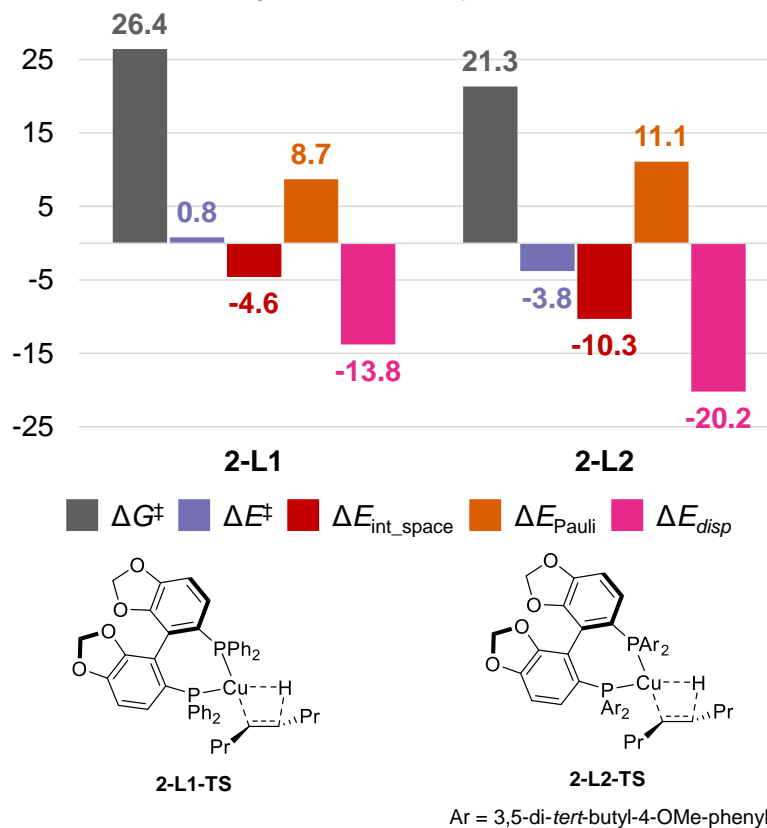
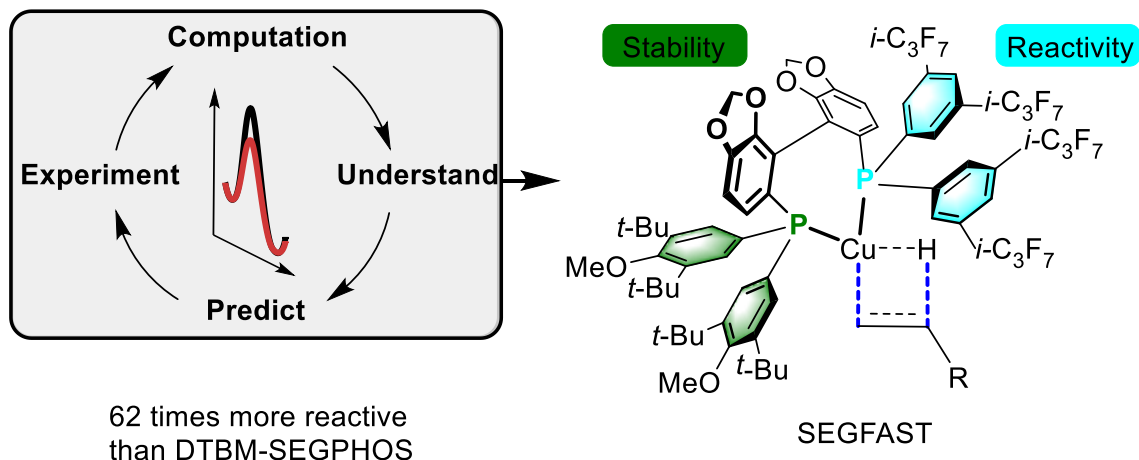


Figure 2-3 a) Ligand-substrate interaction model to study the origin of reactivity in hydrocupration. b)

London dispersion interactions lowering the hydrocupration barrier for L2CuH.

With this knowledge at hand, we decided to undertake the task of designing a more effective ligand that would promote the hydrocupration further. Since the original study in 2013, which used the DTBM-SEGPHOS ligand, the same catalyst has been used in several reactions, but none of the previous experimental studies were able to discover a more effective ligand. We surmised that rational design of a more effective ligand could proceed in two ways, by either further promoting London dispersion forces or promoting other types of through-space and through-bond interactions<sup>44</sup> while maintaining dispersion interactions. Non-covalent interactions can be facilitated by installing heteroatom substituents,<sup>11</sup> and through-bond interactions could also be fine-tuned by altering electronic characteristics of the ligand. However, when designing catalysts capable of promoting reactivity through an assortment of stabilizing interactions, infinite possibilities are conceivable. With the unique ability to computationally quantify and experimentally verify these interactions, an iterative catalyst design approach was envisioned.<sup>45,46</sup> This approach comprised of four stages: (1) experimentally identifying a suitable class of ligand derivatives; (2) using computational analysis to understand what fundamental interactions can stabilize the transition state; (3) using this knowledge to predict a more effective ligand computationally and (4) experimentally test the ligand providing feedback for the next round of ligand optimization (Figure 2-4).





**Figure 2-4 Iterative ligand design approach**

The preliminary experimental studies revealed promising results with the CF<sub>3</sub>-SEGPHOS **2-L4** derivative. However, it was unclear what further modifications could lead to additional reactivity enhancement. Although successful predictions of new transition metal catalysts from computational results alone are still rare,<sup>47</sup> several examples have recently been described wherein a combination of computational and experimental evaluations has led to the discovery of catalysts with improved reactivity and selectivity.<sup>46</sup> Such synergetic efforts effectively utilize the predictive power of computation, while the experimental verification helps resolve the uncertainty of calculated energies and issues that cannot be readily addressed by calculations alone, such as catalyst decomposition.<sup>48</sup>

## 2.2 Computational details

Geometry optimizations and single-point energy calculations were carried out using Gaussian 09.<sup>13</sup> Geometries of intermediates and transition states were optimized using the B3LYP

functional<sup>15</sup> with a mixed basis set of SDD for Cu and 6-31G(d) for other atoms in the gas phase. Vibrational frequency calculations were performed for all of the stationary points to confirm if each optimized structure is a local minimum or a transition state structure. Truhlar and Cramer's quasi-harmonic corrections<sup>49</sup> were applied for entropy calculations using 100 cm<sup>-1</sup> as the frequency cut-off. Solvation energy corrections were calculated in THF solvent with the CPCM continuum solvation model<sup>20</sup> based on the gas-phase optimized geometries. The  $\omega$ B97X-D functional<sup>18</sup> with a mixed basis set of SDD for Cu and 6-311+G(d,p) for other atoms was used for solvation single-point energy calculations. The computed gas-phase activation energy ( $\Delta E^\ddagger$ ) was dissected using the following ligand-substrate interaction model analysis.<sup>40</sup>

$$\Delta E^\ddagger = \Delta E_{\text{dist}} + \Delta E_{\text{int-bond}} + \Delta E_{\text{int-space}} \quad \text{eq.1}$$

The distortion energy ( $\Delta E_{\text{dist}}$ ) is the sum of the energies required to distort the LCuH catalyst and the substrate into their transition state geometries.  $\Delta E_{\text{int-space}}$  was calculated from the interaction energy of a supramolecular complex of the phosphine ligand and the olefin substrate at the transition state geometry but in the absence of the CuH moiety ( $\Delta E_{\text{int-space}} = E_{\text{lig+sub}} - E_{\text{lig}} - E_{\text{sub}}$ )<sup>40</sup>. Then, the through bond interaction was calculated from  $\Delta E_{\text{int-bond}} = \Delta E^\ddagger - \Delta E_{\text{dist}} - \Delta E_{\text{int-space}}$ . The  $\Delta E_{\text{dist}}$  and  $\Delta E_{\text{int-space}}$  were both calculated using the  $\omega$ B97X-D functional with the SDD basis set for Cu and 6-311+G(d,p) for other atoms. The  $\omega$ B97X-D functional was chosen because it has been shown to accurately describe non-covalent interactions,<sup>50</sup> which we expected to be important in this system. The computed free energy barriers using this method provided very good agreement with the experimental reaction rate constants. The through-space interaction energy ( $\Delta E_{\text{int-space}}$ ) between the ligand and the substrate is further dissected according to the following equation:

$$\Delta E_{\text{int-space}} = \Delta E_{\text{Pauli}} + \Delta E_{\text{elstat}} + \Delta E_{\text{pol}} + \Delta E_{\text{ct}} + \Delta E_{\text{disp}} \quad \text{eq. 2}$$

In accordance with our group's previous study, the dispersion energy component ( $\Delta E_{\text{disp}}$ ) was obtained from the difference of interaction energies calculated using MP2 and HF. The MP2 calculations were performed with Q-Chem 5.0<sup>22</sup> using the SOS(MI)-MP2 method in combination with the dual-basis set approach utilizing the db-cc-pVTZ basis set.<sup>51</sup> The  $\Delta E_{\text{Pauli}}$ ,  $\Delta E_{\text{elstat}}$ ,  $\Delta E_{\text{pol}}$ , and  $\Delta E_{\text{ct}}$  terms in eq 2 were calculated using the second-generation energy decomposition analysis based on absolutely localized molecular orbitals (ALMO-EDA)<sup>21</sup> method implemented in Q-Chem 5.0. The second generation ALMO-EDA provides a further decomposition of the Pauli and electrostatic interaction ( $\Delta E_{\text{rep}}$ ) term into Pauli repulsion ( $\Delta E_{\text{Pauli}}$ ) and electrostatic ( $\Delta E_{\text{elstat}}$ ) energies, which is important in the analysis of through-space electrostatic interactions with the fluorinated ligands. HF method with the 6-311G(d,p) basis set was employed to avoid double counting of dispersion in the energy decomposition analysis (EDA) calculations.

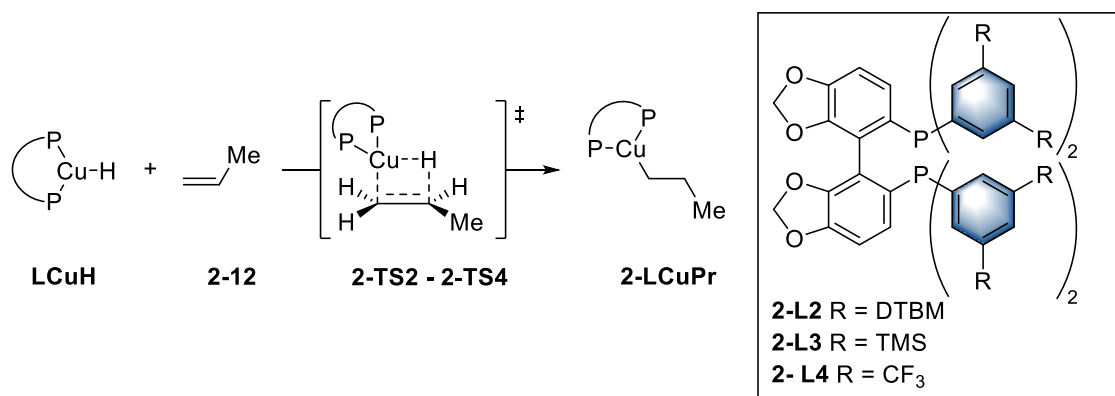
## 2.3 Results and discussions

### 2.3.1 Origin of the reactivity trends with **2-L3** and **2-L4**

With the understanding that bulky substituents in meta- position on the *P*-aryl<sub>2</sub> groups promote reactivity, our collaborators first conducted preliminary kinetic studies using SEGPHOS derivatives with substituents possessing different steric (TMS) and electronic (CF<sub>3</sub>) properties at these positions. Their kinetic studies revealed that both ligands mildly promoted ( $k/k_0 = 3.3$ ; 6.7 respectively (Table 2-1)) the reactivity.

To fully understand the underlying principles and interactions that lead to the enhanced reaction rates with **2-L3** and **2-L4** supported CuH catalysts, a computational analysis of the

hydrocupration transition step was performed to study the origin of the different hydroamination reactivities between the DTBM-SEGPHOS **2-L2**, TMS-SEGPHOS **2-L3**, and CF<sub>3</sub>-SEGPHOS **2-L4**-supported CuH catalysts (Figure 2-5).



**Figure 2-5 Hydrocupration with CuH catalysts supported by different SEGPHOS-derived ligands**

The activation energies of the rate-determining hydrocupration transition states were computed using propene (**2-12**) as the model substrate with the method outlined above (Table 2-1). The computed activation barriers did not reproduce the slight difference in experimental rate constants between the hydroamination with TMS-SEGPHOS (**2-L3**) and DTBM-SEGPHOS (**2-L2**) ligands. Although the reaction with the TMS-SEGPHOS ligand is three times faster experimentally, computations predicted essentially the same hydrocupration barriers for **2-TS2** and **2-TS3**. The ligand-substrate interaction model analysis showed that there were no significant differences between these two ligands for any of the individual energy terms (Figure 2-6).

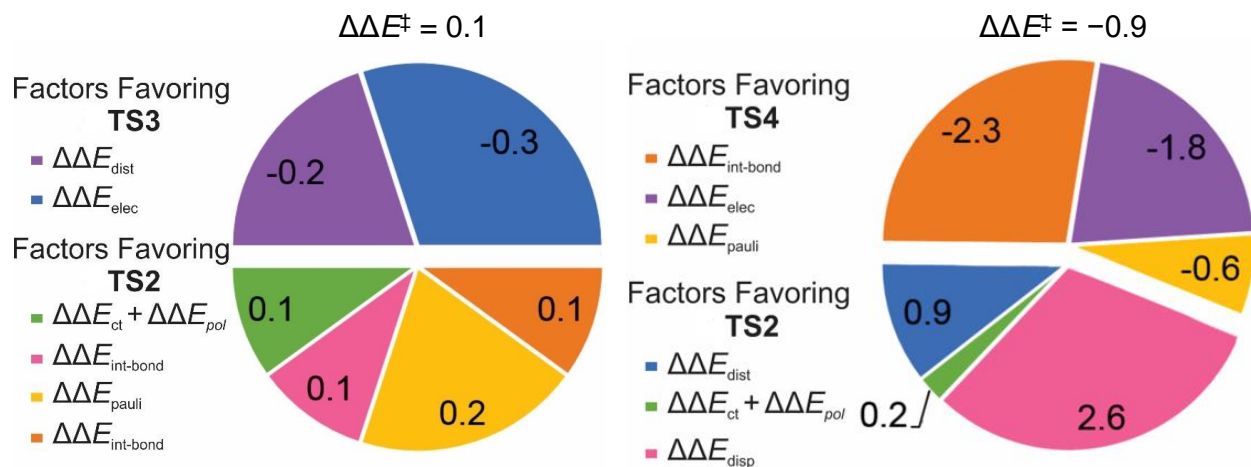
**Table 2-1 Activation free energies of the hydrocupration transition states and energy components derived from the ligand-substrate interaction model for initially screened ligands.<sup>a</sup>**

Ligand	DTBM- SEGPPOS ( <b>2-L2</b> )	TMS-SEGPPOS ( <b>2-L3</b> )	CF <sub>3</sub> -SEGPPOS ( <b>2-L4</b> )
hydrocupration transition state	<b>2-TS2</b>	<b>2-TS3</b>	<b>2-TS4</b>
$\Delta G_{\text{solv}}^{\ddagger}$	20.2	20.3	18.7
$\Delta E^{\ddagger}$	-0.1	0.0	-1.0
distortion ( $\Delta E_{\text{dist}}$ )	28.6	28.3	29.4
through-bond interaction ( $\Delta E_{\text{int-bond}}$ )	-23.9	-23.8	-26.2
through-space interaction ( $\Delta E_{\text{int-space}}$ )	-4.8	-4.5	-4.3
Pauli repulsion ( $\Delta E_{\text{Pauli}}$ )	9.0	9.2	8.4
electrostatic ( $\Delta E_{\text{elstat}}$ )	0.3	0.1	-1.5
London dispersion ( $\Delta E_{\text{disp}}$ )	-13.3	-13.2	-10.7
charge transfer ( $\Delta E_{\text{ct}}$ )	-0.2	-0.2	-0.2
polarization ( $\Delta E_{\text{pol}}$ )	-0.6	-0.5	-0.4
$k_{\text{rel}}$	1.0	3.3	6.7
$\Delta\Delta G_{\text{comp}}^{\ddagger}$	0.0	0.1	-1.5
$\Delta\Delta G_{\text{exp}}^{\ddagger}$	0.0	-0.7	-1.1

<sup>a</sup> All energies are reported in kcal/mol. The activation energies ( $\Delta G_{\text{solv}}^{\ddagger}$  and  $\Delta E^{\ddagger}$ ) are with respect to the separated CuH catalyst and propene (**2-12**).  $\Delta\Delta G_{\text{comp}}^{\ddagger}$  values were calculated by subtracting  $\Delta G_{\text{solv}}^{\ddagger}$ -**2-L2** from  $\Delta G_{\text{solv}}^{\ddagger}$ -**2-LX**.  $\Delta\Delta G_{\text{exp}}^{\ddagger}$  were derived from the experimental relative rate constants ( $k_{\text{rel}}$ ) obtained by our collaborators from the Buchwald research group.

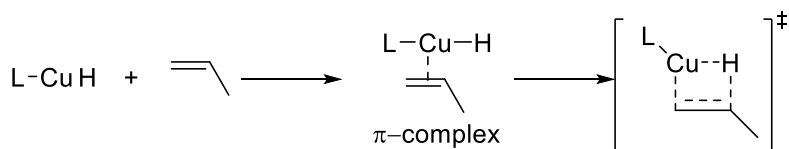
The computed barrier of hydrocupration with the CF<sub>3</sub>-SEGPPOS **2-L4**CuH complex was in good agreement with the experimentally observed rate increase with **2-L4** compared to DTBM-

SEGPLHOS **2-L2**CuH ( $\Delta\Delta G_{\text{comp}}^{\ddagger} = 1.5$  kcal/mol *vs.*  $\Delta\Delta G_{\text{exp}}^{\ddagger} = 1.1$  kcal/mol). In order to quantify the different factors that lead to the improved reactivity, the ligand-substrate interaction model analysis was employed to dissect the overall hydrocupration activation energies (Eqs. 1 and 2, see *Computational Methods* for details). Energy decomposition analysis of the hydrocupration transition state with **2-L4**CuH revealed that the increase in the reaction rate was due to significantly stronger through-bond interactions ( $\Delta E_{\text{int-bond}}$ ), resulting in an extra 2.3 kcal/mol stabilization of **2-TS4** compared to the DTBM-SEGPLHOS-bound **2-TS-2** (Figure 2-6). This is because of the electron-withdrawing nature of the CF<sub>3</sub>-substituents, which consequently results in enhanced Lewis acidity of the CuH catalyst and more favorable binding of the olefin substrate. The alkene–copper  $\pi$ -complexes were calculated for DTBM-SEGPLHOS (**2-L2**) and CF<sub>3</sub>-SEGPLHOS (**2-L4**) (Table 2-2) to confirm that Lewis acidity of CuH was promoting favorable bonding interactions. The calculations confirmed that the more electron-deficient catalyst with **2-L4** ligand binds to the olefin significantly more favorably by 2.5 kcal/mol (Figure 2.4.2A).



**Figure 2-6** Contributions of different types of catalyst-substrate interactions to the reactivity. The  $\Delta\Delta E$  values are calculated from the energy difference between 2-TS3 (L=TMS-SEGPHOS)/ 2-TS4 (L=CF<sub>3</sub>-SEGPHOS) and 2-TS2 (L=DTBM-SEGPHOS). Positive  $\Delta\Delta E$  values indicate effects that promote reactions catalyzed by the DTBM-SEGPHOS supported catalyst; negative  $\Delta\Delta E$  values indicate effects that promote reactions catalyzed by the other ligand supported catalyst. The energies are in kcal/mol.

**Table 2-2** Gibbs free energies of the  $\pi$ -complexes and hydrocupration transition states with the DTBM-SEGPHOS (2-L2) and CF<sub>3</sub>-SEGPHOS (2-L4) ligands.<sup>a</sup>

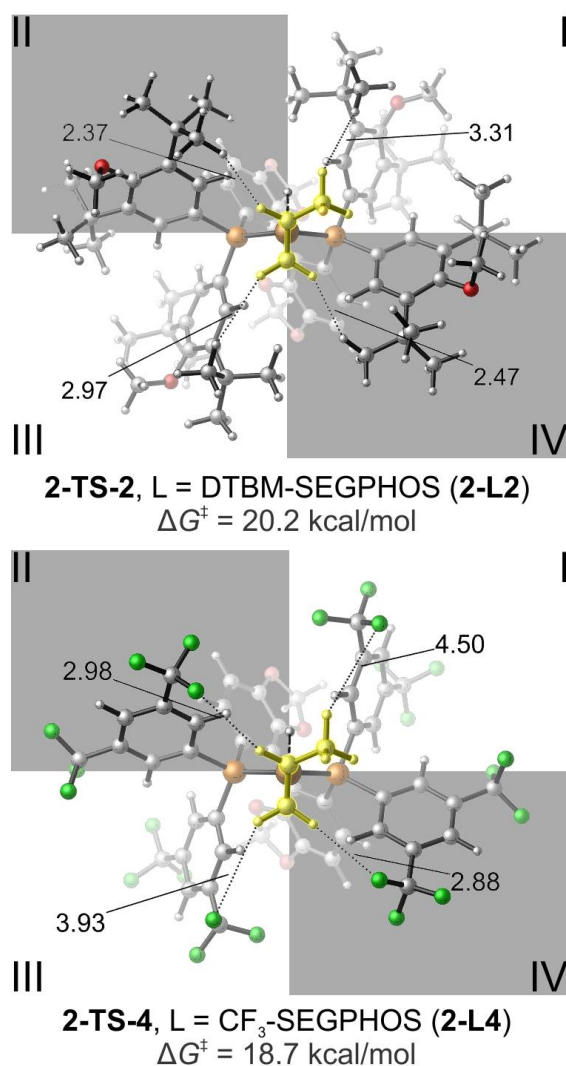


Ligand	DTBM-SEGPHOS (2-L2)	CF <sub>3</sub> -SEGPHOS (2-L4)
$\Delta G$ ( $\pi$ -complex)	9.0	6.5
$\Delta G^\ddagger$	20.2	18.7

<sup>a</sup> All energies are in kcal/mol and with respect to separated LCuH catalyst and the substrate.

While the through-space interaction energies ( $\Delta E_{\text{int-space}}$ ) are comparable in 2-TS2 and 2-TS4, the origins are different. Using the second-generation ALMO-EDA methods, the  $\Delta E_{\text{int-space}}$

term was further dissected into its individual energy components (Eq. 2). While **2-TS2** is stabilized by stronger attractive London dispersion ( $\Delta E_{\text{disp}} = -13.3$  kcal/mol for **2-TS2** compared to  $-10.7$  kcal/mol for **2-TS4**), electrostatic interactions are more favorable in **2-TS4** ( $\Delta E_{\text{elstat}} = 0.3$  kcal/mol for **2-TS2** compared to  $-1.5$  kcal/mol for **2-TS4**). The optimized geometry of **2-TS4** revealed multiple C–F $\cdots$ H–C contacts, which are responsible for the through-space electrostatic interactions between **2-L4** and the olefin substrate, thereby lowering  $\Delta E^\ddagger$  (Figure 2-7).

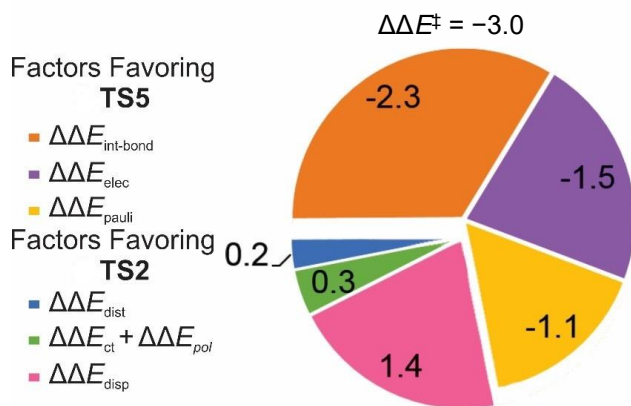


**Figure 2-7** Optimized geometries of hydrocupration transition states with the DTBM-SEGPHOS (**2-TS-2**) and CF<sub>3</sub>-SEGPHOS ligands (**2-TS-4**). Distances are in Ångström [Å].



### 2.3.2 Proposal of a more reactive CuH-catalyst supported by ligand 2-L5

Although the use of CF<sub>3</sub>-SEGPPOS **2-L4** leads to a relatively moderate increase of reactivity, the computational analysis suggested types of modifications that might result in a more effective ligand. Considering that the CF<sub>3</sub>-SEGPPOS **2-L4** ligated LCuH complex has weakened dispersion interactions when compared to the **2-L2**CuH complex, we hypothesized that the installation of a larger perfluorinated substituent would be beneficial. Since the *i*-C<sub>3</sub>F<sub>7</sub> group is sterically more demanding than CF<sub>3</sub>, we assumed that it should increase stabilizing London dispersion while maintaining the favorable through-space electrostatic attractions and through-bond electronic effects.

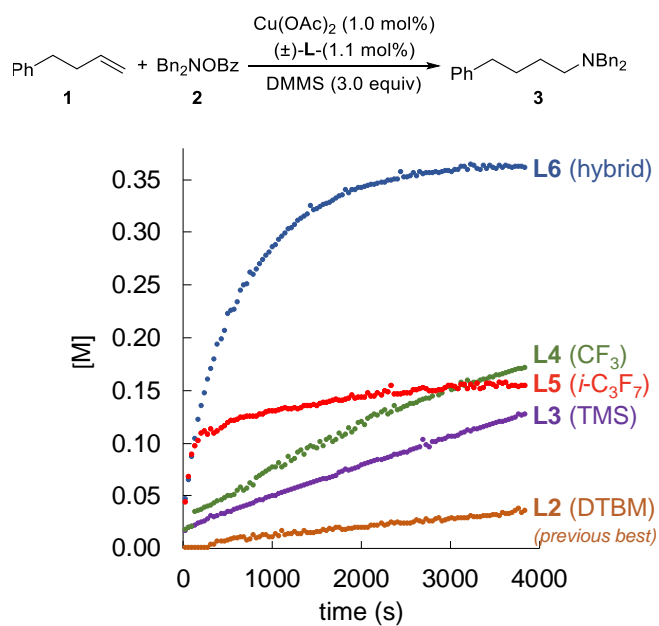


**Figure 2-8 Contributions of different types of catalyst-substrate interactions to the regioselectivity.** The  $\Delta\Delta E$  values are calculated from the energy difference between 2-TS5 (L=*i*-C<sub>3</sub>F<sub>7</sub>-SEGPPOS) and 2-TS2 (L=DTBM-SEGPPOS). Positive  $\Delta\Delta E$  values indicate effects that promote reactions catalyzed by the DTBM-SEGPPOS catalyst; negative  $\Delta\Delta E$  values indicate effects that promote reactions catalyzed by the *i*-C<sub>3</sub>F<sub>7</sub>-SEGPPOS-supported catalyst. The energies are in kcal/mol.

Indeed, the calculated hydrocupration transition state **2-TS5** indicated that the use of *i*-C<sub>3</sub>F<sub>7</sub>-SEGPPOS **L5** as the ligand led to an additional 1.5 kcal/mol lower activation energy compared to the hydrocupration with **L4CuH** (Table 2-3). The ligand-substrate interaction model analysis validated our hypothesis, as the  $\Delta E_{\text{dist}}$  and  $\Delta E_{\text{int-bond}}$  terms of **2-TS5** remained essentially unchanged when compared to **2-TS4**. Meanwhile, the through-space interaction of **2-TS5** was 1.7 kcal/mol more stabilizing. Further dissection of the through-space interactions revealed that while favorable electrostatic interactions were maintained, **2-TS-5** had significantly more favorable dispersion interactions, only 1.4 kcal/mol less than DTBM-SEGPPOS (Figure 2-8).

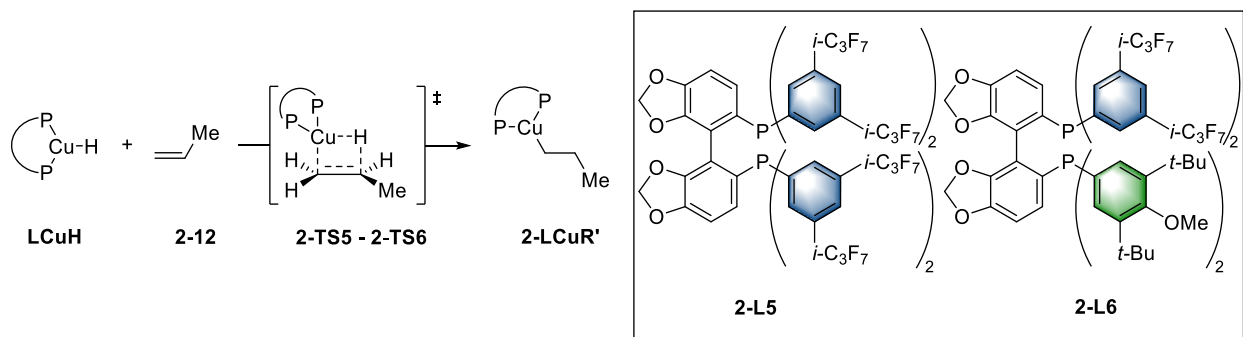
### 2.3.3 Computational studies of hybrid SEGPPOS ligands

Kinetic experiments conducted by our collaborators revealed that while reactions catalyzed by **2-L5**-supported catalyst possessed a high initial rate, the catalyst was unstable and led to decomposition after the initial burst of reactivity (Figure 2-9). This catalyst decomposition is most likely the consequence of the diminished Lewis basicity of the phosphorus atoms in **2-L5** due to the electron-withdrawing nature of the *i*-C<sub>3</sub>F<sub>7</sub> substituents, which results in weaker binding of the ligand to the copper center. To exhibit both high reactivity and stability, the Lewis acidity of the copper center needed to be finely tuned.



**Figure 2-9** Experimental kinetic studies of hydroamination of 4-phenyl-1-butene. Experiments conducted by the Buchwald group

**Table 2-3 Activation free energies of the hydrocupration transition states and energy components derived from the ligand-substrate interaction model for newly designed ligands.**



Ligand	<i>i</i> -C <sub>3</sub> F <sub>7</sub> ( <b>2-L5</b> )	SEGFAST ( <b>2-L6</b> )
hydrocupration transition state	<b>2-TS5</b>	<b>2-TS6</b>
$\Delta G_{\text{solv}}^\ddagger$	17.2	17.0
$\Delta E^\ddagger$	−3.4	−3.0
distortion ( $\Delta E_{\text{dist}}$ )	28.8	27.9
through-bond interaction ( $\Delta E_{\text{int-bond}}$ )	−26.2	−25.4
through-space interaction ( $\Delta E_{\text{int-space}}$ )	−6.0	−5.6
Pauli repulsion ( $\Delta E_{\text{Pauli}}$ )	7.9	7.8
electrostatic ( $\Delta E_{\text{elstat}}$ )	−1.2	−0.3
London dispersion ( $\Delta E_{\text{disp}}$ )	−11.9	−13.0
charge transfer ( $\Delta E_{\text{ct}}$ )	−0.1	0.0
polarization ( $\Delta E_{\text{pol}}$ )	−0.4	−0.4
$k_{\text{rel}}$	61.3	61.5
$\Delta \Delta G_{\text{comp}}^\ddagger$	−3.0	−3.2
$\Delta \Delta G_{\text{exp}}^\ddagger$	−2.4	−2.4

<sup>a</sup> All energies are reported in kcal/mol. The activation energies ( $\Delta G_{\text{solv}}^\ddagger$  and  $\Delta E^\ddagger$ ) are with respect to the separated CuH catalyst and propene (**2-12**).  $\Delta \Delta G_{\text{comp}}^\ddagger$  values were calculated by subtracting  $\Delta G_{\text{solv}}^\ddagger$ -**2-L2** from  $\Delta G_{\text{solv}}^\ddagger$ -**2-LX**.  $\Delta \Delta G_{\text{exp}}^\ddagger$  were derived from the experimental relative rate constants ( $k_{\text{rel}}$ ) obtained by our collaborators from the Buchwald research group.

To harness the increased reactivity that we observed using the *i*-C<sub>3</sub>F<sub>7</sub> substituents without sacrificing the stability of the resulting complex, we had two options: either to test various new derivatives with different substituents, to find a suitable ligand that provides a catalyst system that combines high activity and stability, or exchange one *P*-aryl<sub>2</sub> substituent for a more electron-donating group in order to stabilize the resulting copper complex. To avoid significant structural changes at the 3- and 5-positions of the aryl groups, we reasoned that the merger of DTBM-**2-L2** and *i*-C<sub>3</sub>F<sub>7</sub>-**2-L5**, the ligands with higher catalyst stability and reactivity, might result in the perfect balance of their respective beneficial interactions. This hypothesis found further support in examining the transition-state structure **2-TS5**, in which the improved through-space ligand-substrate interactions primarily arise from the C–F···H–C interactions in the 1<sup>st</sup> and 4<sup>th</sup> quadrants (Figure 2-10). The *i*-C<sub>3</sub>F<sub>7</sub> groups in the 2<sup>nd</sup> and 3<sup>rd</sup> quadrants are further away from the substrate and thus are less significant in promoting the hydrocupration step.

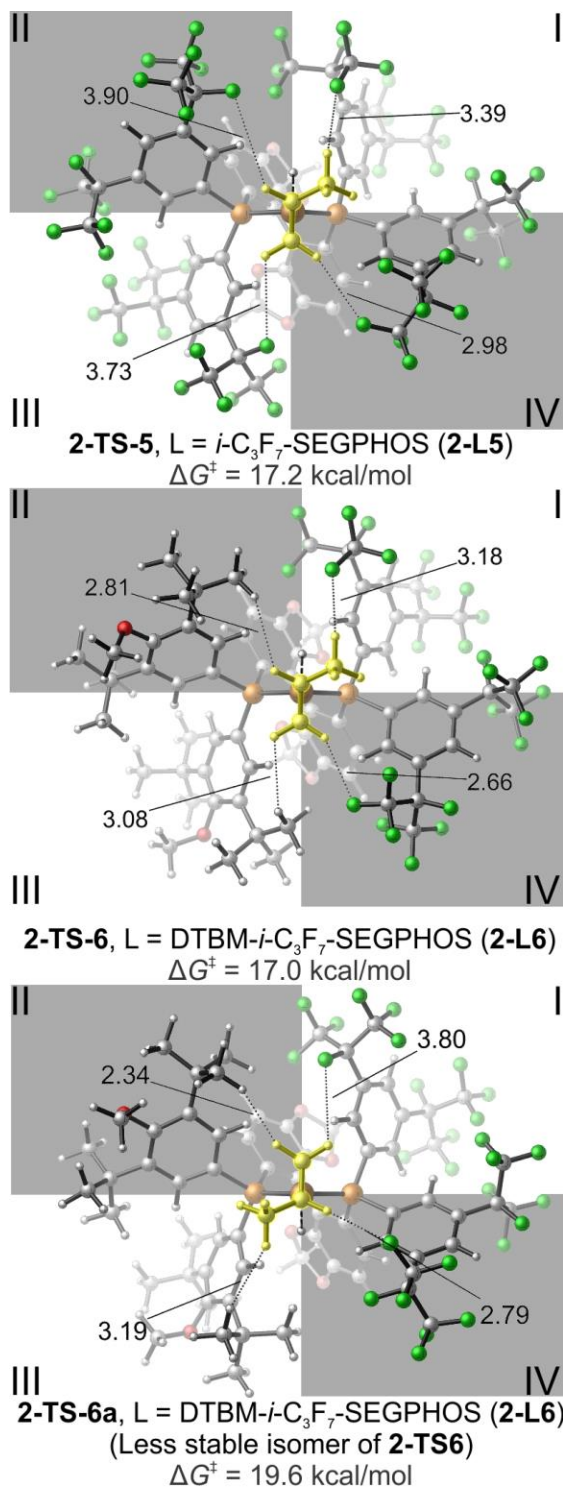
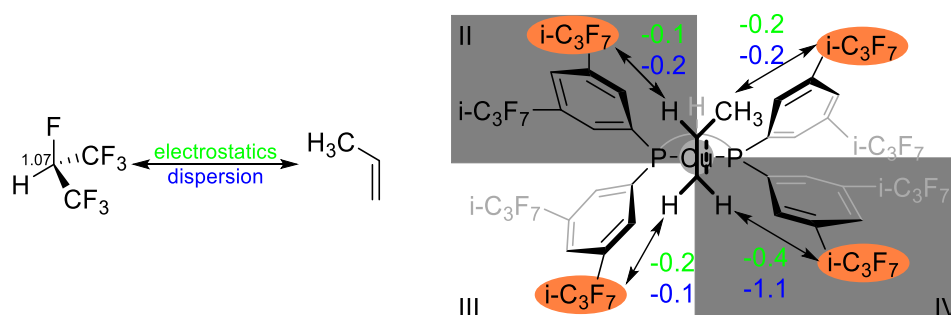


Figure 2-10 Optimized geometries of hydrocupration transition states with the *i*-C<sub>3</sub>F<sub>7</sub>-SEGPPOS (**2-TS-5**) and the hybrid DTBM-*i*-C<sub>3</sub>F<sub>7</sub>-SEGPPOS ligand (**2-TS-6** and **2-TS-6a**). Distances are reported in angström [Å].

To further support this hypothesis, we separately calculated the electrostatic and dispersion interactions between the propene and *i*-C<sub>3</sub>F<sub>7</sub>- substituents in *i*-C<sub>3</sub>F<sub>7</sub>-SEGP<sub>2</sub>HOS ligand using the ALMO-EDA2 method. The geometry of each pairwise interaction was taken from the geometry of the transition state **2-TS5**. The rest of the structure was displaced with an H atom at 1.07 Å. The total electrostatic interaction between the four closest *i*-C<sub>3</sub>F<sub>7</sub>- groups and the propene corresponds to 0.9 kcal/mol, showing that C–F...H–C interactions are the origin of electrostatic interactions. Dispersion interaction between the substituents and the substrate amounted to 1.6 kcal/mol. Furthermore, results indicated that the 1<sup>st</sup> and 4<sup>th</sup> quadrants amounted to most of these interactions (Figure 2-11). Therefore, exchanging the *P*-aryl<sub>2</sub> groups in the 2<sup>nd</sup> and 3<sup>rd</sup> quadrants with DTBM substitution was not expected to impact the enhanced reactivity gained from the *i*-C<sub>3</sub>F<sub>7</sub> moieties significantly.



**Figure 2-11** Electrostatic and dispersion interactions between heptafluoro isopropyl groups and propene.

Energies are reported in kcal/mol.

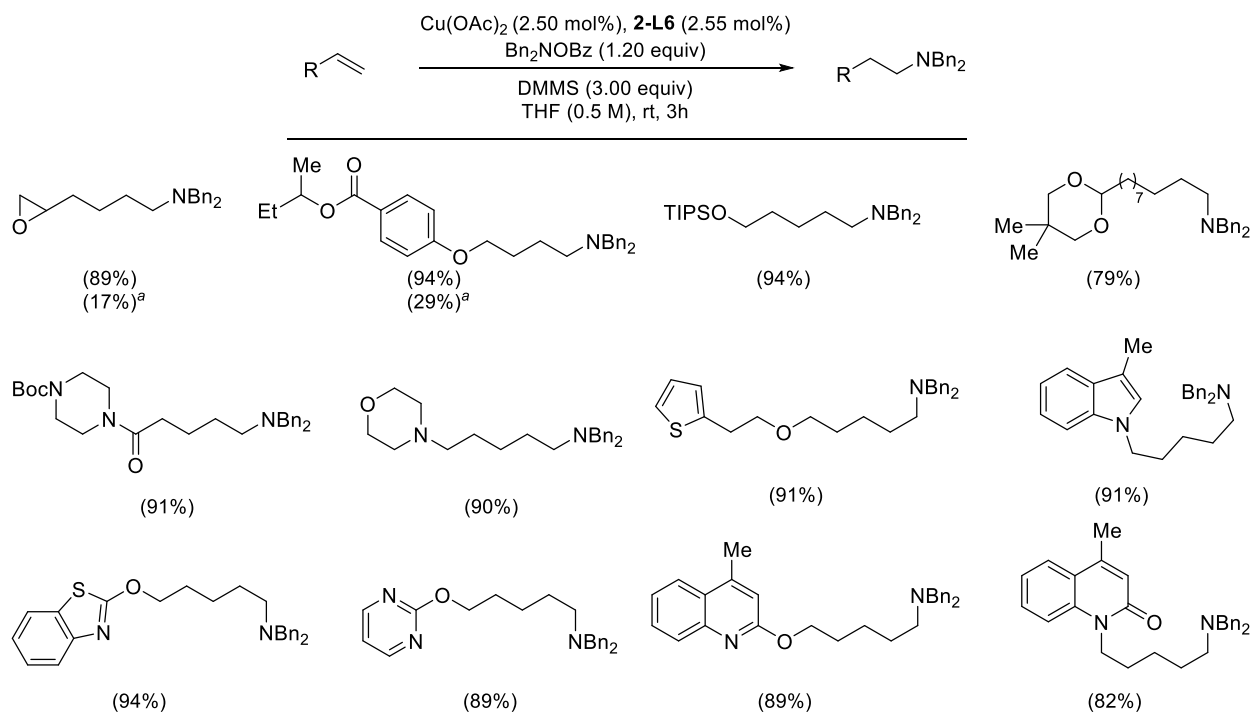
The computational investigations showed that the hydrocupration barrier for the hybrid SEGP<sub>2</sub>HOS derivative **2-L6CuH** was similar to that of the symmetric derivative **2-L5CuH** (see Table 2-3). Further energy decomposition analysis showed similar through-space interaction energies ( $\Delta E_{\text{int-space}}$ ) in **2-TS6** and **2-TS5** (Table 2-3). While electrostatic interactions in **2-TS6**

were slightly decreased relative to those in **2-TS5**, London dispersion interactions were increased as a result of the larger *t*-butyl substituents in the 2<sup>nd</sup> and 3<sup>rd</sup> quadrants of **2-TS6**, indicating that a comparable energy barrier might be obtained from **2-L6CuH**.

Based on the established stereoinduction model for hydrocupration involving SEGPHOS-type ligands, the methyl substituent on the propene should prefer to occupy the unoccupied quadrants in the hydrocupration transition state. With the hybrid ligand, two different isomers for the hydrocupration transition states are possible. A different isomer of the hydrocupration transition state with **2-L6** (**2-TS6a**) is shown in Figure 2-10, where the methyl group on the substrate occupies the third quadrant. Our calculations revealed that the activation free energy for **2-TS6a** ( $\Delta G^\ddagger=19.6$  kcal/mol) is 2.6 kcal/mol less stable than **2-TS6** ( $\Delta G^\ddagger=17.0$  kcal/mol), reflecting the significance of through-space interactions between the substrate and *i*-C<sub>3</sub>F<sub>7</sub> groups on the ligand and indicating the C–F $\cdots$ H–C non-covalent interactions with the *i*-C<sub>3</sub>F<sub>7</sub> group are more favorable than the C–H $\cdots$ H–C interactions with the *t*-Bu group.

Following the design of the new hybrid ligand **2-L6**, our collaborators in the Buchwald group investigated the utility of the **2-L6CuH** catalyst on the hydroamination of the terminal olefins. These results indicate that the newly designed ligand improved the reactivity with a wide variety of less reactive terminal olefins (Figure 2-12).

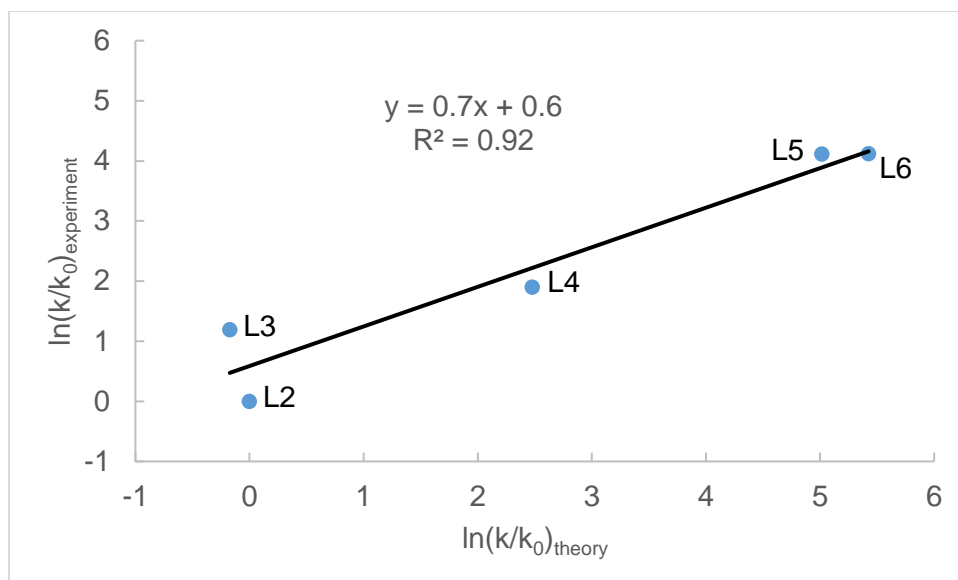




**Figure 2-12 Scope of hydroamination of terminal olefins with SEGFAST 2-L6 ligand. Experiments were conducted by the Buchwald group. <sup>a</sup>Reaction conducted with DTBM-SEGPHOS.**

### 2.3.4 Validation of computationally predicted reactivity trends

To validate the computationally predicted activation energies with the different LCuH catalysts, we plotted the experimentally observed relative rate constants ( $\ln(k/k_0)$ ) from kinetic studies against the relative rate constants derived from computed activation free energies ( $\Delta G^\ddagger_{\text{solv}}$ ) (Figure 2-13). These results show a good agreement between the computation and experiment and thus validated the ability of DFT calculations to predict the ligand effects on the reactivity of CuH-catalyzed hydroamination with quantitative accuracy.



**Figure 2-13 Linear correlation between the computed relative rates ( $\ln(k/k_0)_{\text{theory}}$ ) and experimental relative initial rates ( $\ln(k/k_0)_{\text{experiment}}$ ).**

### 2.3.5 Comparison of the 1<sup>st</sup> and 2<sup>nd</sup> generation ALMO-EDA methods

The second generation of ALMO-EDA was employed in the current study. This method was employed because it offers a significant advantage over the first generation of ALMO-EDA. While the first generation ALMO-EDA provides a chemically meaningless ( $\Delta E_{\text{frz}}$ ) term, the second generation ALMO-EDA further decomposes this energy into chemically meaningful electrostatic interaction energy and Pauli repulsion energy. In our previous study, the first-generation ALMO-EDA was used. We compared the first and the second generation ALMO-EDA results for the decomposition of the through-space interaction energy of **2-TS2** with DTBM-SEGPHOS. The HF/6-311G(d,p) method was used in both calculations. Dispersion energies were calculated using the same MP2-HF methodology in both approaches. As shown in Table 2-4, the second generation ALMO-EDA provides almost identical  $\Delta E_{\text{pol}}$  and  $\Delta E_{\text{ct}}$  terms as the first

generation ALMO-EDA results. In addition, the sum of the Pauli repulsion energy ( $\Delta E_{\text{pauli}}$ ) and electrostatic energy ( $\Delta E_{\text{elstat}}$ ) from the second generation ALMO-EDA is very close to the “repulsive term” ( $\Delta E_{\text{rep}}$ ) (frozen interaction term ( $\Delta E_{\text{frz}}$ )) in the first generation ALMO-EDA. Thus, the significant difference between the two different versions of ALMO-EDA for the through-space interactions in the hydrocupration TS is the further decomposition of the closed-shell repulsive term into Pauli repulsion energy ( $\Delta E_{\text{pauli}}$ ) and electrostatic energy ( $\Delta E_{\text{elstat}}$ ) in the second generation ALMO-EDA.

**Table 2-4 Comparison of 1<sup>st</sup> and 2<sup>nd</sup> generation ALMO-EDA methodologies.<sup>a,b</sup>**

L	SEGPPOS		DTBM- SEGPPOS	
	EDA1	EDA2	EDA1	EDA2
$\Delta E_{\text{rep}}$	8.0	—	9.2	—
$\Delta E_{\text{pauli}}$	—	7.7	—	9.0
$\Delta E_{\text{elstat}}$	—	0.3	—	0.3
$\Delta E_{\text{pol}}$	-0.5	-0.5	-0.7	-0.6
$\Delta E_{\text{ct}}$	0.1	0.1	-0.1	-0.2
$\Delta E_{\text{disp}}$	-10.1	-10.1	-13.3	-13.3

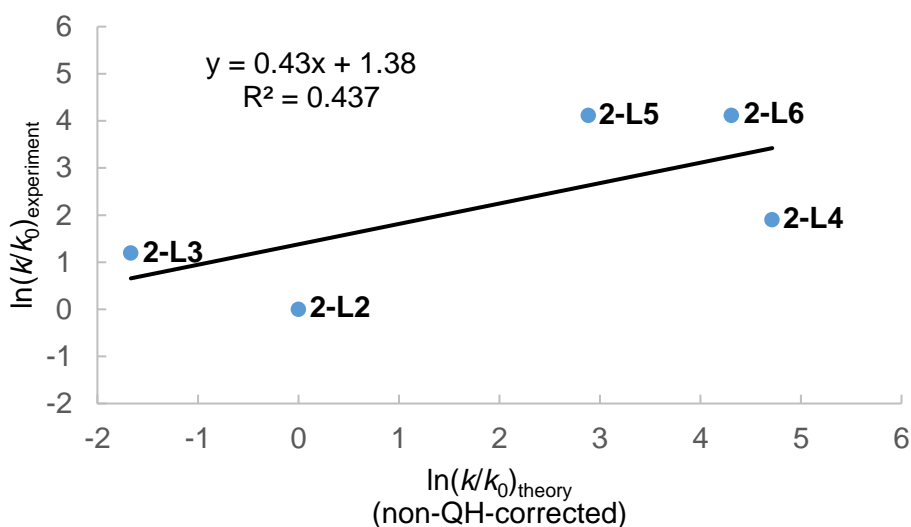
<sup>a</sup> All energies are in kcal/mol.

<sup>b</sup> Energies were obtained from the decomposition of the through-space interaction energy of **2-TS1** and **2-TS2** with SEGPPOS and DTBM-SEGPPOS, respectively.

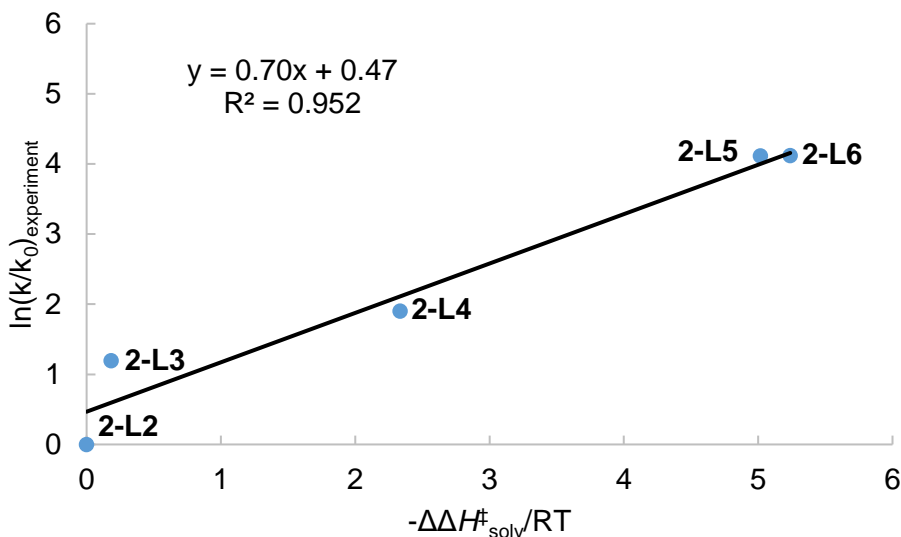
### 2.3.6 The effect of quasiharmonic approximation

The Cramer and Truhlar’s quasiharmonic approximation was used for calculating Gibbs free energies of activation, which raises vibrational frequencies lower than 100 cm<sup>-1</sup> to 100 cm<sup>-1</sup> to correct the harmonic oscillator model for low-frequency vibrational modes. While the computed

Gibbs free energies using the quasiharmonic approximation provided good agreement with the experimental results (Figure 2-13,  $R^2=0.923$ ), Gibbs free energy calculated without Cramer and Truhlar's correction did not provide a good agreement with the experimental results (Figure 2-14,  $R^2=0.437$ ). In addition, a good correlation between the enthalpy of activation and the experimental relative rate constants was observed (Figure 2-15,  $R^2=0.952$ ). This indicated the error of the Gibbs free energy without the quasiharmonic approximation is primarily due to the error in the entropy calculations. This displays the importance of quasiharmonic correction to improve erroneous results that might arise from the computed entropies of molecules with low frequency vibrations, especially when comparing systems with small energy differences.



**Figure 2-14 Linear correlation between the computed relative rates ( $\ln(k/k_0)_{\text{theory}}$ ) without quasi-harmonic correction and experimental relative initial rates ( $\ln(k/k_0)_{\text{experiment}}$ ).**

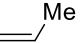
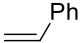
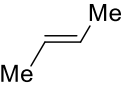
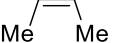

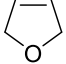


**Figure 2-15** Linear correlation between the computed relative solvated activation energies ( $-\Delta\Delta H^\ddagger_{\text{solv}}$ ) and experimental relative initial rates ( $\ln(k/k_0)_{\text{experiment}}$ ).

### 2.3.7 Catalyst reactivity with other substrates

To show that the newly designed catalyst could be useful in the catalysis with other olefin substrates, we calculated hydrocupration barriers with different olefins using DTBM-SEGPHOS and SEGFAST as ligands (Table 2-5). These calculations show that the SEGFAST-supported catalyst can lower the activation energy barrier to hydrocupration for a wide variety of olefin substrates and could be useful for farther catalytic applications when hydrocupration is rate-determining.

**Table 2-5 Computed hydrocupration barriers with SEGFAST and DTBM-SEGPHOS-supported CuH catalysts and different substrates. All energies are in kcal/mol relative to a free olefin and LCuH.**

Reagent						
	<b>2-12</b>	<b>2-13</b>	<b>2-14</b>	<b>2-15</b>	<b>2-16</b>	<b>2-17</b>
DTBM-SEGPHOS ( <b>2-L2</b> )	20.2	14.3	22.6	25.7	20.1	19.6
SEGFAST ( <b>2-L6</b> )	17.0	10.2	19.8	22.5	17.2	16.6

## 2.4 Conclusions

This study demonstrates how the combination of mechanistic insights, computational prediction, and experimental verification can successfully benefit ligand development. Using this synergistic approach, we were able to discover a new hybrid ligand **2-L6** that is capable of promoting the *anti*-Markovnikov hydroamination of unactivated, terminal olefins with a 62-fold rate increase compared to DTBM-SEGPHOS **2-L2** (Figure 2-16). We demonstrate that the ligand-substrate interaction model can be employed to not only provide the explanation for the increased reactivity but can also be used to rationally propose ligand alterations that can significantly improve the reaction design. By employing energy decomposition analysis methods, we were able to deconvolute each individual energy contributions of the steric, electronic, and dispersion effects that comprise the hydrocupration barrier. During our investigation, we identified that in addition to London dispersion, both electrostatic C–F $\cdots$ H–C non-covalent interactions and inductive effects of the *i*-C<sub>3</sub>F<sub>7</sub> substituents are capable of lowering the energy barrier for hydrocupration even further. Ultimately, the merger of both DTBM and *i*-C<sub>3</sub>F<sub>7</sub> substituents was key to success in

designing **2-L6** with balanced stability and reactivity. Furthermore, calculations with other substrates demonstrate that the designed ligand could be efficient for the catalysis of other less reactive substrates.

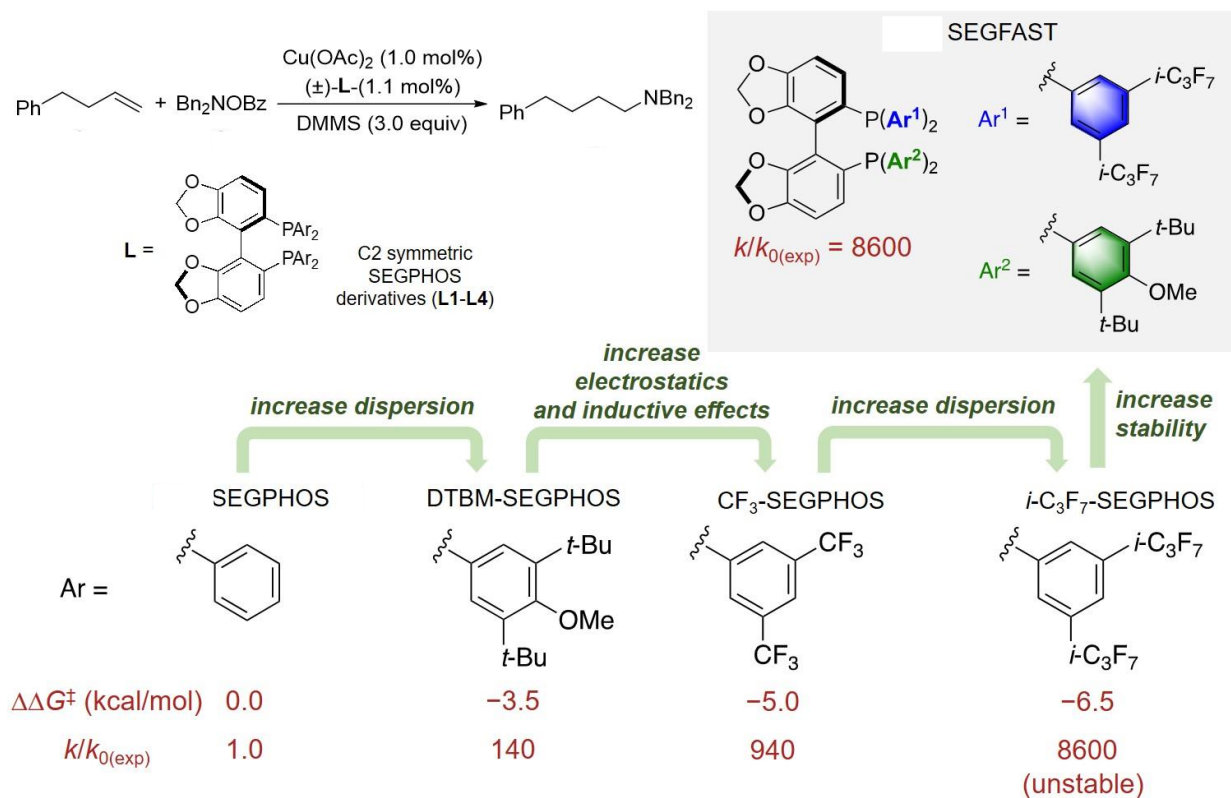
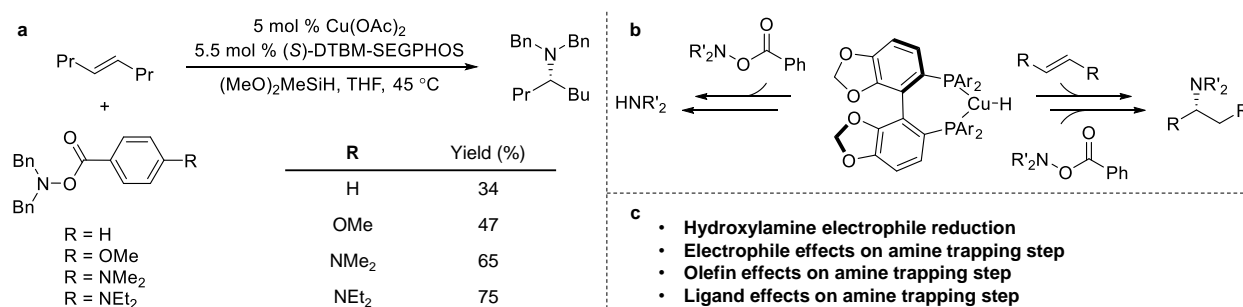


Figure 2-16 Summary of the computationally guided ligand design for CuH-catalyzed olefin hydroamination.

### 3.0 Reactivity of amine electrophiles in CuH-catalyzed hydroamination of olefins

#### 3.1 Introduction

In the previous chapter, we discussed computational ligand design for the hydroamination of terminal olefins, based on the past understanding of the mechanism and ligand effects on the hydrocupration of unactivated olefins. In this chapter, we explore the mechanism of the subsequent step between alkyl copper species and electrophile and reactivity of hydroxylamine electrophiles to understand how different electrophiles, substrates, and ligands affect the reactivity. While the hydrocupration step of the CuH-catalyzed hydroamination reaction has been studied extensively,<sup>40,52</sup> the understanding of how electrophiles react in this reaction is relatively limited.<sup>53</sup> However, in reactions with unactivated internal olefins, the choice of the electrophile plays an important role in promoting the reactivity (Figure 3-1a),<sup>37b</sup> where less electron-rich electrophiles undergo reduction instead of promoting hydroamination of olefins.



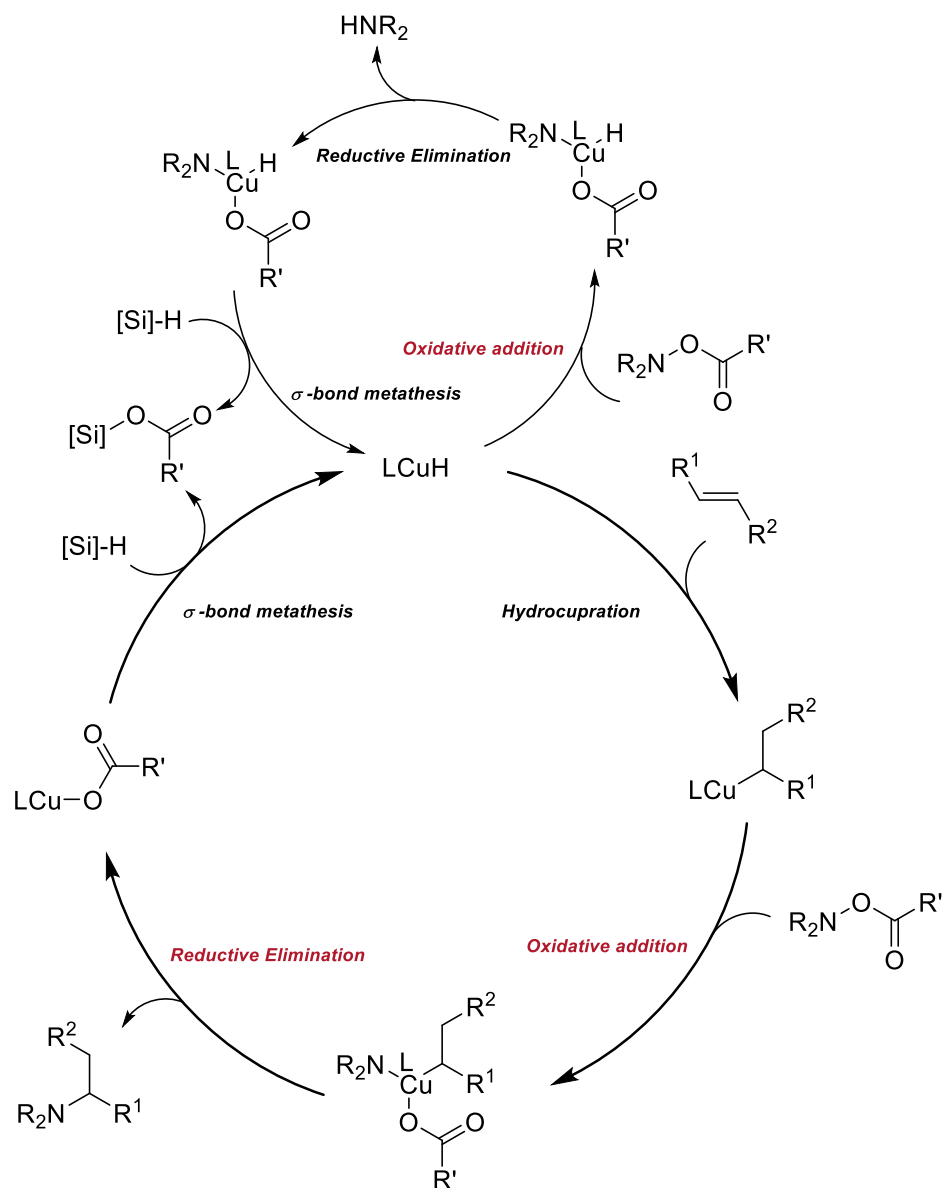
**Figure 3-1 (a) Reactivity of trans-4-octene in CuH-catalyzed hydroamination with different hydroxylamine electrophile reagents. (b) Possible reactions of copper hydride with different reaction components. (c)**

**Challenges associated with the hydroamination of olefins.**



These experimental results indicate that suppressing amine reduction is a significant challenge for the hydroamination of less reactive olefin substrates (Figure 3-1b). Therefore, a detailed understanding of the reaction mechanism of the reduction of the hydroxylamine electrophile, as well as ligand and electrophile effects that promote trapping with alkyl copper species rather than reduction, are important for future optimization to promote the reactivity of unreactive substrates.

In addition to addressing the challenges (Figure 3-1c) associated with the reduction of the electrophile, understanding the reactivity of electrophile will also facilitate the expansion of reaction scope to tertiary C-N bond formation. While copper-catalyzed hydroamination has been successfully implemented to achieve C-N bond formation at primary and secondary carbon centers,<sup>33–37</sup> formation of C–N bonds at a tertiary carbon remains an elusive goal, which could significantly expand the applicability of this procedure. Past experimental<sup>38</sup> studies have shown that styrene derivatives promote hydrocupration at the benzylic position. However, the methodology for installing tertiary C–N bonds on 1,1-disubstituted styrenes is still lacking. One potential challenge associated with the formation of a tertiary C–N bond could be attributed to less favorable kinetics during the electrophile trapping by a tertiary alkyl copper species following the hydrocupration of the 1,1-disubstituted styrene. Based on these challenges, we became interested in understanding the reactivity of hydroxylamine electrophiles in copper-catalyzed hydroamination reactions.



**Figure 3-2 Catalytic cycles for the hydroamination and amine reduction in CuH catalyzed olefin**  
**hydroamination**

Based on the previous computational results,<sup>40,53</sup> we proposed that the reactions of the hydroxylamine electrophile to both copper hydride and copper alkyl complexes proceed through oxidative addition and reductive elimination to generate the hydroamination product and the hydroxylamine reduction product, respectively (Figure 3-2). Based on the available experimental

evidence,<sup>37b</sup> where amine reduction is competitive with hydrocupration of internal olefins, we chose a model reaction system with *trans*-2-butene (**3-S1**), *O*-benzoyl-*N,N*-dibenzylhydroxylamine (**3-E1**), and DTB-SEGPHOS (**3-L2**) ligand to study the reaction mechanism. DTB-SEGPHOS (**3-L2**) was used in the calculations instead of the more commonly employed DTBM-SEGPHOS in order to reduce the ligand conformational space. Past experimental and computational results have shown that the reactivity of hydrocupration with these two ligands is very similar.<sup>40</sup>

### 3.2 Computational details

Geometry optimizations and single-point energy calculations were carried out using Gaussian 16.<sup>14</sup> Geometries of intermediates and transition states were optimized with the dispersion corrected B3LYP-D3 functional,<sup>15</sup> using Grimme's DFT-D3 dispersion correction,<sup>16</sup> with a mixed basis set of SDD for Cu and 6-31G(d) for other atoms in the gas phase. Vibrational frequency calculations were performed for all of the stationary points to confirm if each optimized structure is a local minimum or a transition state structure. Solvation energy corrections were calculated in THF solvent with the SMD solvation model<sup>19</sup> based on the gas-phase optimized geometries. The  $\omega$ B97X-D functional<sup>18</sup> with a mixed basis set of SDD for Cu and 6-311+G(d,p) for other atoms was used for single-point energy calculations in solution. The computed activation energies ( $\Delta E^\ddagger$ ) in the solution were dissected using the following ligand-substrate interaction model analysis.<sup>40</sup>

$$\Delta E^\ddagger = \Delta E_{\text{dist}} + \Delta E_{\text{int-bond}} + \Delta E_{\text{int-space}} \quad \text{eq.1}$$

The distortion energy ( $\Delta E_{\text{dist}}$ ) is the sum of the energies required to distort the LCuR catalyst and the hydroxylamine substrate into their transition state geometries.  $\Delta E_{\text{int-space}}$  was calculated from the interaction energy of a supramolecular complex of the phosphine ligand and the hydroxylamine substrate at the transition state geometry but in the absence of the CuR moiety. Then, the through bond interaction was calculated from  $\Delta E_{\text{int-bond}} = \Delta E^{\ddagger} - \Delta E_{\text{dist}} - \Delta E_{\text{int-space}}$ . The  $\Delta E_{\text{dist}}$  and  $\Delta E_{\text{int-space}}$  were both calculated using the  $\omega$ B97X-D functional in THF solvent with the SMD solvation model and with the SDD basis set for Cu and 6-311+G(d,p) for other atoms.  $\Delta E_{\text{int-space}}$  was further decomposed according to the following equation using the second-generation energy decomposition analysis based on absolutely localized molecular orbitals (ALMO-EDA)<sup>21</sup> method implemented in Q-Chem 5.3.<sup>22</sup>

$$\Delta E_{\text{int-space}} = \Delta E_{\text{Pauli}} + \Delta E_{\text{elstat}} + \Delta E_{\text{pol}} + \Delta E_{\text{ct}} + \Delta E_{\text{disp}} + \Delta E_{\text{solvation}} \quad \text{eq. 2}$$

In this analysis, Pauli repulsion energy ( $\Delta E_{\text{Pauli}}$ ) describes steric repulsions between the ligand and the substrate. Electrostatic interaction energy ( $\Delta E_{\text{elstat}}$ ) describes permanent electrostatics interactions between two fragments. Polarization energy ( $\Delta E_{\text{pol}}$ ) describes the charge-induced electrostatics interactions between ligand and the substrate. Charge transfer energy ( $\Delta E_{\text{ct}}$ ) describes the secondary orbital interactions between the two fragments. Dispersion interaction ( $\Delta E_{\text{disp}}$ ) corresponds to the Van Der Waals interactions between the two fragments, and the solvation energy ( $\Delta E_{\text{solvation}}$ ) corresponds to the solvation effects on the interacting fragments. Since the solvation effect will primarily impact through space electrostatic interactions of the two fragments, in this study, I have combined the permanent electrostatic interactions ( $\Delta E_{\text{elstat}}$ ) and solvation energy ( $\Delta E_{\text{solvation}}$ ) to describe solvated electrostatic interactions.

Conformational sampling of some of the key transition states was carried out using the iterative metadynamic sampling and genetic crossover (iMTD-GC) method implemented in the

CREST program,<sup>25</sup> with GFN2-xtb method<sup>26</sup> including additional geometry optimization of the final conformer ensemble using the B3LYP-D3/SDD-6-31G(d) method. NBO analysis of some key intermediates and transition states was performed using NBO version 3<sup>54</sup> embedded in Gaussian 16.

### 3.3 Results and discussions

#### 3.3.1 Hemilabile nature of SEGPHOS ligands in the oxidative addition of hydroxylamine electrophiles

In the reaction between DTB-SEGPHOS (**3-L1**) ligated copper hydride (**3-1**), *trans*-2-butene (**3-S1**), and the hydroxylamine (**3-E1**), copper hydride could competitively react with either the olefin or the electrophile. The hydrocupration of the internal olefin requires an activation energy barrier of 27.2 kcal/mol (**3-TS1**, Figure 3-3). On the other hand, the oxidative addition of the hydroxylamine to the copper hydride requires a barrier of 27.0 kcal/mol (**3-TS2**, Figure 3-3). These computed results are consistent with the past experimental findings, where **3-E1** was not as effective for the hydroamination of *trans*-4-octene, and more electron-rich electrophiles were necessary to suppress the hydroxylamine reduction (Figure 3-1). Following the hydrocupration, the formation of the resulting alkyl copper intermediate **3-2** is exergonic by 1.2 kcal/mol. Following the formation of the alkyl copper intermediate, an approximately 180-degree rotation about the C(biaryl)–P bond on the DTB-SEGPHOS ligand (Figure 3-4) leads to the dissociation of one of the bisphosphine arms to form the mono-phosphine ligated alkyl copper intermediate **3-3** ( $\Delta G = 6.3$  kcal/mol), which is 7.5 kcal/mol less stable than the bisphosphine-ligated isomer **3-2**.

Complex **3-3** then undergoes a relatively facile oxidative addition (**3-TS3**,  $\Delta G^\ddagger = 21.6$  kcal/mol with respect to **3-2**) to form the cationic Cu(III) complex **3-4**. Following the recombination with the benzoate anion, complex **3-5** undergoes a facile reductive elimination (**3-TS4**,  $\Delta G^\ddagger = 1.4$  kcal/mol with respect to **3-4**) to generate the desired hydroamination product and copper(I) benzoate **3-6**

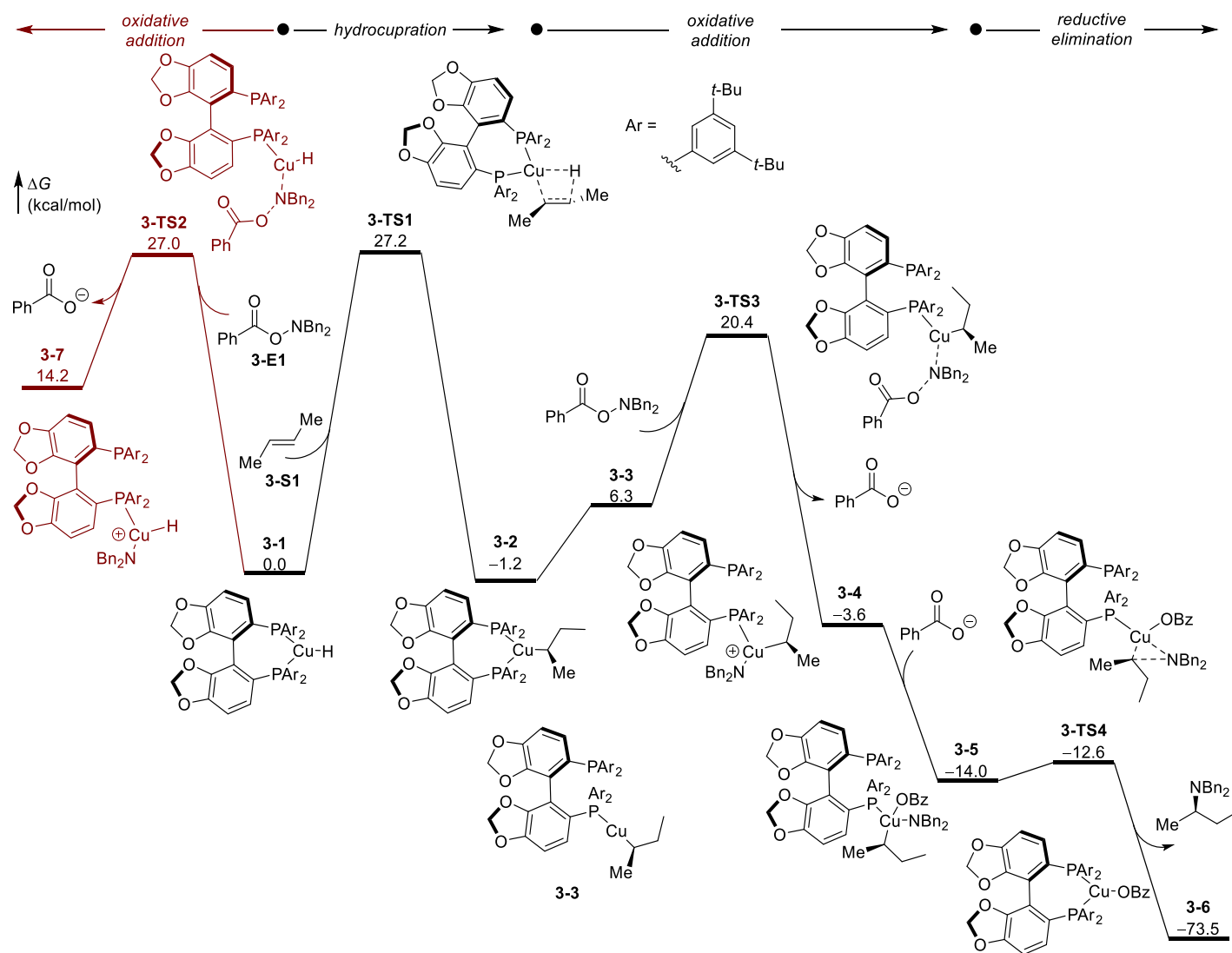
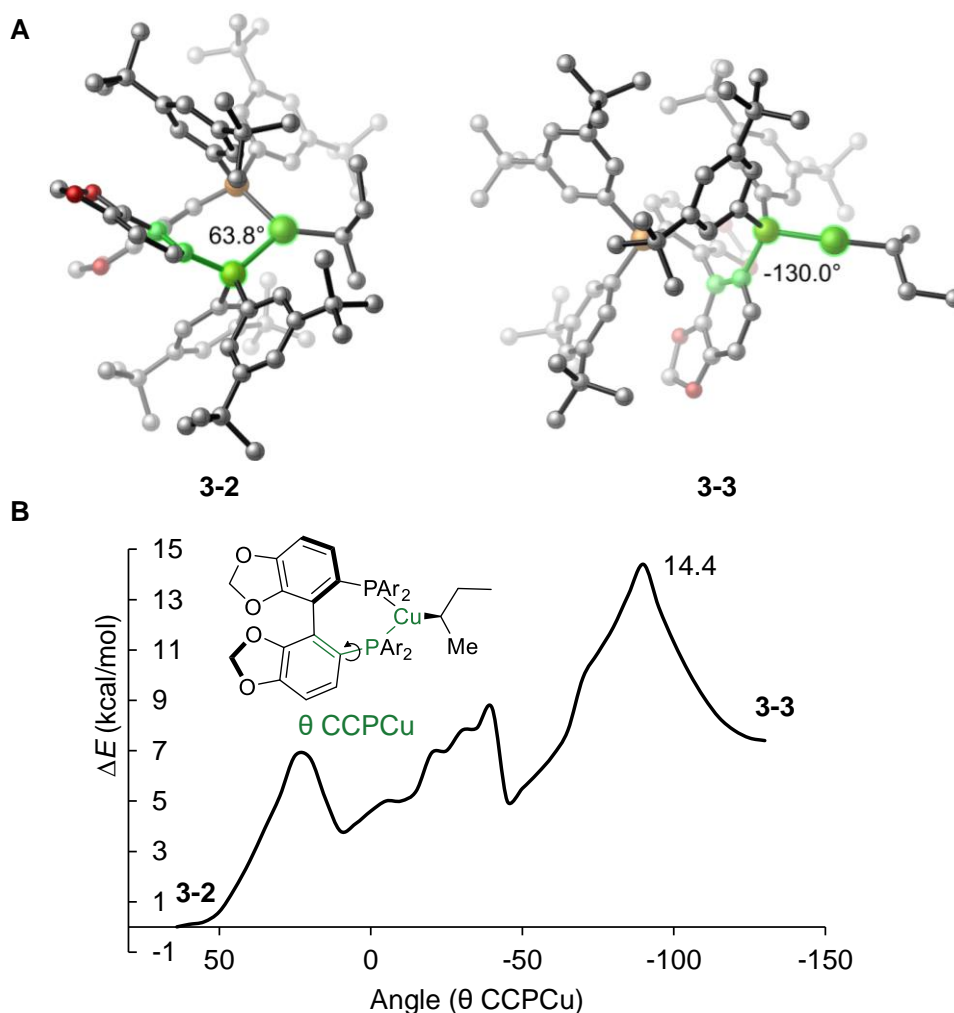


Figure 3-3 Reaction mechanism for the hydroamination of trans-2-butene. All energies are relative to 3-1, 3-S1, and 3-E1.

To ensure that the partial ligand dissociation to form mono-phosphine ligated intermediate **3-3** is kinetically accessible, we calculated the reaction coordinate of the rotation of the  $\theta(\text{CCPCu})$  dihedral from the complex **3-2** (Figure 3-4). These calculations show that the C–P bond rotation should be kinetically accessible, with the highest energy point occurring at  $-90^\circ$ , with the relative energy of 14.4 kcal/mol with respect to **3-2**.

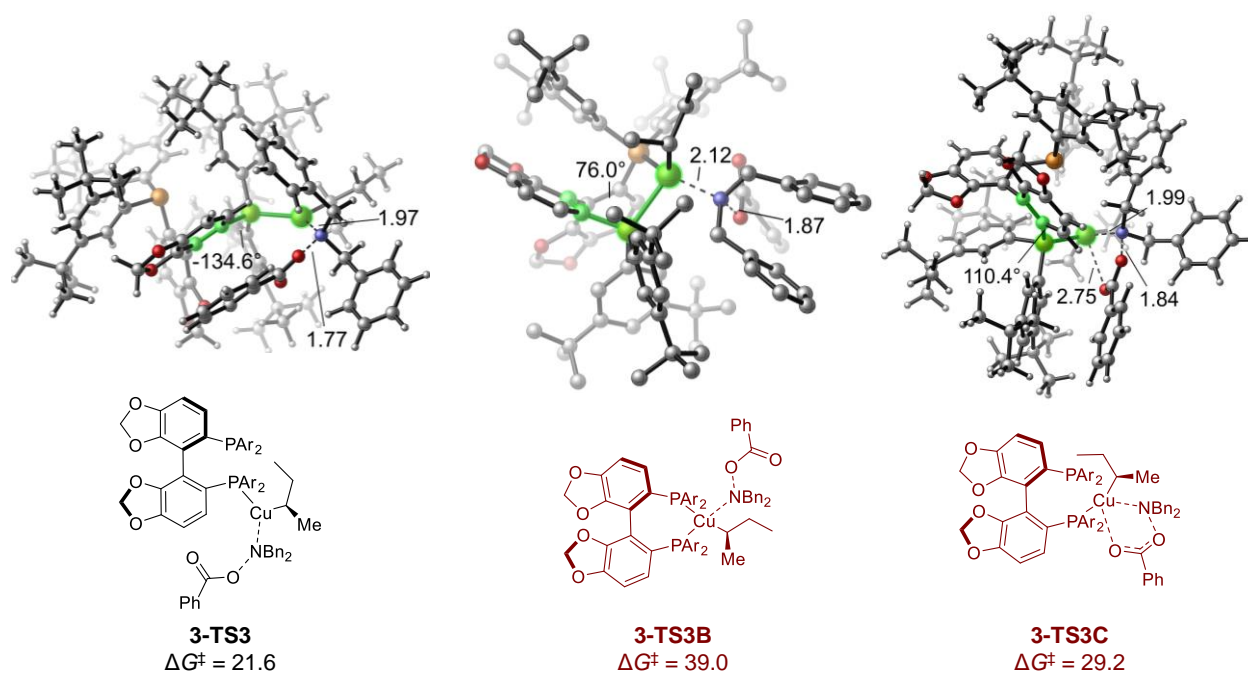


**Figure 3-4 A.** 3D structures of bidentate alkyl copper complex **3-2** and the monodentate ligated complex **3-3**.

**B.** potential energy surface for the rotation of CCPCu dihedral. All energies are relative to complex **3-2**.



While the most favorable pathway proceeds through dissociation of one of the phosphine arms via rotation of the C(biaryl)–P bond, alternate ligand conformations in the oxidative addition of the electrophile were also considered. Direct addition of the electrophile (i.e., the S<sub>N</sub>2 type oxidative addition) to the bidentate phosphine complex **3-2** requires a barrier of 39.0 kcal/mol (**3-TS3B**, Figure 3-5). The oxidative addition after partial dissociation of one of the phosphine arms through a 5-member transition state is also kinetically less favorable, with a barrier of 29.2 kcal/mol. (**3-TS3C**, Figure 3-5).



**Figure 3-5 3D structures for different ligand conformations during electrophile oxidative addition. All energies are relative to the intermediate 3-2 and 3-E1**

The less favorable pathways can be attributed to unfavorable steric effects, where the approach of relatively large electrophile is hindered by the bulky catalyst. The rotation about the C(biaryl)–P bond makes the copper center less sterically hindered, and therefore promotes the

reactivity towards oxidative addition. This hypothesis is further supported by considering the transition state structure, where **3-TS3** has the shortest distance between the Cu and the N atom on the hydroxylamine (1.97, 2.12, 1.99 Å for **3-TS3**, **3-TS3B**, and **3-TS3C**, respectively, Figure 3-5). This is further supported by considering the distortion-interaction analysis, where the distortion energies are significantly more unfavorable in **3-TS3B** and **3-TS3C** due to unfavorable steric environment around the metal center (Table 3-1). Without the conformation change following Cu–P dissociation, the steric environment around the metal center does not change significantly. However, this allows the binding of the carbonyl group through the five-member transition state to promote bonding interactions. However, this leads to increased catalyst distortion and significantly larger electrophile distortion. Nonetheless, the interaction energy of **3-TS3B** is weaker, and **3-TS3C** is comparable to that in **3-TS3**.

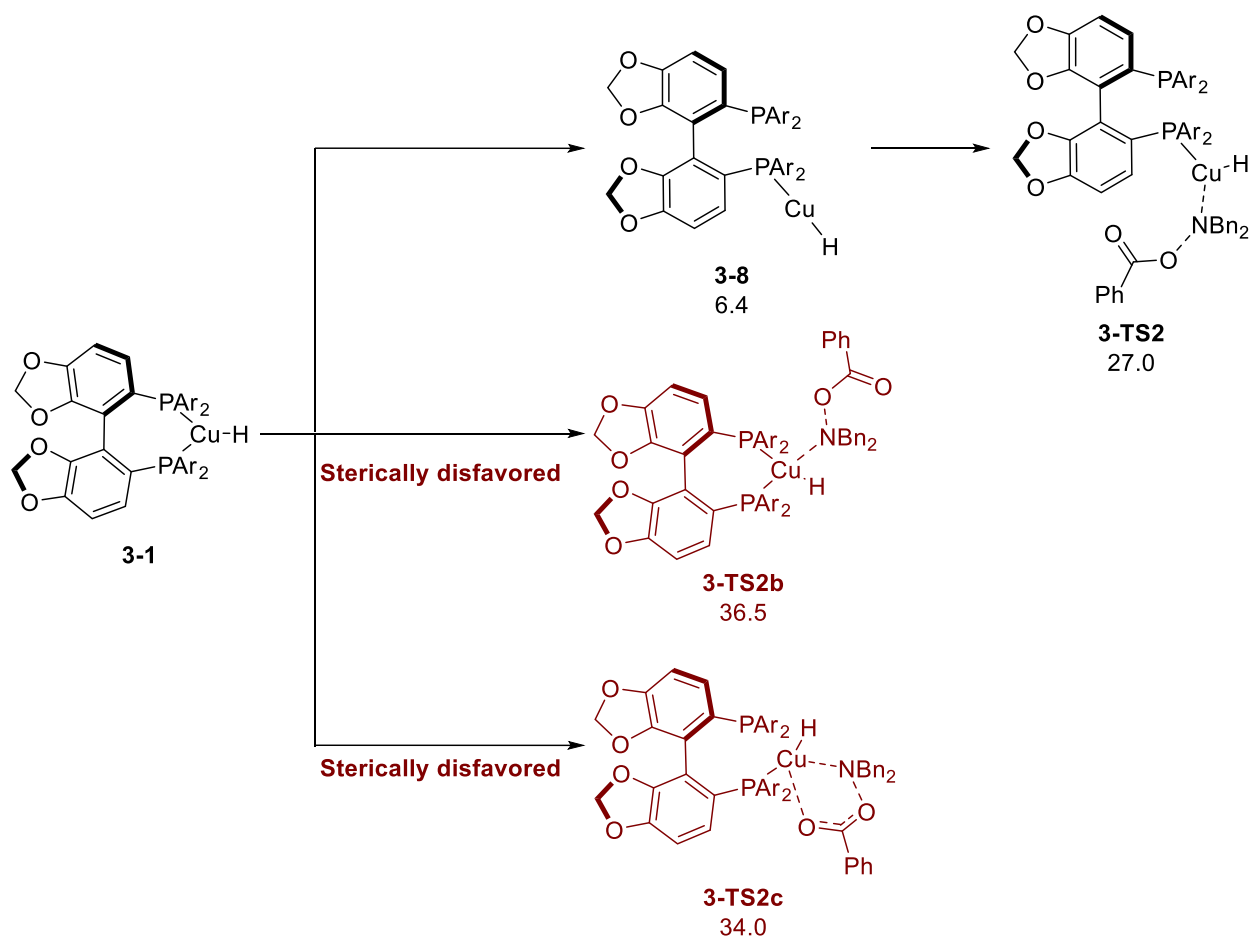
**Table 3-1 Distortion interaction analysis of the three competing oxidative addition transition states<sup>a</sup>**

	<b>3-TS3</b>	<b>3-TS3B</b>	<b>3-TS3C</b>
$\Delta E^\ddagger$	0.1	15.4	6.8
$\Delta E_{\text{dist\_catalyst}}$	20.1	21.4	22.5
$\Delta E_{\text{dist\_electrophile}}$	18.5	28.8	24.4
$\Delta E_{\text{interaction}}$	−38.5	−34.9	−40.1

<sup>a</sup> All energies are reported in kcal/mol.

We also considered ligand conformations in the oxidative addition of the electrophile to the copper hydride, which leads to electrophile reduction. We found that the most favorable oxidative addition to the copper hydride (**3-TS2**,  $\Delta G^\ddagger = 27.0$  kcal/mol) also proceeds through the initial dissociation of one of the phosphine arms and the subsequent C–P bond rotation. The similar

computed activation energies of electrophile reduction and hydrocupration are in good agreement with previous experimental results that showed that the electrophile reduction is competitive with the olefin hydrocupration. The oxidative addition to the bidentate phosphine ligated copper hydride is highly disfavored, requiring activation energy of 36.5 kcal/mol (**3-TS2B**, Figure 3-6). Furthermore, the five-membered transition state is also highly disfavored, requiring activation energy of 34.0 kcal/mol (**3-TS2C**, Figure 3-6). These results indicate that the C–P bond rotation is necessary to promote the oxidative addition, despite the size of the substituent on the copper center. Ligand conformation change of copper hydride is endergonic by 6.4 kcal/mol (**3-8**), which is comparable to the energy required for the conformational change of alkyl copper complex **3-3** from bidentate conformer **3-2** (Figure 3-6). Therefore, this process should also be accessible kinetically.

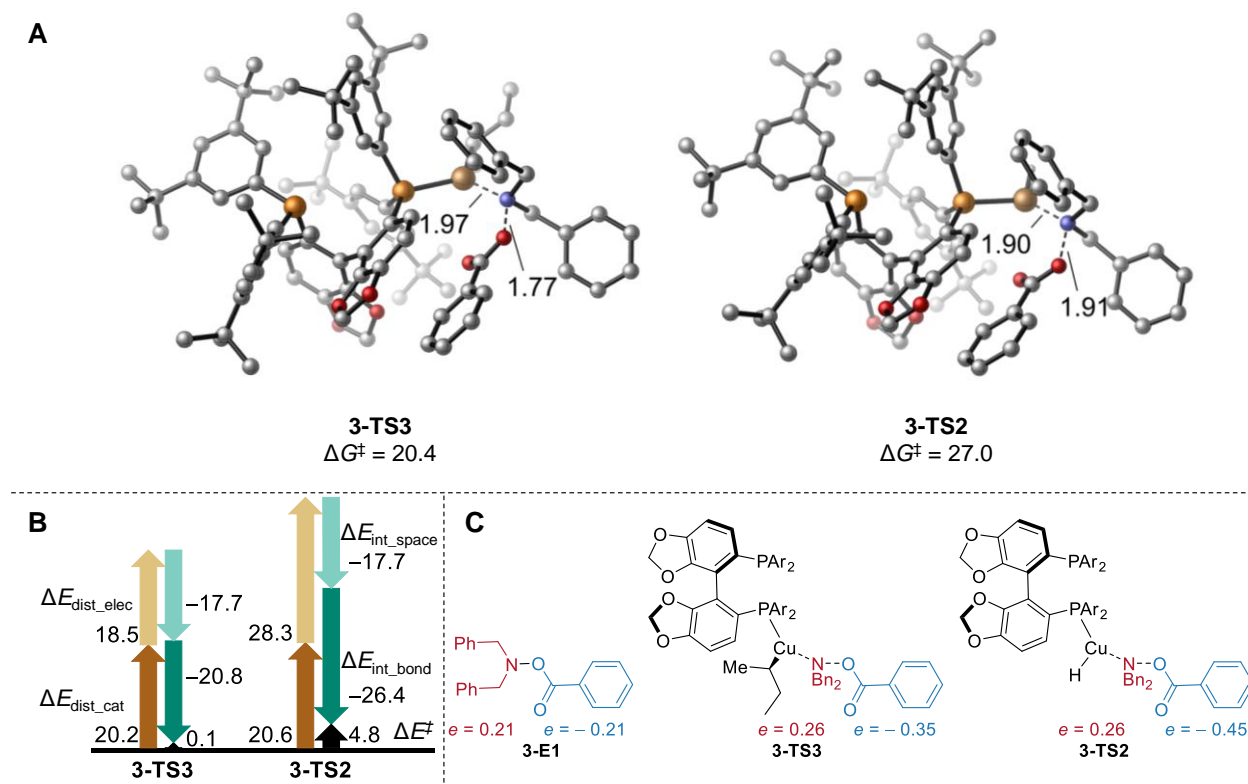


**Figure 3-6** Competing conformations for the oxidative addition transition states to the copper hydride, leading to the amine reduction. All energies are relative to 3-1 and 3-E1

### 3.3.2 Oxidative addition to copper hydride is more sensitive to electrophile electronic effects than oxidative addition to alkyl complexes

The oxidative addition of the electrophile to the copper alkyl complex **3-TS3** is significantly more favorable than the oxidative addition to the copper hydride **3-TS2**. The addition to the copper alkyl complex **3-TS3** has an earlier transition state with a shorter N–O bond (1.77 Å) and a longer Cu–N bond (1.97 Å) when compared to the oxidative addition to the copper hydride ( $d(\text{N–O}) = 1.91$  Å,  $d(\text{Cu–N}) = 1.90$  Å Figure 3-7A). This difference can be attributed to

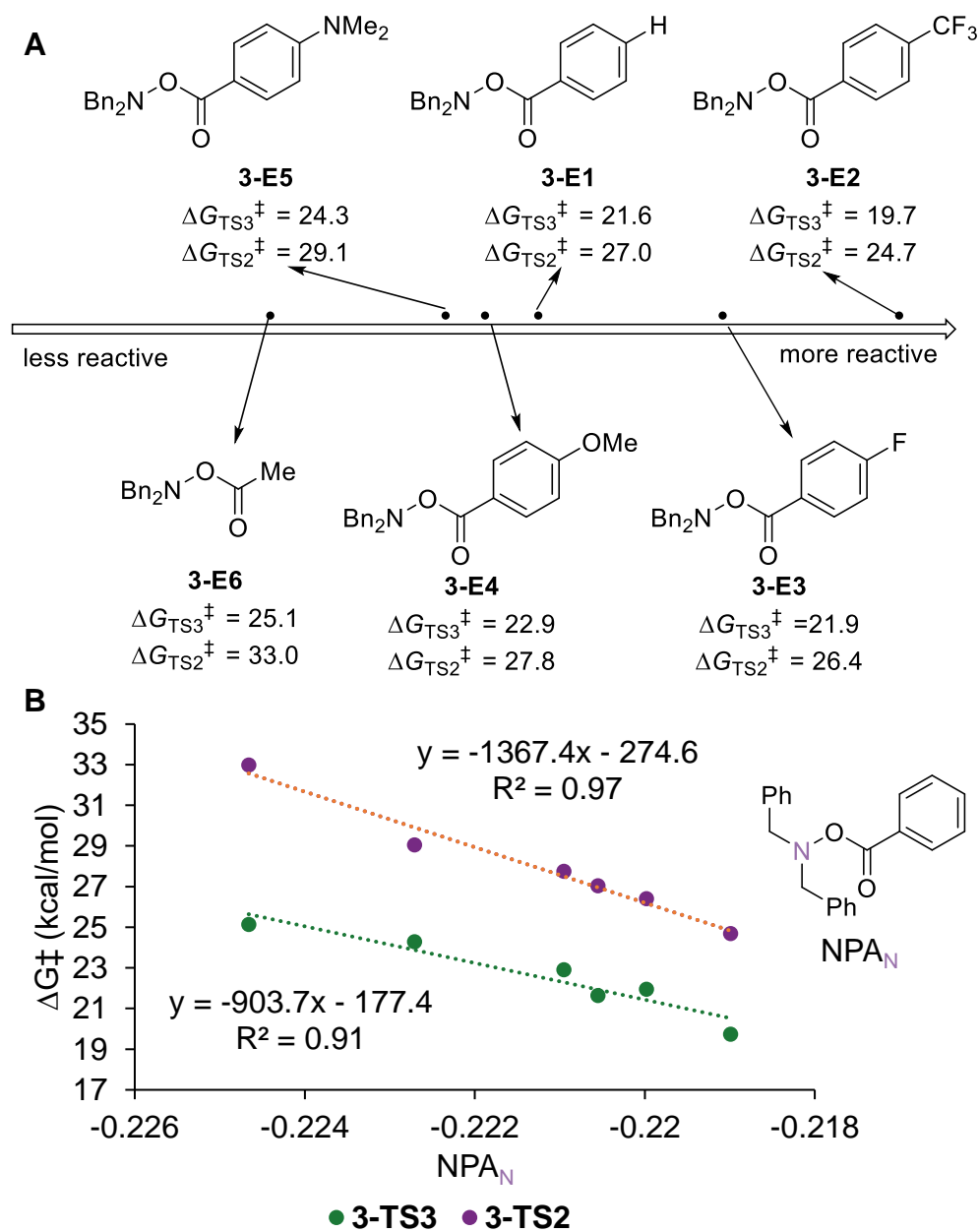
oxidative addition being less favorable with the copper hydride complex (Figure 3-3). Further investigation of these two transition states using the ligand-substrate interaction model revealed that the substrate distortion is significantly higher in **3-TS3** than in **3-TS2** ( $\Delta\Delta E_{\text{dist\_electrophile}} = 9.8$  kcal/mol; Figure 3-7B). This difference can be attributed to the later transition state during the oxidative addition to copper hydride. On the other hand, while the bonding interaction between copper and nitrogen is also increased for **3-TS3** ( $\Delta\Delta E_{\text{int\_bond}} = -5.6$  kcal/mol; Figure 3-7B), the increased favorable interaction does not balance out increased distortion energy for the substrate. These results suggest that the oxidative addition to the alkyl copper complex is favored through electronic effects, where more electron-donating alkyl ligand, relative to hydride, promotes the oxidative addition transition state. Better donor ligand raises the HOMO energy in monodentate phosphine-coordinated alkyl copper complex ( $\text{HOMO}(\mathbf{3-3}) = -6.69$  eV) when compared to monodentate phosphine-coordinated copper hydride ( $\text{HOMO}(\mathbf{3-8}) = -7.48$  eV), which leads to the greater nucleophilicity of the alkyl copper complex **3-3** and higher reactivity in the  $\text{S}_{\text{N}}2$ -type oxidative addition when compared to a copper hydride (**3-8**).



**Figure 3-7** A. 3D structures of two oxidative addition transition states. The activation free energies for **3-TS3** and **3-TS2** are in kcal/mol with respect to **3-2** and **3-1**, respectively B. Ligand substrate-interaction analysis of two oxidative addition transition states. Color code: Brown – catalyst distortion, light brown – electrophile distortion, light green – through space interaction, dark green – bonding interaction, black – activation energy. C. NPA charge analysis of **3-E1** and oxidative transition states **3-TS3** and **3-TS2**.

Furthermore, natural population analysis (NPA) charges of the two oxidative addition transition states show that the later transition state in **3-TS2** leads to more charge transfer onto the benzoate fragment of the electrophile ( $\Delta\Delta e = -0.10$ , Figure 3-7C). This led us to stipulate that the oxidative addition of the electrophile to copper hydride **3-TS2** leading to the reduction of the electrophile might be more sensitive to the electronic effects of the electrophile. To support this hypothesis, we carried out calculations with different electrophiles with varying electronic characters (Figure 3-8A). NPA charge on the nitrogen atom of the hydroxylamine was chosen as

the electronic descriptor to compare the relative sensitivity of two types of transition states on the nature of the electrophile. The calculated results show that the activation energies for both types of transition states correlate well with the NPA charge on the nitrogen atom of the electrophile (Figure 3-8B). Furthermore, the activation free energy of the oxidative addition to the copper hydride is more sensitive to the NPA charge on the nitrogen. This result suggests that the later transition state in **3-TS2**, relative to **3-TS3**, leads to the increased amount of charge transfer to the carboxylate group and thus increases the sensitivity of amine reduction to the electronic effects of the hydroxylamine. Therefore, the hydroamination reaction can be improved further by choosing more electron-rich hydroxylamines, which will lead to an increased barrier for the amine reduction pathway without significantly hindering facile oxidative addition to primary or secondary alkyl copper complexes. Among the electrophiles considered in Figure 3-8, **3-E1–3-E4** have been found to be ineffective for the hydroamination of internal olefins due to the issue of amine reduction being kinetically more favorable than hydrocupration of olefins. On the other hand, even for most electron-rich electrophiles **3-E5** and **3-E6**, the barrier for the oxidative addition to the alkyl copper complex **3-2** is still relatively low, at 24.3 kcal/mol and 25.1 kcal/mol, respectively.



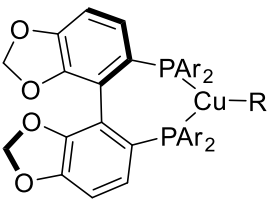
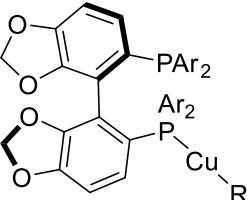
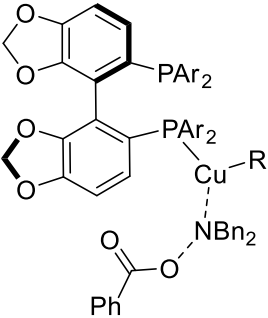
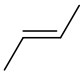
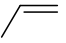

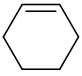
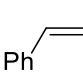
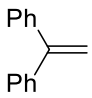
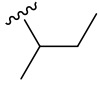
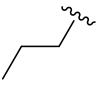
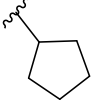
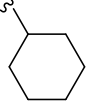
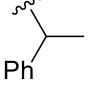
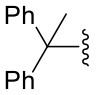
**Figure 3-8 A.** Activation energies for the oxidative addition to copper hydride (3-TS2) and alkyl copper complex (3-TS3) with different hydroxylamines. **B.** Correlation between the activation energies for the oxidative addition transition states with LCuH and with LCuR where R = 2-butyl and NPA charge on the nitrogen atom of the hydroxylamine.



### 3.3.3 Tertiary alkyl copper complexes hinder oxidative addition due to unfavorable steric effects

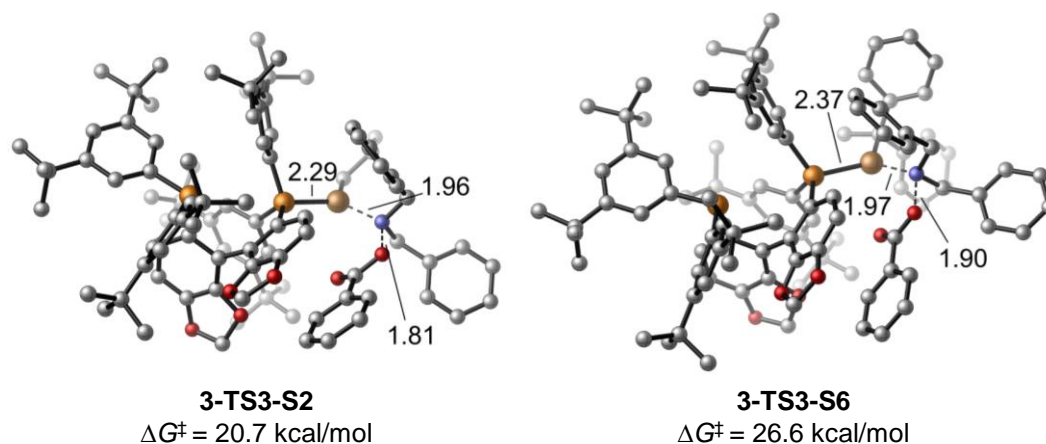
To investigate whether the identity of the olefin can significantly affect the barrier to the oxidative addition of the hydroxylamine to the alkyl copper complex, we calculated the oxidative addition barriers of alkyl copper complexes originating from a wide variety of hydrocupration products of olefins **3-S1** – **3-S6** with different steric and electronic characters (Table 3-2). Electrophile XX was used in these calculations. These calculations indicate that primary (olefin **3-S2**) and secondary (olefin **3-S1**) alkyl copper complexes have similar reactivities towards oxidative addition. Furthermore, cyclic alkyl copper complexes (olefins **3-S3** and **3-S4**) were found to be more reactive towards the oxidative addition than acyclic alkyl copper complexes. Additionally, the oxidative addition to a secondary benzylic copper complex (olefin **3-S5**) was also found to be more favorable than the addition to secondary alkyl copper complexes, despite it being sterically more hindered than the secondary alkyl copper complexes. Finally, the addition to the tertiary benzylic alkyl complex (olefin **3-S6**) was found to be significantly less favorable, requiring activation energy of 26.6 kcal/mol (Table 3-2).

**Table 3-2 Activation energies for the oxidative addition of hydroxylamine 3-E1 to various different alkyl copper complexes. All energies are relative to the alkyl copper complex and electrophile 3-E1.**

						
	<b>a</b>		<b>b</b>		<b>c</b>	
substrate						
	<b>3-S1</b>	<b>3-S2</b>	<b>3-S3</b>	<b>3-S4</b>	<b>3-S5</b>	<b>3-S6</b>
R =						
<b>a</b>	0.0	0.0	0.0	0.0	0.0	0.0
<b>b</b>	6.3	6.6	6.2	8.4	10.7	7.5
<b>c</b>	20.6	20.7	17.6	19.0	17.5	26.6

To better understand the origin of substrate effects on the reactivity, we performed ligand-substrate interaction analysis on primary alkyl complex **3-TS3-S2** and tertiary benzylic complex **3-TS3-S6**. These calculations indicate that due to the dissociation of the phosphine ligand, the steric difference between primary and secondary alkyl complexes does not lead to significant differences in reactivity, with similar distortion energies for the reactions with primary (**3-TS3-S2**,  $\Delta E_{\text{dist}} = 39.2$  kcal/mol), and secondary acyclic (**3-TS3**,  $\Delta E_{\text{dist}} = 38.7$  kcal/mol) alkyl complexes. On the other hand, in the addition to the tertiary benzylic complex (**3-TS3-S6**), steric effects play a more significant role, resulting in significant elongation of the Cu–P bond (2.37 Å, Figure 3-9) during the transition state, leading to significantly larger distortion energy in this transition state

( $\Delta E_{\text{dist}} = 53.3$  kcal/mol). This makes the oxidative addition of hydroxylamines to the tertiary complexes more challenging.



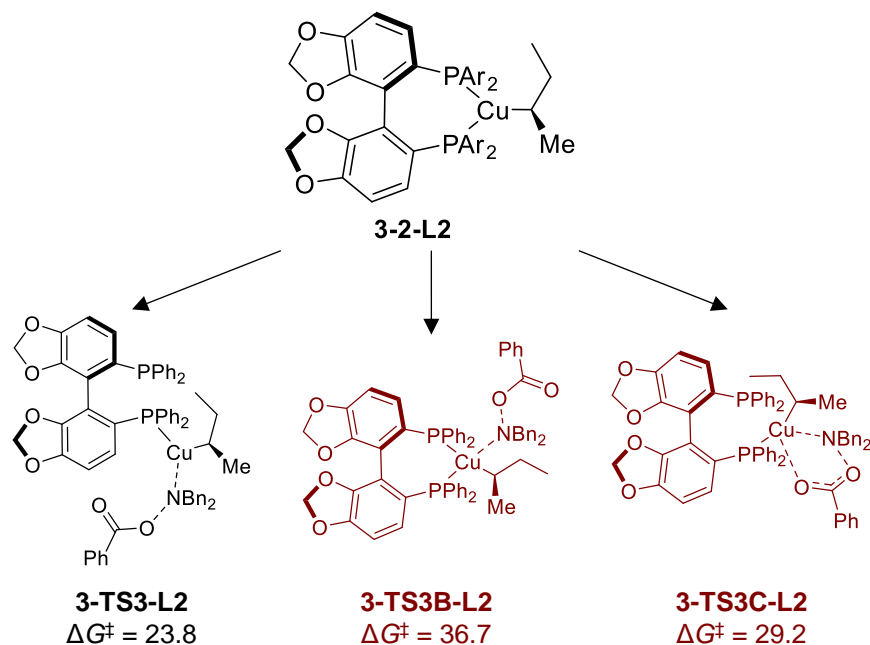
**Figure 3-9 A. 3D structures of oxidative addition transition states with primary alkyl copper complex 3-TS3-S2 and tertiary alkyl copper complex 3-TS3-S6**

These results indicate that while oxidative addition is easily accessible for primary and secondary alkyl copper complexes, as well secondary benzylic copper complexes, oxidative addition to the tertiary alkyl copper complexes is more challenging and is the rate-determining step in hydroamination reactions involving sterically hindered tertiary alkyl copper complexes.

### 3.3.4 Through space ligand electrophile dispersion interactions promote oxidative addition transition states

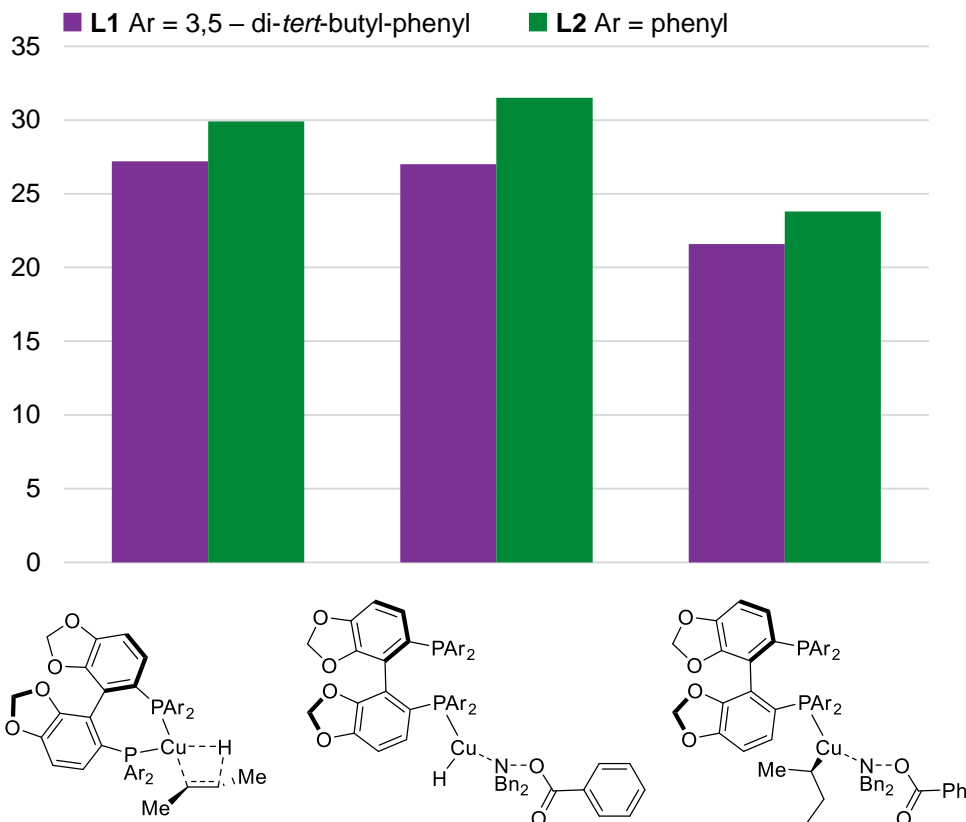
To understand the ligand effects on the oxidative addition, we first considered different ligand conformations in the oxidative addition of hydroxylamine **3E-1** to SEGPHOS (**L2**) ligated 2-butyl copper complex (**3-2-L2**). These calculations show that despite the smaller size of the

SEGPPOS ligand compared to DTB-SEGPPOS, the most favorable oxidative addition with **3-2-L2** still proceeds through the dissociation of one of the phosphine arms of **L2** and subsequent C–P bond rotation (Figure 3-9). The activation Gibbs free energy of the oxidative addition following the bond rotation (3-TS3-L2) is 23.8 kcal/mol, whereas the transition state without phosphine dissociation (3-TS3B-L2) requires a barrier of 36.7 kcal/mol, and the transition state without the bond rotation following phosphine dissociation (3-TS3C-L2) has an activation Gibbs free energy of 29.2 kcal/mol. These results indicate that the size of the aryl substituents on the SEGPPOS-derived ligands has an insignificant role in the mechanism of the oxidative addition, and bond rotation is always more favorable to promote the oxidative addition.



**Figure 3-10** Competing conformations for the oxidative addition transition states to the SEGPPOS-ligated copper 2-butyl complex. All energies are relative to 3-2-L2 and 3-E1

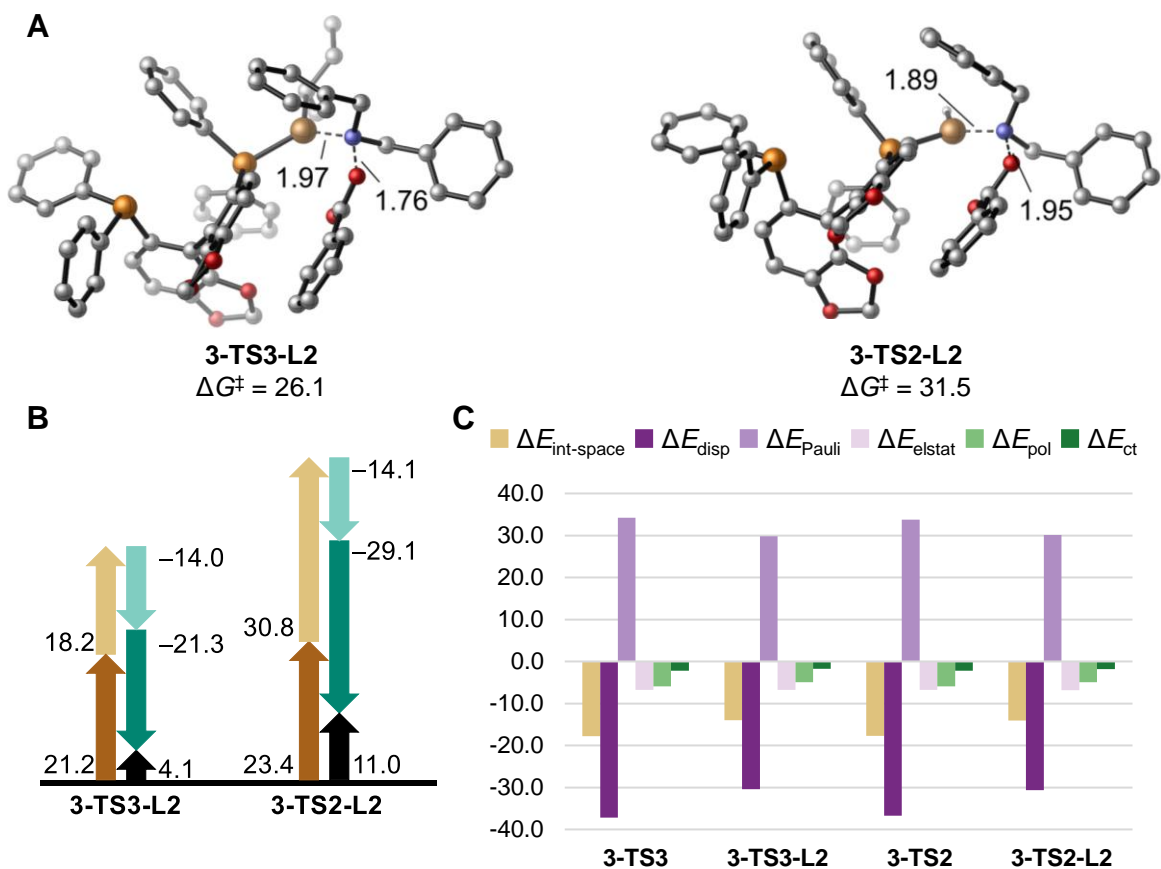
Following the understanding that the ligand C(biaryl)-P bond rotation is still necessary to promote the oxidative addition with a smaller SEGPHOS ligand, we proceeded to calculate other two key transition states (**3-TS1-L2**, and **3-TS2-L2**, Figure 3-12A) using the SEGPHOS-ligated copper hydride, to compare their reactivity in electrophile reduction to that of the DTB-SEGPHOS-ligated copper hydride. Our calculations indicate that DTB-SEGPHOS not only promotes the reactivity towards hydrocupration of olefins but also promotes the reactivity towards oxidative addition, both to copper hydride and copper alkyl complexes (Figure 3-11).



**Figure 3-11 Ligand effects on the CuH catalyzed hydroamination of olefins. Computed activation free energies ( $\Delta G^\ddagger$ ) of the hydrocupration and oxidative addition to copper hydride steps with respect to the separated LCuH, olefin 3-S1, and hydroxylamine 3-E1. Oxidative addition to copper alkyl groups is calculated with respect to the LCuR complex and hydroxylamine 3-E1.**

While past computational studies have carefully explored the key factors promoting reactivity with 3,5-disubstituted SEGPHOS ligands in hydrocupration, understanding of ligand effects on the oxidative addition step is more limited. To better understand the origin of the ligand effects, we performed ligand-substrate interaction analysis on these two oxidative addition transition states. Our calculations show that the primary difference between the reactivity of DTB-SEGPHOS-ligated copper hydride and alkyl copper complexes (**3-TS2**, **3-TS3**, Figure 3-7B) and SEGPHOS-ligated complexes (**3-TS2-L2**, **3-TS3-L2**, Figure 3-12B) arises from more favorable

through-space interactions between the DTB-SEGPHOS ligand and the electrophile ( $\Delta\Delta E_{\text{int\_space}} = -3.6$  and  $-3.7$  kcal/mol for oxidative addition to  $\text{LCuH}$  and  $\text{LCu(2-butyl)}$ , respectively). Further decomposition of the through-space interaction reveals that the primary factor that promotes reactivity towards oxidative addition with DTB-SEGPHOS-ligated species arises from favorable dispersion interactions, where dispersion with DTB-SEGPHOS is favored by 6.1 kcal/mol in the oxidative addition transition state with copper hydride complex, and by 6.7 kcal/mol in the oxidative addition transition state with alkyl copper complex (Figure 3-12C).

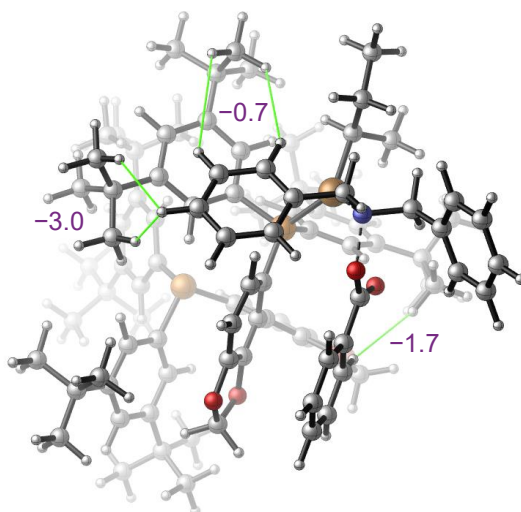


**Figure 3-12** 3D structures of oxidative addition transition states with SEGPHOS ligated copper **3-TS3-L2** and **3-TS2-L2**. **B.** Ligand substrate-interaction analysis of three oxidative addition transition states. Color code: Brown – catalyst distortion, yellow – electrophile distortion, blue – through space interaction, green – through bond interaction, black – activation energy. **C.** Energy decomposition analysis of through space ligand-electrophile interaction.

To understand the origin of the increased dispersion interactions, we performed pairwise dispersion energy calculations between key *tert*-butyl groups and the electrophile in oxidative addition transition state with the alkyl copper complex (**3-TS3**). The CuH and all atoms on the biphosphine ligand except the *tert*-butyl group were removed from the transition state geometry to perform this analysis. Then, each *tert*-butyl group was capped with hydrogen with a bond length of 1.07 Å. Next, the interaction energies and the dispersion interactions between the *tert*-butane



and the electrophile were calculated. This analysis suggests that the favorable dispersion interactions in **3-TS3** arise primarily between two *tert*-butyl groups on the *P*-aryl group interacting with the benzylic substituent on the amine, as well as the interactions between the benzoate group and the *tert*-butyl group (Figure 3-13). These interactions together add up to 5.4 kcal/mol, which largely accounts for the increased dispersion interactions observed with EDA analysis of the through-space interactions. There are no significant dispersion interactions between an electrophile and the dissociated phosphine phenyl groups, as they are placed far away from the electrophile.

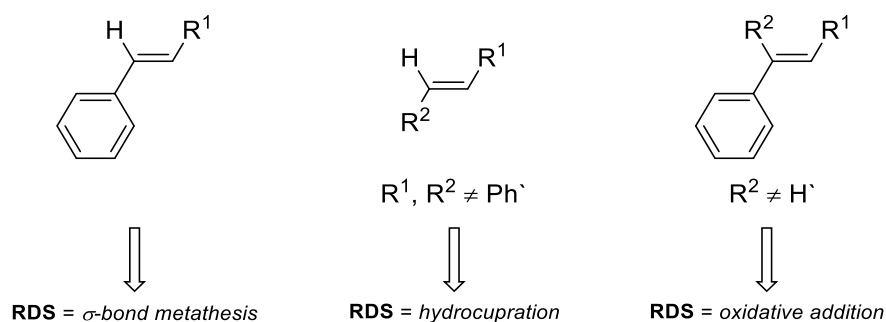


**Figure 3-13** Key dispersion interactions between the electrophile and *tert*-butyl groups. Numbers in purple represent the favorable dispersion interactions between an electrophile and corresponding *tert*-butyl group in kcal/mol.

### 3.4 Conclusion

DFT calculations were performed to study the mechanisms of the electrophile addition step in the copper-catalyzed hydroamination of olefins. DFT calculations indicate that the SEGPHOS-derived ligands act as a hemilabile ligand through the dissociation of one of the phosphine arms.

The partially dissociated ligand conformation promotes the oxidative addition of the electrophile by reducing steric repulsions between the bisphosphine ligand and the electrophile. The reaction with hydroxylamine electrophile takes place via the SN2-type oxidative addition pathway. Investigation of the electrophile effects reveals that the oxidative addition to copper hydrides, leading to undesired hydroxylamine reduction, is more sensitive to the electronic effects of the electrophile than the oxidative addition to alkyl copper complexes. Therefore, using *e*-rich hydroxylamine electrophiles such as **3-E5** or **3-E6** suppresses their oxidative addition to the copper halide complex, therefore suppressing hydroxylamine reduction without significantly increasing the barrier to the OA with alkyl copper species. The oxidative addition becomes significantly hindered when reacting with tertiary alkyl copper complexes. Based on this understanding, combined with past experimental and computational results, olefin substrates can be combined into three distinct classes depending on their reactivity and rate-determining steps, where copper hydride regeneration through  $\sigma$ -bond metathesis is the RDS for activated olefins, hydrocupration is the RDS for the unactivated olefins, and oxidative addition is the RDS for 1,1-disubstituted activated styrenes (Figure 3-14).



**Figure 3-14 Reactivity of different olefin reagents**

The investigation of ligand effects on oxidative addition transition states revealed that sterically bulky 3,5- substituents promote oxidative addition leading to electrophile reduction. This

activation method is comparable to interactions that promote hydrocupration of olefins. These results indicate that achieving reactivity with less reactive olefins will require a careful ligand/electrophile tuning approach in order to achieve olefin hydrocupration without promoting amine reduction or significantly hindering subsequent oxidative addition to the alkyl copper complexes.

## 4.0 Cu-H catalyzed allylation of indazoles to form a C3-quaternary chiral center

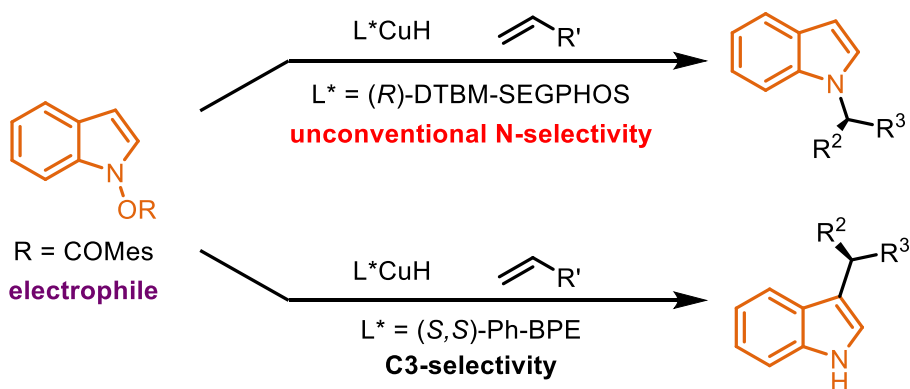
A significant part of this chapter was published as Ye, Y.; Kevlishvili, I.; Feng, S.; Liu, P.; Buchwald, S. L. *J. Am. Chem. Soc.* **2020**, *142*, 10550–10556.

### 4.1 Introduction

Functionalization of nitrogen containing heterocycles is an important area in organic synthesis because of their importance in pharmaceutical applications.<sup>55</sup> Particularly, the functionalization of indazoles is of great interest due to their utility in pharmaceutical and medicinal chemistry.<sup>56</sup> One of the most efficient methodologies for the functionalization of indazoles involves their direct alkylation, where indazole acts as a nucleophile.<sup>57</sup> In these applications, the functionalization is usually either N1- or N2- selective.<sup>58</sup> On the other hand, transformations for C3-selective alkylation are less common.<sup>59</sup>

Recently, the Buchwald group developed a method to prepare enantioenriched alkylated indole derivatives using CuH-catalyzed reactions with alkene substrates.<sup>60</sup> In this reaction, N-(benzoyloxy)indoles acted as an electrophile, and depending on the choice of the ligand, the reaction could proceed through either N1- or C3- regioselectivity (Figure 4-1a). Based on this novel methodology, the Buchwald group hypothesized that a similar reaction with N-(benzoyloxy)indazole as an electrophile could overcome the inherent N1- or N2- selectivity of indazoles to instead promote functionalization at the C3 position (Figure 4-1b).

(a) CuH-catalyzed asymmetric alkylation of indole electrophiles



(b) Proposed indazole C3-functionalization using electrophilic indazole reagent

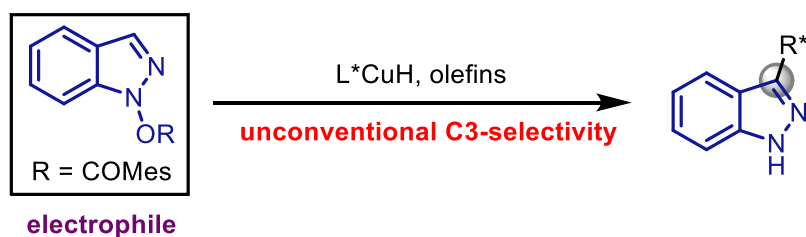
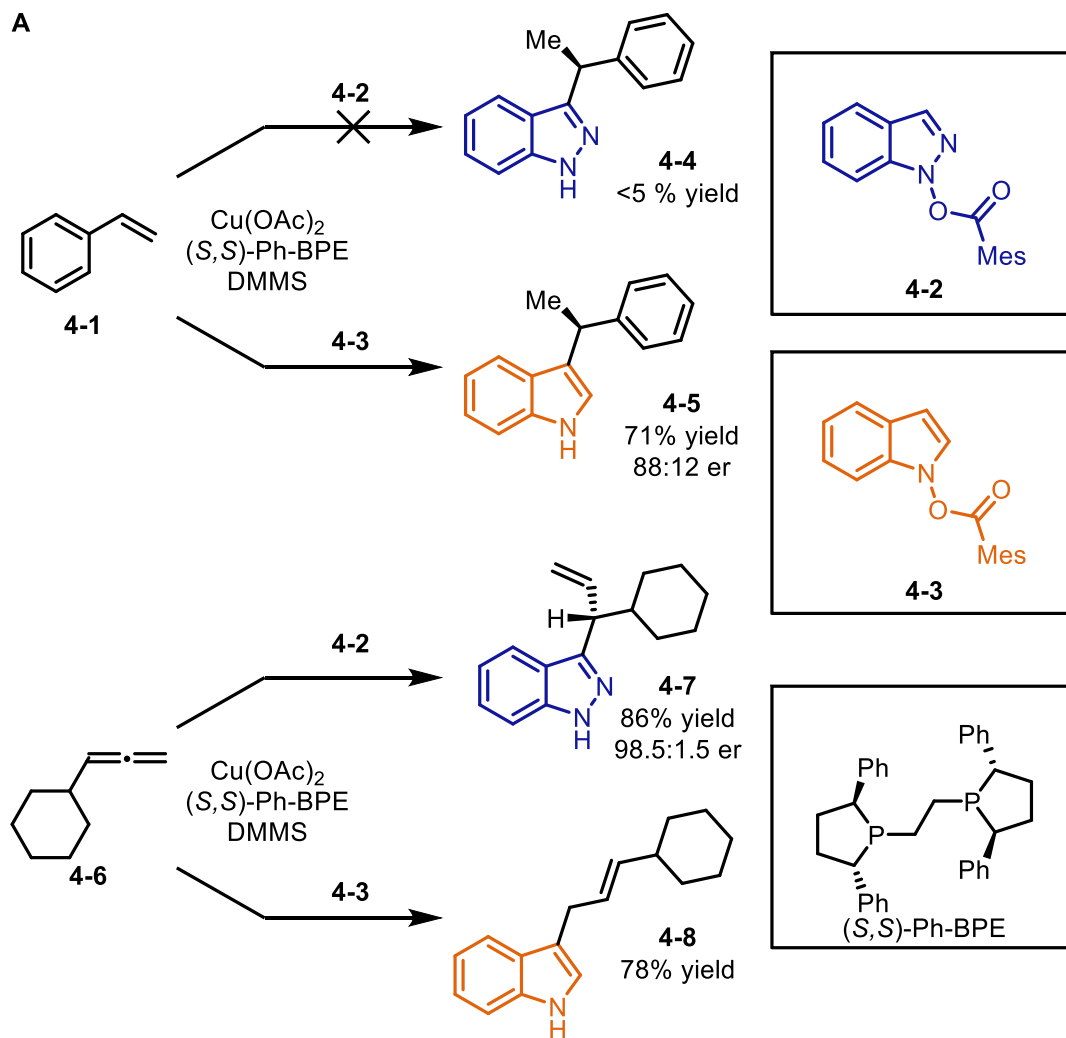


Figure 4-1 (a) CuH-catalyzed asymmetric alkylation of indole electrophiles. (b) Proposed CuH-catalyzed asymmetric C3-alkylation of indazole electrophiles. Mes: mesityl group.

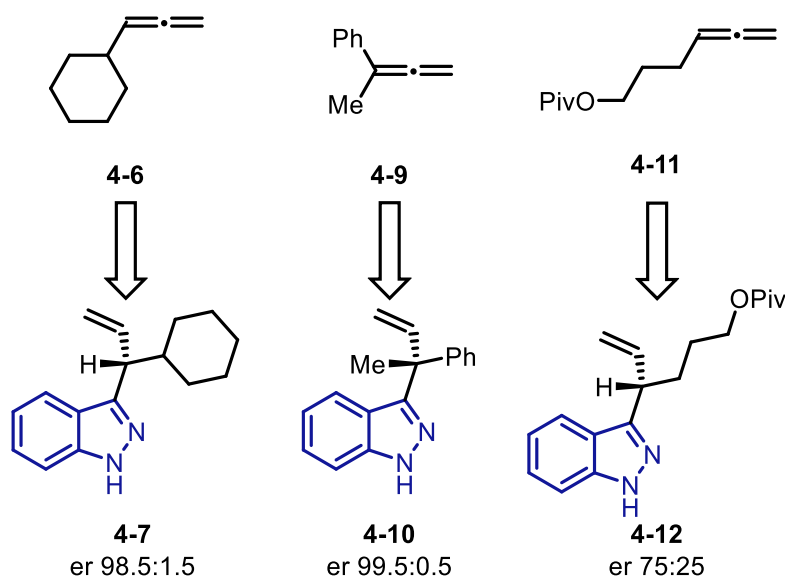
Initial experiments from the Buchwald group between styrene **4-1** and indazole **4-2** under the standard reaction conditions developed for the indole electrophile **4-3** were not successful, with C3-alkylated indazole **4-4** obtained in a low yield (yield < 5%, Figure 4-2). On the other hand, cyclohexyl allene afforded corresponding allyl indazole product **4-7** in high yield and very high C3 selectivity. Furthermore, the reaction led to the formation of the branched product exclusively. Meanwhile, the reaction with indole electrophile **4-3** led to the formation of the linear product, with a lower yield. The reactivity differences between indazole and indole electrophiles have important implications on the mechanisms of these reactions that are intriguing for computational investigations.



- B**
- 1) To investigate reaction mechanism and rate- and enantioselectivity determining steps.
  - 2) To understand the difference in reactivity and regioselectivity of indole and indazole electrophiles.
  - 3) To study the ligand and substrate effects on enantioselectivity.

**Figure 4-2 Comparison of indazole and indole electrophiles with styrene and allene pronucleophiles. B. Goals of computational investigation.**

Finally, the reactions with different allenes in this reaction (Figure 4-3) showed that the enantioselectivity was strongly affected by the size difference of the two substituents on the allene.



**Figure 4-3 Enantioselectivity of allenes with different substitution patterns in the indazole allylation reaction**

Based on these experimental results, we were interested in addressing few mechanistic questions using computational investigations. First, we wanted to study the reaction mechanisms for the allylation of indoles and indazoles. Furthermore, we wanted to understand the origin of different reactivity and selectivity between indoles and indazoles and explain the origin of low reactivity between indazole electrophile and olefins for the alkylation reaction (Figure 4-2B). Finally, we were interested in understanding ligand and substrate effects on the enantioselectivity of the reaction.

## 4.2 Computational details

All calculations were performed with Gaussian 09.<sup>13</sup> Images of the 3D structures of molecules were generated using CYLview.<sup>61</sup> The geometries of all intermediates and transition states were optimized with the B3LYP functional<sup>15</sup> and the mixed basis set with SDD for Cu and

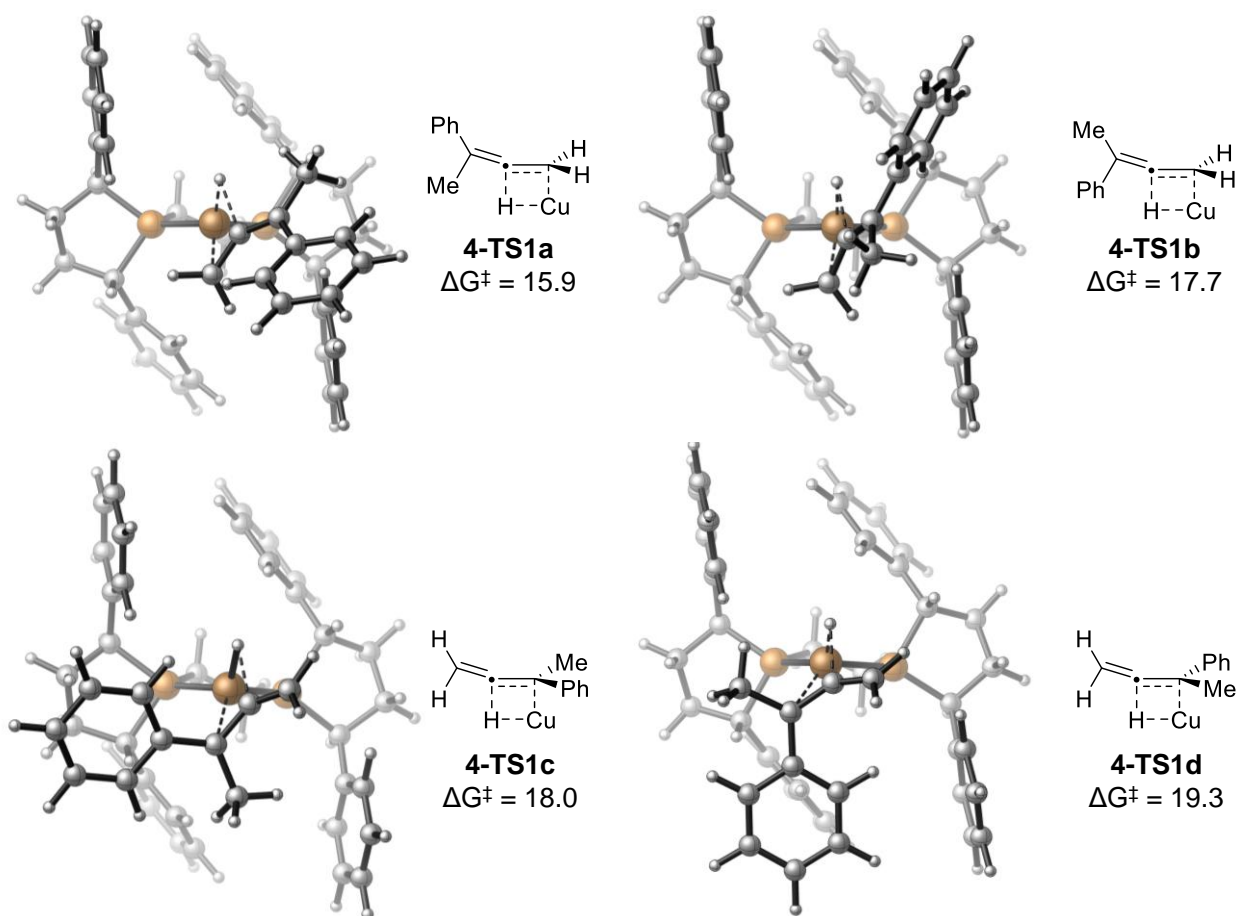
6-31G(d) basis set for other atoms. Vibrational frequency calculations were performed for all of the stationary points to confirm if each optimized structure is a local minimum or a transition state structure. Single-point energy calculations were performed with M06 functional<sup>17</sup> and the mixed basis set with SDD for Cu and 6-311+G(d,p) basis set for other atoms. Solvation effects were considered by applying the implicit SMD solvation model<sup>19</sup> with THF as a solvent in single-point energy calculations.

## 4.3 Results and discussions

### 4.3.1 Hydrocupration of allenes

The first step of the reaction proceeds through the hydrocupration of allenes. Allene **4-9** was used as the substrate in the calculations. Four competing hydrocupration transition states were calculated, leading to the formation of allylic copper intermediates (Figure 4-4). The most stable transition state (**4-TS1a**) requires 15.9 kcal/mol activation energy and leads to the formation of **4-14**. Isomer **4-TS1b** leading to the formation of **4-16** is 1.8 kcal/mol higher in energy than **4-TS1a** and is destabilized by steric repulsions between the ligand and the bulkier phenyl group, which is oriented towards the copper center. Two isomers **4-TS1c** and **4-TS1d**, leading to the formation of tertiary benzylic Cu complexes, also require higher activation barriers by 2.1 kcal/mol and 3.4 kcal/mol, respectively. These differences can be attributed to increased strain associated with the formation of tertiary C–Cu bonds.





**Figure 4-4** Calculated energies and 3D structures of competing hydrocupration transition states. All energies are relative to the separated LCuH catalyst **4-13** and allene **4-9**. All energies are in kcal/mol.

### 4.3.2 Reactivity differences between indole and indazole

To obtain more mechanistic understanding of the origin of reactivity differences, we computed the energy profiles of allylation reactions of **4-2** and **4-3** with 1-phenyl-1-methylallene **4-9** using density functional theory (DFT) calculations (Figure 4-5). Both reactions initiate via the hydrocupration of allene **4-9** with copper hydride **4-13** with a 15.9 kcal/mol activation energy as described above. This step leads to the irreversible formation of the Z-isomer of the terminal allylic copper species (**4-14**). Complex **4-14** can rapidly isomerize to form either of the diastereomers of

the tertiary benzylic copper intermediate (**4-15**), which undergoes subsequent isomerization to afford the thermodynamically more stable E-isomer of the terminal allylic copper (**4-16**).<sup>62</sup> In the presence of the indole electrophile **4-3**, the most favorable reaction pathway proceeds through the SN2' type oxidative addition (**4-TS6**,  $\Delta G^\ddagger = 23.3$  kcal/mol with respect to **4-16**), leading to the formation of C3-allyl indole product with linear selectivity, which is consistent with the experimental results (Figure 4-2). The competing SN2 type oxidative addition **4-TS7** leading to the N-allyl indole product is disfavored by 5.9 kcal/mol. These results are consistent with the previously studied ligand effects, where Ph-BPE ligand promoted the formation of C3-alkylated product.

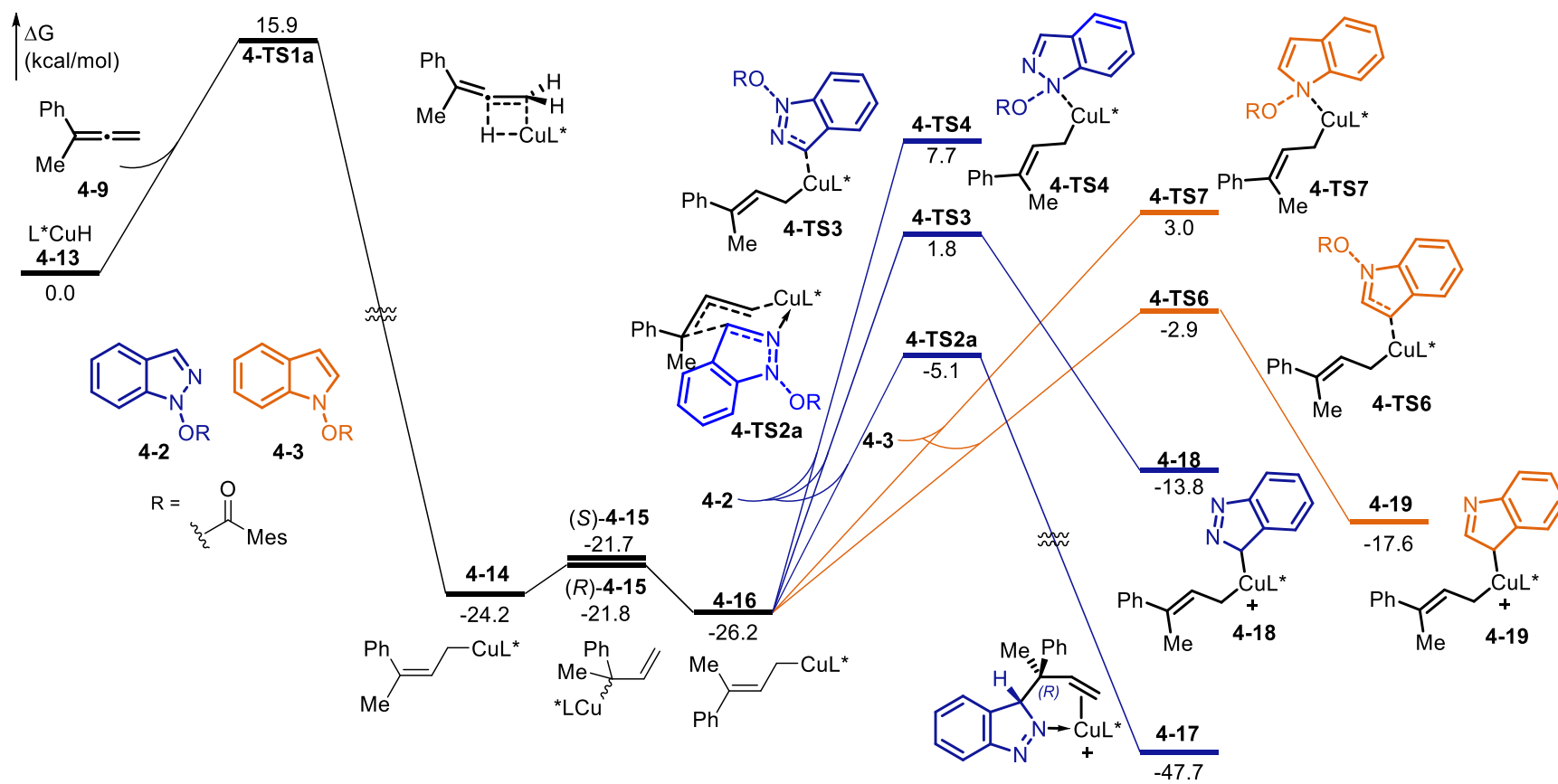
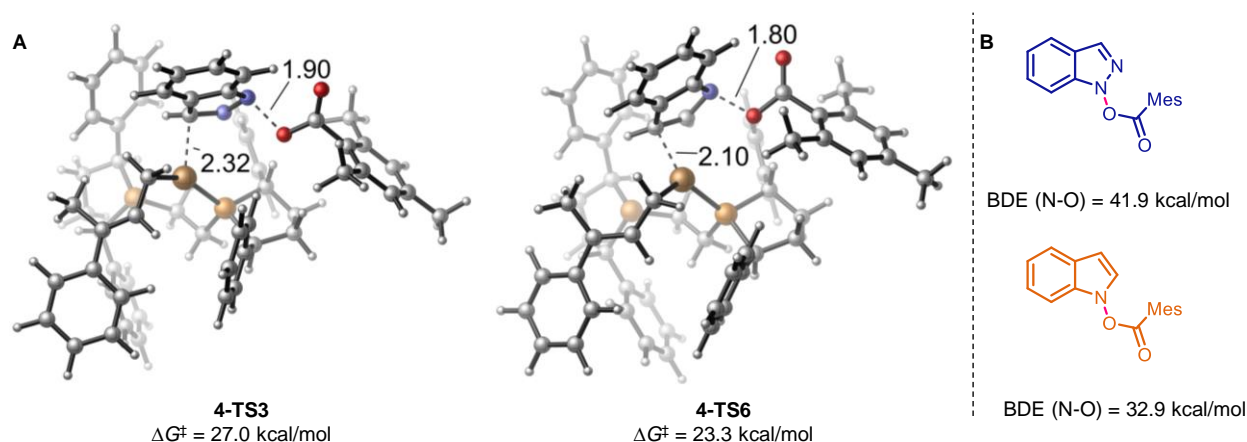


Figure 4-5 Energy profiles of the allylation of indazole (4-2) and indole (4-3) electrophiles.

In the reaction with the indazole electrophile (**4-2**), we found that the SN2' oxidative addition (**4-TS3**) requires a higher activation barrier of 28.0 kcal/mol with respect to **4-16** when compared to the reaction with indole (**4-TS6**), and the product is thermodynamically destabilized by 3.6 kcal/mol (**4-18** versus **4-19**). Since the C3 oxidative additions are endergonic, the transition states are more product-like and exhibit significant N–O bond elongations (Figure 4-6). The computed kinetic and thermodynamic trends can therefore be attributed to the cleavage of a stronger N–O bond in the indazole electrophile, which is supported by calculated BDEs where the cleavage of the N–O bond in **1a** requires 9.0 kcal/mol higher energy than the corresponding bond cleavage in **6** (Figure 4-6). In addition to the relatively high calculated energy barrier, this oxidative addition pathway would lead to the linear allylation products, which are inconsistent with the branched selectivity observed in the experiment. Highly kinetically disfavored oxidative addition mechanisms for indazole are also consistent with their low reactivity with alkene pronucleophiles.



**Figure 4-6 (A) Optimized structures of the C3-oxidative addition transition states with indazole (**4-TS3**) and indole (**4-TS6**) substrates. (B) Calculated N–O bond dissociation enthalpies (BDEs) of **4-2** and **4-3**.**

Our DFT calculations revealed a more feasible mechanism with indazole **4-2** via a Zimmerman-Traxler type six-member transition state (**4-TS2a**).<sup>63</sup> This mechanism is favored because it forgoes the generation of the less stable Cu(III) intermediate. Furthermore, this transition state is stabilized by the presence of a dative Cu–N2 bond, which is not available with the indole substrate. This model is consistent with the branched regioselectivity as well as the observed enantioselectivity in the reaction (Figure 4-7).

### 4.3.3 Origin of enantioselectivity

The indazole electrophile **1a** can add at either face of the C=C bond of DFT calculations of competing six-member reaction pathways **4-16** or **4-14** (**4-TS2a-d**). Here, the C–C bond formation and the dissociation of 2,4,6-trimethylbenzoate anion are concerted processes, leading directly to 3H-indazole complexes (**4-17a-d**), which form the 1H-indazole product upon tautomerization. The enantioselectivity of the C3-allylation product is determined in the indazole addition step (**4-TS2**, Figure 4-7).

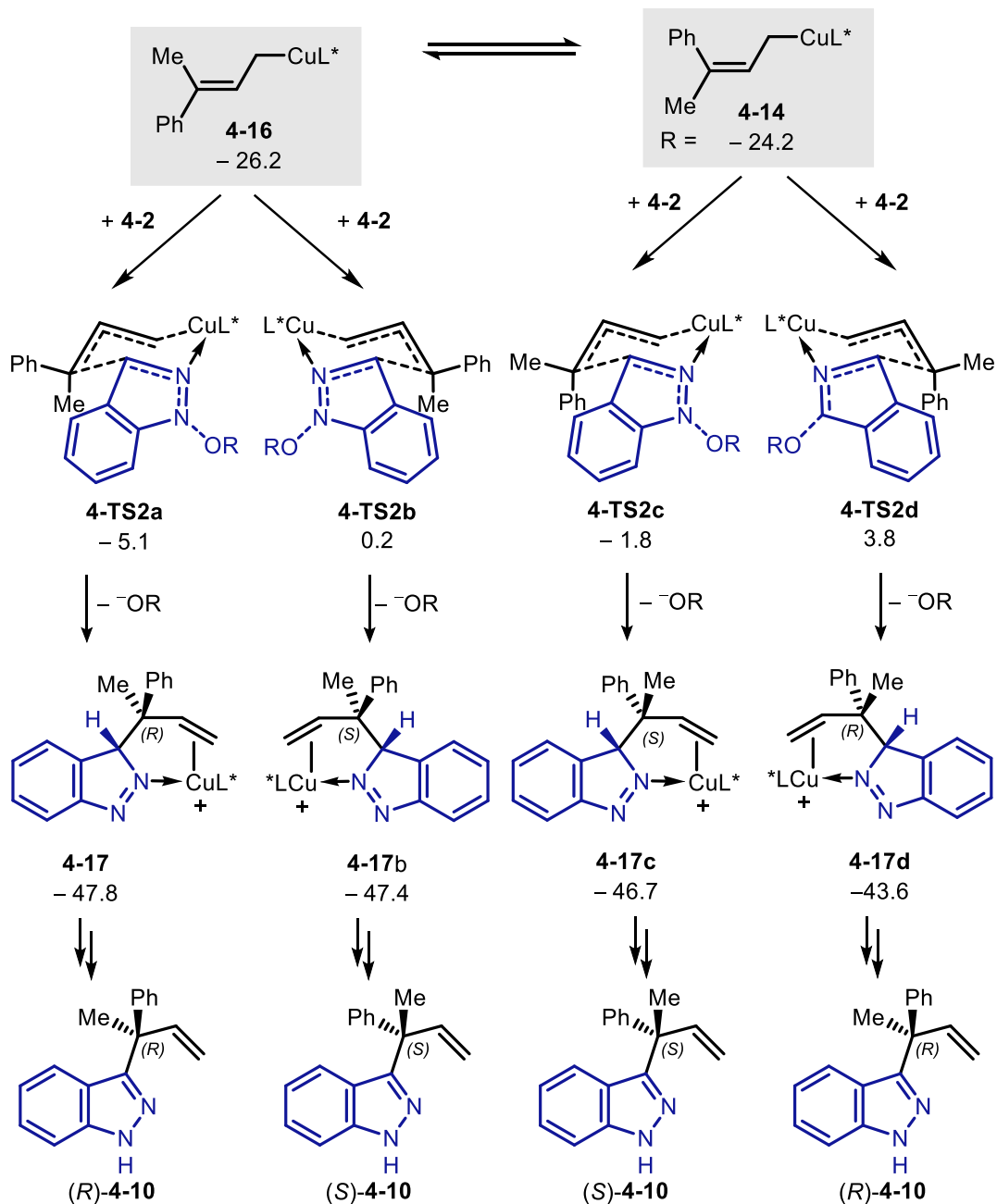
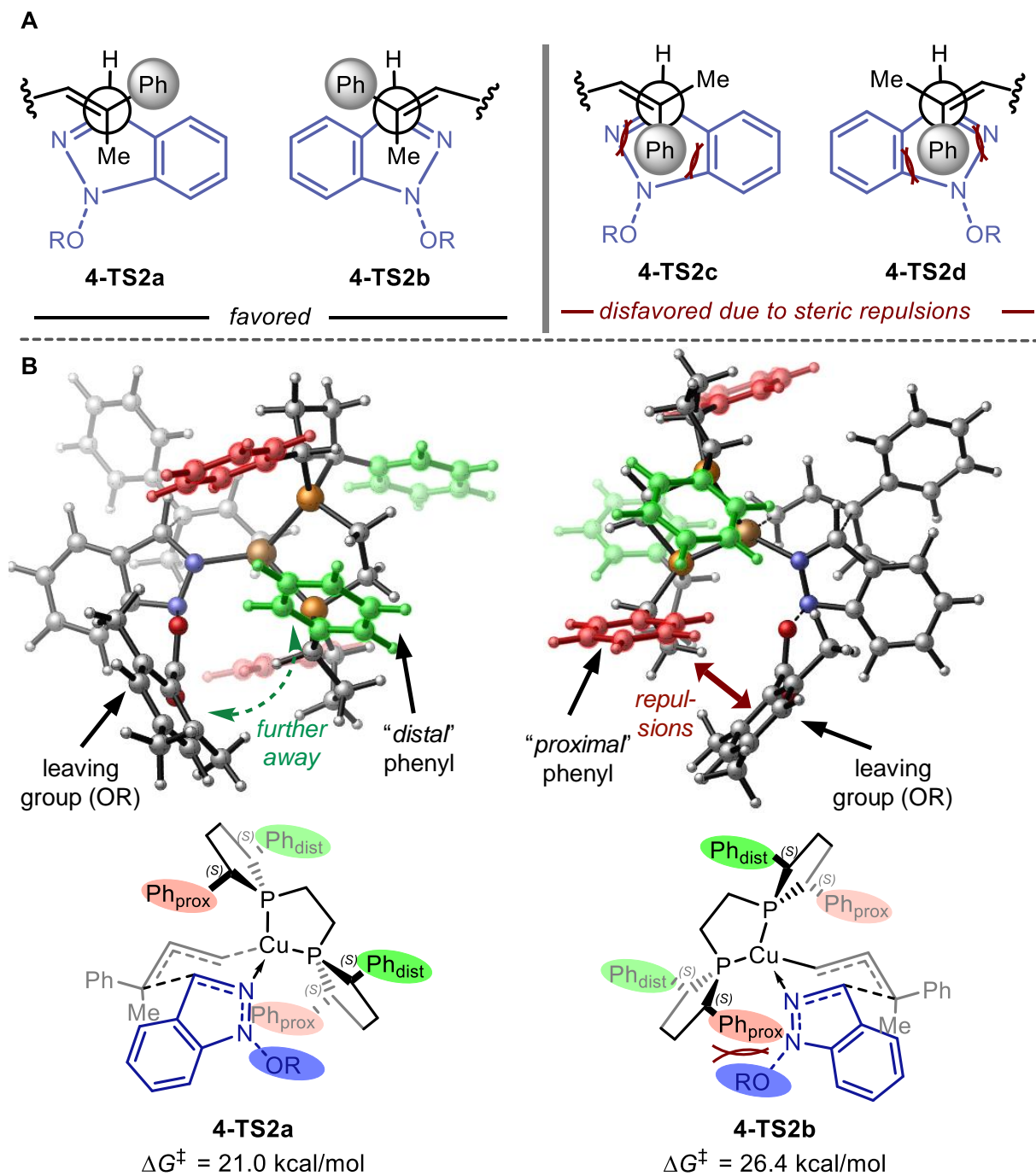


Figure 4-7 Calculations of competing six-member reaction pathways

Among the four competing transition states, **4-TS2c** and **4-TS2d** originating from the Z-allyl complex **4-14** are both disfavored (3.3 and 8.0 kcal/mol higher than **4-TS2a**, respectively) due to the pseudoaxial placement of the bulky phenyl group, which leads to increased repulsions

with the indazole ring (Figure 4-8A). In **4-TS2a** and **4-TS2b**, the smaller methyl group is placed at the pseudoaxial position, and the steric repulsions about the forming C–C bond are decreased. From intermediate 10, the addition of the indazole to form product (*S*)-**4-10** through **4-TS2b** is 5.4 kcal/mol less favorable than the addition to form (*R*)-3a through **4-TS2a**. The relative instability of **4-TS2b** arises from unfavorable steric repulsions between the (*S,S*)-Ph-BPE ligand and the 2,4,6-trimethylbenzoate leaving group. In **4-TS2b**, the bulky leaving group is placed in the quadrant occupied by a “proximal” phenyl group on the ligand (Figure 4-8B). By contrast, in **4-TS2a**, the leaving group is in a less occupied quadrant with a “distal” phenyl group.

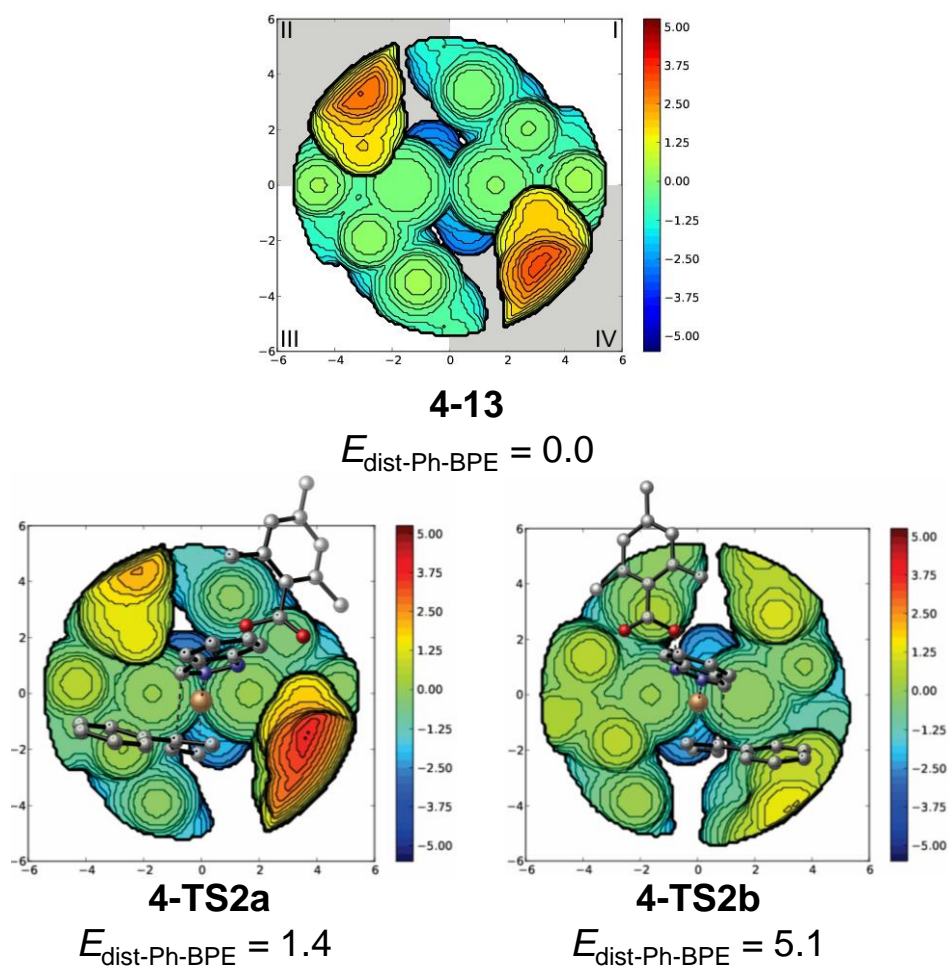


**Figure 4-8 (A) Newman projections along the forming C-C bond. (B) Origin of enantioselectivity**

The enantioselectivity of the reaction is controlled by the unfavorable steric repulsions between the carboxylate leaving group and the proximal phenyl group on the Ph-BPE ligand in 4-



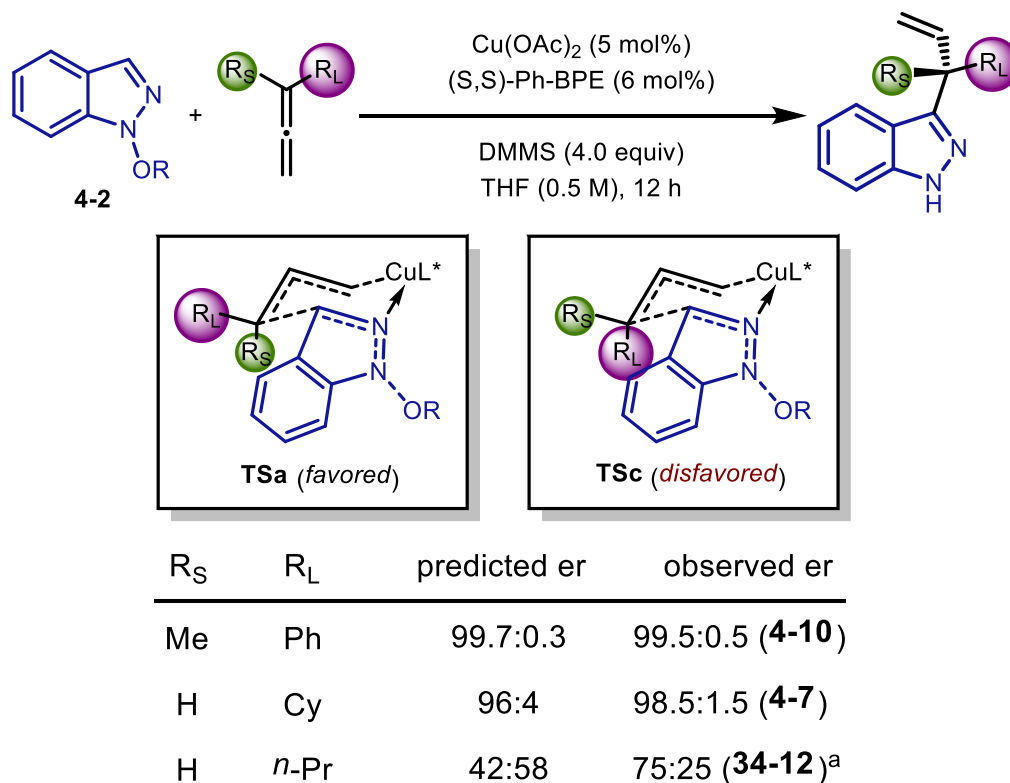
**TS2b**, which are avoided in the favorable transition state **4-TS2a**. To further quantify these steric repulsions, we calculated the distortion energies of Ph-BPE ligand in their transition state geometries (**4-TS2a**, **TS2b**) relative to the Ph-BPE in CuH species **7** ( $\Delta E_{\text{dist-Ph-PBE}}$ ). These results indicate that the ligand is significantly less distorted in **4-TS2a** ( $\Delta E_{\text{dist-Ph-PBE}} = 1.4$  kcal/mol) relative to that in **4-TS2b** ( $\Delta E_{\text{dist-Ph-PBE}} = 5.1$  kcal/mol). The difference in distortion energies ( $\Delta E_{\text{dist-Ph-PBE}} = 3.7$  kcal/mol) contributes to the relative stabilities of these two transition states ( $\Delta\Delta G^\ddagger = 5.4$  kcal/mol). Furthermore, the distortion of the Ph-BPE ligand can be visualized via steric contour plots, which show that the ligand in **4-TS2a** resembles the structure in **7** more closely when compared to the ligand in **4-TS2b** where the substrate is placed in an occupied quadrant (indicated by orange and yellow in the contour plots), leading to the greater distortion of the ligand.



**Figure 4-9** Calculated ligand distortion energies ( $\Delta E_{\text{dist-Ph-PBE}}$ ) and steric contour plots of the Ph-BPE ligand in **4-13**, **4-TS2a**, and **4-TS2b**. All energies are in kcal/mol.

To further verify the mechanistic model, we calculated the enantioselectivities of the allylation reaction with allenes containing substituents of varying degrees of steric hindrance. The enantioselectivities were computed from transition states **4-TS<sub>a</sub>** and **4-TS<sub>c</sub>** arising from the same facial addition of **4-2** to the E- and Z-isomers of the corresponding allylic copper species (Figure 4-10). The calculated enantioselectivity trend is in good qualitative agreement with the experimental data (Figure 4-3). While reactions with allenes **4-6** and **4-9** are both highly enantioselective, using a less bulky primary alkyl allene (**4-11**) almost completely diminishes the

predicted er. Although this computed value is underestimated when compared to the observed er, both computational and experimental results demonstrated the role of steric effects of allene substituents on the er of the allylation product.



**Figure 4-10** Computed enantioselectivities with different allene substrates.

## 4.4 Conclusion

DFT calculations were performed to study the reaction mechanisms and electrophile and ligand effects in the CuH catalyzed allylation of indazoles and indoles. The calculations revealed that the allylation proceeds through different mechanisms for the two electrophiles. Following the

initial allene hydrocupration, indole substrate **4-3** proceeds through the SN2' oxidative addition, followed by reductive elimination to generate the linear addition product.

This pathway is highly disfavored for the indazole substrate **4-2** due to the breaking of a stronger N–O bond in indazole. Instead, the addition to indazole occurs through the concerted six-member Zimmerman-Traxler transition state, where a new C–C bond is formed concurrently with the breaking of the N–O bond. This transition state is also responsible for determining the enantioselectivity of the reaction, and both the substituents on the allene and the ligand play an important role in the enantioselectivity of the reaction.

## 5.0 Regio-controlled cross-coupling of 3,5-dibromo-2-pyrones

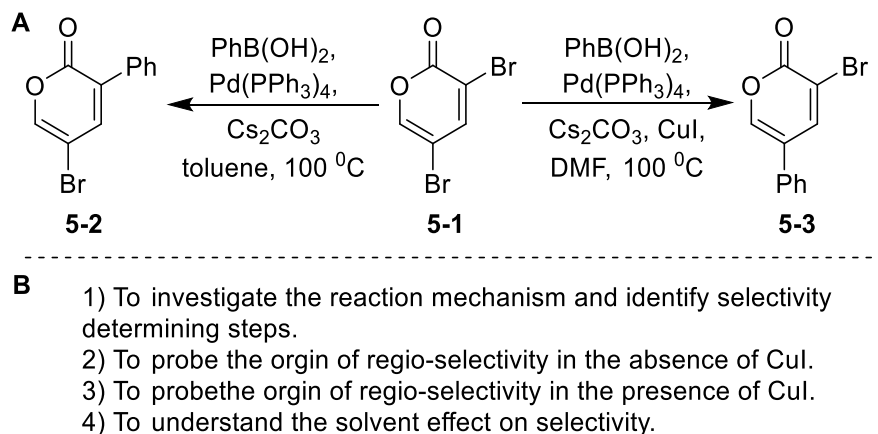
A significant part of this chapter was published as Palani, V.; Hugelshofer, C. L.; Kevlishvili, I.; Liu, P.; Sarpong, R. *J. Am. Chem. Soc.* **2019**, *141*, 2652–2660.

### 5.1 Introduction

In the previous chapter, we discussed an allylation of a common heterocycle. In this chapter, we will discuss the cross-coupling reaction of a heterocycle, which is one of the most prominent methodologies for the functionalization of halogenated heterocycles.<sup>64</sup> Because of this, selective coupling of poly(pseudo)halogenated heterocycles is an active field in synthetic chemistry.<sup>65</sup> In recent years, there have been several examples of chemoselective coupling reactions where coupling preferentially proceeds with a particular (pseudo)halogen.<sup>66</sup> An interesting example for a reversible chemo-selectivity is the case of aryl chloro triflates,<sup>67</sup> which can be controlled by either ligand,<sup>68</sup> solvent,<sup>69</sup> or additives.<sup>69</sup>

On the other hand, achieving selectivity in reactions with identical halogen atoms is more challenging and requires careful reaction optimization. In the case of polyhalogenated heterocycles, the selectivity is often inherent to the substrate and can be often explained with either molecular orbitals<sup>70</sup> or with relative bond strengths of reacting C–X bonds.<sup>71</sup> On the other hand, controlling the selectivity is often more difficult, but there have been a few examples where ancillary ligand can alter the selectivity of the reaction.<sup>72</sup> One interesting selective coupling reaction involves 3,5-dibromo-2-pyrone, an  $\alpha$ -pyrone derived polyhalogenated heterocycle

bearing two inequivalent C–Br bonds.<sup>73</sup> Cho and coworkers have demonstrated various cross-coupling conditions where regio-selectivity can be altered depending on the solvent and CuI additives without changing the ancillary ligand (Figure 5-1)<sup>74</sup>.



**Figure 5-1 A. Regiodivergent coupling of 3,5-dibromo-2-pyrone (5-1) controlled by the solvent and additives.**

#### **B. Goals of computational investigation**

Several studies, both experimental and computational, have emerged to understand the basis for selectivity in the site-selective coupling of various polyhalogenated heterocycles over the past few decades. However, predicting and rationalizing the selectivity outcome has remained challenging. One predictive method for site-selectivity, which has been used to understand the basis behind the selective coupling of polyhalogenated heterocycles, is <sup>1</sup>H NMR chemical shift method.<sup>75</sup> However, this method makes a wrong prediction when it comes to 3,5-dibromo-2-pyrone, which makes this coupling an intriguing case for mechanistic investigation. Past computational studies have also considered bond dissociation energies (BDE)<sup>71</sup> and LUMO coefficients<sup>70</sup> to rationalize regioselectivity in cross-coupling reactions. This reaction is one of the few known examples where the regioselectivity is altered by the choice of solvent and the additive,

and this observation cannot be explained by any of the predictive methods, which makes this reaction a particularly interesting example for a mechanistic investigation.

**Table 5-1 Suzuki couplings with 3,5-dibromo-2-pyrone**

$\epsilon$	Solvent	Yield (%) 5-2:5-3:5-4		
		$\Delta$ (w/o CuI)	rt (w/ CuI)	$\Delta$ (w/ CuI)
47	DMSO	N/A	nd:12:nd	8:13:nd
38.25	DMF	tr:nd:nd	nd:18:nd	15:37:nd
21.01	Acetone	53:nd:nd	tr:32:nd	16:29:nd
10.42	DCE	70:nd:nd	57:13:nd	58:tr:11
7.52	THF	47:nd:19	27:8:nd	49:17:nd
2.38	toluene	52:nd:nd	55:tr:nd	56:tr:tr

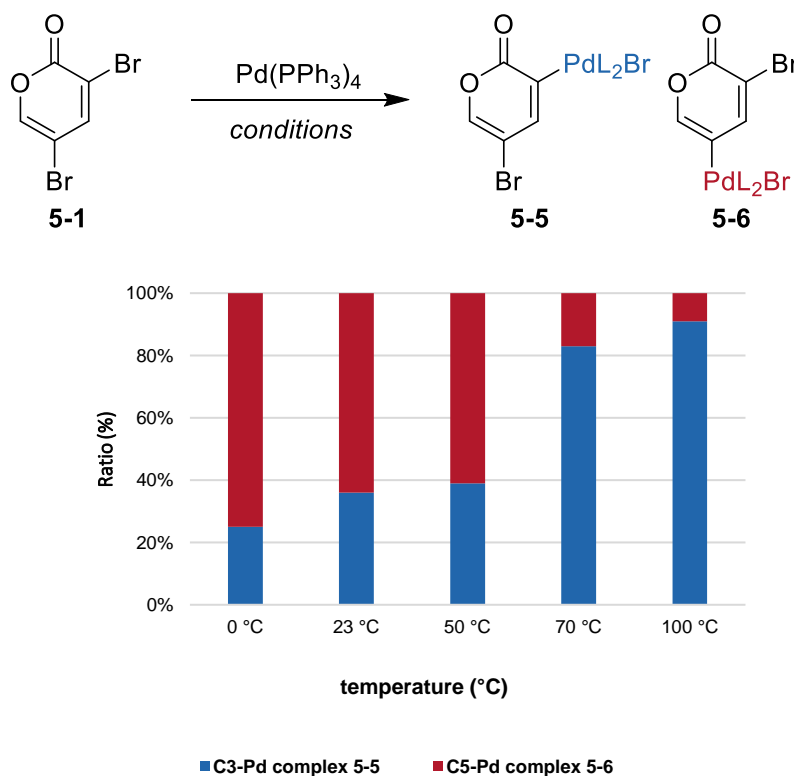
Conditions:  $\text{PhB(OH)}_2$  (1.2 equiv),  $\text{Pd(PPh}_3)_4$  (10 mol%), CuI (1.0 equiv),  $\text{K}_2\text{CO}_3$  (2.0 equiv), solvent (0.1 M). nd = not detectable, tr = trace. Experiments were conducted by the Sarpong group

To gain mechanistic insights into the selective coupling of 3,5-dibromo-2-pyrones, the Sarpong group first examined the oxidative addition step in the reaction. It was observed that in non-polar solvents such as toluene, the oxidative addition always occurred at the 3- position and the additive had no effect on the selectivity. On the other hand, in a polar solvent such as DMF, the addition of CuI lead to a switch in the selectivity, with coupling being more favored at the C5- position (Table 5-1). Interestingly, with the increase of temperature, the oxidative addition in DMF

with CuI lead to the C3-adduct (Figure 5-2). These results suggest that in these given conditions, C5-adduct is kinetically favored, while C3-adduct is thermodynamically favored. Furthermore, when a mixture of Pd oxidative adducts **5-5** and **5-6** were treated with tributylphenylstannane in DMF, only the C5-coupled product (**5-3**) was formed, indicating that **5-5** can also interconvert to **5-6** prior to cross-coupling. In summary, experimental observations suggest that C5-Pd complex **5-6** is the *kinetic* oxidative adduct, whereas C3-Pd complex **5-5** is the *thermodynamic* oxidative adduct. Moreover, **5-5** and **5-6** can interconvert, and in Stille coupling, the rate of transmetallation/reductive elimination is faster for C5-Pd complex **5-6** when compared to that of C3-Pd complex **5-5**. This describes a Curtin–Hammett scenario<sup>76</sup> wherein rapid interconversion of the Pd-complexes (**5-5** and **5-6**) occurs, and where the ratio of the resulting cross-coupled products (i.e., **5-2:5-3**) is solely dependent on the energy difference between the two respective rate-limiting transition states of transmetallation/reductive elimination.

In the following chapter, I will conduct DFT calculations to gain insights on the mechanistic origin of the regio-divergence of this cross-coupling reaction in the absence and presence of copper iodide additives. Secondary goal of this study is to identify the solvent effects on regio-selectivity (Figure 5-1B).





**Figure 5-2 Influence of temperature on ratios of C3- to C5-Pd complexes. Conditions:  $\text{Pd(PPh}_3)_4$  (10 mol%), CuI (1.0 equiv), DMF (0.1 M).**

## 5.2 Computational details

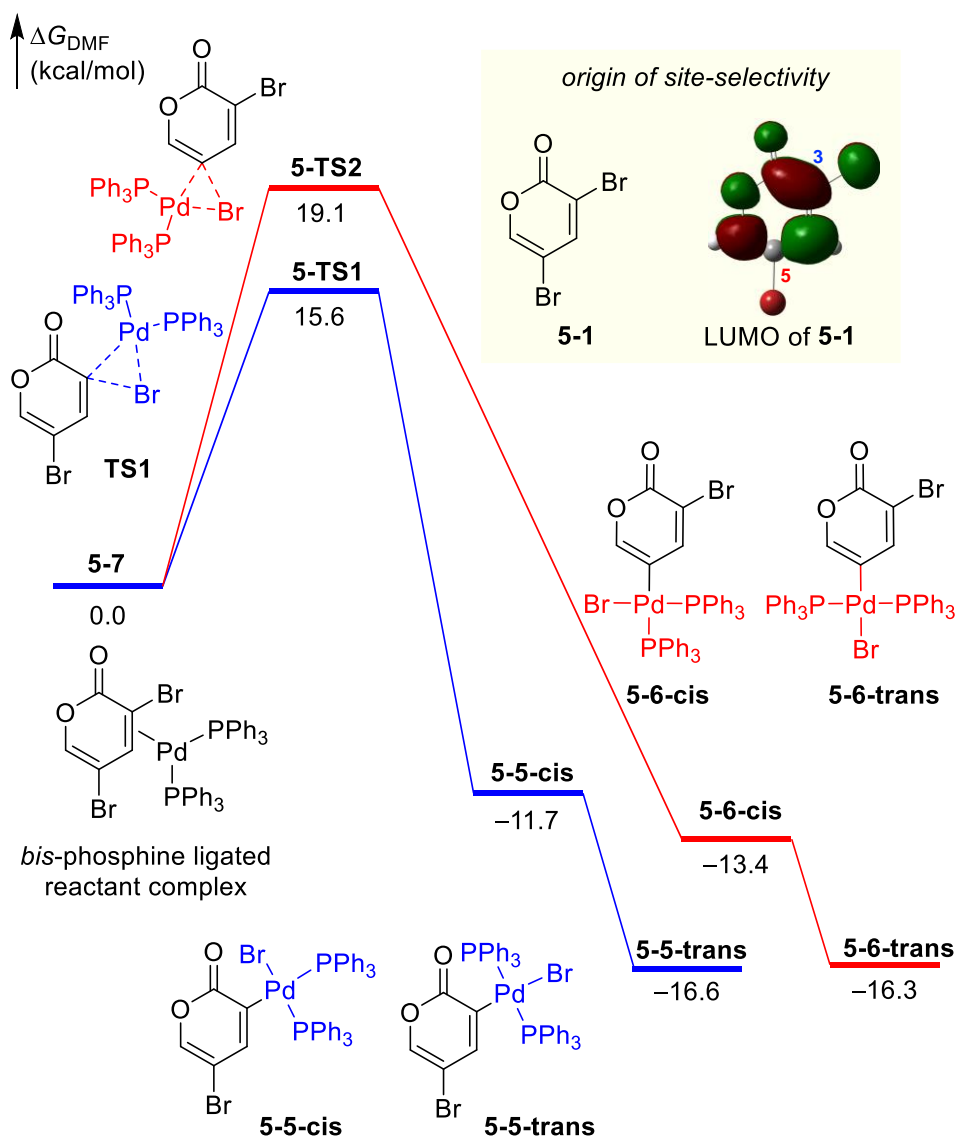
All calculations were carried out with the Gaussian 09 package.<sup>13</sup> Geometry optimizations were performed with B3LYP.<sup>15</sup> Mixed basis set of SDD was used for palladium and tin, and 6-31G(d) for other atoms. Frequency analysis was conducted at the same level of theory to verify the stationary points to be minima or saddle points and to obtain zero-point energy (ZPE) and thermal energy corrections at 298.15 K. Single-point energy calculations on B3LYP-optimized geometries were performed with the M06 functional,<sup>17</sup> a mixed basis set of SDD for palladium, copper and tin, and 6-311+G(d,p) for other atoms, and the SMD solvation model<sup>19</sup> with DMF as

the solvent. The computed gas-phase activation energy ( $\Delta E^\ddagger$ ) was studied using the distortion-interaction analysis.<sup>27</sup> The distortion energy ( $\Delta E_{\text{dist}}$ ) is the sum of the energies required to distort the reactants into their transition state geometries.  $\Delta E_{\text{int}}$  was calculated using the equation  $\Delta E_{\text{int}} = \Delta E^\ddagger - \Delta E_{\text{dist}}$ . BDEs were computed using B3LYP/6-31G(d).

## 5.3 Results and discussions

### 5.3.1 Oxidative addition in the absence of CuI

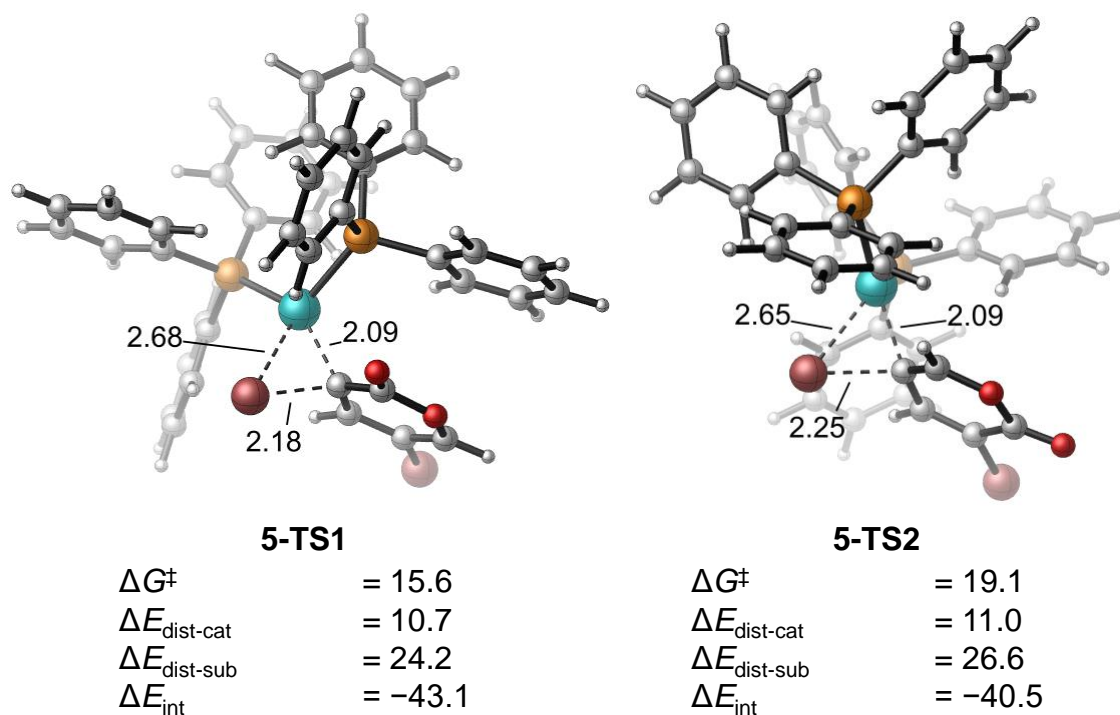
In the copper free pathway, the reaction occurs with bisphosphine-ligated palladium,<sup>77</sup> with a barrier to the oxidative addition at C3 (**5-TS1**; Figure 5-3) is 3.5 kcal/mol lower than that at C5 (**5-TS2**). Following *cis/trans* isomerization of the phosphine ligands on the oxidative addition complexes (*i.e.*, **5-5-cis** and **5-6-cis**, respectively), the C3 adduct (**5-5-trans**) is slightly (0.3 kcal/mol) more stable than the C5 adduct (**5-6-trans**). These results are consistent with the experimentally observed C3-selectivity for oxidative addition in DMF and toluene in the absence of CuI (see Table 5-1).



**Figure 5-3** Oxidative addition in the absence of copper iodide at the C3- (shown in blue) and C5- (in red) positions of 3,5-dibromo-2-pyrene 5-1. Inset: LUMO of 5-1.

To understand the factors governing the C3 site-selectivity, we performed a distortion/interaction analysis to investigate the distortion energies of the catalyst ( $\Delta E_{\text{dist-cat}}$ ) and the pyrene substrate ( $\Delta E_{\text{dist-sub}}$ ) to reach their transition state geometries as well as the stabilizing interaction energy ( $\Delta E_{\text{int}}$ ) between the two fragments (Figure 5-4). Although the C3-oxidative addition has an earlier transition state, as evidenced by the smaller substrate distortion energy

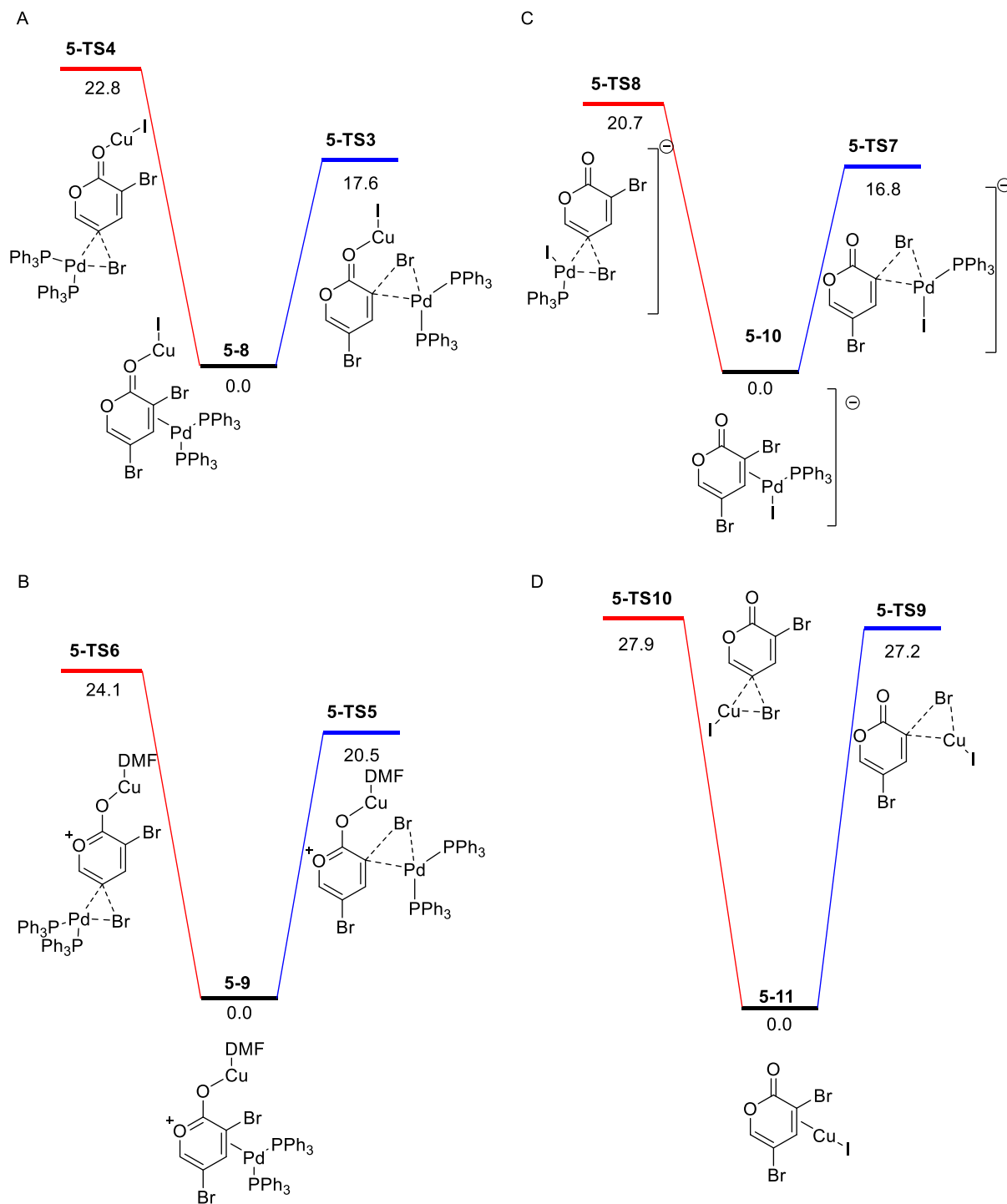
( $\Delta E_{\text{dist-sub}}$ ) and the shorter C–Br bond distance in **5-TS1**, the interaction between the catalyst and the substrate in **5-TS1** ( $\Delta E_{\text{int}}$ ) is still stronger than that in **5-TS2** by 2.6 kcal/mol. The stronger catalyst-substrate interaction is due to a more favorable frontier molecular orbital (FMO) interaction between the LUMO( $\pi^*$ ) of **5-1** and the HOMO ( $d_{xy}$ ) of the Pd in **5-TS1**. The computed LUMO of **5-1** showed a much larger coefficient at the C3-position than at the C5 position (Figure 5-3 inset).



**Figure 5-4** The distortion energies of the PdL<sub>2</sub> catalyst ( $\Delta E_{\text{dist-cat}}$ ) and the pyrone substrate ( $\Delta E_{\text{dist-sub}}$ ), and the interaction energies between these two fragments in the oxidative addition transition states ( $\Delta E_{\text{int}}$ ) in the absence of CuI

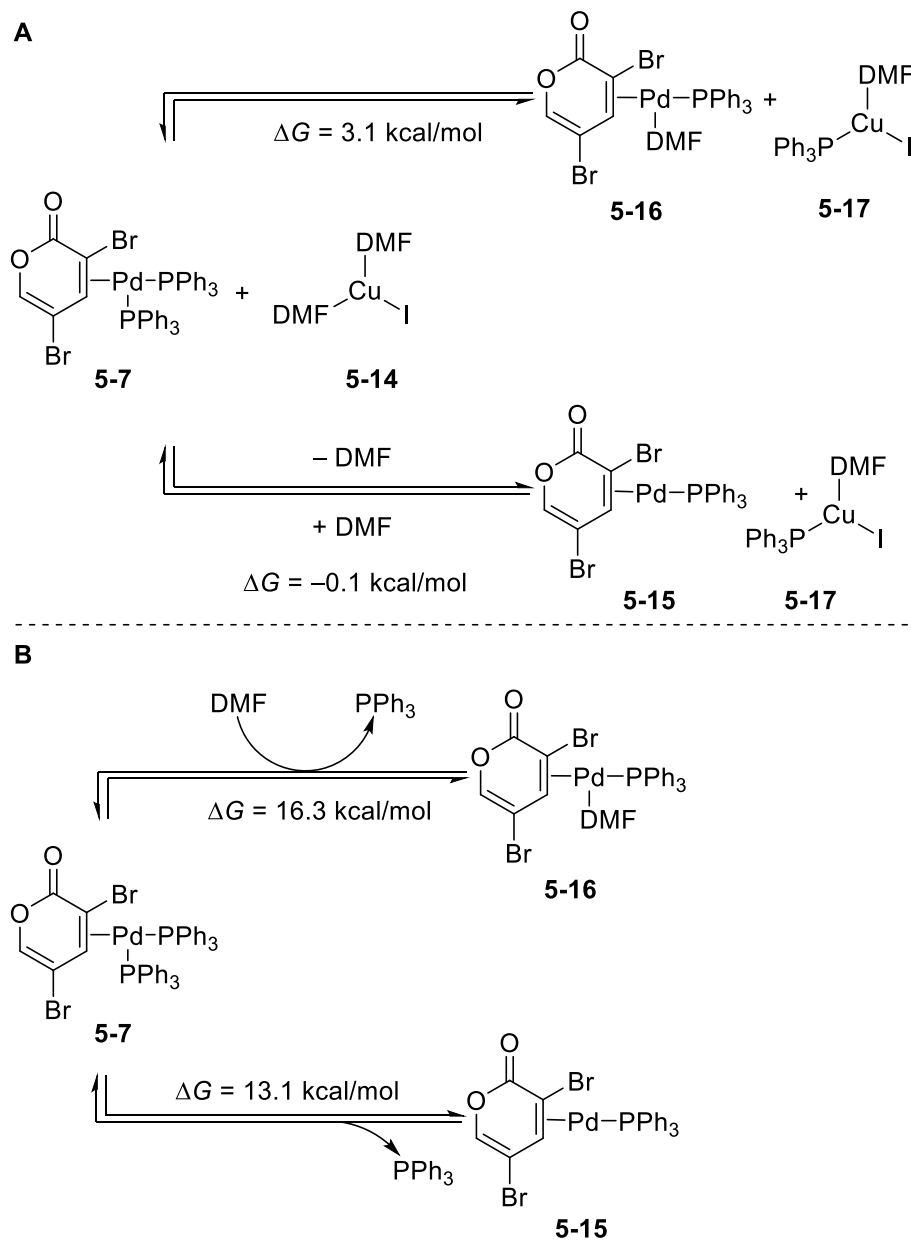
### 5.3.2 Oxidative addition in the presence of CuI

We first computationally considered the Lewis-acid activation of the pyrone through coordination of CuI (**TS3**, **TS4**) or cationic (DMF)Cu<sup>+</sup> (**TS5**, **TS6**) to the carbonyl group of **5-1** (Figure 5-5). However, these results indicated that the CuI or Cu<sup>+</sup> coordination has a minimal impact on the site-selectivity of oxidative addition and thus cannot explain the experimentally observed site-selectivity trend under the different conditions. We also considered an anionic pathway where one phosphine ligand is displaced by iodide (**TS7**, **TS8**). However, this pathway also favored addition at the C3 position. Additionally, we considered the pathway involving oxidative addition of pyrone **5-1** to CuI (**TS9**,  $\Delta G^\ddagger = 27.2$  kcal/mol, with respect to the pyrone-CuI  $\pi$ -complex **5-11**). This pathway requires a higher barrier than the oxidative addition to Pd(0) and does not support the observed reversal of site-selectivity in the presence of CuI.



**Figure 5-5** Alternative oxidative addition mechanisms in the presence of CuI A) CuI acting as the Lewis acid. B) Cu<sup>+</sup>DMF acting as the Lewis acid. C) Anionic pathway with mono-phosphine ligated Pd bound to iodide anion D) CuI acting as the catalyst to promote oxidative addition

As such, we surmised that in the presence of CuI, the oxidative addition might occur through an alternative mechanism with a different active Pd catalyst. Because previous computational studies have suggested a bisphosphine ligated Pd complex is more favored for oxidative addition with PPh<sub>3</sub> as ligand, the oxidative addition in the absence of CuI is expected to occur via tri-coordinated (PPh<sub>3</sub>)<sub>2</sub>Pd(0)-pyrone complex **5-7** (Figure 5-6). Additionally, based on empirically established precedent supporting the ability of CuI to promote phosphine ligand exchange at Pd,<sup>78</sup> we hypothesized that CuI could have a similar effect in this system. In this way, CuI could promote phosphine ligand dissociation from **5-7** to form a mono-phosphine ligated Pd complex (**5-13** or **5-14**, Figure 5-6) as the operative intermediate in the catalytic cycle, which has been reported to be relatively more reactive toward oxidative addition. Indeed, our DFT calculations show that exchanging one of the PPh<sub>3</sub> ligands in **5-7** with (DMF)<sub>2</sub>CuI (**5-12**) to form mono-phosphine ligated Pd complexes **5-13** and **5-14** are both thermodynamically feasible, indicating an equilibrium between the bis- and mono-phosphine ligated Pd complexes before the oxidative addition step. Furthermore, in the absence of CuI, the formation of the mono-phosphine ligated Pd complexes are highly endergonic ( $\Delta G \geq 13$  kcal/mol), supporting the assumption that the bis-phosphine ligated Pd complex **5-7** is operative under these conditions.



**Figure 5-6** Computed ligand exchange energies from the bis-phosphine ligated Pd complex **5-7** to form the mono-phosphine ligated complexes **5-15** and **5-16** A) In the presence of CuI. B) In the absence of CuI

In the presence of CuI, the C3 and C5 oxidative additions of the mono-phosphine ligated Pd complex **5-13** (**5-TS11** and **5-TS12**, respectively, Figure 5-7) both require lower barriers as compared to those of bis-phosphine ligated Pd complex **5-7**. Notably, the mono-phosphine ligated



Pd complex oxidative addition no longer kinetically favors the formation of C3-Pd complex **5-5**, and the barriers for **5-TS11** and **5-TS12** are comparable. This is consistent with the low selectivity for the site of oxidative addition observed empirically in the presence of CuI in DMF (Figure 5-2).

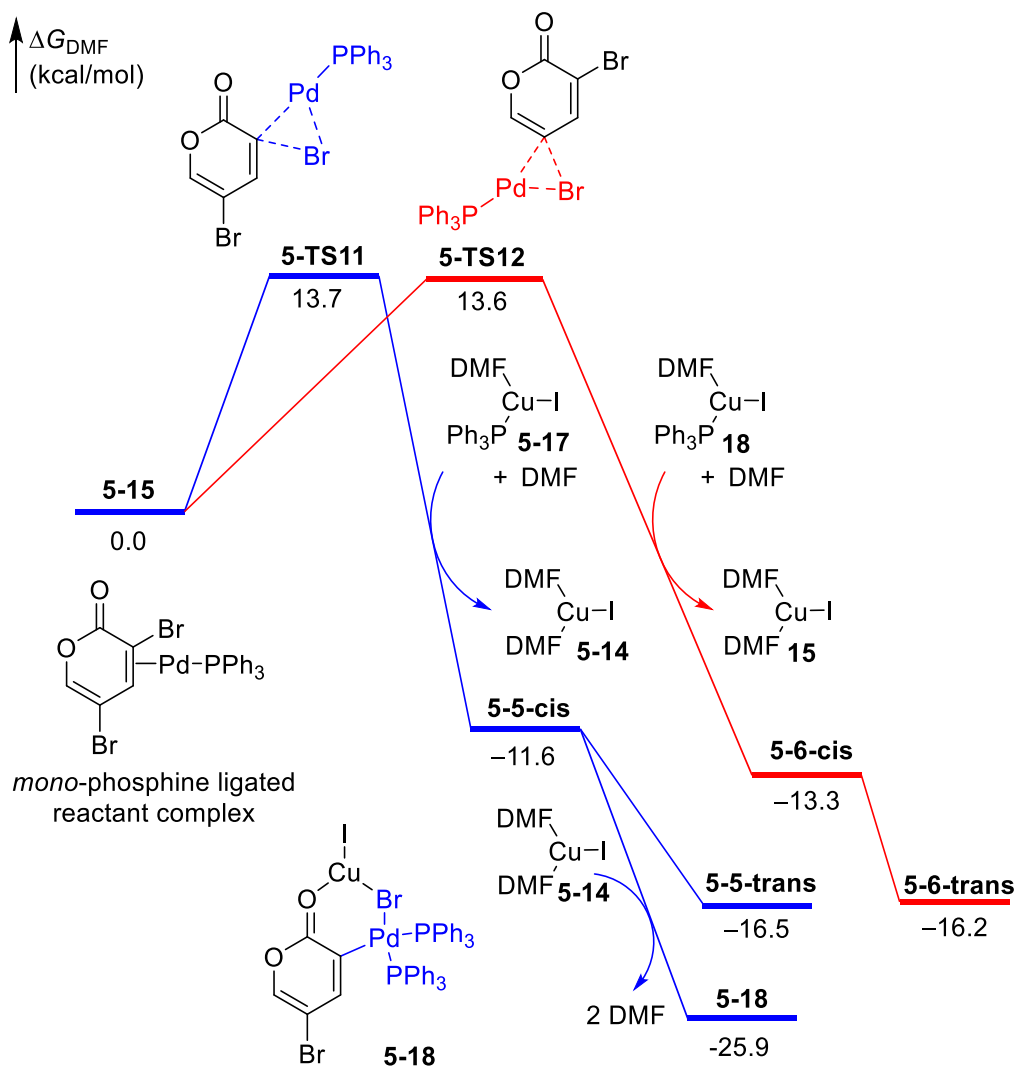
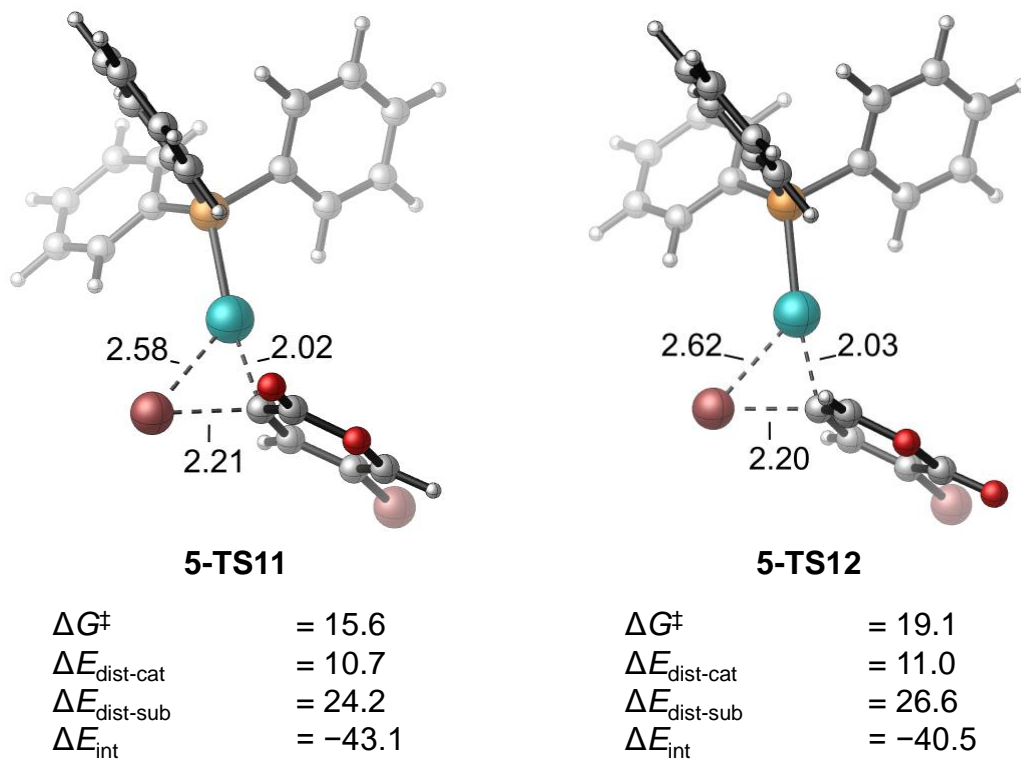


Figure 5-7 Oxidative addition in the presence of CuI (monophosphine ligated complex)

Distortion/interaction analysis of **5-TS11** and **5-TS12** reveals that **5-TS12** has a more favorable interaction energy as compared to **5-TS11**. However, **5-TS12** is a later transition state

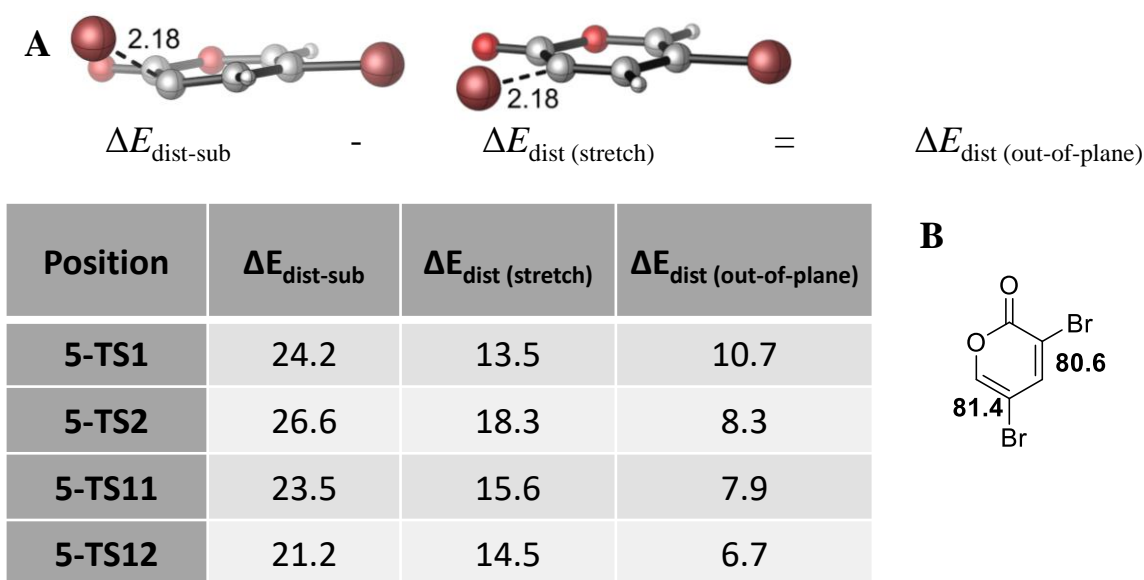
with a greater distortion penalty of the substrate ( $\Delta E_{\text{dist-sub}}$ ), which compensates for the interaction energy difference and leads to similar barriers for the two oxidative addition transition states. In this mono-phosphine ligated Pd complex pathway, Pd is less nucleophilic due to a lower-lying HOMO.<sup>29</sup> Therefore, the FMO interaction between the Pd center and the substrate is less prominent, and the preference for the C3 oxidative addition selectivity is diminished.



**Figure 5-8** The distortion energies of the  $\text{PdL}_1$  catalyst ( $\Delta E_{\text{dist-cat}}$ ) and the pyrone substrate ( $\Delta E_{\text{dist-sub}}$ ) and the interaction energies between these two fragments in the oxidative addition transition states ( $\Delta E_{\text{int}}$ ) in the presence of  $\text{CuI}$ .

The bond dissociation energy for the C–Br bond in 3,5-dibromo-2-pyrone (**5-1**) was calculated to analyze the distortion of the substrate (Figure 5-9). BDE is a good descriptor of stretching distortion of the substrate. The analysis showed that the BDE of these two bonds does not differ significantly, and the stretching of the bond should not significantly affect the differences

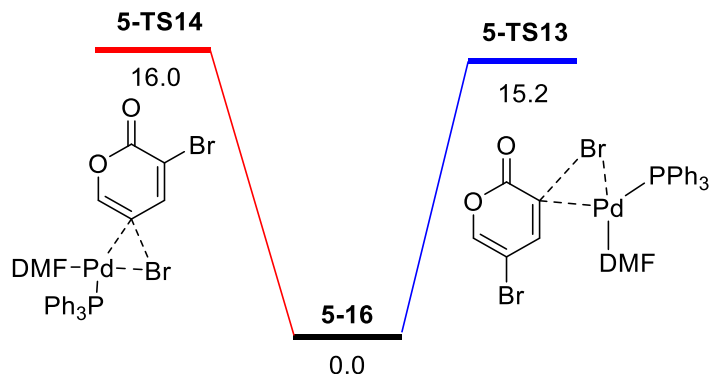
between the coupling at these two positions. On the other hand, distortion interaction analysis indicates that the distortion slightly favors addition at the C5 position. To further analyze the distortion of the substrate, we further decomposed the substrate distortion into the stretching distortion and out of plane distortion by calculating the energy required to stretch the C–Br bond into the transition state, which shows that while BDEs are comparable, and therefore stretching distortion energies are comparable and consistent with the C–Br bond length in the TS, out of plane bending favors addition at the C5 position generally.



**Figure 5-9 A) Decomposition of substrate distortion energy. B) BDEs of C–Br bonds of 3,5-dibromo-pyrone**

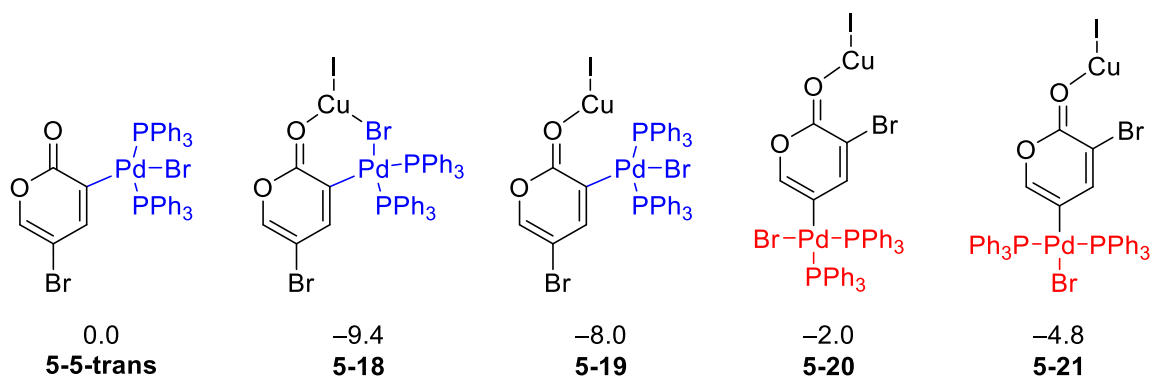
**5-1. Substrate distortion was decomposed into stretching distortion energy ( $\Delta E_{\text{dist (stretch)}}$ ) and out of plane bending distortion energy ( $\Delta E_{\text{dist (out-of-plane)}}$ )**

We also considered the oxidative additions of the DMF-coordinated mono-phosphine ligated Pd complex **5-16** (Figure 5-10). From **5-16**, the selectivity between the C3 and C5 oxidative addition transition states is also diminished ( $\Delta\Delta G^\ddagger = 0.8$  kcal/mol).



**Figure 5-10** Oxidative addition with mono-phosphine ligated palladium bound to DMF.

Overall, these results highlight a significant effect of the number of PPh<sub>3</sub> ligands on the selectivity of oxidative addition. While oxidative addition of bis-phosphine ligated Pd complex **5-7** is strongly preferred at C3, the site-selectivity is diminished in reactions with the mono-phosphine ligated Pd complexes (**5-15** or **5-16**).



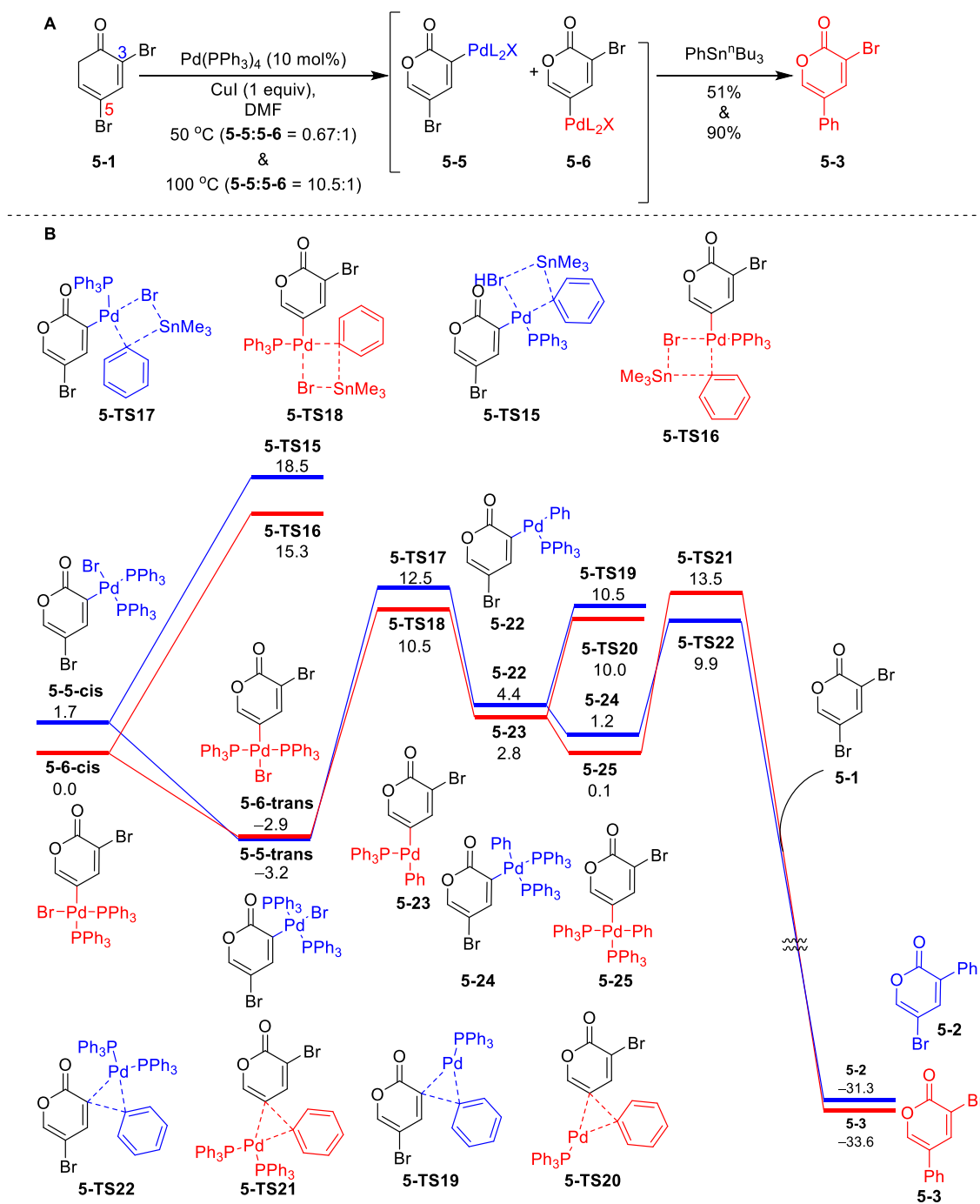
**Figure 5-11** Binding of CuI to all bis-phosphine ligated palladium (II) oxidative addition products. All energies are Gibbs free energies in kcal/mol with respect to **12-trans** and **15**.

Following oxidative addition, the more electron-deficient Pd(II) adduct binds another PPh<sub>3</sub> through ligand exchange with the CuI-phosphine complex to form tetracoordinated Pd(II) complexes **5-5** and **5-6** (Figure 5-7). The cis isomer of the C3 adduct (**5-5-cis**) can bind to CuI to

form a relatively stable ternary Cu complex (**5-18**) in which the Cu center is coordinated to both the pyrone carbonyl oxygen and the bromide attached to the Pd center. It should be noted that similar chelating complexes cannot be formed from **5-6** or either of the trans-isomers (Figure 5-11). Because of the greater stability of **5-18** compared to other C3 and C5 adducts, the C3 oxidative addition pathway is thermodynamically more favorable. This is consistent with the experimentally observed trend that increasing temperature leads to the C3 adduct as the major product (Figure 5-2).

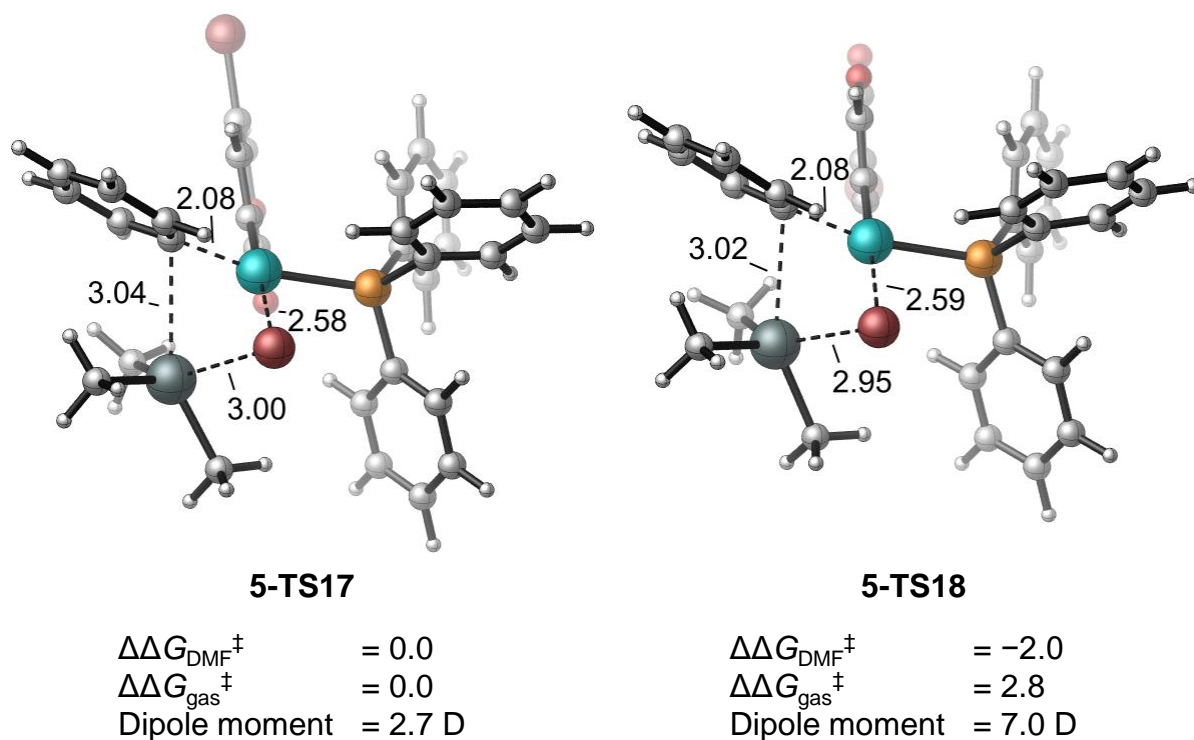
### 5.3.3 C5 selectivity in Stille coupling

We next sought to gain computational insight into the origin of C5-site-selectivity of the Stille coupling reactions (Figure 5-12A) under conditions where oxidative addition has been established to be reversible. In these cases, the selectivity is expected to be determined in the subsequent transmetallation or reductive elimination steps. We calculated the C3- and C5-selective pathways for the transmetallation and reductive elimination steps from the oxidative adducts **5-5** and **5-6** using trimethylphenylstannane as a model coupling partner (Figure 5-12). We located the cyclic transmetallation transition states where the substrate and bromide are either cis- or trans-disposed. In accordance with previous computational studies, the trans-transmetallation transition states (**5-TS17** and **5-TS18**) are about 5-6 kcal/mol more favorable than the corresponding cis-TS (**5-TS15** and **5-TS16**). The transition state associated with the transmetallation of the C5-adduct (**5-TS18**) is 2.0 kcal/mol more favorable than that of the C3-adduct (**5-TS18**) (Figure 5-12B).



**Figure 5-12 A.** Stille cross-coupling reaction of 3,5-dibromo-pyrone. The experiment was conducted by the Sarpong group. **B.** Transmetalation and reductive elimination steps in the Pd-catalyzed Stille cross-coupling reaction of 3,5-dibromo-2-pyrone. . The C3- and C5-selective pathways are shown in blue and in red, respectively. All energies are with respect to 5-6-cis

These computational results are consistent with the empirically observed preferable coupling of 5-6 over 5-5 when this mixture is exposed to tributylphenylstannane. To better understand the origin of this preference, we considered the polarity of the transmetallation transition states. We hypothesized that since **5-TS18** is significantly more polar than **5-TS17** due to the greater separation of the partial positive (on Pd) and negative (on the pyrone carbonyl oxygen) charges, more favorable stabilization of this transition state would occur in a polar solvent. In support of this hypothesis, we calculated the gas phase energies for TS5 and TS6. These calculations show that the relative stability is reversed in the gas phase, where TS5 is favored by 2.6 kcal/mol (Figure 5-13). Therefore, the polar solvent plays an important role in determining the selectivity for transmetallation. The transmetallation and subsequent ligand exchange with CuI(PPh<sub>3</sub>)(DMF) **5-17** leads to a four-coordinate PdII species (**5-24** or **5-25**), which then undergoes reductive elimination via either a bis-phosphine or mono-phosphine ligated transition state to form coupling products **5-2** and **5-3** (Figure 5-12B).



**Figure 5-13** Relative activation energies of transmetalation in an implicit solvent ( $\Delta\Delta G^\ddagger_{\text{DMF}}$ ) and in the gas phase ( $\Delta\Delta G^\ddagger_{\text{gas}}$ ). All energies are with respect to 5-TS17

## 5.4 Conclusion

Computations were performed to investigate the origin of reversible regioselectivity in the coupling of 3,5-dibromo-2-pyrone. The calculations indicated that bis-phosphine ligated palladium can catalyze oxidative addition at the 3- position due to more favorable HOMO-LUMO interactions between the palladium and the substrate. Additionally, combined experimental and computational investigations suggest that the oxidative addition in the presence of CuI happens via a monoligated pathway, where the OA is reversible. In this case, the selectivity is determined



by the transmetallation, which favors the coupling at the 5- position due to a more favorable solvation effect of more polar species.

## 6.0 Cross-coupling of carbohydrates for the synthesis of C-aryl glycosides

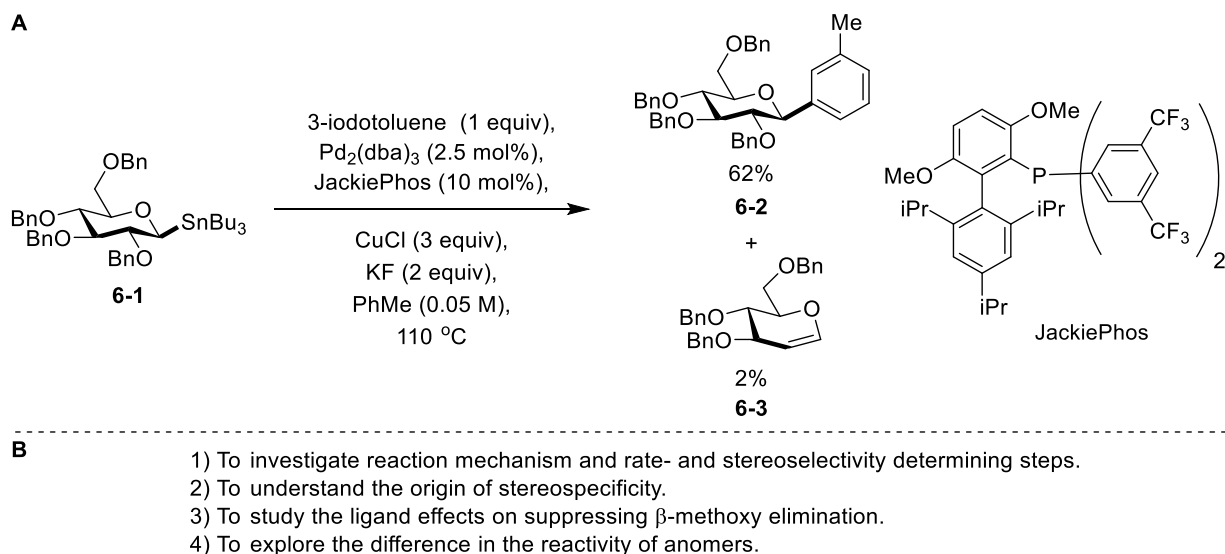
A significant part of this chapter was published as Zhu, F.; Rodriguez, J.; Yang, T.; Kevlishvili, I.; Miller, E.; Yi, D.; O'Neill, S.; Rourke, M. J.; Liu, P.; Walczak, M. A. *J. Am. Chem. Soc.* **2017**, *139*, 17908–17922.

### 6.1 Introduction

In the previous chapter, we discussed the mechanism of regiodivergent cross-coupling reactions with a heterocycle pyrone. In this chapter, we will discuss the mechanism of cross-coupling reactions of carbohydrates, with the emphasis on stereo- and regio-selectivity. Carbohydrates are one of the most abundant biomolecules and play a vital role in a wide range of biological functions.<sup>79</sup> Therefore, synthetic modification of the carbohydrate structure is an attractive approach in the development of novel pharmaceuticals. One of the most important approaches in preparative carbohydrate chemistry centers around the stereoselective manipulations at the C1 anomeric position of saccharides. Even though the synthesis of saccharides is a relatively mature field going all the way back to the works of Michael<sup>80</sup> and Fischer,<sup>81</sup> stereoselective manipulations at the anomeric position still pose a significant challenge. A class of glycosides containing C–C bond with C1 carbon of the saccharide ring called C-glycosides is found in several bioactive natural products. Because of the importance of this class of compounds, various methods have been described towards the stereoselective introduction of the aryl group in an anomeric position.<sup>82</sup> Despite a large number of existing methodologies, these

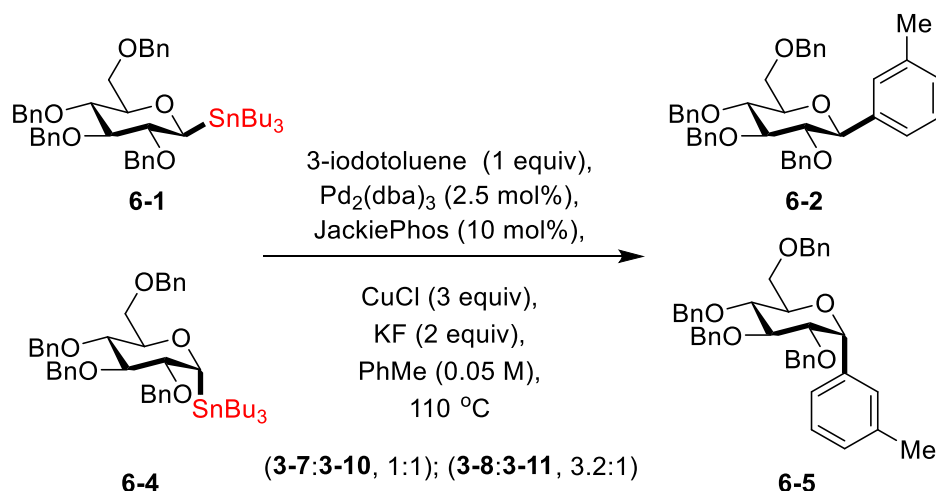
methods still have significant limitations, such as the control of the anomeric configuration of the product being dependent on the identity of saccharide and the C2 substituents, limited scope of nucleophilic reagents, and additional manipulations required for establishing carbohydrate core.

To overcome these limitations, Walczak's group proposed that an optimal solution to this problem would involve the process, where the configuration of the C-aryl glycoside would be established solely on the configuration of the substrate.<sup>83,84</sup> The control would be achieved by highly stereocontrolled transformation of the saccharide substrate. The substrate of choice was a series of configurationally stable anomeric stannanes that could undergo Stille coupling with aryl iodides (Figure 6-1). This process required careful optimization of the reaction conditions, including the choice of the ligand, to achieve desirable reactivity, as well as suppress the undesirable side reaction of  $\beta$ -methoxy elimination. Ligand screening revealed that the JackiePhos was the optimal choice for this reaction.



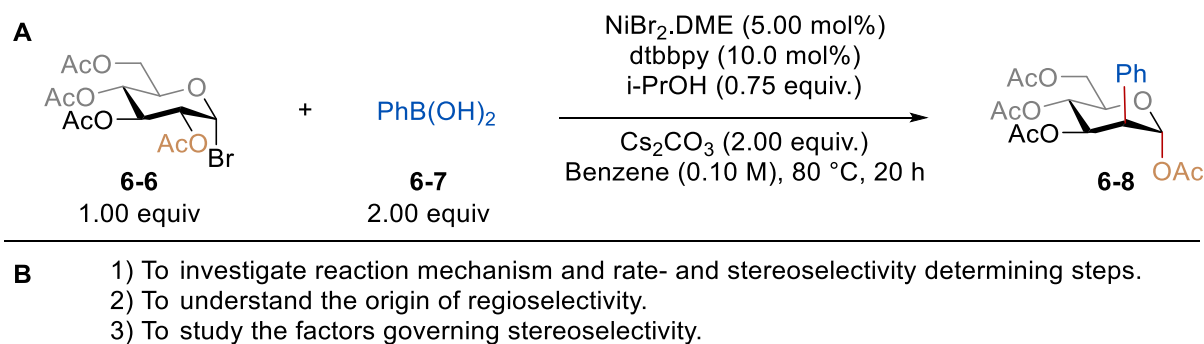
**Figure 6-1 A. Stereoretentive Stille coupling of anomeric stannanes. The use of JackiePhos suppresses the production of undesirable glycal 6-3. B. Goals of computational investigation.**

Additionally, a direct competition experiment of  $\alpha$  and  $\beta$  anomers of D-glucose stannanes (**6-4:6-1**, 1:1) with 3-iodotoluene revealed that the coupling of the  $\beta$ -anomer **6-1** is 3.2 times faster than the reaction leading to the  $\alpha$  anomer **6-5** (Figure 6-2). Section 6.2.1 of this chapter describes a computational mechanistic study of Stille coupling between bromobenzene **6-9** and organostannane **6-10** as a model substrate. DFT calculations were used to address some key aspects of this reaction, such as the less explored mechanism of  $sp^2$ - $sp^3$  Stille cross-coupling, high enantio-specificity, and ligand effects on suppressing side reactivity (Figure 6-1B).



**Figure 6-2 Competition of the  $\alpha$  and  $\beta$  anomeric stannanes.**

In addition to C1- functionalized carbohydrates, C2- functionalized carbohydrates are another important class of sugars that have found a wide array of applications in medicine, molecular imaging, cell engineering, and catalysis.<sup>85</sup> Despite the wide variety of their applications, there is a dearth of general catalytic approaches to prepare C2- functionalized 2-deoxy carbohydrates from readily available sugar precursors.<sup>86,87</sup> Furthermore, there is no synthetic method for the preparation of saturated, fully oxygenated 2-aryl-2-deoxy sugars from a readily available sugar precursor.<sup>88</sup> Instead, common methods for their preparation include multi-step synthesis.<sup>89</sup> To address this issue, the Ngai group developed a nickel-catalyzed migratory Suzuki cross-coupling reaction (Figure 6-3).



**Figure 6-3 A. Ni-catalyzed migratory cross-coupling reaction for the catalytic synthesis of challenging 2-aryl-2-deoxy sugars B. Goals of computational investigation**

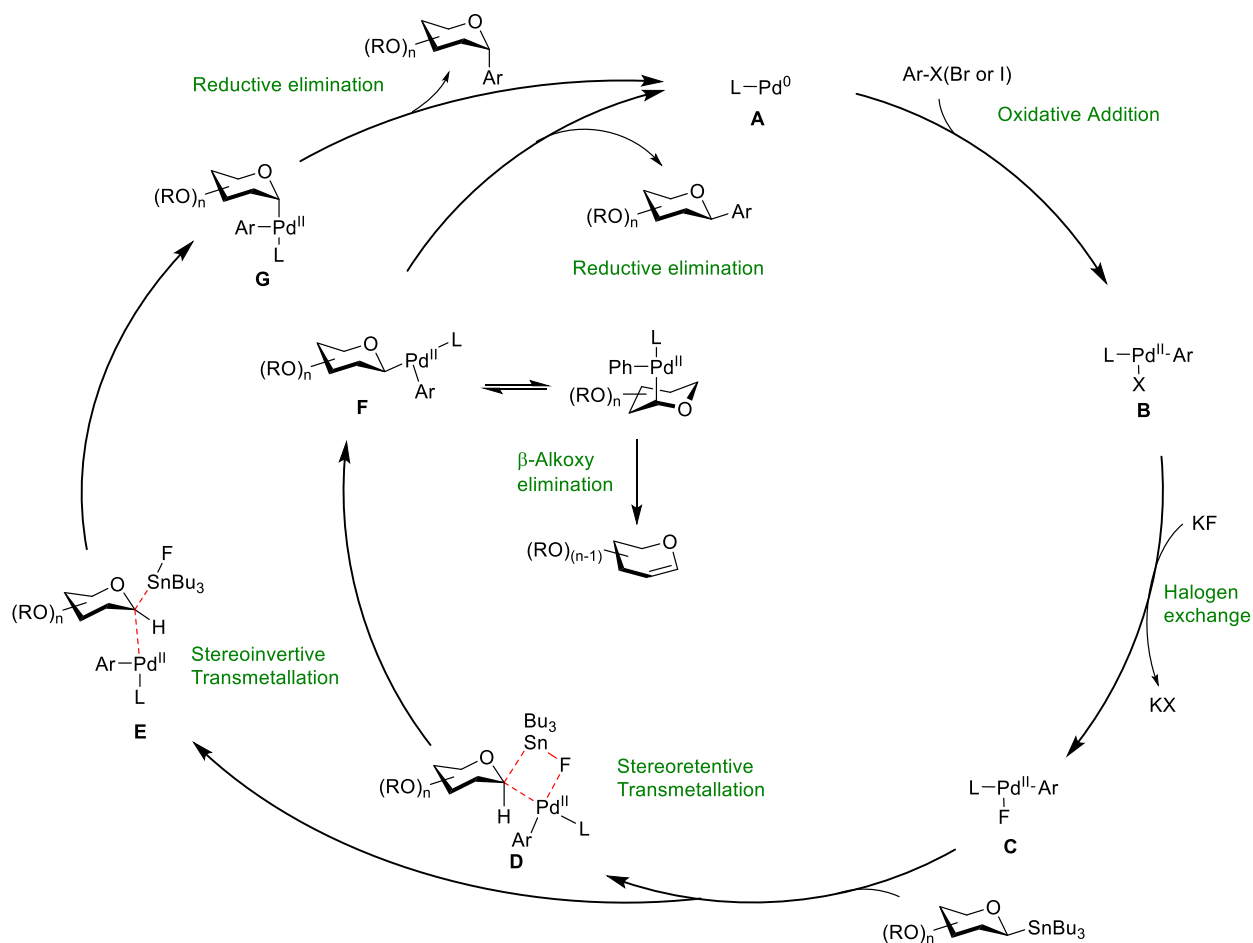
This reaction poses several interesting mechanistic aspects that can be explored through DFT calculations. This includes the mechanism of the 1,2 migration, the origin of regioselectivity, and diastereoselectivity. Section 6.3 of this chapter describes a computational mechanistic study of Suzuki migratory cross-coupling between phenylboronic acid **6-7** and carbohydrate **6-20** as a model substrate, where I study the reaction mechanism, and origin of regio- and stereoselectivity (Figure 6-3B).

## 6.2 Computational study on the stereospecific cross-coupling reactions of anomeric stannanes for the synthesis of C-aryl glycosides

### 6.2.1 Mechanistic background

While there is a substantial body of computational<sup>90</sup> and experimental<sup>91</sup> data on the mechanism of the Stille  $\text{C}(sp^2)\text{--}\text{C}(sp^2)$  cross-coupling reactions, very little is known about the Stille reactions that form a  $\text{C}(sp^3)\text{--}\text{C}(sp^2)$  bond<sup>92</sup> with optically active alkyl stannanes. The key

questions pertaining to the outcome of these reactions are (a) the origin of high stereospecificity, (b) the special ligand effect of JackiePhos, and the control of C-C cross-coupling versus  $\beta$ -elimination pathways, and (c) more facile cross-coupling of 1,2-*trans* anomeric stannanes. From the previous studies of the Stille coupling reaction, the catalytic cycle of the coupling reaction consists of oxidative addition, followed by transmetallation and reductive elimination leading to the final product and regeneration of the palladium catalyst. A key step in this coupling reaction is the transmetallation, which can proceed through both cyclic, stereoretentive pathway and open, stereoinvertive pathway. Furthermore, previous computational studies have demonstrated that fluoride additives can promote transmetallation. With this understanding, we proposed a catalytic cycle for this reaction (Figure 6-4) to be studied computationally.



**Figure 6-4 Proposed catalytic cycle for the Stille coupling reaction.**

Three major points of interest were examined in the computational investigations. First, although the mechanisms of  $C(sp^2)-C(sp^2)$  Stille coupling has been extensively studied computationally, there were no existent computational studies involving  $C(sp^3)-C(sp^2)$  bond formation in Stille coupling. Stereoretentive transmetallation with vinyl stannanes and halides is known to occur via the “closed” pathway involving a four-membered cyclic transition state (**D** in Figure 6-4). It was of interest to investigate whether such cyclic transmetallation transition state with sterically more encumbered alkyl stannanes is energetically accessible. A previous computational study from Yates<sup>90g</sup> indicated that the addition of  $F^-$  led to increased reactivity of



vinyl stannane reagents towards transmetallation. Here, we will investigate whether the potentially more challenging transmetallation with alkyl stannanes is promoted by  $F^-$ . Furthermore, efficient  $C(sp^3)-C(sp^2)$  reductive elimination is the key to prevent the competing  $\beta$ -elimination of the oxygen-based groups at C2. The effects of JackiePhos ligand on the rates of reductive elimination and  $\beta$ -alkoxy elimination will be elucidated by computational methods. Finally, the origin of the difference in reactivity between  $\alpha$  and  $\beta$  anomeric stannanes will be elucidated computationally.

### 6.2.2 Computational details

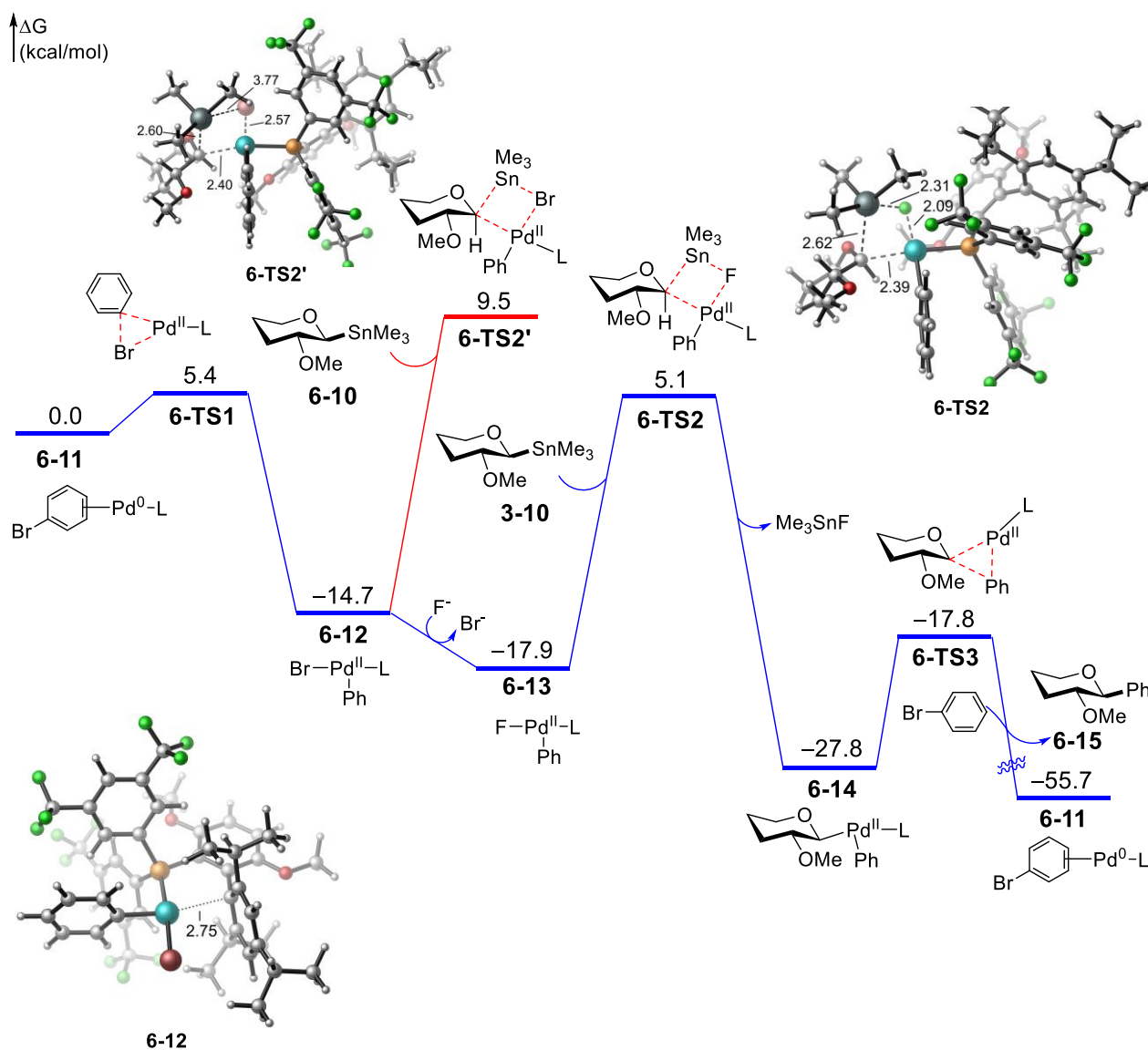
All calculations were carried out with the Gaussian 09 package.<sup>13</sup> Geometry optimizations were performed with B3LYP.<sup>15</sup> Mixed basis set of SDD was used for palladium and tin, and 6-31G(d) for other atoms. Frequency analysis was conducted at the same level of theory to verify the stationary points to be minima or saddle points and to obtain zero-point energy (ZPE) and thermal energy corrections at 298.15 K. Single-point energy calculations on B3LYP-optimized geometries were performed with the M06 functional,<sup>17</sup> a mixed basis set of SDD for palladium and tin, and 6-311+G(d,p) for other atoms, and the SMD solvation model<sup>19</sup> with 1,4-dioxane as the solvent. The entropic contributions to the Gibbs free energies were calculated from partition functions using Cramer and Truhlar's quasiharmonic approximation,<sup>49</sup> which raises vibrational frequencies lower than  $100\text{ cm}^{-1}$  to  $100\text{ cm}^{-1}$  to correct the harmonic oscillator model for low-frequency vibrational modes.

## 6.2.3 Results and discussions

### 6.2.3.1 Reaction mechanisms

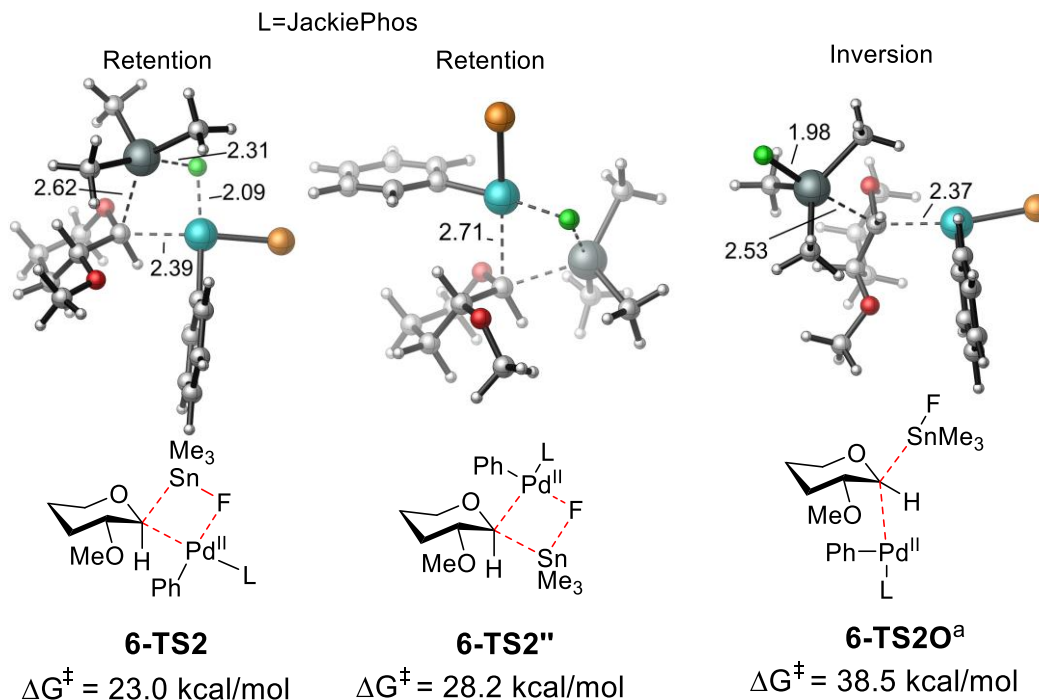
The calculated reaction energy profile of the Pd-catalyzed coupling of simplified substrates bromobenzene **6-9** and stannane **6-10** using JackiePhos ligand is shown in Figure 6-5. The palladium(0)-bromobenzene complex **6-11** undergoes oxidative addition with a barrier of 5.4 kcal/mol (**6-TS1**), leading to phenyl palladium(II) bromide complex **6-12**. The JackiePhos ligand in the three-coordinate palladium complex **6-12** adopts the conformation where the biaryl group shields the remaining open site of the palladium (Figure 6-5).

From **6-12**, the stereoretentive transmetallation via a four-membered cyclic transition state (**6-TS2'**) requires activation energy of 24.2 kcal/mol with respect to **6-12**. This transmetallation is facilitated in the presence of  $F^-$ . Halide exchange with **6-12** forms a more stable palladium(II) fluoride species **6-13**, which then undergoes transmetallation via **6-TS2** and requires a barrier of 23.0 kcal/mol to form intermediate **6-14**. The fluoride effects are consistent with the Yates study that the transmetalation with palladium fluoride is faster due to the formation of the stronger Sn–F bond.



**Figure 6-5** Reaction energy profile of the Pd-catalyzed Stille coupling of bromobenzene and tetrahydropyranyl stannane 3-12 using JackiePhos ligand.

In both **6-TS2** and **6-TS2'**, the palladium approaches the stannane from the same side of the C1 hydrogen. The transition state isomer of **6-TS2** in which the palladium approaches from the opposite side of the C1 hydrogen is less stable by 5.2 kcal/mol due to unfavorable steric repulsions of the palladium catalyst with the six-membered ring (Figure 6-6).



**Figure 6-6** Different possible transmetallation mechanisms. In **6-TS2** and **6-TS2''** palladium is approaching from two different sides of the stannane. **6-TS2O** refers to stereoinvertive transmetallation transition state.

All energies are relative to the complex **3-15**. JackiePhos emitted for clarity. <sup>a</sup> The energy refers to the constrained optimization of the open transition state.

Attempts to locate the open form transmetallation transition state that leads to stereoinversion were unsuccessful. Constrained geometry optimization of such transition state suggested significantly higher energy compared to the closed-form transition state (Figure 6-6). Intermediate **6-15** undergoes reductive elimination to form the arylation product **6-15** with a relatively low barrier of only 10.0 kcal/mol (**6-TS3**). Here, the reductive elimination is promoted by the bulky and electron-deficient JackiePhos ligand.<sup>93</sup>

### 6.2.3.2 $\beta$ -Methoxy elimination suppressed by the JackiePhos ligand

We then computed the energy profile of the  $\beta$ -methoxy elimination from **6-14** to investigate the origin of the ability of the JackiePhos ligand to suppress this undesired pathway (Figure 6-7). The elimination of the *trans*- $\beta$ -methoxy most likely occurs via the antiperiplanar elimination from the ring flip isomer (**6-16**). Under the reaction conditions, this elimination could be promoted by the stabilization of the methoxide leaving group by a Lewis acid (e.g., CuCl) and the stabilization of the cationic Pd(II) by coordination with an  $F^-$ . Due to the diaxial repulsion with the phenyl and the JackiePhos ligand on the Pd, the ring flip isomer **6-16** is 5.7 kcal/mol less stable than **6-14**. However, it should be noted that this energy difference would be further amplified with the real experimental substrate due to additional diaxial interactions. Coordination of CuCl and  $F^-$  to **6-16** requires 9.9 kcal/mol in terms of Gibbs free energy. The relatively unfavorable binding of  $F^-$  is again attributed to the steric hindrance of the JackiePhos ligand, which partially blocked the remaining binding site on Pd in **6-16**. With the assistance of CuCl and  $F^-$ , the E2-type elimination from **6-18** is relatively facile, requiring an activation barrier of 9.2 kcal/mol. Nonetheless, the overall barrier of the  $\beta$ -methoxy elimination from **6-14** to **6-TS4**, which includes the energies required for ring flip and CuCl and  $F^-$  coordination, is 24.8 kcal/mol, significantly higher than the C–C reductive elimination from **6-14**, requiring only 10.0 kcal/mol. These computational results suggest that bulky phosphine ligands, such as JackiePhos, not only promote reductive elimination but also increase the barrier to  $\beta$ -alkoxy elimination by preventing ring flip and  $F^-$  coordination to the Pd center.

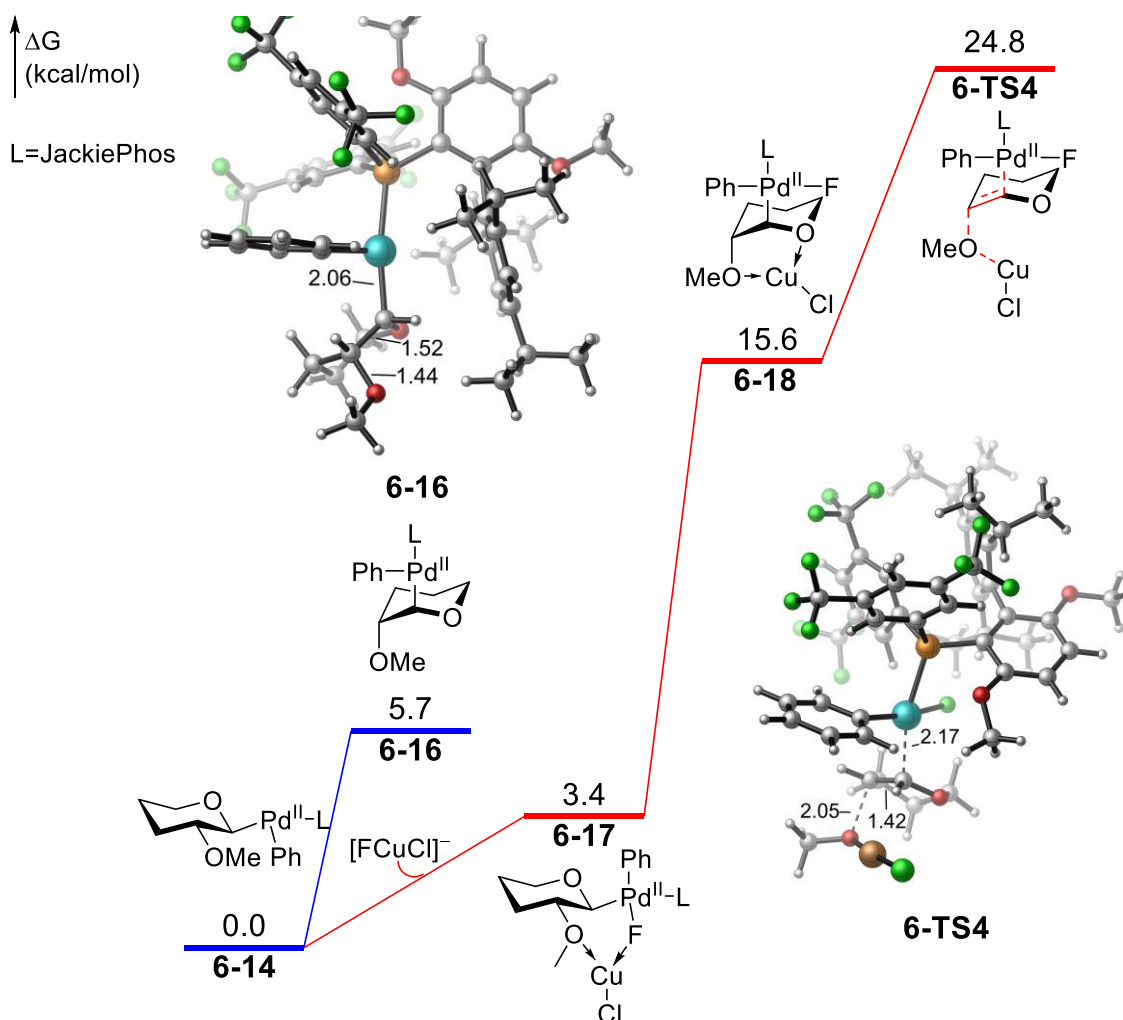
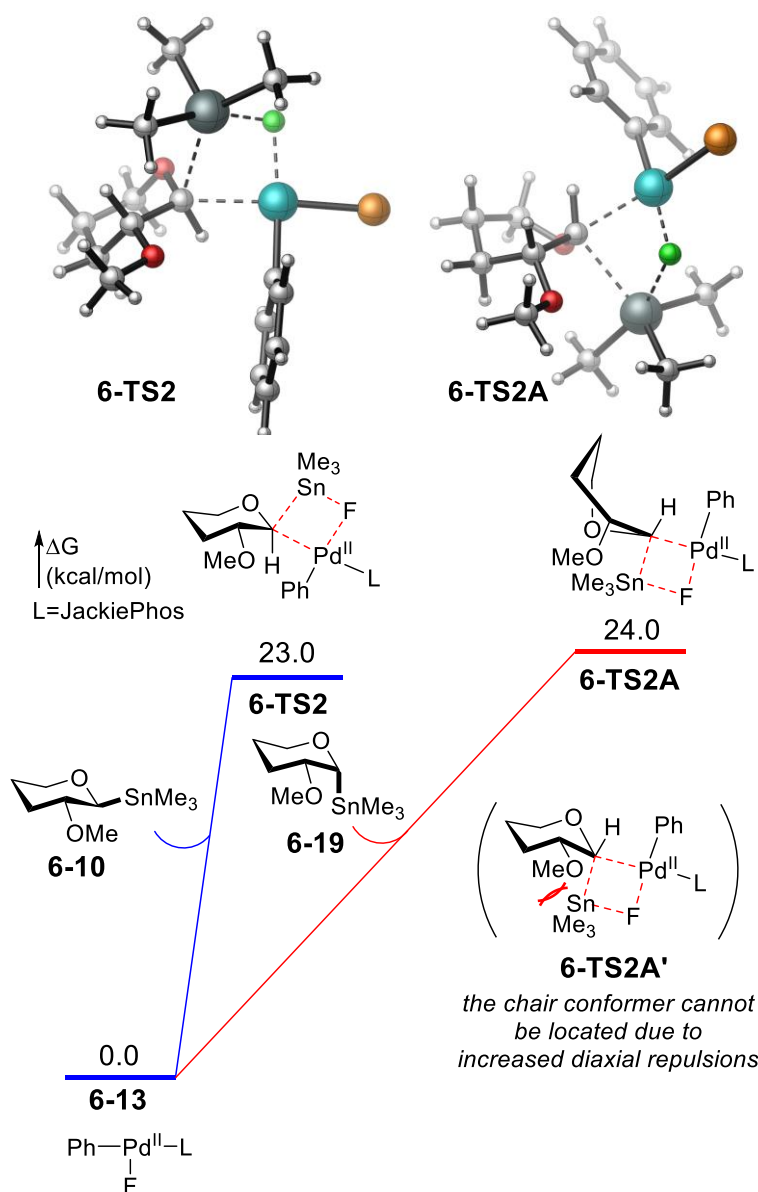


Figure 6-7 Reaction energy profile of the  $\beta$ -methoxy elimination pathway. All energies are with respect to complex 6-16.

### 6.2.3.3 Reactivities of $\alpha$ and $\beta$ anomers

We then performed a computational analysis to understand the origin of the reactivity differences between the two anomers. Based on the computationally predicted reaction mechanism, the transmetalation is irreversible and rate-determining. Thus, we calculated the transmetalation transition states with stannanes **6-10** and **6-19** as models of  $\beta$  and  $\alpha$  anomers **6-1** and **6-4**, respectively (Figure 6-1). Both transmetalations occur via the stereoretentive four-membered cyclic transition state. However, unlike **6-TS2**, the six-membered ring in **6-TS2A**

changes to a twist-boat-like conformation, leading to the diminished reactivity of the  $\alpha$  anomer. Transition state **6-TS2A** is 1.0 kcal/mol higher in energy than the transmetallation involving the  $\beta$  anomer (**6-TS2**). This twist-boat conformation in **6-TS2A** is achieved to relieve the amplified 1,3-diaxial interactions between tin and the two axial hydrogens in the chair-like transition state structure (**6-TS2A'**).



**Figure 6-8** Transition states of transmetalation of  $\alpha$  and  $\beta$  anomers (6-19 and 6-10). All energies are with respect to complex 6-13. The JackiePhos ligand is not shown in the 3D structures for clarity.

#### 6.2.3.4 Summary

The computational study revealed that the transmetalation of alkyl stannanes occurs via a stereoretentive four-member cyclic transition state. With the use of JackiePhos, reductive elimination is facile due to its steric bulk and electron-deficient nature. It furthermore suppresses

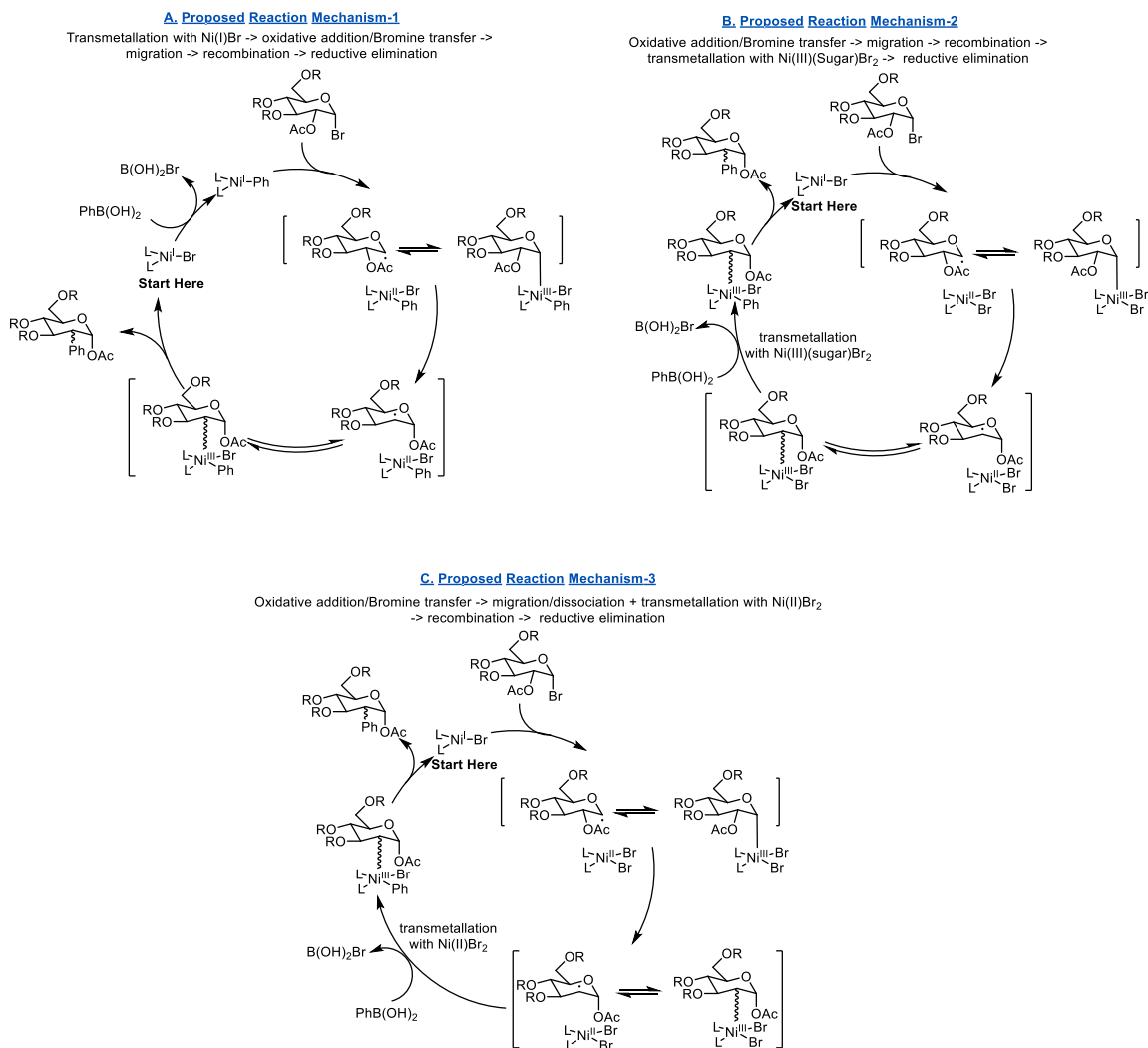


$\beta$ -alkoxy elimination by destabilizing the ring flip isomer due to its steric bulk and fluoride binding due to a blocked Pd binding site. Finally, the lower reactivity of  $\alpha$ -anomers can be attributed to the increased 1,3-diaxial repulsions between the tin and the two axial hydrogens.

## **6.3 Nickel-catalyzed C-2 arylation of carbohydrates via radical migratory coupling**

### **6.3.1 Mechanistic background**

Nickel-catalyzed alkyl halide Suzuki cross-coupling has been successful as a method to form new carbon-carbon bonds.<sup>94</sup> Therefore, a series of experimental<sup>95</sup> and computational<sup>96</sup> investigations have been carried out to understand the reaction mechanisms. Migratory cross-coupling (MCC) with alkyl halides have also been studied recently,<sup>97</sup> where the nickel catalyst typically migrates from the activation site to the cross-coupling site *via* the 2-electron  $\beta$ -hydrogen elimination/migratory insertion sequence. On the other hand, Ni-catalyzed MCC reactions that proceed through a radical migration pathway, such as a 1,2-spin-center shift (SCS),<sup>98</sup> are less common.<sup>99</sup> In past computational studies, a Ni(0) – Ni(II) cycle has been shown to be highly disfavored due to a kinetically unfavorable reductive elimination to regenerate Ni(0) catalyst. Based on this understanding, we limited the computational investigation to the possible Ni(I) – Ni(III) cycles (Figure 6-9).



**Figure 6-9 Possible Ni(I) catalyzed migratory cross-coupling mechanisms A. Transmetalation with Ni(I) B. Transmetalation with Ni(II). C. Transmetalation with Ni(III).**

We envisioned that the reaction could be catalyzed through three distinct pathways, where several different species could potentially undergo transmetalation (Figure 6-9). First, Ni(I) bromide could undergo transmetalation with boronic acid (Figure 6-9A). Alternatively, Ni(I) bromide could undergo bromine atom transfer or oxidative addition followed by homolytic dissociation to form Ni(II) dibromide, which could then undergo transmetalation (Figure 6-9B). Finally, Ni(III) species could undergo transmetalation, followed by the reductive elimination

(Figure 6-9C). Based on the few possible mechanisms, we investigated the coupling reaction between model carbohydrate **6-20** and phenylboronic acid. Acetate groups not involved in MCC were truncated to OMe groups in model carbohydrate 6-20 to simplify the highly complex conformation space of the real substrate **6-6**. We were interested first to elucidate the operative reaction mechanism. Furthermore, using computational studies, we also wanted to investigate the origin of the C2 selectivity of this reaction. Finally, we wanted to understand the origin of the diastereoselectivity of this reaction.

### 6.3.2 Computational details

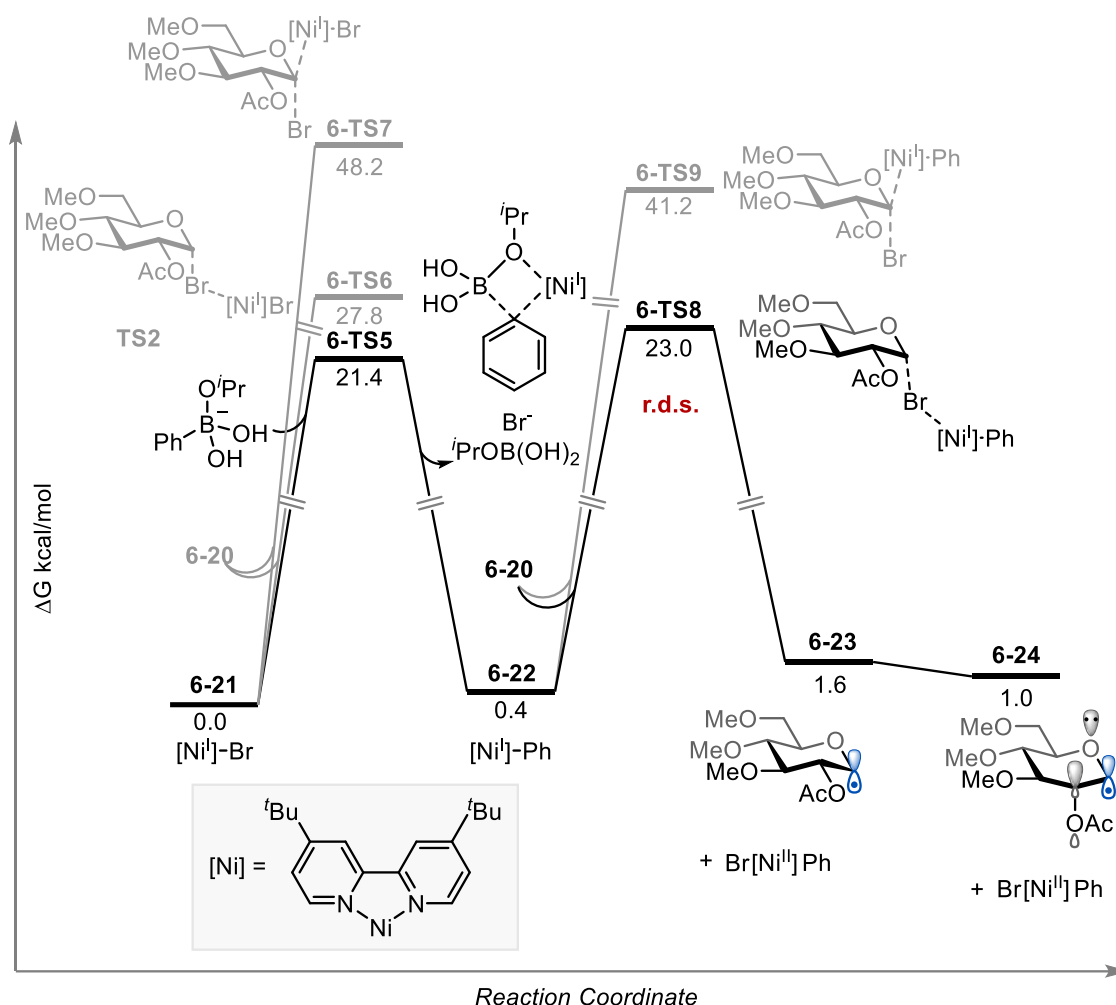
All density functional theory (DFT) calculations were carried out using Gaussian 16.<sup>14</sup> Geometries of intermediates and transition states were optimized using the dispersion-corrected B3LYP-D3 functional,<sup>15</sup> using Grimme's DFT-D3 dispersion correction,<sup>16</sup> with a mixed basis set of SDD for Ni and 6-31G(d) for other atoms in the gas phase. Vibrational frequency calculations were performed for all the stationary points to confirm if each optimized structure is a local minimum or a transition state structure. Truhlar's quasi-harmonic corrections<sup>49</sup> using 100 cm<sup>-1</sup> as the frequency cutoff and temperature correction to 80 °C were applied to entropy calculations with GoodVibes,<sup>100</sup> Solvation energy corrections were calculated in benzene solvent with the SMD continuum solvation model<sup>19</sup> based on the gas-phase optimized geometries. The M06 functional<sup>17</sup> with a mixed basis set of SDD for Ni and 6-311+G(d,p) for other atoms was used in solvation single-point energy calculations. Conformational sampling of carbohydrate structures was carried out using the iterative metadynamic sampling and genetic crossover (iMTD-GC) method implemented in the CREST program,<sup>25</sup> with GFN2-xtb method,<sup>26</sup> including additional geometry optimization of the final conformer ensemble using B3LYP-D3/SDD-6-31G(d) method. NBO

analysis of some key intermediates and transition states was performed using NBO version 3 embedded in Gaussian 16.<sup>54</sup>

### 6.3.3 Results and discussions

#### 6.3.3.1 C-Br activation mechanism

DFT calculations showed that bromine atom abstraction (**6-TS6**) and oxidative addition (**6-TS7**) by  $[\text{Ni}^{\text{I}}]\text{Br}$  is less favorable than the formation of  $[\text{Ni}^{\text{I}}]\text{Ph}$  (**6-22**) through isopropoxide-mediated transmetallation (**6-TS5**, Figure 6-10). Prior to the transmetallation step, a base likely promotes the deprotonation of *i*-PrOH to form isopropoxide anion, which then binds to the phenylboronic acid to form a phenyl dihydroxyisopropylboronate complex. Although the base-mediated deprotonation is challenging to calculate because the insoluble base ( $\text{Cs}_2\text{CO}_3$ ) is involved, our calculations indicate that the binding of the isopropoxide anion to  $\text{PhB}(\text{OH})_2$  is highly exergonic by 23.9 kcal/mol. Therefore, we used the phenyl dihydroxyisopropylboronate complex as the energy zero in the calculations of the transmetallation pathway. The effect of the cesium counteraction was not considered in the calculations. The complex **6-22** then undergoes rate-determining radical bromine atom abstraction (**6-TS8**) to generate  $\text{Br}[\text{Ni}^{\text{II}}]\text{Ph}$  species and a chair 1-glucosyl radical (**6-23**). This pathway is more favorable than the two-electron  $\text{S}_{\text{N}}2$  type oxidative addition **6-TS9**. The 1-glucosyl radical prefers the  $\text{B}_{2,5}$  boat conformation (**6-24**) by 0.6 kcal/mol. These results suggest that the most favorable reaction pathway proceeds through the proposed reaction mechanism 1 (Figure 6-9), where the transmetallation occurs with  $\text{Ni}(\text{I})$  species and precedes the bromine atom abstraction.



**Figure 6-10 Determination of the most favorable reaction pathway**

We then performed ligand substrate interaction analysis on two bromine abstraction transition states (**6-TS5** and **6-TS8**) to understand the preference for mechanism 1. These results indicate that the driving factor for the more favorable reactivity with Ni(I)Ph intermediate **6-22** when compared to Ni(I)Br **6-21** species can be attributed to the stronger bonding interaction between nickel and bromine atom in **6-TS8**. Even though the C-Br bond is more elongated in **6-TS5**, indicating a later transition state, bonding interaction is still more favorable with the Ni(I)Ph

species. This can be attributed to aryl ligand being a better donor ligand when compared to bromide. Therefore, nickel becomes more susceptible to oxidation.

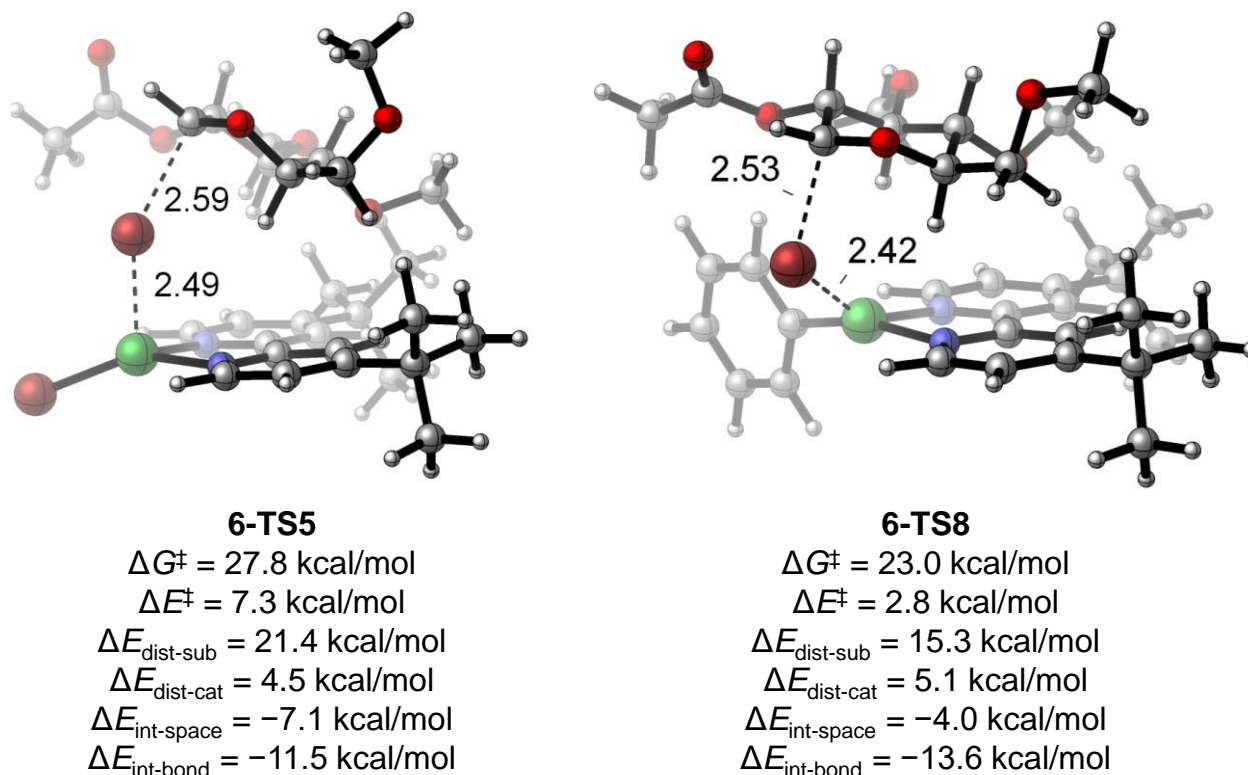


Figure 6-11 Ligand substrate interaction analysis of two bromine atom abstraction transition states

### 6.3.3.2 Carbon-carbon coupling pathways and regioselectivity

We then computed the coupling mechanism at the C1 position to understand why this pathway was disfavored. Following the formation of intermediate **6-24**, 1 glycosyl radical can recombine with Ni(II)PhBr intermediate (Figure 6-12). The addition can occur through either the addition at the alpha (**6-TS11**) or beta (**6-TS10**) positions. These additions are relatively facile, requiring the barrier of 14.2 and 11.3 kcal/mol, relatively. However, the addition to form Ni(III) intermediates are endergonic. Furthermore, following reductive eliminations to form the C1 arylated products are even more disfavored, requiring the barrier of 16.3 and 21.3 kcal/mol,

respectively. These results indicate that the formation of the C1 coupled products requires high activation energy during the reductive elimination.

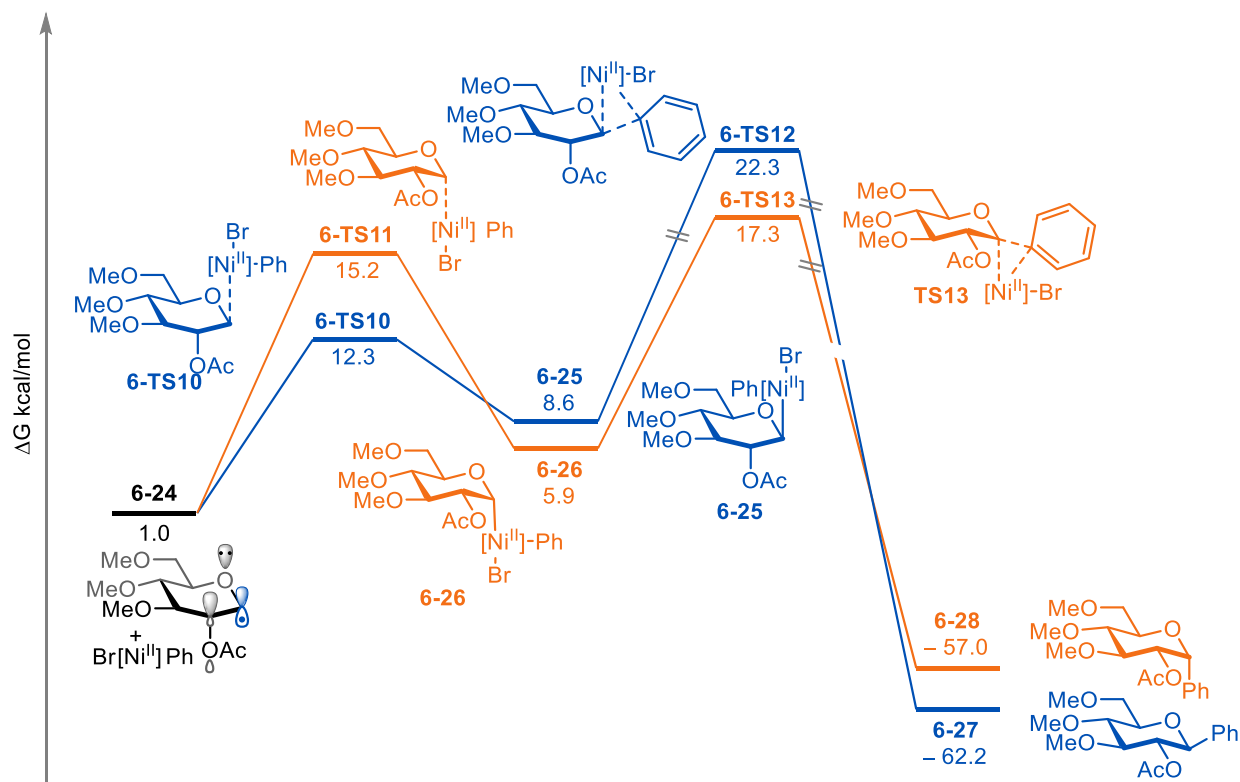
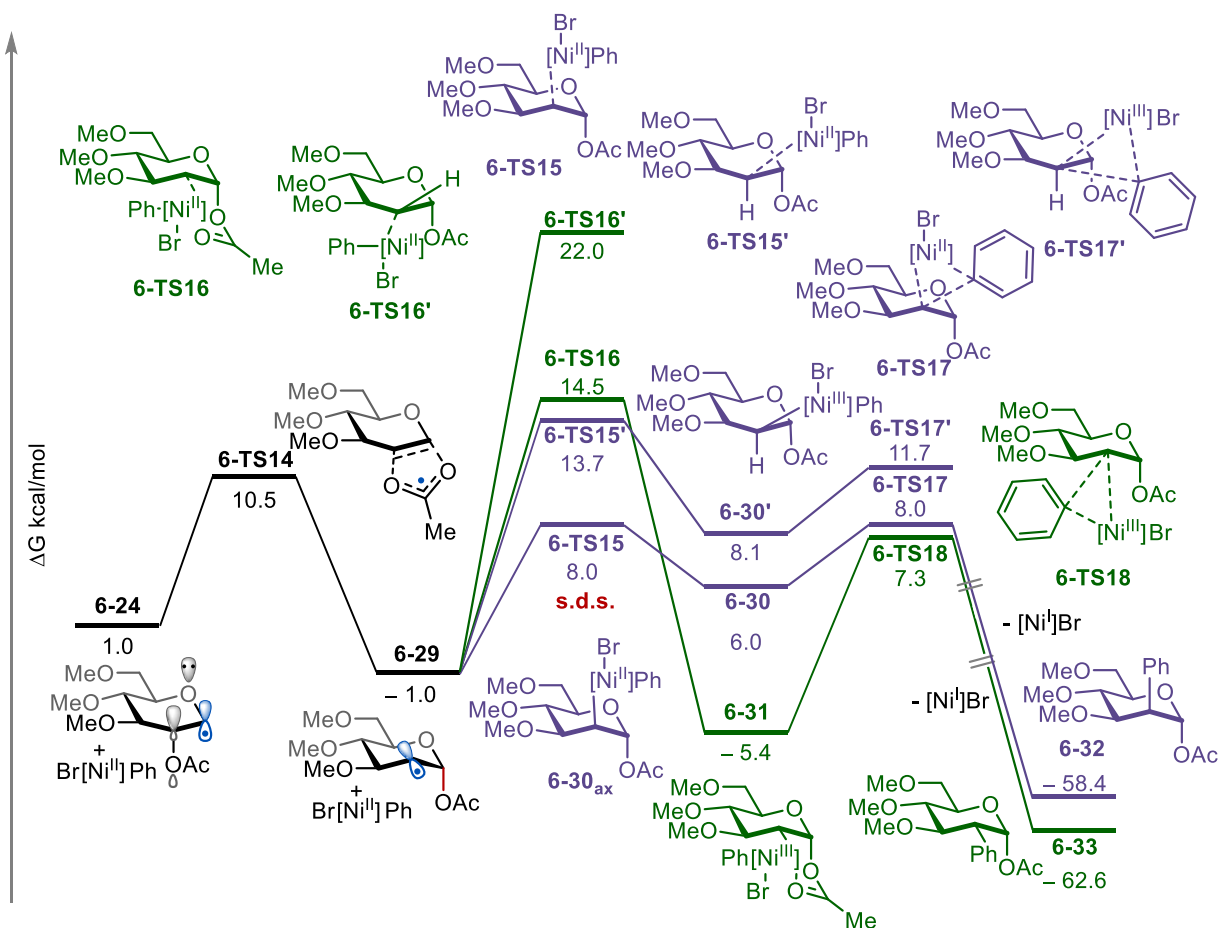


Figure 6-12 Mechanism for bond formation at the C1 position

On the other hand, the coupling at the C2 position first requires migration of the acetoxyl position. More favorable B<sub>2,5</sub> boat conformation (**6-24**) stems from the extended anomeric interaction between the lone-pair electron of the endocyclic-O, the singly occupied molecular orbital (SOMO), and the  $\sigma^*_{C-O}$  orbital of the C-2 OAc group.<sup>101</sup> This interaction weakens the C-2 OAc bond and promotes the 1,2-SCS through a concerted 1,2-acyloxy rearrangement *via* a cyclic five-membered ring transition state (**6-TS14**), affording the deoxypyranosan-2-yl radical (**6-29**). Although a typical secondary alkyl radical would be less stable than an anomeric radical, in this

case, the molecular stability gained from the formation of an anomeric C–O bond in **6-29** drives the desired 1,2-SCS and makes this step exergonic by 2.0 kcal/mol.



**Figure 6-13 Mechanism for coupling at the C2 position**

The next step is the addition of the  $[\text{Ni}^{\text{II}}](\text{Br})\text{Ph}$  species to deoxypyranosan-2-yl radical, where the axial addition (**TS6**) is more favorable than the equatorial addition (**TS7**). Following the formation of Ni(III) intermediate **6-30**, the reductive elimination is highly facile, requiring the activation energy of 2.0 kcal/mol. The high reactivity of this intermediate towards reductive elimination is in contrast with the lower reactivity at the C1 position (**6-TS13**). To understand why



reductive elimination is favored at the C2 position but highly disfavored at the C1 position, we performed an NPA charge analysis. In complex **6-30**, the negative charge is localized at the C2 center (NPA charge on C2 =  $-0.407$ ), which makes this intermediate highly reactive towards reductive elimination. On the other hand, the negative charge in **6-26** is delocalized onto the neighboring oxygen (NPA charge on C1 =  $0.030$ ), which makes this complex less susceptible to reductive elimination, leading to a much higher barrier in spite of these two complexes (**VI<sub>ax</sub>** &  **$\alpha$ -III'**) having similar energies.

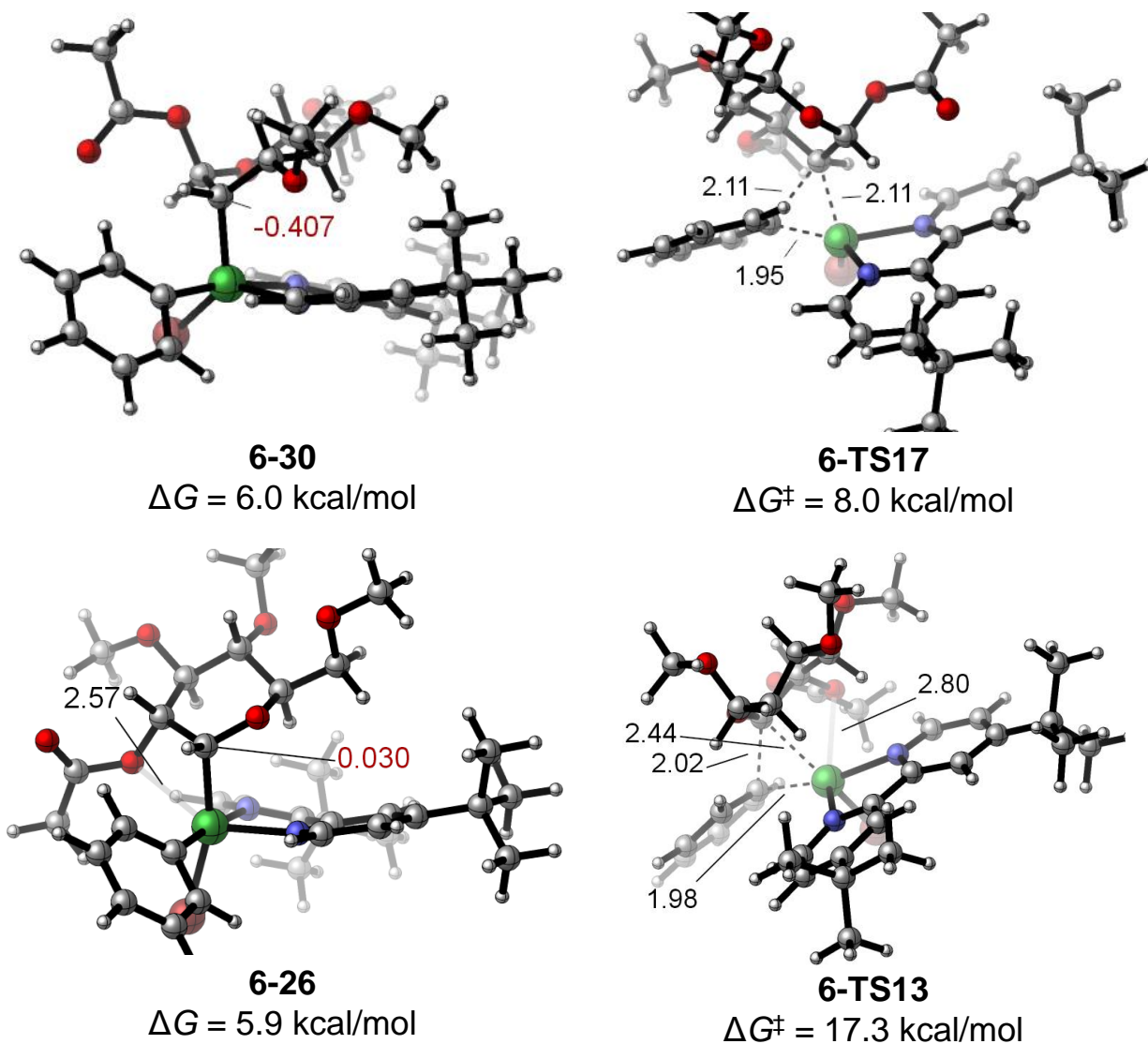
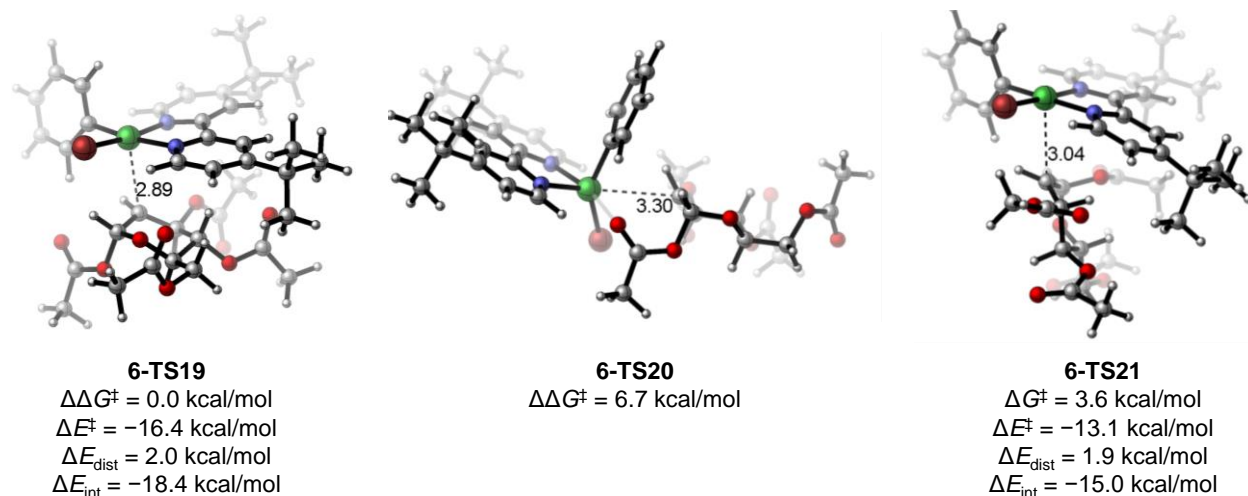


Figure 6-14 NPA charge analysis of Ni(III) intermediates, 6-26 and 6-30, and corresponding reductive elimination transition state structures.

### 6.3.3.3 Origin of stereoselectivity

DFT calculations suggested that the stereoselectivity-determining step (s.d.s.) is the addition of the  $[\text{Ni}^{\text{II}}](\text{Br})\text{Ph}$  species to deoxypyranosan-2-yl radical where the axial addition (**6-TS15**) is more favorable than the equatorial addition (**6-TS16**) because the equatorial addition to square planar Ni complex is hindered by unfavorable steric interactions with the *cis* C1-acetoxy

group (**6-TS16'**). While these results agree with the experimentally observed stereoselectivity for the 1,2-*trans* product qualitatively, the difference between the activation barrier for these two products is overestimated significantly. We hypothesized that the model substrate could not fully capture some key interactions. Therefore, we repeated the calculations for competing stereoselectivity determining radical rebound transition states with the real substrate **6-6** (**6-TS19**, **6-TS20** Figure 6-15). However, this did not decrease the free energy activation barrier ( $\Delta\Delta G^\ddagger = 6.5$  kcal/mol). On the other hand, using the real substrate, we were able to locate a new transition state (**TS21**, comparable TS cannot be located using the model substrate), where substrate approaches Br[NiII]Ph at the apical position in chair conformation. This transition state improved the free energy barrier difference ( $\Delta\Delta G^\ddagger = 3.6$  kcal/mol). While the energy difference is still overestimated, the newly proposed mechanism for the formation of a less favorable diastereomer is in better agreement with the experiment. Distortion interaction analysis further revealed that the difference is interaction controlled. This can be attributed to increased Ni–C distance in the transition state, which is induced by the unfavorable steric repulsions between axial acetate and the ligand.



**Figure 6-15** Relative energies of radical rebound transition states using real substrate and their distortion interaction analysis.

#### 6.3.3.4 Summary

Based on these results, the known acyloxy migration and the nickel-catalyzed Suzuki-Miyaura coupling, a plausible catalytic cycle is shown in Figure 6-16. The  $[\text{Ni}^{\text{I}}]\text{Br}$  (**I**) formed under standard reaction conditions undergoes transmetalation with an arylboronic acid, forming a  $[\text{Ni}^{\text{I}}]\text{Ph}$  species (**II**). Bromine atom abstraction by **II** from the C-Br bond of  $\alpha$ -glycosyl bromide generates  $\text{Br}[\text{Ni}^{\text{II}}]\text{Ph}$  species and chair 1-glycosyl radical (**III**). This intermediate could directly recombine with  $\text{Br}[\text{Ni}^{\text{II}}]\text{Ph}$  species, but the subsequent reductive elimination to form C-1 arylated side products is not kinetically accessible. Instead, DFT calculations showed that the conversion of **III** to its  $\text{B}_{2,5}$  boat conformation (**IV**) followed by a concerted 1,2-acyloxy rearrangement is more favorable under standard reaction conditions. The addition of the resulting deoxypyranosan-2-yl radical (**V**) to  $[\text{Ni}^{\text{II}}](\text{Br})\text{Ph}$  species affords the C-2  $\text{Ni}^{\text{III}}$ -glycosyl complex (**VI**), which undergoes facile reductive elimination to liberate the desired C-2 arylated glycoside and regenerate the  $[\text{Ni}^{\text{I}}]\text{Br}$  (**I**) catalyst.

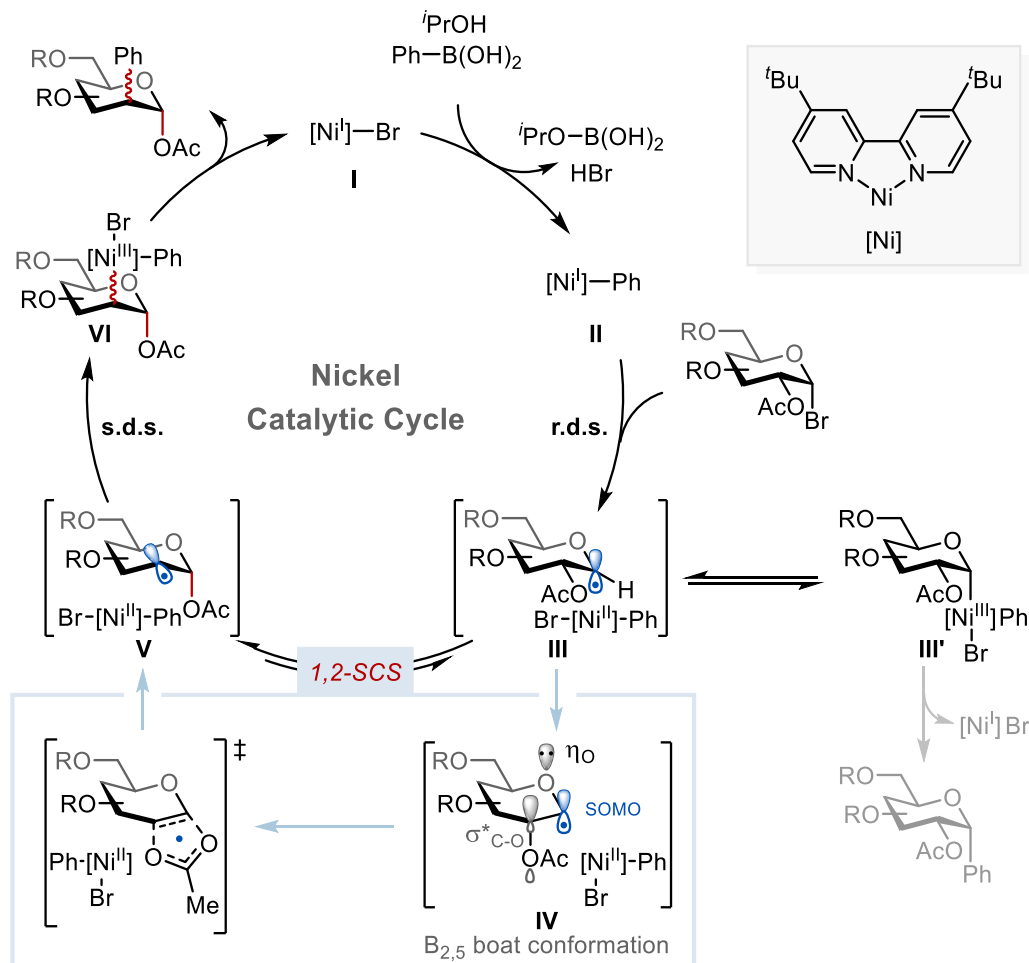


Figure 6-16 Proposed catalytic cycle

## 6.4 Conclusion

DFT calculations were performed to investigate the mechanisms of two different carbohydrate cross-coupling reactions. Different approaches were employed to address the vast conformational space of carbohydrates, where the conformational space of carbohydrates was restricted by using a model substrate in the cross-coupling reaction of anomeric stannanes. For the more recent study involving nickel-catalyzed migratory cross-coupling reaction, I employed

CREST software to carefully consider the conformation of the carbohydrate substrates along the potential energy surface. Calculations of Stille coupling of glycosyl stannanes proceed through a closed transmetallation pathway with a four-membered cyclic transition state. Fluoride additive promotes the transmetallation by forming stronger Si–F bonds in the transmetallation. Jackie-Phos ligand was found to suppress  $\beta$ -methoxy elimination by promoting reductive elimination and blocking the open site of the palladium. Substrate effects were also addressed using calculations by considering different reactivities of alpha and beta anomers, where the reactivity of alpha anomers is disfavored due to increased steric repulsions between stannanes and palladium center resulting in distortion of the carbohydrate six-member ring.

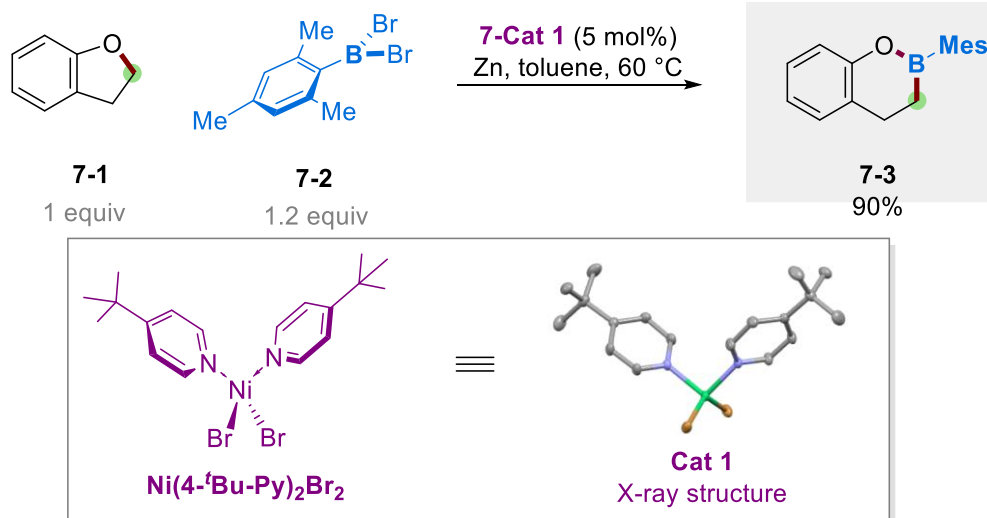
The calculations of nickel-catalyzed migratory Suzuki cross-coupling showcase an interesting reaction mechanism, with initial transmetallation followed by halogen atom transfer. Calculations indicate that the carbohydrate reacts more favorably with the Ni(I)Ph complex. The halogen atom transfer was found to be the rate determining step. Unfavorable reductive elimination at the anomeric position was found to suppress the C1-reactivity. Reductive elimination of the desired product is a facile process, and nickel radical rebound at the C2 position was found to be the stereoselectivity determining step.

## 7.0 Boron insertion into alkyl ether bonds via reductive zinc and nickel catalysis

A significant part of this chapter was published as Lyu, H.; Kevlishvili, I.; Liu, P.; Dong, G. *Science*. **2021**, 372, 175–182.

### 7.1 Introduction

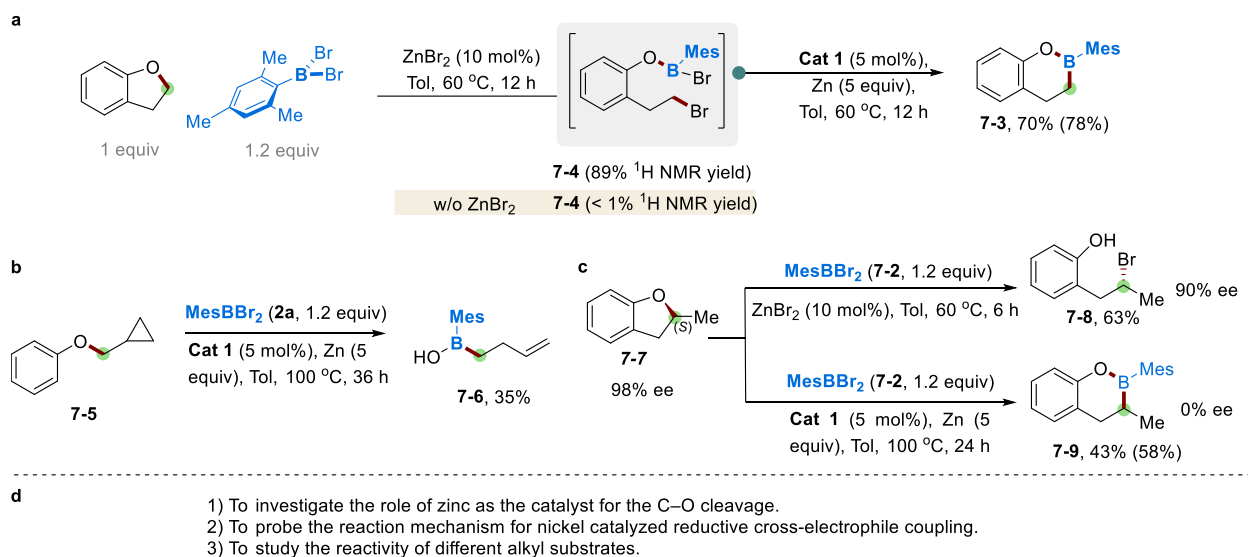
Ether moieties are a common feedstock chemical that is ubiquitous in nature.<sup>102</sup> In particular, cyclic ethers are common in a wide variety of biologically relevant molecules, such as drugs, agrochemicals, and natural products. Furthermore, due to their stability, ether moieties are often employed as protecting groups in organic synthesis.<sup>103</sup> Therefore, developing methodologies to edit ether bonds under mild conditions represents an interesting approach for late-stage functionalization in organic synthesis.<sup>104</sup> While some methods have been developed for the functionalization of ether bonds with SP<sup>2</sup> hybridized carbons under mild conditions,<sup>105</sup> the functionalization of ether bonds with SP<sup>3</sup> hybridized carbons is more limited and requires strained ethers.<sup>106</sup> Inspired by a previous example of photocatalyzed borylene insertion into a C(SP<sup>3</sup>)–O bond,<sup>107</sup> Dong's group developed a novel mild methodology for the insertion of borylene, using MesBBr<sub>2</sub> **7-2** as borylene source into an ether bond **7-1**, catalyzed by nickel catalyst (**7-Cat1**) and Zinc powder (Figure 7-1).



**Figure 7-1** Nickel/Zinc tandem catalyzed C–O bond borylation reaction

Reaction optimization studies revealed that in the absence of nickel catalyst (**7-cat1**), the borylene insertion product **7-3** was observed with <1% yield, and instead, the ring-opening product **7-4** was formed. Furthermore, the use of other reductants instead of zinc led to the loss of reactivity. Further mechanistic investigations showed that the reaction between the ether **7-1** and the MesBBr<sub>2</sub> in the absence of nickel catalyst (**7-cat1**) and zinc powder led to no reaction, while the addition of the catalytic amount of zinc dibromide led to the formation of the ring-opening product (Figure 7-1a). Furthermore, the ring-opening product **7-4** could be transformed to 2*H*-benzoxaborin product (**7-3**) under the standard conditions. These results suggest that zinc is not only involved in the reaction as reductant, but zinc dibromide also serves an important role as a catalyst for the cleavage of the C–O bond, while nickel catalyst is involved in the C–B rebound cycle.





**Figure 7-2 a. Identification of reaction intermediate. b. Radical-clock experiment. c. Control experiments with a 98% ee substrate. d. Goals of computational investigations.**

To shed more light on the C–B rebound cycle, Dong’s group also conducted radical-clock experiments using cyclopropyl substituted ether (**7-5**), which only led to the formation of a ring-opening product **7-6**, suggesting an involvement of a radical species in the mechanism. Furthermore, an experiment with a secondary 98% ee substrate **7-7** led to the full racemization during the formation of oxaborinane **7-9**. On the other hand, the ring-opening intermediate **7-8** retained enantiopurity (90% ee). These results together indicate that the radical intermediate would not be involved in initial C–O cleavage, but the nickel-catalyzed C–B rebound cycle would involve a radical intermediate.

This reaction is very interesting from a mechanistic standpoint. First, we wanted to study the role of the zinc catalyst in promoting the ring-opening reaction. Furthermore, while nickel-catalyzed reductive cross-coupling reactions between alkyl and aryl halides have been studied previously, there is a distinct lack of understanding of the reductive cross-coupling between alkyl- and boryl- halides. In this chapter, I will discuss our DFT mechanistic investigation of the boron

insertion into alkyl ether bonds. I will investigate the active form of the zinc dibromide catalyst and its role in promoting C–O bond cleavage (Figure 7-2d). I will also investigate the reductive cross-coupling reaction catalyzed by nickel and discuss different possible mechanisms that could be involved in this reaction. Put together, I will propose the most likely mechanism for this reaction.

## 7.2 Computational details

All density functional theory (DFT) calculations were carried out using Gaussian 16.<sup>14</sup> Geometries of intermediates and transition states were optimized using the dispersion-corrected B3LYP functional,<sup>15</sup> using Grimme's DFT-D3 dispersion correction,<sup>16</sup> with a mixed basis set of SDD for Ni, Zn, and 6-31G(d) for other atoms in the gas phase. Vibrational frequency calculations were performed for all the stationary points to confirm if each optimized structure is a local minimum or a transition state structure. Solvation energy corrections were calculated in toluene solvent with the SMD continuum solvation model<sup>19</sup> based on the gas-phase optimized geometries. The M06 functional<sup>17</sup> with a mixed basis set of SDD for Ni, Zn, and 6-311+G(d,p) for other atoms was used in solvation single-point energy calculations. We have considered the spin states for Ni in all the computed intermediates and transition states. The stability of wavefunction was tested for all singlet species. Open-shell singlet species were calculated using the broken-symmetry spin unrestricted formalism. The triplet of Ni(II) species **7-23**, **7-24**, **7-TS20**, NiL<sub>2</sub>Br<sub>2</sub>, and NiLBr<sub>2</sub> are more stable than a singlet, and thus their triplet structures and energies were reported. All other Ni species considered involve either singlet or doublet as the ground state. Translational entropy in toluene solution was calculated using the free-volume theory proposed by Whitesides.<sup>108</sup> The

relative energies of two key transition states, **7-TS4** and **7-TS5**, were also computed by single point energy calculations using  $\omega$ B97X-D and B3LYP-D3 functional with the SDD/6-311+G(d,p) basis set. These methods give similar relative energies between the two transition states compared to the results from the M06 method ( $\Delta\Delta G^\ddagger = 1.3, 0.9$ , and  $3.2$  kcal/mol for energies calculated using M06,  $\omega$ B97X-D, and B3LYP-D3, respectively).

## 7.3 Results and discussions

### 7.3.1 Most favorable pathway

The most favorable pathway from the calculations supported the “cleavage-then-rebound” mechanism via Zn/Ni tandem catalysis (Figure 7-3). First, MesBBr<sub>2</sub> binds to the ether oxygen assisted by the *in-situ* generated **7-1**•ZnBr<sub>2</sub> dimer (**7-10**) to form complex **7-11**, which then undergoes facile Zn-promoted bromide anion abstraction (**7-TS1**,  $\Delta G^\ddagger = 11.4$  kcal/mol) to form an ion pair **7-11**, followed by an S<sub>N</sub>2-type C–O cleavage (**7-TS2**,  $\Delta G^\ddagger = 16.2$  kcal/mol)<sup>109</sup>. The low barriers in this ring-opening process agree with the facile formation of alkyl bromide **7-4** observed experimentally. Several mechanistic pathways are possible in the subsequent Ni-catalyzed C–Br/B–Br coupling with intermediate **7-4**.<sup>110</sup> Among these, a radical chain reaction and a double oxidative addition would both be consistent with the radical clock experiment. Our DFT calculations suggest that the most favorable pathway involves the facile B–Br bond oxidative addition of **7-4** with Ni<sup>(0)</sup>(**L1**)<sub>2</sub> (**7-TS3**,  $\Delta G^\ddagger = 3.0$  kcal/mol with respect to the **7-4**•Ni(0) complex **7-13**)<sup>111</sup> to generate a Ni(II) boryl species **7-14**.<sup>112</sup> Single electron reduction of **7-14** by zinc powder forms a Ni(I) boryl complex **7-15**. From **7-15**, the C–Br bond cleavage may occur via

either the S<sub>N</sub>2-type C–Br oxidative addition (**7-TS4**,  $\Delta G^\ddagger = 18.2$  kcal/mol)<sup>113</sup> or the bromine atom transfer (**7-TS5**,  $\Delta G^\ddagger = 19.5$  kcal/mol) to form an alkyl radical **IM7**, which then recombines intramolecularly with the Ni(II) center. The comparable barriers of these transition states suggest either pathway may operate depending on the steric environment of the alkyl bromide intermediate (e.g., primary vs. secondary). For example, the reaction with the  $\alpha$ -substituted ether (**7-7**) favors the bromine-atom-transfer pathway by 4.2 kcal/mol, consistent with the complete product racemization observed in the experiment. Both C–Br bond cleavage pathways lead to transient Ni(III) species (**7-17** and **7-18**), which then undergo fast reductive elimination to form the cyclic boron-insertion product **7-3**. The resulting Ni(I)Br intermediate could be reduced by zinc to form ZnBr<sub>2</sub> and regenerate the Ni(0) catalyst.

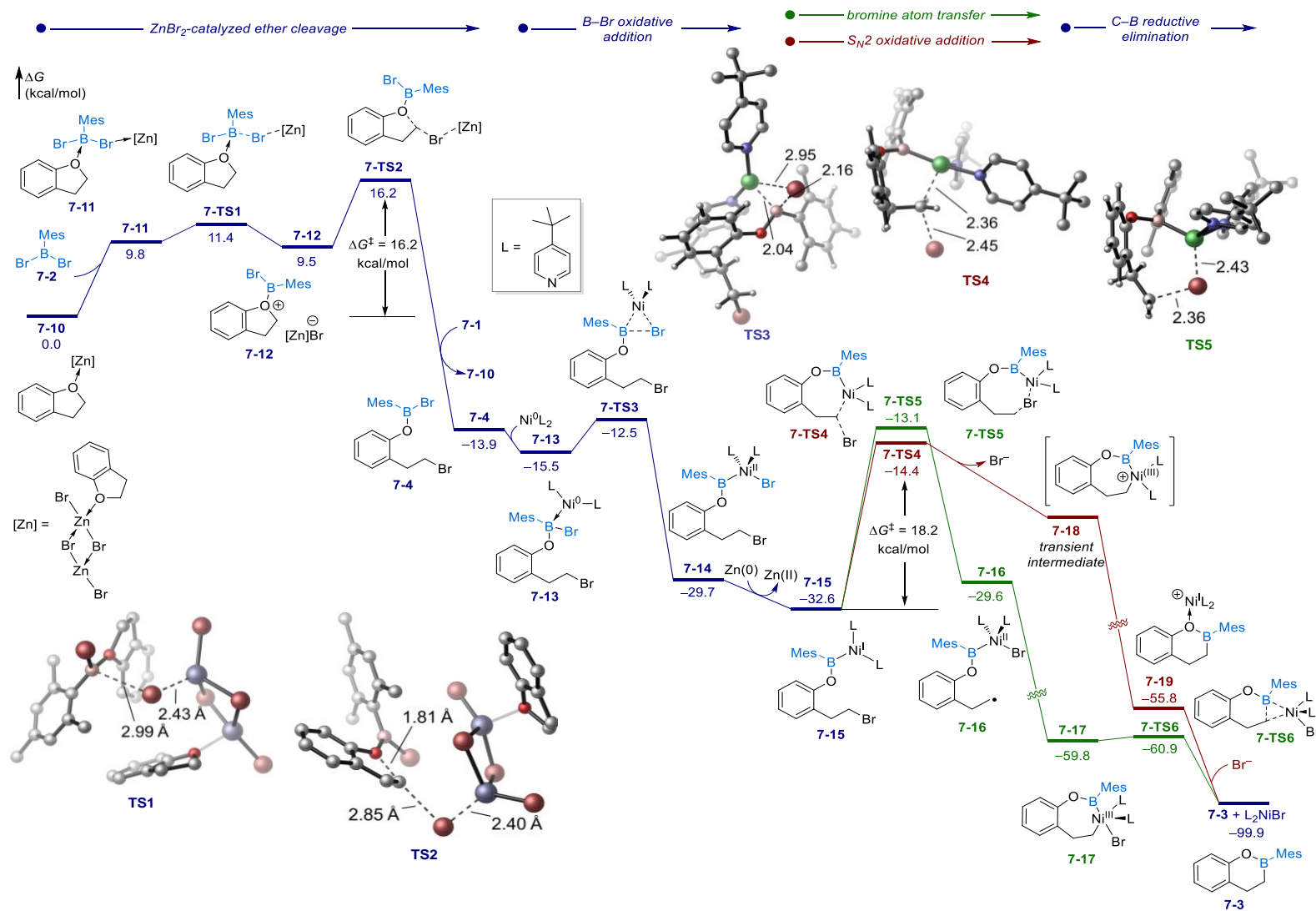
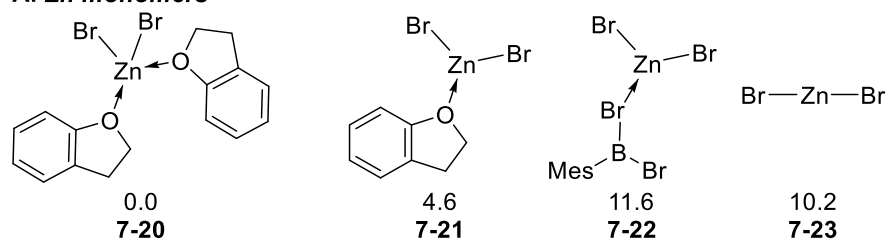


Figure 7-3 Computed energy profile of the catalytic borylation of ether 1a.

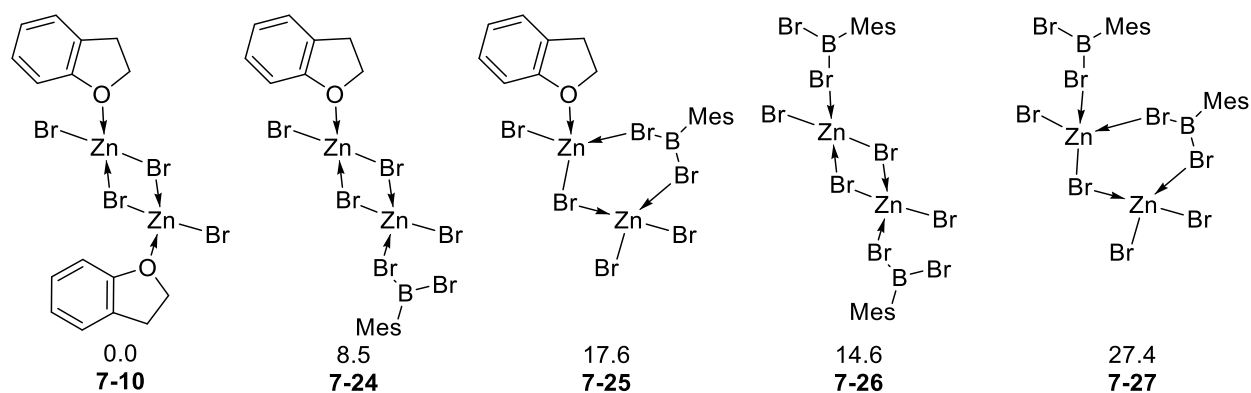
### 7.3.2 Mechanisms of the C–O cleavage (ring-opening) cycle

Because various Zn(II) species may exist under the experimental conditions, we calculated the relative energies of different monomeric (Figure 7-4A) and dimeric (Figure 7-4B) zinc species. Furthermore, we calculated the reaction energies of dimerization and tetramerization from the most stable monomeric Zn(II) and dimeric Zn(II) structures, respectively (Figure 7-5). The calculations show that the most stable zinc species (**7-10**) is a dimer where both zinc has a tetrahedral geometry, with two bridging bromides and an ether **7-1** bound to each zinc. Because dissociation of dimer **7-10** to form monomers and the dimerization of **7-10** to form tetramer **7-28** are both endergonic, **7-10** was used as the energy zero when calculating the reaction energy profile.

**A. Zn monomers**

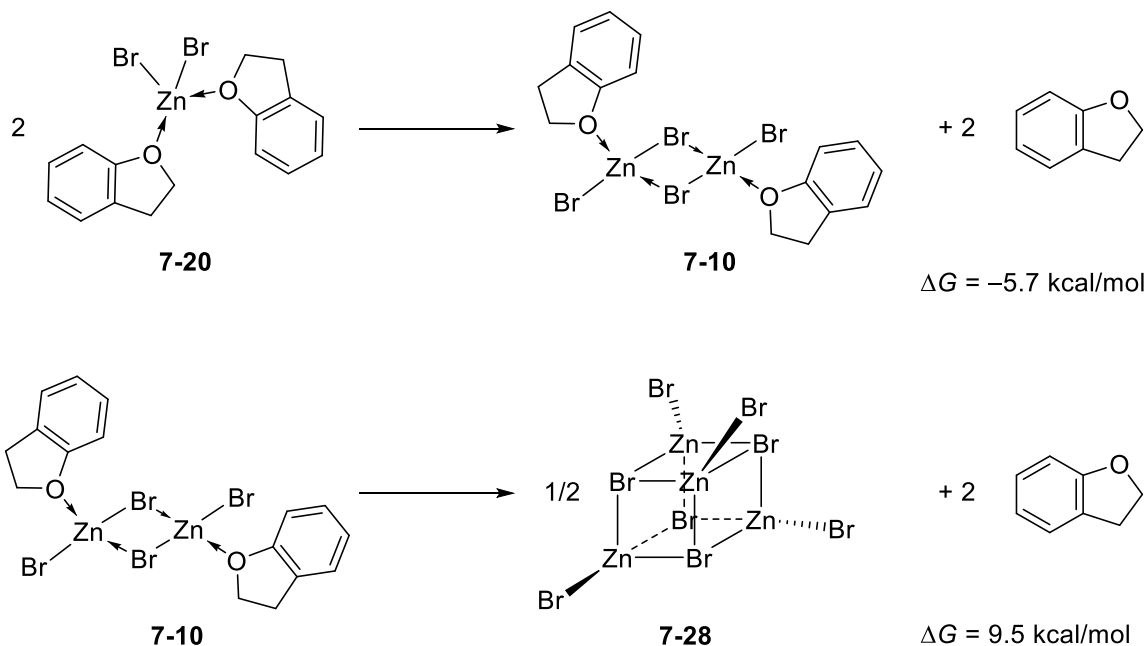


**B. Zn dimers**



**Figure 7-4 A. Gibbs free energies of monomeric zinc complexes. All energies are in kcal/mol relative to 7-20.**

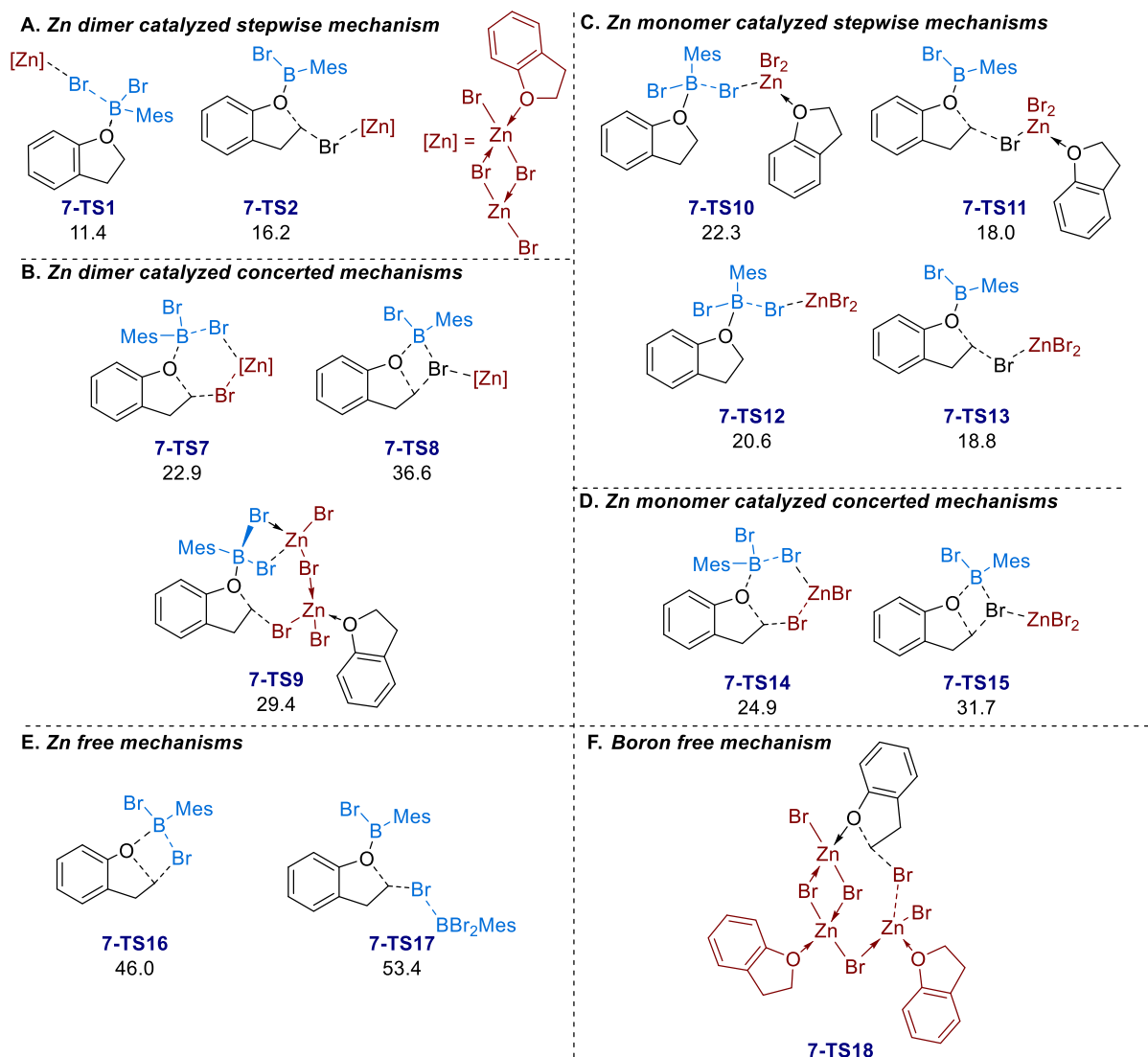
**B. Gibbs free energies of dimeric zinc complexes. All energies are in kcal/mol relative to 7-10.**



**Figure 7-5 Reaction Gibbs free energies of dimerization of 7-20 and 7-10 to form Zn(II) dimer and tetramers (7-10 and 7-28, respectively).**

The most favorable ring-opening mechanism in the reaction of **7-1** is the zinc dimer-catalyzed stepwise bromide anion abstraction/S<sub>N</sub>2 substitution pathway (Figure 7-6). Additionally, we considered the concerted ring-opening mechanisms catalyzed by the zinc dimer that can happen through different possible pathways (Figure 7-6B), including a six-membered transition state (**7-TS7**,  $\Delta G^\ddagger = 22.9$  kcal/mol), where the cleavage of Zn–Br bond occurs at the same time as the formation of the new Zn–Br bond on the same zinc atom. Additionally, zinc dimer catalyzed  $\sigma$ -bond metathesis (**7-TS8**,  $\Delta G^\ddagger = 36.6$  kcal/mol) and an eight-membered cyclic transition state (**7-TS9**,  $\Delta G^\ddagger = 29.4$  kcal/mol), where both Zn atoms are involved, were found to have higher activation energies than the stepwise pathway (**7-TS1** and **7-TS2**).





**Figure 7-6** Different mechanisms explored for the ring-opening of the ether. Activation free energies for the mechanisms where dimeric zinc is involved (A, B, F) are calculated with respect to the most stable zinc dimer (7-10). The most stable zinc monomer 7-20 is used as the energy zero in the mechanisms where monomeric zinc is the active catalyst (C, D). Separated ether 7-1 and  $\text{BBr}_2\text{Mes}$  7-2 are used as the energy zero in zinc free mechanism (E). All energies are Gibbs free energies in kcal/mol.

In addition to the zinc dimer-catalyzed mechanisms, we also considered pathways with monomeric zinc as the active catalyst. The most favorable pathway for monomeric species still

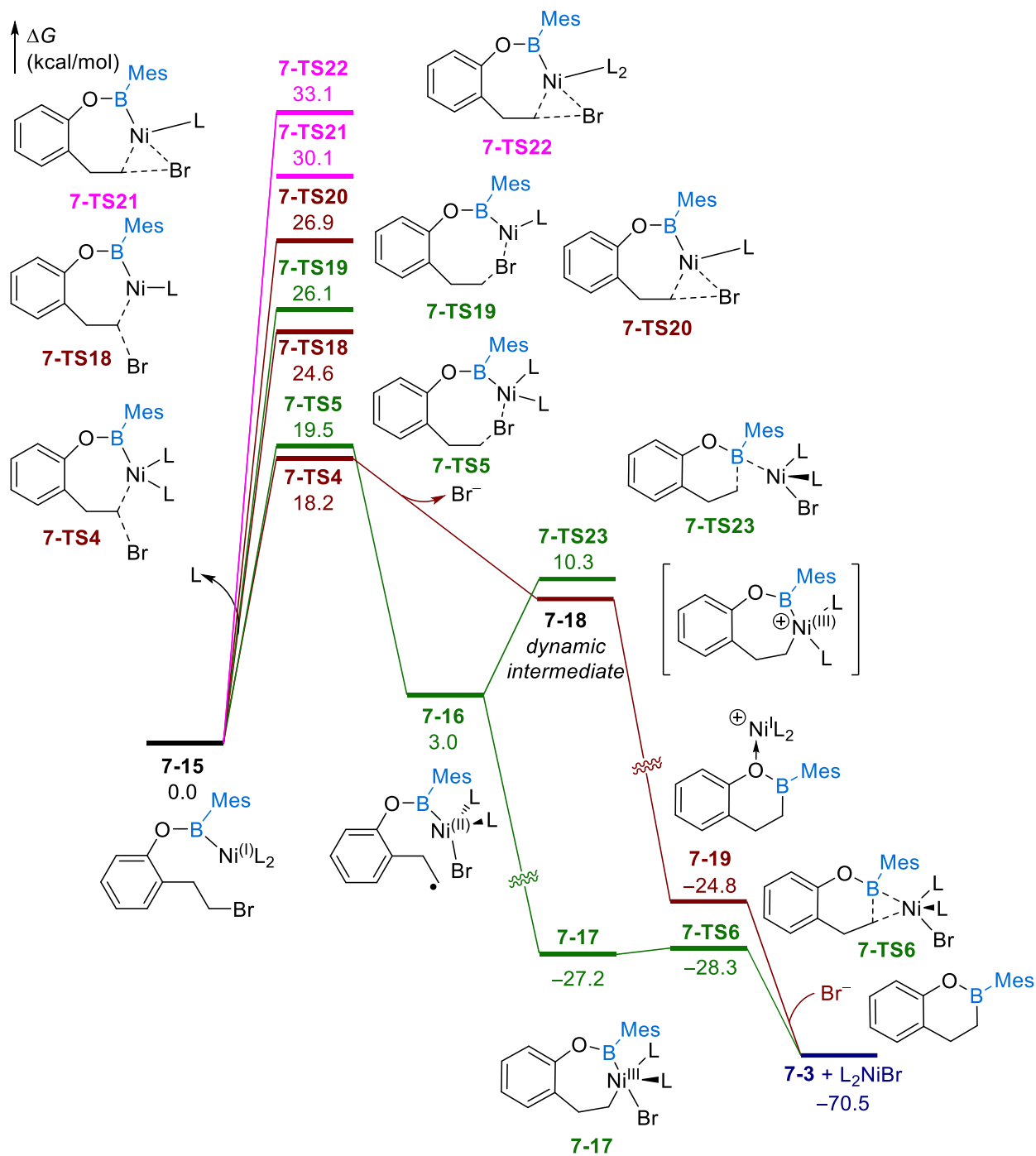
involves the stepwise bromide anion abstraction/ $S_N2$  substitution mechanism (Figure 7-6C). However, this pathway still requires an activation Gibbs free energy of 20.6 kcal/mol (**7-TS12**) relative to the most stable zinc monomer (**7-20**). Because this barrier is higher than that of the dimeric mechanism, the dimeric Zn species (**7-10**) is not only more stable than monomeric Zn but also more reactive in promoting the ring-opening of **7-1**. Therefore, these results suggest that the most favorable ring-opening pathway should involve the dimeric zinc species.

We also calculated a zinc free ring-opening mechanism (Figure 7-6E). However, this pathway has significantly higher activation energy. A boron-free zinc-catalyzed ring-opening mechanism (Figure 7-6F) also has higher activation energy (**7-TS18**,  $\Delta G^\ddagger = 33.2$  kcal/mol) than the Zn dimer-catalyzed stepwise process involving  $BBr_2Mes$  **7-2**.

### 7.3.3 C-Br cleavage and C-B bond formation mechanisms

Following the formation of the nickel (I) boryl complex (**7-15**) via C-Br oxidative addition of **7-4** to Ni(0) and single-electron reduction, there are several distinct possibilities towards the formation of the cyclized product (Figure 7-7). The two most favorable mechanisms involving the  $S_N2$ -type oxidative addition (**7-TS4**) and the bromine atom transfer (**7-TS5**)/radical rebound were discussed in the main manuscript. Additionally, the inner sphere oxidative addition of the C-Br bond via a three-membered cyclic transition state (**7-TS22**) was considered, which requires a higher barrier of 33.1 kcal/mol. Additionally, C-Br cleavage mechanisms involving monoligated nickel complexes were considered. Calculations suggest that the monoligated pathways for both the  $S_N2$  oxidative addition (**7-TS19**) and the bromine atom transfer (**7-TS20**) are both higher in energy than the corresponding bisligated transition states (**7-TS4** and **7-TS5**, respectively). The more sterically demanding three-centered oxidative addition favors the monoligated pathway (**7-**

**TS21**,  $\Delta G^\ddagger = 30.1$  kcal/mol) compared to the bisligated **7-TS22**. Nonetheless, both **TS21** and **TS22** are much higher in energy than **7-TS4** and **7-TS5**.



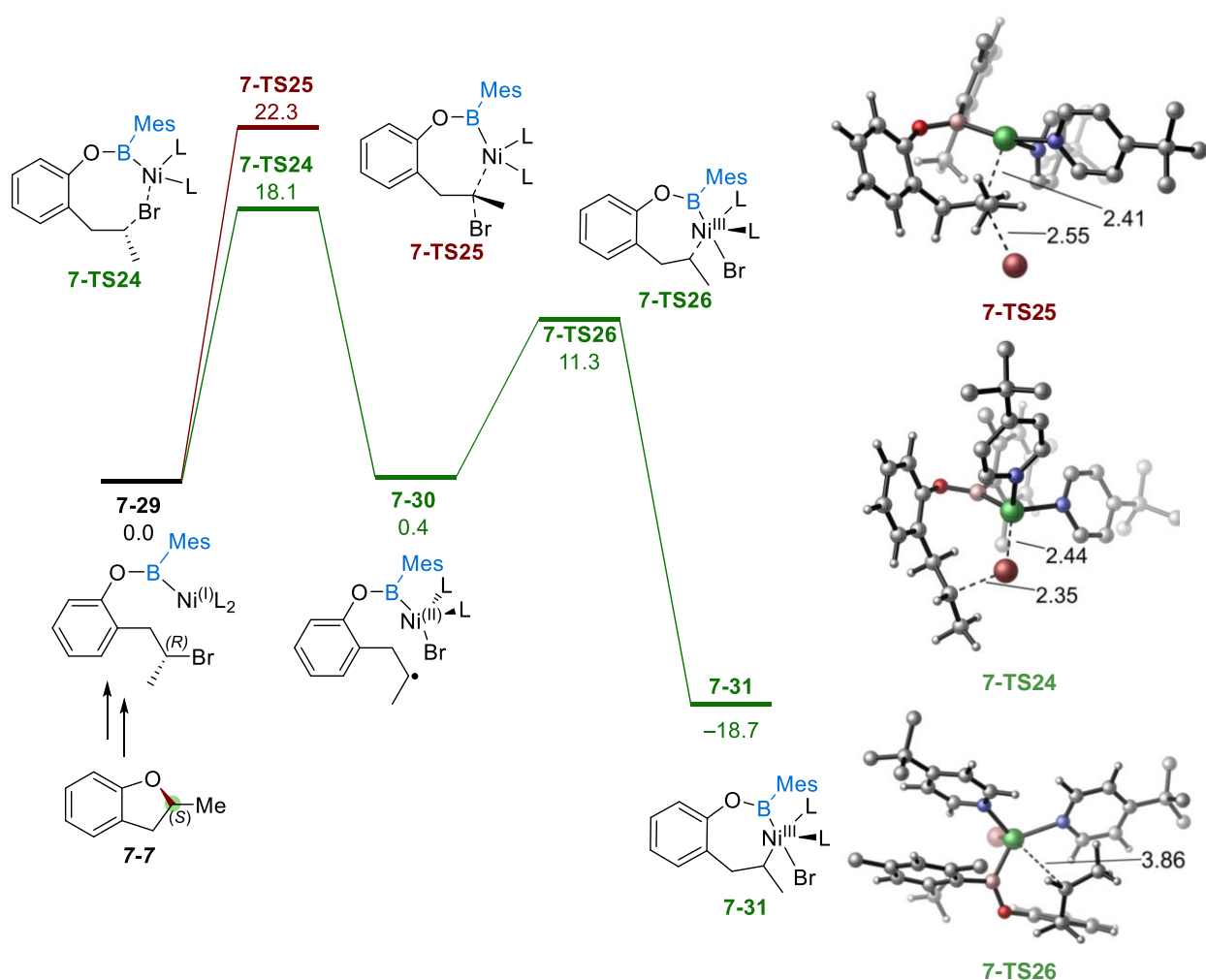
**Figure 7-7** Possible mechanisms for the C-Br cleavage and C-B bond formation from the nickel(I) boryl intermediate. All energies are relative to complex **7-15**.

Bromine atom transfer from **7-15** (via **7-TS5**) leads to the formation of the alkyl radical **7-16**. The alkyl radical in this species can recombine intramolecularly with the Ni(II) center to form a Ni(III) complex **7-17**, which is 30.2 kcal/mol more stable than **7-16**. We also considered the direct product formation via the attack of the alkyl radical on the boron through **7-TS23**. However, this pathway requires a relatively high activation energy of 10.3 kcal/mol, suggesting that it is less favorable than the radical recombination/reductive elimination pathway via the Ni(III) intermediate.

### 7.3.4 C–Br cleavage mechanism in the reaction with secondary alkyl ether

Mechanistic studies involving the reaction with the  $\alpha$ -substituted ether (**7-7**) lead to the full racemization of the product. This suggests the involvement of a radical intermediate. To validate whether our computational mechanistic studies are consistent with this experimental finding, we calculated the bromine atom transfer and the C–Br oxidative addition transition states from complex **7-29** (Figure 7-8). The bromine atom transfer from the secondary alkyl bromide (**7-TS24**) requires an 18.1 kcal/mol activation energy with respect to **7-29**, which is lower in energy than **7-TS5** – the bromine atom transfer from the primary alkyl bromide. This is due to the increased stability of the secondary alkyl radical. On the other hand, the  $S_N2$  oxidative addition **7-TS25** requires a barrier of 22.3 kcal/mol, which is significantly higher than the corresponding  $S_N2$  substitution from the primary alkyl radical – **TS4**, due to the increased steric bulk of the secondary alkyl bromide destabilizing the  $S_N2$  type transition state. Overall, the bromine atom transfer with the secondary alkyl bromide is significantly more favorable ( $\Delta\Delta G^\ddagger = 4.2$  kcal/mol) than the corresponding  $S_N2$  type transition state. Furthermore, we calculated the radical rebound transition state **7-TS26** to form the Ni(III) intermediate **7-29**. This step is sterically hindered due to

unfavorable interactions between the methyl group and pyridine ligand and requires an activation barrier of 10.9 kcal/mol, which is sufficient to allow the racemization of the chiral center via the relatively long lifetime secondary radical intermediate. These observations are consistent with the experimental mechanistic studies, which suggest the involvement of radical species in this reaction and full racemization of the product.



**Figure 7-8 C-Br cleavage mechanisms and radical rebound in the reaction with the secondary alkyl ether. All energies are in kcal/mol relative to 7-29.**

### 7.3.5 Radical chain mechanism

In addition to the double oxidative addition mechanism, another possible mechanism for the Ni-catalyzed C–B bond formation of the ring-opened intermediate **7-4** is the radical chain mechanism (Figure 7-9). The radical chain mechanism would also be consistent with the experimental mechanistic studies and thus was studied computationally.

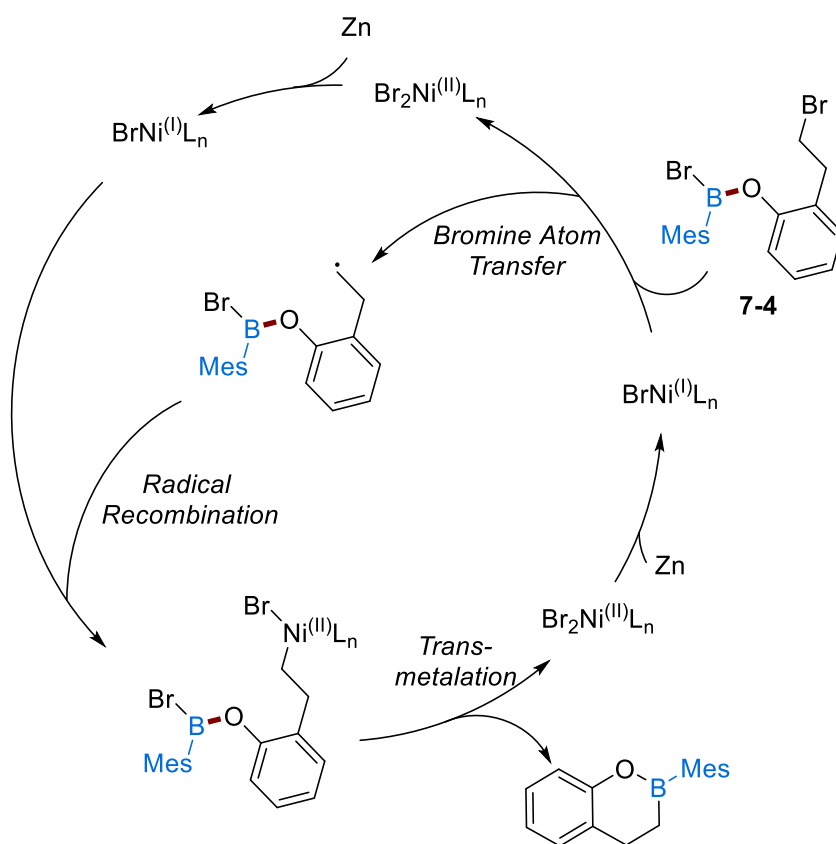
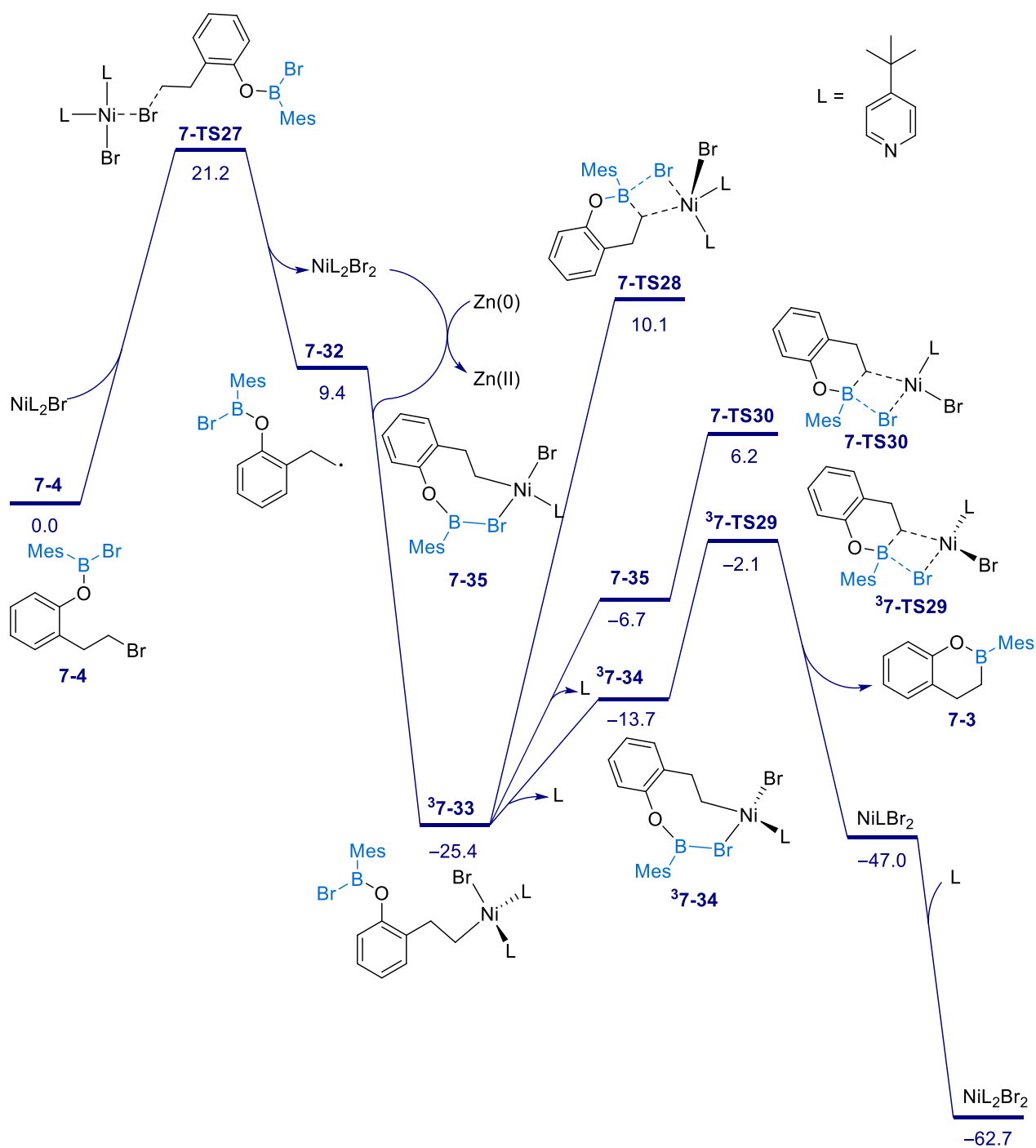


Figure 7-9 Modified nickel-catalyzed radical chain mechanism with intermediate **7-4**.

In this mechanism, we considered the initial bromine atom transfer from **7-4** to the Ni(I) bromide ( $\text{L}_2\text{NiBr}$ ) through transition state **7-TS27**, which requires an activation barrier of 21.2

kcal/mol (Scheme S5). This process requires higher activation energy than the intramolecular bromine atom transfer from the Ni(I) boryl intermediate **7-15**. Here, the intermolecular C–Br activation is disfavored entropically, as well as thermodynamically, because the conversion of **7-4** and Ni(I) bromide to Ni(II) dibromide and **7-32** is endergonic by 9.4 kcal/mol while the reaction of Ni(I) boryl species **7-15** to form Ni(II) boryl bromide (**7-16**) is only endergonic by 3.0 kcal/mol. Following the formation of the alkyl radical (**7-32**), it can recombine with Ni(I) bromide to form the triplet Ni(II) alkyl species **7-33**. Following the dissociation of one of the pyridine ligands, this intermediate can undergo an intramolecular transmetalation (**<sup>3</sup>7-TS29**) with a barrier of 23.3 kcal/mol to form the cyclization product **3a**. Here, the discussed “radical chain” mechanism is less favorable than the intramolecular C–Br cleavage via **7-TS4** or **7-TS5** due to the entropic effect in the intermolecular bromine atom transfer as well as the less favorable reaction energy in the bromine atom transfer step. These computational results suggest that the “radical chain” mechanism is less likely, and the double oxidative addition mechanism is likely to be the operative pathway for the C–B rebound cycle.



**Figure 7-10** Potential energy profile of the radical chain mechanism. All energies are Gibbs free energies in kcal/mol relative to 7-4 and  $\text{NiL}_2\text{Br}_2$ .

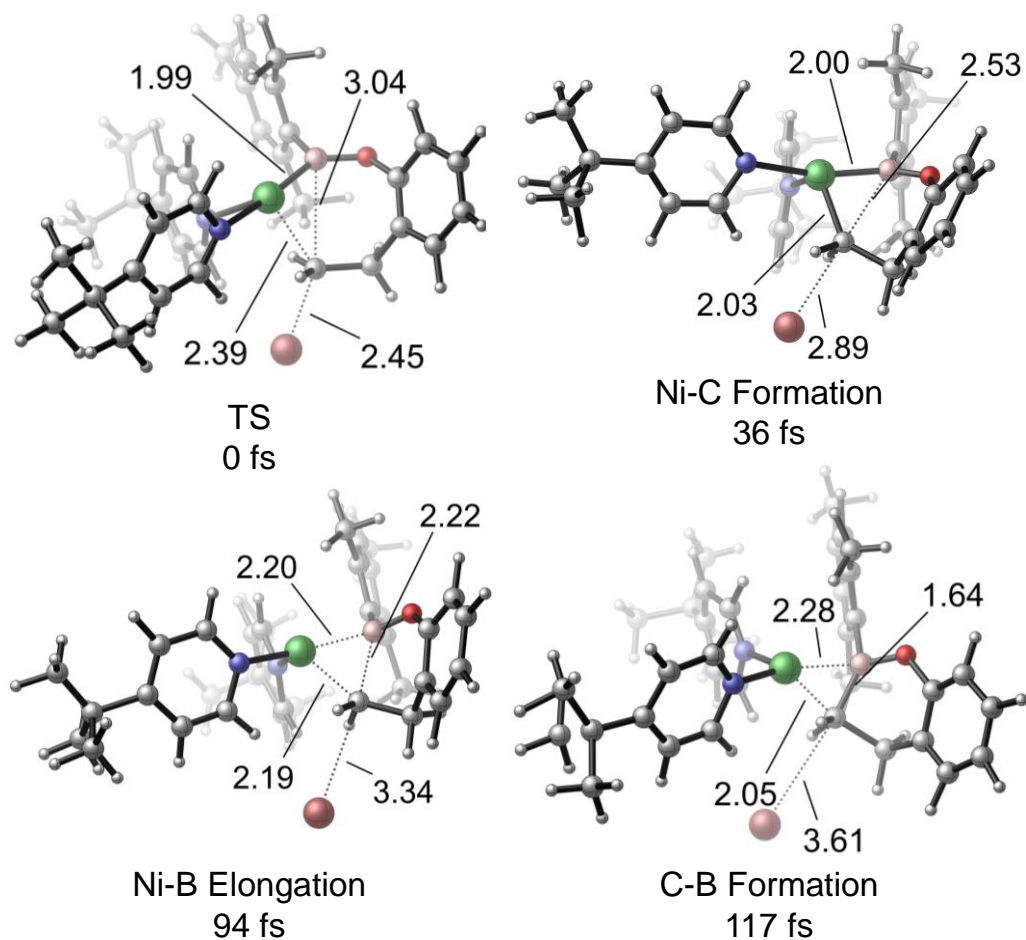


### 7.3.6 Born-Oppenheimer molecular dynamics (BOMD) trajectory simulations

Quasi-classical Born-Oppenheimer molecular dynamics (BOMD) trajectory simulations<sup>29</sup> were performed using Gaussian 16 to investigate the nature of the S<sub>N</sub>2-type oxidative addition transition state **7-TS4**. The optimized geometry of **7-TS4** and the vibration of the imaginary frequency of this transition state indicate that this transition state involves the outer sphere attack of the Ni (I) center onto the primary alkyl bromide. However, it was not immediately clear what bond formation and cleavage events will take place after this transition state. Therefore, BOMD trajectory simulations were performed to investigate the outcome of the reaction trajectories after passing through this transition state. The initial geometries and velocities of the BOMD trajectories were generated from the normal mode sampling of transition state **7-TS4** at 333.15 K. A total of 20 trajectories were generated and were propagated using the classical equations of motion with energies and forces computed using B3LYP-D3/SDD-6-31G(d). The initial kinetic energy of 0.6 kcal/mol was added along the transition vector. Starting from the transition state, the trajectory propagation was performed in the forward direction to form the product. A time step of about 0.6 fs was used in the trajectory propagation. The Hessian was updated every 12 steps. All trajectories finished within 250 fs.

The BOMD simulations indicated that the transition state proceeds with the initial formation of a transient cationic Ni(III) species **7-15**, which then rapidly undergoes a very fast C–B reductive elimination to form the cyclized product. Snapshots from a representative trajectory are shown in Figure S6 to illustrate these bond formation/cleavage events. In this trajectory, the Ni–C bond is formed first, at around 36 fs after the transition state. Then, the elongation of the Ni–C, and Ni–B bonds accompanies the shortening of the C–B bond to form the cyclized product via C–B reductive elimination. Although our DFT calculations could not successfully optimize the

cationic Ni(III) species **7-15** because the attempted geometry optimizations of this intermediate all lead to the C–B reductive elimination product, the results of the BOMD simulations suggest that this transient intermediate is indeed formed after **7-TS4**, albeit with a very short lifetime.

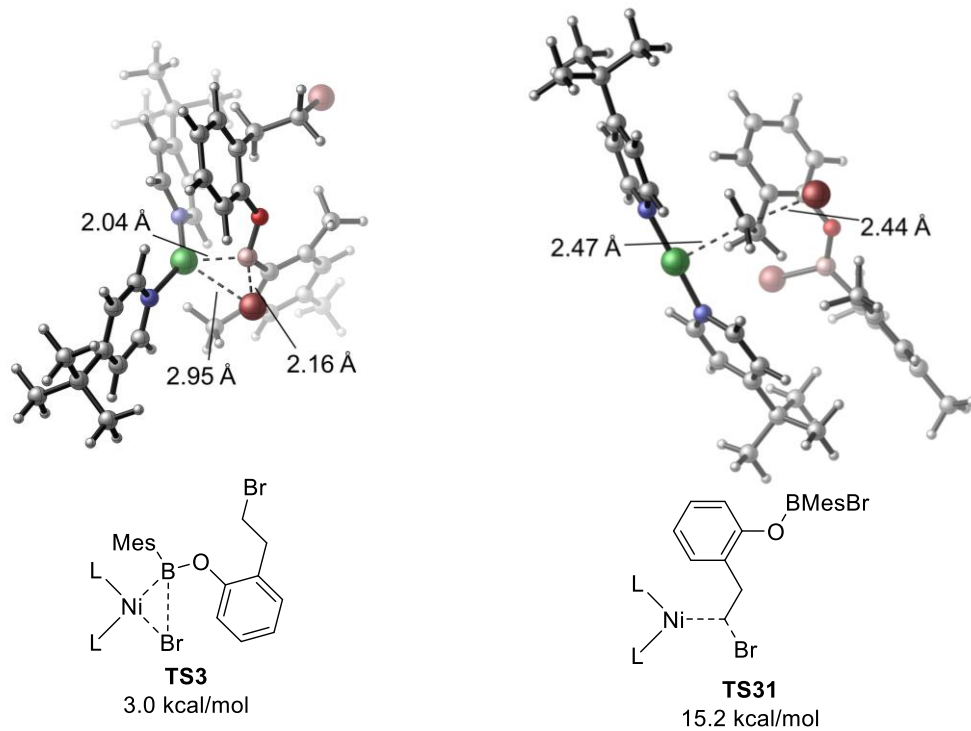


**Figure 7-11** Snapshots from a representative trajectory of the BOMD simulation from **7-TS4**.

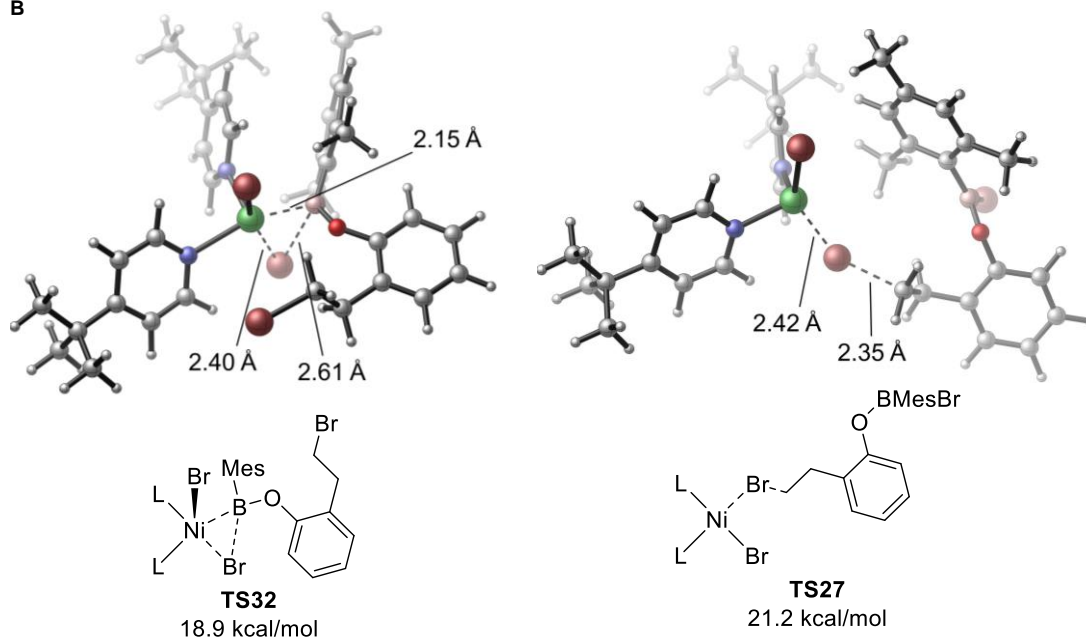
### 7.3.7 Calculations of the C–Br and B–Br cleavage of **7-4** with different nickel species

The C–B rebound mechanism can be initiated by several possible mechanisms promoted by Ni(0) or Ni(I) species. To investigate these possibilities, we calculated the different C–Br and B–Br cleavage pathways in the C–B rebound cycle with the ring-opened intermediate **7-4**. The most favorable pathway involves the oxidative addition of the B–Br bond to the Ni(0) species **7-TS3** with a low activation barrier of only 3.0 kcal/mol with respect to **7-13**. The competing pathway involving the S<sub>N</sub>2 type oxidative addition of the C–Br bond of **7-4** to Ni(0) (via **7-TS31**) is significantly less favorable with a barrier of 13.6 kcal/mol. The reaction of **7-4** with Ni(I) bromide was also considered. The oxidative addition of the B–Br bond of **7-4** to the Ni(I) bromide (**7-TS32**) requires a lower barrier ( $\Delta G^\ddagger = 18.9$  kcal/mol) than the bromine atom transfer to the Ni(I) bromide that cleaves the C–Br bond (**7-TS27**,  $\Delta G^\ddagger = 21.2$  kcal/mol). These results indicate that the B–Br cleavage is more favorable kinetically than the C–Br cleavage pathway in reactions with both Ni(0) and Ni(I) species, and the reaction with Ni(0) (**7-TS3**) is much more favorable than the reaction with Ni(I) bromide.

A



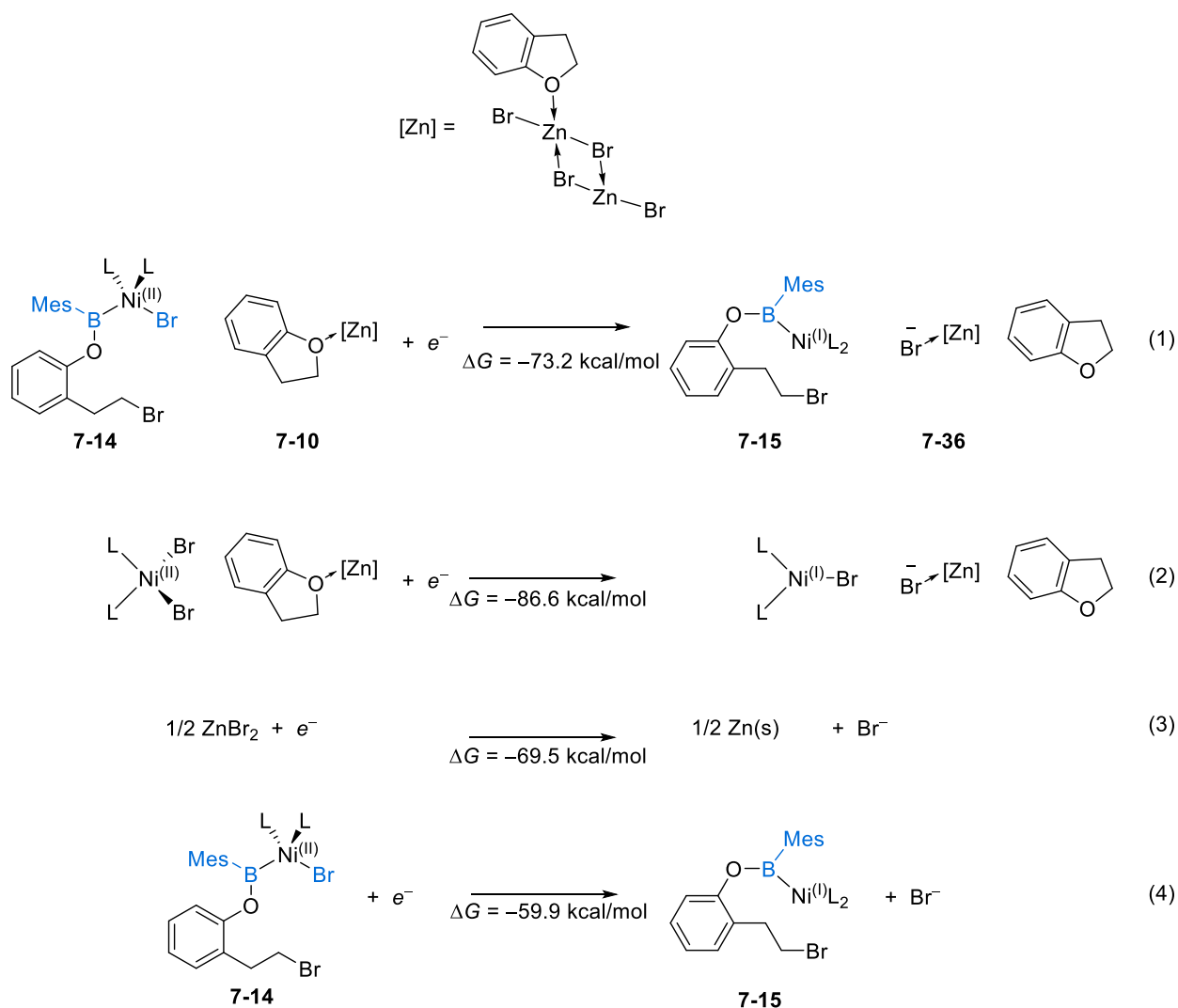
B



**Figure 7-12** Activation Gibbs free energies of the B–Br and C–Br cleavage pathways to initiate the C–B rebound cycle. **A.** Reactions with a Ni(0) species. All energies are relative to complex 7-13. **B.** Reactions with a Ni(I) bromide species. All energies are relative to the 7-4 and NiL<sub>2</sub>Br.

### 7.3.8 Calculations of the reduction of Ni species by Zn

The Gibbs free energies of the reduction of nickel(II) intermediates by zinc powder to form Ni(I) species were calculated using the following half-reactions. The reaction energies of half-reactions (1) and (2) were calculated using DFT in toluene. The Gibbs free energy of an electron ( $-0.867$  kcal/mol) was used.<sup>114</sup> We surmised that the free bromide anion generated after the reduction could be stabilized by coordination with Zn(II) species. Because our calculations indicate **7-10** is the most stable, and therefore the most abundant Zn(II) species, in our calculations of the first two half-reactions, we used **7-10** as a Lewis acid to stabilize the free bromide anion generated in these reactions. Comparison of energies of half-reactions (1) and (4) indicates that generating a free bromide anion would be much less exergonic. In the experimental half-reaction (eq. 3), we expect that the bromide anion is similarly stabilized by coordination to a Zn(II) species in the system.



**Figure 7-13 Gibbs free energies of half-reactions used to calculate the reaction energies of the Zn-mediated reduction of Ni(II) species.**

The reaction energy of half-reaction (3) was derived using the experimental standard reduction potential of Zn(s)/ZnBr<sub>2</sub> (−1.26 V vs. SHE).<sup>115</sup> We used the experimental reduction potential measured in DMA because the experimental redox potential in toluene was not available. The experimental reduction potential was converted to the absolute reduction potential according to the following equation:

$$E_{solvent}^{\ominus,abs} = E_{solvent}^{\ominus,SHE} + E_{SHE,aq}^{abs} - E_L$$

Where  $E_{SHE,aq}^{abs}$  is the absolute standard potential for the aqueous standard hydrogen electrode (4.44 V) and  $E_L$  is the interliquid (intersolvent) potential. The redox potential was obtained in DMA, but since the experimental interliquid potential was not available for DMA, we used the interliquid potential for DMF ( $E_L = 0.172$ ). Then we can calculate the absolute reduction potential

$$E_{solvent}^{\ominus,abs} = -1.26 + 4.44 - 0.172$$

$$E_{solvent}^{\ominus,abs} = 3.01 \text{ V}$$

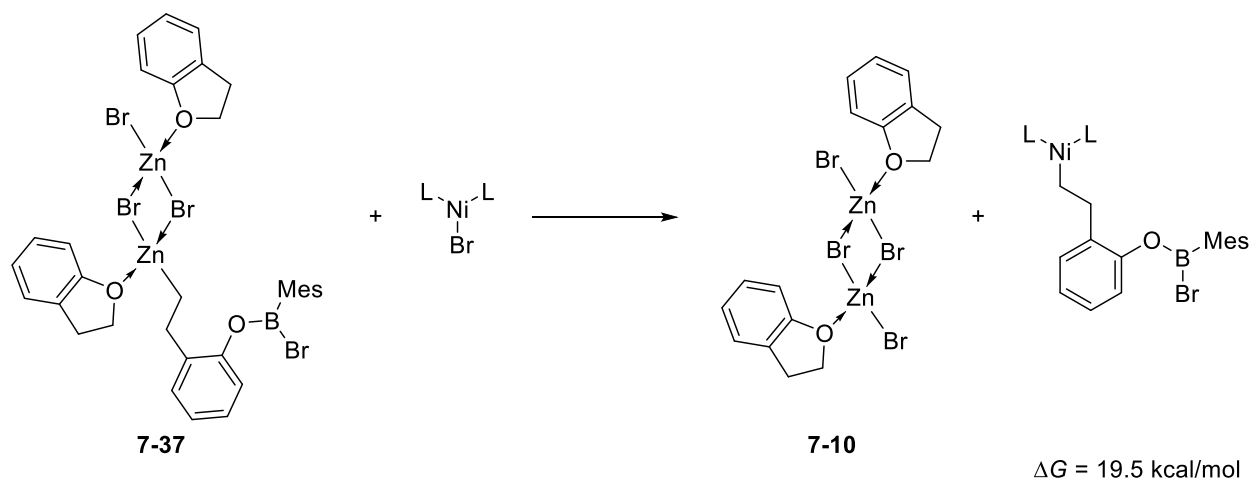
The absolute reduction potential can be converted to the Gibbs free energy by  $\Delta G = -nFE = -69.5 \text{ kcal/mol}$ .

Using the Gibbs free energies of the half-reactions shown in Scheme S6, we can calculate the thermodynamics of the reduction of nickel species. Based on our calculations, the reduction of  $L_2NiBr_2$  and **7-14** to corresponding Ni(I) species are both thermodynamically favorable using Zn.

### 7.3.9 Reaction energy of transmetalation between an organozinc and a nickel(I) bromide

A potential ring-opening mechanism with both nickel and zinc involves the reduction of the alkyl halide to form an organozinc species (**7-37**), followed by the transmetalation of the organozinc compound with Ni(I) bromide. Our calculations indicate that the transmetalation reaction is highly endergonic ( $\Delta G = 19.5 \text{ kcal/mol}$ , Figure 7-14). Considering the activation free energy of the most favorable C–B rebound mechanism is only 18.2 kcal/mol, this transmetalation

pathway is unlikely to be involved in the catalytic cycle due to the endergonicity of the transmetalation.



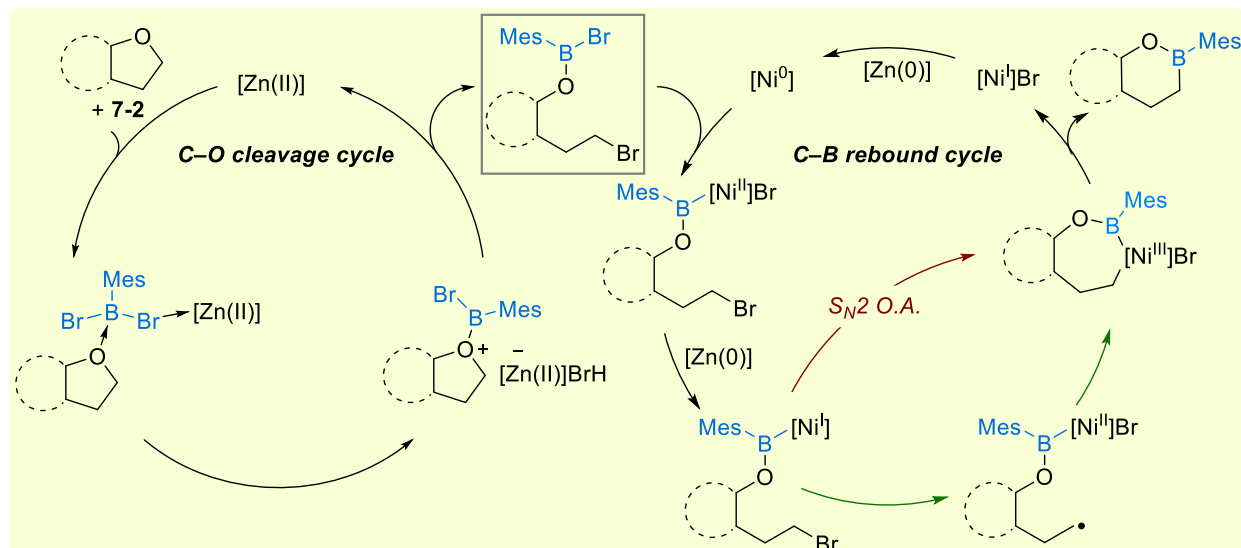
**Figure 7-14** Calculated Gibbs free energy of the transmetalation reaction between the organozinc and nickel bromide.

## 7.4 Conclusion

DFT calculations were performed to investigate the reaction mechanism for zinc and nickel tandem catalyzed boron insertion into an  $(SP^3)C-O$  bond. Based on the DFT calculations, we proposed that the initial C–O cleavage is catalyzed by zinc dimer acting as a Lewis acid. Zinc dimer promotes the formation of the B–O dative bond and promotes the dissociation of bromide from boron to form an ion pair. Following the cleavage of the B–Br bond, bromide can attack the activated C–O bond through an  $SN2$  mechanism. Following the C–O cleavage, the nickel catalyst promotes the C–B rebound reaction by initially promoting B–Br cleavage through inner-sphere oxidative addition. Following the B–Br cleavage, two different mechanisms for the C–Br cleavage



can contribute to the reaction mechanism, depending on the identity of the ether substrate (Figure 7-15). Reactions with primary substrates proceed through the  $S_N2$  type oxidative addition mechanism, and substrates that can form more stable alkyl radicals proceed through the bromine atom transfer mechanism. After oxidative addition, both pathways proceed with a facile reductive elimination to generate the final product.



**Figure 7-15** Proposed reaction mechanism based on the DFT calculations and mechanistic experiments.

## Appendix A List of publications

### Publications:

1. Ilia Kevlishvili, Katherina Murcek, Peng Liu, “Computational investigation of reactivity of amine electrophiles in CuH catalyzed hydroamination of olefins” – manuscript in preparation.
2. Gaoyuan Zhao, Wang Yao, Ilia Kevlishvili, Jaclyn N. Mauro, Peng Liu, Ming-Yu Ngai, “Nickel-Catalyzed Radical Migratory Coupling Enables C-2 Arylation of Carbohydrates” – *J. Am. Chem. Soc.* 2021 (in revision).
3. Hairong Lyu, Ilia Kevlishvili, Xuan Yu, Peng Liu, Guangbin Dong, “Boron insertion into alkyl ether bonds via zinc/nickel tandem catalysis” – *Science*, **2021**, 372, 175–182.
4. Xiaoyun He, Ilia Kevlishvili, Katherina Murcek, Peng Liu, Alexander Star, “[ $2\pi + 2\pi$ ] Photocycloaddition of Enones to Single-Walled Carbon Nanotubes Creates Fluorescent Quantum Defects” – *ACS Nano* **2021**, 15, 4833–4844.
5. Hui-Qi Ni, Ilia Kevlishvili, Pranali G. Bedekar, Joyann S. Barber, Shouliang Yang, Michelle Tran-Dubé, Andrew M. Romine, Hou-Xiang Lu, Indrawan J. McAlpine, Peng Liu, Keary M. Engle, “Anti-selective [3+2] (Hetero)annulation of non-conjugated alkenes via directed nucleopalladation” – *Nature Commun.* **2020**, 11, 6432.
6. Yuxuan Ye, Ilia Kevlishvili, Sheng Feng, Peng Liu, Stephen L. Buchwald, “Highly Enantioselective Synthesis of Indazoles with a C3-Quaternary Chiral Center Using CuH Catalysis” – *J. Am. Chem. Soc.* **2020**, 142, 10550–10556.

7. Masaki Shimoi, Ilia Kevlishvili, Takashi Watanabe, Katsuhiko Maeda, Steven J. Geib, Dennis P. Curran, Peng Liu, Tsuyoshi Taniguchi, “The Thermal Rearrangement of an NHC-Ligated 3-Benzoborepin to an NHC-Boranorcaradiene” – *Angew. Chem. Int. Ed.* **2020**, *132*, 913–919. (Co-first author)
8. Vignesh Palani, Cedric L. Hugelshofer, Ilia Kevlishvili, Peng Liu\*, and Richmond Sarpong, “A Short Synthesis of Delavatine A Unveils New Insights into Site-Selective Cross-Coupling of 3,5-Dibromo-2-pyrone” – *J. Am. Chem. Soc.* **2019**, *141*, 2652–2660.
9. Andy A. Thomas, Klaus Speck, Ilia Kevlishvili, Zhaohong Lu, Peng Liu, Stephen L. Buchwald, “Mechanistically Guided Design of Ligands That Significantly Improve the Efficiency of CuH-Catalyzed Hydroamination Reactions” *J. Am. Chem. Soc.* **2018**, *140*, 13976–13984. (Co-first author)
10. Feng Zhu, Jacob Rodriguez, Tianyi Yang, Ilia Kevlishvili, Eric Miller, Duk Yi, Sloane O’Neill, Michael J. Rourke, Peng Liu, Maciej A. Walczak, “Glycosyl Cross-Coupling of Anomeric Nucleophiles: Scope, Mechanism, and Applications in the Synthesis of Aryl C-Glycosides” *J. Am. Chem. Soc.* **2017**, *139*, 17908–17922.

## Bibliography

---

- 1 Johansson Seechurn, C. C. C.; Kitching, M. O.; Colacot, T. J.; Snieckus, V. *Angew. Chem. Int. Ed.* **2012**, *51*, 5062–5085.
- 2 Buskes, M. J.; Blanco, M.-J. *Molecules*, **2020**, *25*, 3493.
- 3 Chen, F.; Wang, T.; Jiao, N. *Chem. Rev.* **2014**, *114*, 8613–8661.
- 4 Trowbridge, A.; Walton, S. M.; Gaunt, M. J. *Chem. Rev.* **2020**, *120*, 2613–2692.
- 5 Vitaku, E.; Smith, D. T.; Njardarson, J. T. *J. Med. Chem.* **2014**, *57*, 10257–10274.
- 6 (a) Tang, W.; Zhang, X. *Chem. Rev.*, **2003**, *103*, 3029–3070. (b) Fu, W.; Tang, W. *ACS Catal.*, **2016**, *6*, 4814–4858.
- 7 (a) Cesar, V., Bellemin-Laponnaz, S.; Gade, L. H. *Chem. Soc. Rev.*, **2004**, *33*, 619–636. (b) Diez-Gonzalez, S.; Nolan, S. P. *Coord. Chem. Rev.*, **2007**, *251*, 874–883.
- 8 (a) Shaughnessy, K. H.; Hartwig, J. F. *J. Am. Chem. Soc.*, **2001**, *123*, 2677–2678. (b) Sigman, M. S.; Jacobsen, E. N. *J. Am. Chem. Soc.*, **1998**, *120*, 4901–4902. (c) Kieseewetter, J.; Kaminsky, W. *Chem. Eur. J.*, **2003**, *9*, 1750–1758.
- 9 Cheng, G.-J.; Zhang, X.; Chung, L. W.; Xu, L.; Wu, Y.-D. *J. Am. Chem. Soc.* **2015**, *137*, 1706–1725.
- 10 (a) Noyori, R. *Angew. Chem. Int. Ed.*, **2002**, *41*, 2008–2022. (b) Martin, R.; Buchwald, S. L.: *Acc. Chem. Res.*, **2008**, *41*, 1461–1473. (c) Fu, G. C. *Acc. Chem. Res.*, **2008**, *41*, 1555–1564. (d) Tolman, C. A. *Chem. Rev.*, **1977**, *77*, 313–348.
- 11 (a) Kui, S. C. F.; Zhu, N.; Chan, M. C. W. *Angew. Chem. Int. Ed.* **2003**, *42*, 1628 – 1632. (b) Mitani, M.; Mohri, J.; Yoshida, Y.; Saito, J.; Ishii, S.; Tsuru, K.; Matsui, S.; Furuyama, R.; Nakano, T.; Tanaka, H.; Kojoh, S.;

---

Matsugi, T.; Kashiwa, N.; Fujita, T. *J. Am. Chem. Soc.*, **2002**, *124*, 3327–3336. (c) Furuyama, R.; Saito, J.; Ishii, S.; Makio, H.; Mitani, M.; Tanaka, H.; Fujita, T. *J. Organomet. Chem.*, **2005**, *690*, 4398–4413.

12 (a) Wagner, J. P.; Schreiner, P. R. *Angew. Chem. Int. Ed.*, **2015**, *54*, 12274–12296. (b) Lyngvi, E.; Sanhueza, I. A.; Schoenebeck, F. *Organometallics*, **2015**, *34*, 805–812. (c) Wolters, L. P.; Koekkoek, R.; Bickelhaupt, F. M. *ACS Catal.*, **2015**, *5*, 5766–5775.

13 Gaussian 09, Revision D.01 Frisch, M. J.; Trucks, G. W.; Schlegel, H. B.; Scuseria, G. E.; Robb, M. A.; Cheeseman, J. R.; Scalmani, G.; Barone, V.; Mennucci, B.; Petersson, G. A.; Nakatsuji, H.; Caricato, M.; Li, X.; Hratchian, H. P.; Izmaylov, A. F.; Bloino, J.; Zheng, G.; Sonnenberg, J. L.; Hada, M.; Ehara, M.; Toyota, K.; Fukuda, R.; Hasegawa, J.; Ishida, M.; Nakajima, T.; Honda, Y.; Kitao, O.; Nakai, H.; Vreven, T.; Montgomery, J. A., Jr.; Peralta, J. E.; Ogliaro, F.; Bearpark, M.; Heyd, J. J.; Brothers, E.; Kudin, K. N.; Staroverov, V. N.; Kobayashi, R.; Normand, J.; Raghavachari, K.; Rendell, A.; Burant, J. C.; Iyengar, S. S.; Tomasi, J.; Cossi, M.; Rega, N.; Millam, N. J.; Klene, M.; Knox, J. E.; Cross, J. B.; Bakken, V.; Adamo, C.; Jaramillo, J.; Gomperts, R.; Stratmann, R. E.; Yazyev, O.; Austin, A. J.; Cammi, R.; Pomelli, C.; Ochterski, J. W.; Martin, R. L.; Morokuma, K.; Zakrzewski, V. G.; Voth, G. A.; Salvador, P.; Dannenberg, J. J.; Dapprich, S.; Daniels, A. D.; Farkas, Ö.; Foresman, J. B.; Ortiz, J. V.; Cioslowski, J.; Fox, D. J. Gaussian, Inc., Wallingford, CT, 2009.

14 Gaussian 16, Revision C.01, Frisch, M. J.; Trucks, G. W.; Schlegel, H. B.; Scuseria, G. E.; Robb, M. A.; Cheeseman, J. R.; Scalmani, G.; Barone, V.; Petersson, G. A.; Nakatsuji, H.; Li, X.; Caricato, M.; Marenich, A. V.; Bloino, J.; Janesko, B. G.; Gomperts, R.; Mennucci, B.; Hratchian, H. P.; Ortiz, J. V.; Izmaylov, A. F.; Sonnenberg, J. L.; Williams-Young, D.; Ding, F.; Lipparini, F.; Egidi, F.; Goings, J.; Peng, B.; Petrone, A.; Henderson, T.; Ranasinghe, D.; Zakrzewski, V. G.; Gao, J.; Rega, N.; Zheng, G.; Liang, W.; Hada, M.; Ehara, M.; Toyota, K.; Fukuda, R.; Hasegawa, J.; Ishida, M.; Nakajima, T.; Honda, Y.; Kitao, O.; Nakai, H.; Vreven, T.; Throssell, K.; Montgomery, J. A., Jr.; Peralta, J. E.; Ogliaro, F.; Bearpark, M. J.; Heyd, J. J.; Brothers, E. N.; Kudin, K. N.; Staroverov, V. N.; Keith, T. A.; Kobayashi, R.; Normand, J.; Raghavachari, K.; Rendell, A. P.; Burant, J. C.; Iyengar, S. S.; Tomasi, J.; Cossi, M.; Millam, J. M.; Klene, M.; Adamo, C.; Cammi, R.; Ochterski, J. W.; Martin, R. L.; Morokuma, K.; Farkas, O.; Foresman, J. B.; Fox, D. J. Gaussian, Inc., Wallingford, CT, 2016.

- 
- 15 (a) Lee, C.; Yang, W.; Parr, R. G. *Phys. Rev. B* **1988**, *37*, 785; (b) Becke, A. D. *J. Chem. Phys.* **1993**, *98*, 5648–5652.
- 16 Grimme, S.; Antony, J.; Ehrlich, S.; Krieg, H. *J. Chem. Phys.* **2010**, *132*, 154104.
- 17 Zhao, Y.; Truhlar, D. G. *Theor. Chem. Acc.* **2008**, *120*, 215.
- 18 Chai, J. D.; Head-Gordon, M. *Phys. Chem. Chem. Phys.* **2008**, *10*, 6615–6620.
- 19 Marenich, A. V.; Cramer, C. J.; Truhlar, D. G. *J. Phys. Chem. B* **2009**, *113*, 6378–6396.
- 20 (a) Cossi, M.; Rega, N.; Scalmani, G.; Barone, V. *J. Comp. Chem.*, **2003**, *24*, 669–681. (b) Barone, V.; Cossi, M. *J. Phys. Chem. A*, **1998**, *102*, 1995–2001.
- 21 (a) Horn, P. R.; Head-Gordon, M. *J. Chem. Phys.* **2016**, *144*, 084118. (b) Horn, P. R.; Mao, Y.; Head-Gordon, M. *J. Chem. Phys.* **2016**, *144*, 114107. (c) Horn, P. R.; Mao, Y.; Head-Gordon, M. *Phys. Chem. Chem. Phys.*, **2016**, *18*, 23067–23079.
- 22 Shao, Y.; Gan, Z.; Epifanovsky, E.; Gilbert, A. T. B.; Wormit, M.; Kussmann, J.; Lange, A. W.; Behn, A.; Deng, J.; Feng, X.; Ghosh, D.; Goldey, M.; Horn, P. R.; Jacobson, L. D.; Kaliman, I.; Khaliullin, R. Z.; Kus, T.; Landau, A.; Liu, J.; Proynov, E. I.; Rhee, Y. M.; Richard, R. M.; Rohrdanz, M. A.; Steele, R. P.; Sundstrom, E. J.; Woodcock, H. L.; Zimmerman, P. M.; Zuev, D.; Albrecht, B.; Alguire, E.; Austin, B.; Beran, G. J. O.; Bernard, Y. A.; Berquist, E.; Brandhorst, K.; Bravaya, K. B.; Brown, S. T.; Casanova, D.; Chang, C.-M.; Chen, Y.; Chien, S. H.; Closser, K. D.; Crittenden, D. L.; Diedenhofen, M.; DiStasio, R. A.; Do, H.; Dutoi, A. D.; Edgar, R. G.; Fatehi, S.; Fusti-Molnar, L.; Ghysels, A.; Golubeva-Zadorozhnaya, A.; Gomes, J.; Hanson-Heine, M. W. D.; Harbach, P. H. P.; Hauser, A. W.; Hohenstein, E. G.; Holden, Z. C.; Jagau, T.-C.; Ji, H.; Kaduk, B.; Khistyayev, K.; Kim, J.; Kim, J.; King, R. A.; Klunzinger, P.; Kosenkov, D.; Kowalczyk, T.; Krauter, C. M.; Lao, K. U.; Laurent, A. D.; Lawler, K. V.; Levchenko, S. V.; Lin, C. Y.; Liu, F.; Livshits, E.; Lochan, R. C.; Luenser, A.; Manohar, P.; Manzer, S. F.; Mao, S.-P.; Mardirossian, N.; Marenich, A. V.; Maurer, S. A.; Mayhall, N. J.; Neuscamman, E.; Oana, C. M.; Olivares-Amaya, R.; O'Neill, D. P.; Parkhill, J. A.; Perrine, T. M.; Peverati, R.; Prociuk, A.; Rehn, D. R.; Rosta, E.; Russ, N. J.; Sharada, S. M.; Sharma, S.; Small, D. W.; Sodt, A. *Mol. Phys.* **2015**, *113*, 184–215.

- 
- 23 Khaliullin, R. Z.; Cobar, E. A.; Lochan, R. C.; Bell, A. T.; Head-Gordon, M. *J. Phys. Chem. A* **2007**, *111*, 8753-8765.
- 24 Ess, D. H.; Nielsen, R. J.; Goddard, W. A.; Periana, R. A. *J. Am. Chem. Soc.*, **2009**, *131*, 11686–11688.
- 25 (a) Grimme, S. *J. Chem. Theory Comput.* **2019**, *15*, 2847-2862; (b) Pracht, P.; Bohle, F.; Grimme, S., *Phys. Chem. Chem. Phys.* **2020**, *22*, 7169-7192.
- 26 (a) Grimme, S.; Bannwarth, C.; Shushkov, P. *J. Chem. Theory Comput.* **2017**, *13*, 1989-2009; (b) Bannwarth, C.; Ehlert, S.; Grimme, S. *J. Chem. Theory Comput.* **2019**, *15*, 1652-1671.
- 27 Bickelhaupt, F. M.; Houk, K. N. *Angew. Chem., Int. Ed.* **2017**, *56*, 10070–10086
- 28 Falivine, L.; Credendino, R.; Poater, A.; Petta, A.; Serra, L.; Oliva, R.; Scarano, V.; Cavallo, L. *Organometallics*, **2016**, *35*, 2286–2293.
- 29 (a) Helgaker, T.; Uggerud, E.; Jensen, H. J. A. *Chem. Phys. Lett.* **1990**, *173*, 145–150. (b) Uggerud, E.; Helgaker, T. *J. Am. Chem. Soc.* **1992**, *114*, 4265–4268.
- 30 Oyola, Y.; Singleton, D. A. *J. Am. Chem. Soc.* **2009**, *131*, 3130–3131.
- 31 Black, K.; Liu, P.; Xu, L.; Doubleday, C.; Houk, K. N. *Proc. Natl. Acad. Sci. U. S. A.* **2012**, *109*, 12860–12865.
- 32 Dewick, P. M. *Medicinal natural products: a biosynthetic approach*, 3<sup>rd</sup> edition. ed., Wiley, Chichester, West Sussex, England; New York, NY, USA, 2009.
- 33 Zhu, S.; Niljianskul, N.; Buchwald, S.L. *J. Am. Chem. Soc.* **2013**, *135*, 15746–15749.
- 34 (a) Pirnot, M.T.; Wang, Y.M.; Buchwald, S.L. *Angew. Chem. Int. Ed.* **2016**, *55*, 48–57. (b) Zhu, S.; Buchwald, S.L. *J. Am. Chem. Soc.* **2014**, *136*, 15913–15916.
- 35 Niljianskul, N.; Zhu, S.; Buchwald, S.L. *Angew. Chem. Int. Ed.* **2015**, *54*, 1638–1641.
- 36 (a) Shi, S.L.; Buchwald, S.L. *Nat Chem.* **2015**, *7*, 38–44. (b) Severin, R.; Doye, S. *Chem. Soc. Rev.* **2007**, *36*, 1407–1420.

- 
- 37 (a) Friis, S.D.; Pirnot, M.T.; Dupuis, L.N.; Buchwald, S.L. *Angew. Chem. Int.* **2017**, *56*, 7242–7246. (b) Yang, Y.; Shi, S.L.; Niu, D.; Liu, P.; Buchwald, S.L. *Science*. **2015**, *349*, 62–66.
- 38 Bandar, J.S.; Pirnot, M.T.; Buchwald, S.L. *J. Am. Chem. Soc.* **2015**, *137*, 14812–14818.
- 39 For representative examples of aminoboration, see: Xi, Y.; Hartwig, J.F. *J. Am. Chem. Soc.* **2017**, *139*, 12758–12772. (b) Lee, J.; Radomkit, S.; Torker, S.; Pozo, J.D.; Hoveyda, A.H. *Nat. Chem.* **2017**, *10*, 99–108.
- 40 Lu, G.; Liu, R.Y.; Yang, Y.; Fang, C.; Lambrecht, D.S.; Buchwald, S.L.; Liu, P. *J. Am. Chem. Soc.* **2017**, *139*, 16548–16555.
- 41 Echeverria, J.; Aullon, G.; Danovich, D.; Shaik, S.; Alvarez, S. *Nature Chem.*, **2011**, *3*, 323–330.
- 42 (a) Neel, A.J.; Hilton, M.J.; Sigman, M.S.; Toste, F.D. *Nature* **2017**, *543*, 637–646. (b) Wagner, J. P.; Schreiner, P. R. *Angew. Chem., Int. Ed.* **2015**, *54*, 12274–12296.
- 43 (a) Xu, X.; Liu, P.; Lesser, A.; Sirois, L. E.; Wender, P. A.; Houk, K. N. *J. Am. Chem. Soc.* **2012**, *134*, 11012–11025. (b) Wolters, L. P.; Koekkoek, R.; Bickelhaupt, F. M. *ACS Catal.* **2015**, *5*, 5766–5775. (c) Lyngvi, E.; Sanhueza, I. A.; Schoenebeck, F. *Organometallics* **2015**, *34*, 805–812. (d) Meyer, T. H.; Liu, W.; Feldt, M.; Wuttke, A.; Mata, R. A.; Ackermann, L. *Chem. - Eur. J.* **2017**, *23*, 5443–5447. (e) Cundari, T. R.; Jacobs, B. P.; MacMillan, S. N.; Wolczanski, P. T. *Dalton Trans.*, **2018**, *47*, 6025–6030.
- 44 (a) Hale, L.V.A.; Szymczak, N.K. *ACS Catal.* **2018**, *8*, 6446–6461. (b) Chattopadhyay, B.; Dannatt, J.E.; Sanctis, I.L.A.D.; Gore, K.A.; Maleczka, R.E.; Singleton, D.A.; Smith, M.R. *J. Am. Chem. Soc.* **2017**, *139*, 7864–7871. (c) Davis, H.J.; Mihai, M.T.; Phipps, R.J. *J. Am. Chem. Soc.* **2016**, *138*, 12759–12762 (d) Kunitobu, Y.; Ida, H.; Nishi, M.; Kanai, M. *Nat. Chem.* **2015**, *7*, 712–717.
- 45 (a) Luo, S.X.; Engle, K.M.; Dong, X.; Heji, A.; Takase, M.K.; Henling, L.M.; Liu, P.; Houk, K.N.; Grubbs, R.H. *ACS Catal.* **2018**, *8*, 4600–4611. (b) Burrows, L.C.; Jesikiewicz, L.T.; Lu, G.; Geib, S.J.; Liu, P.; Brummond, K.M. *J. Am. Chem. Soc.* **2017**, *139*, 15022–15032.
- 46 (a) Straker, R. N.; Mekareeya, A.; Paton, R. S.; Anderson, E. A. *Nat. Commun.* **2016**, *7*, 10109–10118. (b) Kwon, D.; Fuller, J. T.; Kilgore, U. J.; Sydora, O. L.; Bischof, S. M.; Ess, D. H. *ACS Catal.*, **2018**, *8*, 1138–1142.



---

(c) Nielsen, M. C.; Bonney, K. J.; Schoenebeck, F. *Angew. Chem. Int. Ed.* **2014**, *53*, 5903–5906. (d) Bernales, V.; League, A. B.; Li, Z.; Schweitzer, N. M.; Peters, A. W.; Carlson, R. K.; Hupp, J. T.; Cramer, C. J.; Farha, O. K.; Gagliardi, L. *J. Phys. Chem. C* **2016**, *120*, 23576–23583. (e) Sinha, I.; Lee, Y.; Bae, C.; Tussupbayev, S.; Lee, Y.; Seo, M.; Kim, J.; Baik, M.; Lee, Y.; Kim, H. *Catal. Sci. Technol.*, **2017**, *7*, 4375–4387. (f) Wang, Y.; Wang, J.; Su, J.; Huang, F.; Jiao, L.; Liang, Y.; Yang, D.; Zhang, S.; Wender, P. A.; Yu, Z.-X. *J. Am. Chem. Soc.* **2007**, *129*, 10060–10061. (g) Occhipinti, G.; Koudriavtsev, V.; Törnroos, K. W.; Jensen, V. R. *Dalton Trans.* **2014**, *43*, 11106–11117.

47 (a) Iwamoto, H.; Imamoto, T.; Ito, H. *Nat. Commun.* **2018**, *9*, 2290. (b) Guan, Y.; Wheeler, S. E. *Angew. Chem. Int. Ed.* **2017**, *56*, 9101–9105. (c) Poree, C.; Schoenebeck, F. *Acc. Chem. Res.*, **2017**, *50*, 605–608.

48 Sperger, T.; Sanhueza, I. A.; Schoenebeck, F. *Acc. Chem. Res.*, **2016**, *49*, 1311–1319.

49 Ribeiro, R. F.; Marenich, A. V.; Cramer, C. J.; Truhlar, D. G. *J. Phys. Chem. B* **2011**, *115*, 14556–14562.

50 (a) Peverati, R.; Truhlar, D. G. *J. Phys. Chem. Lett.*, **2011**, *21*, 2810–2817. (b) Burns, L. A.; Vázquez-Mayagoitia, A.; Sumpter, B. G.; Sherrill, C. D. *J. Chem. Phys.* **2011**, *134*, 084107.

51 (a) Distasio, R. A., Jr; Head-Gordon, M. *Mol. Phys.* **2007**, *105*, 1073–1083. (b) Steele, R. P.; DiStasio, R. A.; Shao, Y.; Kong, J.; Head-Gordon, M. *J. Chem. Phys.* **2006**, *125*, 074108.

52 Thomas, A. A.; Speck, K.; Kevlishvili, I.; Lu, Z.; Liu, P.; Buchwald, S. L. *J. Am. Chem. Soc.* **2018**, *140*, 13976–13984.

53 Tobisch, S. *Chem. Eur. J.* **2016**, *22*, 8290–8300.

54 a) Reed, A. E.; Weinhold, F. *J. Chem. Phys.* **1985**, *83*, 1736–1740; b) Reed, A. E.; Weinhold, F. *Isr. J. Chem.* **1991**, *31*, 277–285; c) Reed, A. E.; Curtiss, L. A.; Weinhold, F. *Chem. Rev.* **1988**, *88*, 899–926.

55 (a) Vitaku, E.; Smith, D. T.; Njardarson, J. T. *J. Med. Chem.*, **2014**, *57*, 10257–10274. (b) Lamberth, C.; Dinges, J. *Bioactive Heterocyclic Compound Classes: Pharmaceuticals and Agrochemicals*; Wiley-VCH: Weinheim, Germany, **2012**.

- 
- 56 Cerecetto, H.; Gerpe, A.; González, M.; Arán, V. J.; de Ocariz, C. O. *Mini-Reviews in Medicinal Chemistry* **2005**, *5*, 869–878.
- 57 (a) Schmidt, A.; Beutler, A.; Snovydyovych, B. *Eur. J. Org. Chem.* **2008**, 4073–4095. (b) Zhang, S.-G.; Liang, C.-G.; Zhang, W.-H. *Molecules* **2018**, *23*, 2783–2824.
- 58 (a) Hunt, K. W.; Moreno, D. A.; Suiter, N.; Clark, C. T.; Kim, G. *Org. Lett.* **2009**, *11*, 5054–5057. (b) Lin, M.-H.; Liu, H.-J.; Lin, W.-C.; Kuo, C.-K.; Chuang, T.-H. *Org. Biomol. Chem.* **2015**, *13*, 11376–11381. (c) Haydl, A. M.; Breit, B. *Angew. Chem., Int. Ed.* **2015**, *54*, 7149–7153. (d) Slade, D. J.; Pelz, N. F.; Bodnar, W.; Lampe, J. W.; Watson, P. S. *J. Org. Chem.* **2009**, *74*, 6331–6334. (e) Luo, G.; Chen, L.; Dubowchik, G. *J. Org. Chem.* **2006**, *71*, 5392–5395.
- 59 Campetalla, S.; Palmieri, A.; Petrini, M. *Eur. J. Org. Chem.* **2009**, 3184–3188.
- 60 Ye, Y.; Kim, S.-T.; Jeong, J.; Baik, M.-H.; Buchwald, S. L. *J. Am. Chem. Soc.* **2019**, *141*, 3901–3909.
- 61 CYLview, 1.0b; Legault, C. Y., Université de Sherbrooke, 2009 (<http://www.cylview.org>)
- 62 Li, C.; Liu, R. Y.; Jesikiewicz, L. T.; Yang, Y.; Liu, P.; Buchwald, S. L. *J. Am. Chem. Soc.* **2019**, *141*, 5062–5070.
- 63 (a) Grayson, M. N.; Krische, M. J.; Houk, K. N. *J. Am. Chem. Soc.* **2015**, *137*, 8838–8850. (b) Mejuch, T.; Gilboa, N.; Gayon, E.; Wang, H.; Houk, K. N.; Marek, I. *Acc. Chem. Res.* **2013**, *46*, 1659–1669. (c) Kim, S. W.; Meyer, C. C.; Mai, B. K.; Liu, P.; Krische, M. J. *ACS Catal.* **2019**, *9*, 9158–9163
- 64 Schroter, S.; Stock, C.; Bach, T. *Tetrahedron* **2005**, *61*, 2245–2267.
- 65 Fairlamb, I. J. S. *Chem. Soc. Rev.* **2007**, *36*, 1036–1045.
- 66 Kapdi, A. R.; Prajapati, D. *RSC Adv.*, **2014**, *4*, 41245–41259.
- 67 Littke, A. F.; Dai, C.; Fu, G. C. *J. Am. Chem. Soc.* **2000**, *122*, 4020–4028.
- 68 Kamikawa, T.; Hayashi, T. *Tetrahedron Lett.* **1997**, *38*, 7087–7090.
- 69 Lyngvi, E.; Schoenebeck, F. *Tetrahedron*, **2013**, *69*, 5715–5718.

- 
- 70 Legault, C. Y.; Garcia, Y.; Merlic, C. A.; Houk, K. N. *J. Am. Chem. Soc.* **2007**, *129*, 12664-12665.
- 71 Garcia, Y.; Schoenebeck, F.; Legault, C. Y. Merlic, C. A.; Houk, K. N. *J. Am. Chem. Soc.* **2009**, *131*, 6632-6639.
- 72 (a) Yang, w.; Wang, T.; Corte, J. R. *Org. Lett.* **2003**, *5*, 3131-3134. (b) Dai, X.; Chen, Y.; Garrell, S.; Liu, H.; Zhang, L.; Palani, A.; Hughes, G.; Nargund, R. *J. Org. Chem.* **2013**, *78*, 7758-7763. (c) Strotman, N. A.; Chobanian, H. R.; He, J.; Guo, Y.; Dormer, P. G.; Jones, C. M.; Steves, J. E. *J. Org. Chem.* **2010**, *75*, 1733-1739.
- 73 Cho, C.-G.; Park, J.-S.; Jung, I.-H.; Lee, H. *Tetrahedron lett.* **2001**, *42*, 1065-1067.
- 74 (a) Ryu, K.; Gupta, A. K.; Han, J. W.; Oh, C. H.; Cho, C. G. *Synlett* **2004**, *12*, 2197-2199. (b) Lee, J.-H.; Park, J.-S.; Cho, C.-G. *Org. Lett.* **2002**, *4*, 1171. (c) Kim, W.-S.; Kim, H.-J.; Cho, C.-G. *J. Am. Chem. Soc.* **2003**, *125*, 14288.
- 75 Handy, S. T.; Zhang, Y. *Chem. Commun.* **2006**, 299-301.
- 76 Seeman, J. *Chem. Rev.* **1983**, *83*, 83-134.
- 77 McMullin, C. L.; Fey, N.; Harvey, J. N. *Dalton Trans.* **2014**, *43*, 13545-13556.
- 78 (a) Farina, V.; Kapadia, S.; Krishnan, B.; Wang, C.; Liebeskind, L. S. *J. Org. Chem.* **1994**, *59*, 5905-5911. (b) Beauperin, M.; Job, A.; Cattey, H.; Royer, S.; Meunier, P.; Hierso, J.-C. *Organometallics* **2010**, *29*, 2815-2822. (c) Aufiero, M.; Proutiere, F.; Schoenebeck, F. *Angew. Chem., Int. Ed.* **2012**, *51*, 7226-7230.
- 79 (a) Bililign, T.; Griffith, B. R.; Thorson, J. S. *Nat. Prod. Rep.* **2005**, *22*, 742-760. (b) Cañeque, T.; Gomes, F.; Mai, T. T.; Maestri, G.; Malacria, M.; Rodriguez, R. *Nat. Chem.* **2015**, *7*, 744-751. (c) Kang, H.; Ku, S.-K.; Jung, B.; Bae, J.-S. *Inflamm. Res.* **2015**, *64*, 1005-1021. (d) Marrassini, C.; Davicino, R.; Acevedo, C.; Anesini, C.; Gorzalczany, S.; Ferraro, G. *J. Nat. Prod.* **2011**, *74*, 1503-1507. (e) Shie, J.-J.; Chen, C.-A.; Lin, C.-C.; Ku, A. F.; Cheng, T.-J. R.; Fang, J.-M.; Wong, C.-H. *Org. Biomol. Chem.* **2010**, *8*, 4451-4462. (f) Ho, T. C.; Kamimura, H.; Ohmori, K.; Suzuki, K. *Org. Lett.* **2016**, *18*, 4488-4490. (g) Elshahawi, S. I.; Shaaban, K. A.; Kharel, M. K.; Thorson, J. S. *Chem. Soc. Rev.* **2015**, *44*, 7591-7697. (h) Manabe, S.; Ito, Y. *Trends Glycosci. Glycotechnol.* **2003**, *15*, 181-

---

196. (i) De Clercq, E. *J. Med. Chem.* **2016**, *59*, 2301–2311. (j) Singh, S.; Aggarwal, A.; Bhupathiraju, N. V. S. D. K.; Arianna, G.; Tiwari, K.; Drain, C. M. *Chem. Rev.* **2015**, *115*, 10261–10306.

80 Michael, A., *Am. Chem. J.* **1879**, *1*, 305–312.

81 Fischer, E., Ueber die Glucoside der Alkohole. *Ber. Deut. chem. Gesell.* **1893**, *26*, 2400–2412.

82 (a) Bokor, É.; Kun, S.; Goyard, D.; Tóth, M.; Praly, J.-P.; Vidal, S.; Somsák, L. *Chem. Rev.* **2017**, *117*, 1687–1764. (b) Štambaský, J.; Hocek, M.; Kočovský, P. *Chem. Rev.* **2009**, *109*, 6729–6764. (c) Jaramillo, C.; Knapp, S. *Synthesis* **1994**, *1*, 1–20. (d) Lee, D. Y. W.; He, M. *Curr. Top. Med. Chem.* **2005**, *5*, 1333–1350. (e) Gutmann, A.; Nidetzky, B. *Pure Appl. Chem.* **2013**, *85*, 1865–1877. (f) Du, Y.; Linhardt, R. J.; Vlahov, I. R. *Tetrahedron* **1998**, *54*, 9913–9959. (g) Barroso, S.; Lemaire, S.; Farina, V.; Steib, A. K.; Blanc, R.; Knochel, P. *J. Org. Chem.* **2016**, *81*, 2804–2816. (h) Lemaire, S.; Houpis, I. N.; Xiao, T.; Li, J.; Digard, E.; Gozlan, C.; Liu, R.; Gavryushin, A.; Diène, C.; Wang, Y.; Farina, V.; Knochel, P. *Org. Lett.* **2012**, *14*, 1480–1483. (i) Andrews, R. S.; Becker, J. J.; Gagné, M. R. *Angew. Chem. Int. Ed.* **2012**, *51*, 4140–4143. (j) Gong, H.; Gagné, M. R. *J. Am. Chem. Soc.* **2008**, *130*, 12177–12183. (k) Gong, H.; Sinisi, R.; Gagné, M. R. *J. Am. Chem. Soc.* **2007**, *129*, 1908–1909. (l) Yu, X.; Dai, Y.; Yang, T.; Gagné, M. R.; Gong, H. *Tetrahedron* **2011**, *67*, 144–151. (m) Adak, L.; Kawamura, S.; Toma, G.; Takenaka, T.; Isozaki, K.; Takaya, H.; Orita, A.; Li, H. C.; Shing, T. K. M.; Nakamura, M. *J. Am. Chem. Soc.* **2017**, *139*, 10693–10701. (n) dos Santos, R. G.; Jesus, A. R.; Caio, J. M.; Rauter, A. P. *Curr. Org. Chem.* **2011**, *15*, 128–148. (o) Mahling, J.-A.; Schmidt, R. R. *Synthesis* **1993**, *25*, 325–328.

83 Zhu, F.; Rourke, M. J.; Yang, T.; Rodriguez, J.; Walczak, M. A. *J. Am. Chem. Soc.* **2016**, *138*, 12049–12052.

84 Zhu, F.; Yang, T.; Walczak, M. A. *Synlett*, **2017**, *28*, 1510–1516.

85 (a) Lu, S.; Li, X.; Wang, A. *Catal. Today* **2000**, *63*, 531–536; (b) Hang, H. C.; Bertozzi, C. R. *J. Am. Chem. Soc.* **2001**, *123*, 1242–1243; (c) De Lederkremer, R. M.; Marino, C. *Adv. Carbohydr. Chem. Biochem.* **2007**, *61*, 143–216; (d) Pajak, B.; Siwiak, E.; Sołtyka, M.; Priebe, A.; Zieliński, R.; Fokt, I.; Ziemniak, M.; Jaśkiewicz, A.; Borowski, R.; Domoradzki, T. *Int. J. Mol. Sci.* **2020**, *21*, 234.

---

86 Bennett, C. S.; Galan, M. C. *Chem. Rev.* **2018**, *118*, 7931-7985

87 Selected recent reviews and examples of site-selective functionalization of carbohydrates: (a) Wang, H.-Y.; Blaszczyk, S. A.; Xiao, G.; Tang, W. *Chem. Soc. Rev.* **2018**, *47*, 681-701; (b) Dimakos, V.; Taylor, M. S. *Chem. Rev.* **2018**, *118*, 11457-11517; (c) Blaszczyk, S. A.; Homan, T. C.; Tang, W. *Carbohydr. Res.* **2019**, *471*, 64-77; (d) Dimakos, V.; Su, H. Y.; Garrett, G. E.; Taylor, M. S. *J. Am. Chem. Soc.* **2019**, *141*, 5149-5153.

88 For the synthesis of unsaturated or partially oxygenated 2-arylsugars, see: (a) Tenaglia, A.; Karl, F. *Synlett* **1996**, *1996*, 327-329; (b) Cobo, I.; Matheu, M. I.; Castellón, S.; Boutureira, O.; Davis, B. G. *Org. Lett.* **2012**, *14*, 1728-1731; (c) Kusunuru, A. K.; Jaladanki, C. K.; Tatina, M. B.; Bharatam, P. V.; Mukherjee, D. *Org. Lett.* **2015**, *17*, 3742-3745; (d) Probst, N.; Grelier, G.; Dahaoui, S.; Alami, M. d.; Gandon, V.; Messaoudi, S. *ACS Catal.* **2018**, *8*, 7781-7786; (e) Ghouilem, J.; Franco, R.; Retailleau, P.; ALAMI, M.; Gandon, V.; Messaoudi, S. *Chem. Commun.* **2020**, *56*, 7175-7178.

89 (a) Sugimura, H.; Osumi, K.; Koyama, T. *Chem. Lett.* **1991**, *20*, 1379-1382; (b) Robertson, J.; Green, S. P.; Hall, M. J.; Tyrrell, A. J.; Unsworth, W. P. *Org. Biomol. Chem.* **2008**, *6*, 2628-2635. (c) Richards, G. *J. Chem. Soc.*, **1955**, 2013-2016; (b) Hladezuk, I.; Olesker, A.; Cléophax, J.; Lukacs, G. *J. Carbohydr. Chem.* **1998**, *17*, 869-878.

90 (a) Ren, Y.; Jia, J.; Liu, W.; Wu, H. S. *Organometallics* **2013**, *32*, 52-62. (b) Álvarez, R.; Faza, O. N.; López, C. S.; de Lera, Á. R. *Org. Lett.* **2005**, *8*, 35-38. (c) Álvarez, R.; Pérez, M. n.; Faza, O. N.; de Lera, A. R. *Organometallics* **2008**, *27*, 3378-3389. (d) Martin, S. E.; Fernández, I.; Sosa Carrizo, E. D. *Organometallics* **2015**, *34*, 159-166. (e) Nova, A.; Ujaque, G.; Maseras, F.; Lledós, A.; Espinet, P. *J. Am. Chem. Soc.* **2006**, *128*, 14571-14578. (f) García-Melchor, M.; Braga, A. A. C.; Lledós, A.; Ujaque, G.; Maseras, F. *Acc. Chem. Res.* **2013**, *46*, 2626-2634. (g) Ariafard, A.; Yates, B. F. *J. Am. Chem. Soc.* **2009**, *131*, 13981-13991.

91 (a) Farina, V.; Krishnan, B. *J. Am. Chem. Soc.* **1991**, *113*, 9585-9595. (b) Littke, A. F.; Fu, G. C. *Angew. Chem. Int. Ed.* **1999**, *38*, 2411-2413. (c) Littke, A. F.; Schwarz, L.; Fu, G. C. *J. Am. Chem. Soc.* **2002**, *124*, 6343-6348. (d) Casado, A. L.; Espinet, P. *J. Am. Chem. Soc.* **1998**, *120*, 8978-8985. (e) Casado, A. L.; Espinet, P.; Gallego,

---

A. M. *J. Am. Chem. Soc.* **2000**, *122*, 11771–11782. (f) Del Pozo, J.; Carrasco, D.; Pérez-Temprano, M. H.; García-Melchor, M.; Álvarez, R.; Casares, J. a.; Espinet, P. *Angew. Chem., Int. Ed.* **2013**, *52*, 2189–2193.

92 Espinet, P.; Echavarren, A. M. *Angew. Chem. Int. Ed.* **2004**, *43*, 4704–4734.

93 Hicks, J. D.; Hyde, A. M.; Cuezva, A. M.; Buchwald, S. L. *J. Am. Chem. Soc.* **2009**, *131*, 16720–16734.

94 Han, F.-S. *Chem. Soc. Rev.* **2013**, *42*, 5270–5298.

95 Hu, X. *Chem. Sci.* **2011**, *2*, 1867–1886.

96 Singh, S.; Sunoj, R. B. *The Journal of Physical Chemistry A* **2019**, *123*, 6701–6710.

97 (a) Sommer, H.; Juliá-Hernández, F.; Martin, R.; Marek, I. *ACS Cent. Sci.* **2018**, *4*, 153–165; (b) Janssen-Müller, D.; Sahoo, B.; Sun, S. Z.; Martin, R. *Isr. J. Chem.* **2020**, *60*, 195–206.

98 Spin-center shift is broadly defined as shifting the position of the radical center to another atom in the course of the reaction. (a) Wessig, P.; Muehling, O. *Eur. J. Org. Chem.* **2007**, *2007*, 2219–2232; (b) Jin, J.; MacMillan, D. W. *Nature* **2015**, *525*, 87–90; (c) Nacsa, E. D.; MacMillan, D. W. *J. Am. Chem. Soc.* **2018**, *140*, 3322–3330; (d) Dimakos, V.; Gorelik, D.; Su, H. Y.; Garrett, G. E.; Hughes, G.; Shibayama, H.; Taylor, M. S. *Chem. Sci.* **2020**, *11*, 1531–1537.

99 For selected examples of Ni-catalyzed MCC via 1,6-spin-center shift, see: (a) Powell, D. A.; Maki, T.; Fu, G. C. *J. Am. Chem. Soc.* **2005**, *127*, 510–511; (b) Phapale, V. B.; Buñuel, E.; García-Iglesias, M.; Cárdenas, D. J. *Angew. Chem. Int. Ed.* **2007**, *46*, 8790–8795.

100 Luchini, G.; Alegre-Requena, J. V.; Funes-Ardoiz, I.; Paton, R. S. *F1000Research*, **2020**, *9*, 291.

101 (a) Dupuis, J.; Giese, B.; Rüegge, D.; Fischer, H.; Korth, H. G.; Sustmann, R. *Angew. Chem. Int. Ed.* **1984**, *23*, 896–898; (b) Abe, H.; Shuto, S.; Matsuda, A. *J. Am. Chem. Soc.* **2001**, *123*, 11870–11882.

102 Huber, G. W.; Iborra, S.; Corma, A. *Chem. Rev.* **2006**, *106*, 4044–4098.

103 Thebtaranonth, C.; Thebtaranonth, Y. *Cyclization Reaction* (CRC Press, ed. 1, 1993).

104 Cornella, J.; Zarate, C.; Martin, R. *Chem. Soc. Rev.* **2014**, *43*, 8081–8097.

- 
- 105 Su, B.; Cao, Z. C.; Shi, Z. J. *Acc. Chem. Res.* **2015**, *48*, 886–896.
- 106 Ranu, B. C.; Bhar, B. C. *Org. Prep. Proced. Int.* **1996**, *28*, 371–409.
- 107 Pachaly, B.; West, R. *Angew. Chem. Int. Ed.* **1984**, *23*, 454–455.
- 108 Mammen, M.; Shakhnovich, E. I.; Deutch, J. M.; Whitesides, G. M. *J. Org. Chem.* **1998**, *63*, 3821–3830.
- 109 Kosak, T. M.; Conrad, H. A.; Korich, A. L.; Lord, R. L. *Eur. J. Org. Chem.* **2015**, *2015*, 7460–7467.
- 110 Korch, K. M.; Watson, D. A. *Chem. Rev.* **2019**, *119*, 8192–8228.
- 111 Yamamoto, A.; Suginome, M. *J. Am. Chem. Soc.* **2005**, *127*, 15706–15707.
- 112 Chow, W. K.; Yuen, O. Y.; Choy, P. Y.; So, C. M.; Lau, C. P.; Wong, W. T.; Kwong, F. Y. *RSC Advances* **2013**, *3*, 12518–12539.
- 113 Funes-Ardoiz, I.; Nelson, D. J.; Maseras, F. *Chem. Eur. J.* **2017**, *23*, 16728–16733.
- 114 (a) Bartmess, J. E. *J. Phys. Chem.* **1994**, *98*, 6420–6424. (b) Bartmess, J. E. *J. Phys. Chem.* **1995**, *99*, 6755–6755.
- 115 Lin, Q.; Diao, T. *J. Am. Chem. Soc.* **2019**, *141*, 17937–17948.